



Printing quality assessment by image processing and color prediction models

David Nébouy

► To cite this version:

David Nébouy. Printing quality assessment by image processing and color prediction models. Image Processing [eess.IV]. Université Jean Monnet - Saint-Etienne, 2015. English. NNT : 2015STET4018 . tel-01624275

HAL Id: tel-01624275

<https://theses.hal.science/tel-01624275>

Submitted on 26 Oct 2017

HAL is a multi-disciplinary open access archive for the deposit and dissemination of scientific research documents, whether they are published or not. The documents may come from teaching and research institutions in France or abroad, or from public or private research centers.

L'archive ouverte pluridisciplinaire **HAL**, est destinée au dépôt et à la diffusion de documents scientifiques de niveau recherche, publiés ou non, émanant des établissements d'enseignement et de recherche français ou étrangers, des laboratoires publics ou privés.

Ecole doctorale n° 488 : Science Ingénierie et Santé.

Thèse présentée en vue de l'obtention du diplôme de
docteur de l'université Jean Monnet, Université de Lyon

Spécialité Image, Vision et Signal

Par

David Nébouy

Intitulée

Printing quality assessment by image processing and color prediction models

Directeur de these: Thierry Fournel, encadrants: Mathieu Hébert, Jean-Luc Lesur.

Saint-Etienne, FRANCE, 16 Décembre 2015

Membres du Jury:

Dr. Anne Blayot	Ecole internationale du papier, de la communication imprimée et des biomatériaux Grenoble INP – Pagora, FRANCE	Rapporteur
Prof. Franck Marzani	Laboratoire Le2i, UFR Sciences et Techniques, FRANCE	Rapporteur
Dr. Lionel Simonot	Institut Pprime, Université de Poitiers, CNRS UPR 3346, FRANCE	Rapporteur
Prof. Thierry Fournel	Laboratoire Hubert Curien, UMR 5516 CNRS, FRANCE	Directeur de Thèse
Prof. Dinu Coltuc	Univ. Valahia Targoviste, ROUMANIE	Président de Jury
Dr. Mathieu Hébert	Laboratoire Hubert Curien, UMR 5516 CNRS, FRANCE	Examineur
Mr. Jean-Luc Lesur	Gemalto S.A., Gémenos, FRANCE	Examineur
Mr. Joseph Leibenguth	Gemalto Oy, Vantaa, FINLANDE	Examineur

Acknowledgements

As a CIFRE PhD student, I had the chance to discover both the research and academic world, and also the company and engineering world. On the one hand, I am grateful to the Hubert Curien Laboratory which endorsed me in the ERIS group in partnership with Institut d'Optique Graduate School, Saint-Etienne; and on the other hand, to Gemalto S.A. for offering me this position.

I would like to thank first my PhD director, Prof. Thierry Fournel, who recommended me for this work, for his leadership of my PhD. Then, I am thankful for my academic supervisor, Dr. Mathieu Hébert, for countless discussions and reflections on my work. A big thank to Mr. Jean-Luc Lesur, for teaching me so much about laser use for the development of new industrial printing technologies. I also appreciated working with Youssiph, Nina, and Jérôme also from the Color Laser Marking team, managed by Dr. Isabelle Limousin. I would like also to cite my other colleagues of the Innovation Manufacturing Technologies department, David, Eric, Stephane, Fangyao, Julien, Frédéric, Laurent, Sébastien, Olivier, Thierry, and François, managed by Mr. David Byrne.

I would also like to address my heartfelt thanks

to Mr. Joseph Leibenguth, for interesting discussions regarding the printing technologies, and for trusting me along all these three years.

to Prof. Jean-François Bassereau, for his coaching on sensory metrology.

to Dr. Renée Charrière and Dr. Victorien Raulot, two post-doctorants with who I shared my laboratory office, for their help and advice in image processing, color science, and optics fields.

to Claude, for his funny anecdotes and stories he told me during coffee breaks.

to Dr. Hubert Konik, for giving me the opportunity to teach during a couple of lab sessions of image processing courses for engineering school students.

and to Sophie, my brother, and to my parents, for their love and encouragement.

Saint-Etienne, FRANCE, July, 4th 2015.

Abstract

Printing, though an old technique for surface coloration, considerably progressed these last decades especially thanks to the digital revolution: images are now generated or transformed by software, resolution and color management are improved, and most printing systems are now automated with a good reproducibility. Consequently of this progress and of the large spreading of printed images, customers have higher expectations in terms of *quality* regarding the visual rendering. Scientific concern for *printing quality* is recent. The current emergence of quality requirements in the printing domain follows the path drawn a few years ago in the digital color imaging domain, when compressed images started to flood the internet. In both cases, printing and compression have an impact on the way the original digital image is reproduced. Professionals who want to meet the demands of their clients thus want to know to which extent human observers are sensitive to the degradation of an image, and how the printing process can be optimized in order to provide images preferred by most customers. Such questions regarding the perceived quality of a reproduced image can be split into two different topics: the *printing quality* as capacity of a printing system of accurately reproduce an original digital image, and the *printed image quality* which results from both the reproduction quality and the quality of the original image itself. The first concept relies on physical analysis of the way the original image is deteriorated when transferred onto the support, and we propose to couple it with a sensorial analysis, which aims at assessing perceptual attributes by giving them a value on a certain scale, determined with respect to reference samples classified by a set of observers. The second concept includes the degradation due to the printing plus the perceived quality of the original image, not in the scope of this work. In this report, we focus on the *printing quality concept* and propose assessment tools based on image processing and optical models.

Our approach first consists in the definition of several printing quality indices, based on measurable criteria using “objective” image processing algorithms on a printed-then-scanned image. For each index, the measuring range will be addressed thanks to a comparison of various quality levels on our metric scale, and validated by the confrontation of the obtained scores with sensory metrology experiments.

In this report, we start from a study of the human vision and the state of the art concerning the notion of image quality in order to highlight the most relevant criteria used in our natural and subjective human judgment. We retained the following characteristics: The first one is the tone homogeneity, specifically selected as one of the most relevant attributes of printing quality; it is evaluated thanks to image processing algorithms from a scanned image of the printed surface, i.e., the computation of gray level co-occurrence matrices and of a homogeneity attribute inspired of Haralick’s parameters, by taking into account the viewing distance to comply with human vision. The second selected attribute is the edge sharpness. In contrast with homogeneity which needs printing homogenous images, it can be directly measured from natural printed images, being given the original digital image. The algorithm relies on edges detector in both original and scanned images, then on the measurement of the edge smoothness in both images and a comparison between the smoothness in the two images provides information on how much the edge has been blurred or transformed by the printing. Then, the study of color has been addressed, in order to define a third attribute: the colorfulness, which is not mandatory for good printing quality but may be impor-

tant in some applications, for example portrait reproduction on ID cards using the innovative printing technology based on laser, called Color Laser Marking. By using color prediction models necessitating a rather low number of printed color patches, we assessed the quantity of color reproduced in a print, considering the prediction of a Dye Diffusion Thermal Transfer (D2T2) print as reference. Regarding the CLM printing technique, an original prediction model, combining physical flux-transfer model and learning method for its calibration, was developed.

For these three attributes, tone homogeneity, edge sharpness and colorfulness, psycho-visual experiments were carried out in order to be sure that the automated evaluation of the attributes mentioned above is consistent with the human perception. We followed a method proposed by Depledge which consists in asking to a panel of observers to freely position the samples on a metric scale according to their opinion of quality, from 0 m (worst) to 1 m (best). In conclusion, the matching was successful, as the scores given by our objectives methods follow rather well the positioning of the samples by the observers on the metric scale. An interesting following work would be the combination of these different indices to reach a final global score.

This PhD work was made in the Hubert Curien Laboratory, University Jean-Monnet of Saint-Etienne, University of Lyon, in partnership with Gemalto S.A. company.

Keywords

Print quality assessment; Quality index; Quality attributes; Uniformity; Edge sharpness; Human Visual System; Appearance; Scanner; Color printing technologies; Reflection; Color; Image reproduction.

Résumé

L'impression, bien qu'étant une technique ancienne pour la coloration de surfaces, a connu un progrès considérable ces dernières années essentiellement grâce à la révolution du numérique: les images sont désormais générées ou transformées par logiciel, la résolution et les couleurs sont améliorées, et la plupart des systèmes d'impression sont désormais automatisés avec une bonne reproductibilité. En conséquence d'un tel progrès et de cette large diffusion des images imprimées, les clients sont amenés à avoir des attentes toujours plus hautes en termes de *qualité* du rendu visuel. L'intérêt scientifique à propos de la *qualité de l'impression* est récent. L'émergence des exigences de qualité dans le domaine de l'impression suivent le chemin tracé il y a quelques années dans le domaine des images couleur numériques, lorsque des images compressées ont commencé à être massivement diffusées sur internet. Dans ces deux cas, l'impression et la compression ont un impact direct sur la façon dont l'image numérique de départ est reproduite. Les professionnels souhaitant remplir les exigences de leurs clients veulent donc savoir dans quelle mesure des observateurs humains sont sensibles à la dégradation d'une image, et comment optimiser le procédé d'impression afin de fournir des images plus agréables à l'œil de leurs clients. De telles questions concernant la qualité perçue d'une image reproduite peuvent être séparées en deux sujets différents: *La qualité de l'impression*, comme la capacité d'un système d'impression à reproduire fidèlement l'image d'origine, et *la qualité d'une image imprimée*, résultant à la fois de la qualité de reproduction, mais aussi de la qualité même de l'image numérique d'origine. Ce premier concept repose sur une analyse physique de la façon dont l'image d'origine est dégradée lors de son transfert sur un support, et nous proposons de la coupler avec une analyse sensorielle, visant à évaluer des attributs perceptuels et leur donner une valeur sur une certaine échelle, déterminée par des échantillons de référence classés par un ensemble d'observateurs. Le second concept inclut cette dégradation due à l'impression mais aussi la qualité perçue de l'image d'origine, qui ne fait pas parti de notre étude. Dans ce rapport, nous nous intéressons particulièrement au *concept de la qualité d'impression*, et proposons des outils d'évaluation basés sur le traitement d'image et sur des modèles optiques.

Notre approche consiste d'abord à définir les différents indices de qualité, basés sur des critères mesurables en utilisant des algorithmes "objectifs" de traitement d'image, sur une image imprimée-scannée. Pour chaque indice, l'étendue de mesure sera étudiée à travers une comparaison de divers niveaux de qualité sur notre échelle, et validée par la confrontation des scores obtenu avec des expériences de métrologie sensorielle.

Dans ce rapport, nous commençons par une étude sur la vision humaine, ainsi que l'état de l'art sur la notion de qualité d'image, dans le but de souligner les critères les plus pertinents utilisés dans notre jugement humain, naturel et subjectif. Nous retenons les éléments suivant : l'homogénéité d'un aplat, spécifiquement sélectionné comme l'un des attributs les plus pertinents de la qualité de l'impression; est évalué grâce à des algorithmes de traitement d'image à partir d'une image scannée d'une surface imprimée, c'est à dire, par le calcul d'une matrice de cooccurrence et d'un attribut d'homogénéité inspiré d'un paramètre d'Hara-lick, et prenant en compte la distance de visualisation afin d'être conforme à la vision humaine. Le second critère retenu concerne la finesse des contours. Contrairement à l'homogénéité d'un aplat nécessitant l'im-

pression d'images homogènes, ce critère peut être évalué directement à partir d'une image naturelle, connaissant l'image numérique d'origine. L'algorithme repose sur un détecteur de contours à la fois dans l'image d'origine, ainsi que dans l'image scannée, puis sur la mesure de la netteté des contours dans les deux images, pour ensuite les comparer, ce qui donne une information sur le degré de flou introduit par le système d'impression sur ce contour. Enfin, une étude sur la couleur a été menée, dans le but de définir un troisième critère, l'éclat des couleurs (ou quantité de couleur reproduite), qui n'est pas obligatoire pour une bonne qualité d'impression, mais qui peut être importante dans certaines applications, par exemple, la reproduction de portrait sur des cartes d'identité en utilisant une technologie d'impression innovante basée sur l'utilisation de lasers, appelée Color Laser Marking (CLM). Par l'utilisation de modèles de prédiction couleur nécessitant l'impression d'un nombre assez réduit de carrés de couleur, nous évaluons la quantité de couleur reproduite dans un échantillon en considérant celle d'une impression Dye Diffusion Thermal Transfer (D2T2) comme référence. A propos de la technique d'impression CLM, un modèle original de prédiction a été développé, combinant un modèle physique de transferts de flux ainsi que des méthodes d'apprentissage pour sa calibration.

Pour ces trois attributs, l'homogénéité d'aplat, la netteté des contours, et l'éclat des couleurs reproduites, des expériences psycho-visuelles ont été menées dans le but d'aboutir à une évaluation automatique de ces critères conforme à la perception humaine. Nous avons suivi une méthode proposée par Depledge qui consiste à interroger un panel d'observateurs et leur demander de positionner librement les échantillons sur une échelle métrique selon leur opinion de leur qualité, de 0 m (le pire) à 1 m (le meilleur). En conclusion, l'appariement est réussi, car les scores donnés par nos méthodes objectives suivent assez bien le positionnement des échantillons sur l'échelle métrique par les observateurs. Une intéressante perspective de travail futur serait la combinaison de ces différents indices pour atteindre un score final global.

Cette thèse a été réalisée au sein du Laboratoire Hubert Curien, Université Jean-Monnet de Saint-Etienne, Université de Lyon, en partenariat avec l'entreprise Gemalto S.A.

Mots-clés

Evaluation de la qualité de l'impression; Indice de qualité; Attribut de qualité; Uniformité, Finesse des contours; Système visuel humain; Apparence; Scanner, Technologies d'impression couleur; Réflexion; Couleur; Reproduction d'image.

Contents

Acknowledgements.....	iii
Abstract	v
Keywords	vi
Résumé	vii
Mots-clés	viii
General Introduction.....	15
 I. Fundamentals for printed surface assessment	 17
Chapter 1 Spatial image attributes.....	19
1.1 Texture.....	19
1.1.1 Statistical methods	22
1.1.2 Frequential methods	28
1.2 Edges	30
Chapter 2 Perception & colorimetry.....	35
2.1 Human vision	35
2.2 Around the concept of color - CIE experiments & principals laws	39
2.2.1 Definition of color	39
2.2.2 Color-mixing based systems	42
2.2.3 Color perception based systems.....	43
2.2.4 Color matching based systems – The CIE experiments	46
2.2.5 Color tolerancing	52
Chapter 3 Measurement of colored surfaces.....	55
3.1 Flatbed color image scanner	55
3.1.1 Introduction	55
3.1.2 Colorimetric characteristics of the system	58
3.1.3 Spatial characteristics of the system	61

3.1.4	Correction of color drifts of the acquisition system	65
3.2	Spectrophotometer	73
Chapter 4	Color prediction	77
4.1	Absorption in non scattering media	77
4.2	Highly scattering media	78
4.3	Williams-Clapper model.....	85
4.4	Berns' equation.....	86
II.	Attributes for printed images quality assessment	89
Chapter 5	Tone homogeneity index	91
5.1	Introduction	91
5.2	Digitalization of the prints	92
5.3	Background: Image homogeneity analysis	92
5.4	Overview of the method	93
5.5	Pre-processing.....	94
5.6	Application of the image homogeneity analysis method	96
5.7	Construction of the objective Score	97
5.8	Referenced parameters of the method	97
5.9	Experimental testing and comparison with psycho-visual assessment.....	98
5.10	Influence of the size of the studied area	101
5.11	Conclusion.....	102
Chapter 6	Edge sharpness index.....	103
6.1	Introduction	103
6.2	Digitalization of the prints	103
6.3	Overview of the method	103
6.4	Color correction & Pre-processing.....	104
6.5	Application of the edge detection method.....	113
6.6	Computation of the objective sharpness score	115
6.7	Experimental testing and comparison with psycho-visual assessment.....	119
6.8	Conclusion.....	121
Chapter 7	Colorfulness index.....	123
7.1	Introduction	123

7.2	Digitalization of the prints	124
7.3	Overview of the method	124
7.4	Pre-processings	125
7.5	Application of the color prediction models	125
7.6	Computation of the objective colorfulness score	126
7.7	Experimental testing and comparison with psycho-visual assessment.....	132
7.8	Conclusion.....	135
III.	Color prediction models for innovative printing technologies	137
Chapter 8	Prediction of the spectral reflectance of laser-generated color prints.....	138
8.1	Introduction	138
8.2	Application of Berns' equation to D2T2- and CLM-printed cards.....	141
8.3	Application of the method on virtual primaries obtained by PCA.....	144
8.4	From RGB color to spectral reflectance	147
8.5	Performances & accuracy testing	150
8.6	Conclusion.....	151
Chapter 9	CLM-Print simulator.....	153
9.1	Introduction and objectives.....	153
9.2	Development of CLMviewer	155
9.3	First start in CLMviewer	155
9.4	Conclusion.....	157
	General Conclusion	159
	Appendix	163
	List of Figures	170
	References	176

“Anyone who has never made a mistake has never tried anything new.”, “Any fool can know. The point is to understand.”

— Albert Einstein

General Introduction

Printing technologies are in constant evolution for these last decades especially thanks to the digital revolution which provides a large panel of printing solutions for image reproduction [1], and an automation of the processes in order to help or even substitute the traditional expertise of the printman. With this rapid evolution, the quality of color images reproduced on hard supports has considerably increased. This leads to an issue for comparing the different techniques in terms of quality, an intuitive concept that is generally well appreciable visually but difficult to assess by measurable quantities. This thesis also grew out in a context where industrial are more and more needy of automated perceptual assessments of quality. The quality of a product is often defined by its aptitude to satisfy the needs or queries expressed by the customers. For a long time, the customer judged products essentially through their aptitude to meet the demand on its main functionality. Henceforth, they have higher expectations, and look for additional requirements such as an irreproachable appearance [2]. In order to follow this evolution, industry needs automated quality assessment methods in place of the usual methods based on human observation by experts. In the present work, Gemalto S.A. worldwide leader in digital security, sought to develop a new printing quality assessment tool for their ID document printing activities in the Government Program department. A constant printing quality is required on all their production sites. This tool could be a help to measure the quality of production and setup the machines but also rank their new printing technology on polycarbonate cards with respect to other competing technologies. This work thus investigates the way of assessing with physical and digital concepts the notion of printing quality, with the aim of providing an automated evaluation tool.

Scientific concern for printing quality is recent. In 2009 the printing quality is explored in [3] by defining various quality attributes: color, lightness, sharpness, contrast, physical, artifacts. These attributes were estimated from psycho-visual experiments carried out by a panel of 15 observers with various expertises. In contrast with Pedersen et al. [4, 5], we believe that an important distinction should be made between *printing quality*, which is related to the degradation of an original digital image when transferred to the printing support, and *printed image quality*, which includes the printing quality but also involves the perceived quality of the original (digital) image. In [3, 6], Pedersen et al. focused on the perceptual aspect but avoid the explanation of the objective assessment. Later, in [4], they recalled various frameworks to use image quality metrics on prints, and proposed a new one. But once again, no distinction is made between image quality and print quality. In 2012 [5], Gong and Pedersen address the combination of local features obtained by objective image quality assessment algorithms computed on local regions of the image. They propose to use spatial pooling methods to combine five identified quality attribute. Regarding their quality attribute, our opinion is that contrast, lightness, and color rather qualify the image quality. Then, in 2013, another work dedicated to the offset colour printing presents 25 color quality attributes to objectively assess an offset print, in particular dot deformation, misregistration, contrast, ink density are addressed [7].

From a more conceptual point of view, the study of printing quality is founded on three different conceptions of image that blend together in this study: Firstly, we can consider the image in the digital sense, as an array of entries, on which computation can be done thanks to digital algorithms. Besides the printed image is rather to be considered on a physical way, as a planar object whose optical properties vary along the surface, and also according to the depth within the object, leading to the study of physical mod-

els. As a third point of view, the object appearance is assessed according to the mental representation that an observer creates by viewing the object. These three conceptions of image, the digital image, the physical image, and the perceived image, will appear throughout this work: we will deal with low-level algorithm on images in order to study, for example, homogeneity or sharpness of printed images; with physical model, in order to predict for example the color rendering; and with human perception through experimental assessment by observers. Of course, the relationship between these different concepts will also be addressed: digitalization of printed images is a conversion of physical image into digital image, and the way the physical information is preserved in the digital image will be studied, especially regarding color. Conversely, printing means most often today the conversion of a digital image into a physical image, and this is precisely the degradation of the digital image quality due to the printing that we want to evaluate. Moreover, we will study the transformation of a RGB digital color into a surface with a given spectral reflectance. The relationship between perceived image or its mental representation and digital or physical image has been less investigated in this work, but it will be present through the psycho-visual experiments where the quality scores that we propose, issued from computations based on either digital or physical methods, will be compared to perceptual evaluations by observers. The confrontation of these three conceptions of image is the interesting but challenging background of this work.

This report is divided into three main parts. The first one presents some fundamentals for the assessment of printed surfaces, starting with some basic concepts of image processing needed by our development, supplemented by an outline about human perception and colorimetry, continued with a study on measurement of colored surfaces tools, and finally ended by a presentation of some color prediction models for printed surfaces. Then, the second part presents our main contribution on printing quality assessment, regarding the three main quality indices we highlighted: tone homogeneity, edge sharpness, and colorfulness. Criteria will be successively presented, to assess the quality of printed samples where a large panel of printing technologies will be addressed, from desktop inkjet on paper, to Dye Diffusion Thermal Transfert (D2T2) printing system on PVC or polycarbonate cards, passing through desktop laser printer, with various type of substrates. In this part, the physical aspect of the image will predominate. Finally, we conclude this report in a third part concerning our main contributions regarding the optical color prediction models dedicated to new industrial printing processes used and mainly developed at Gemalto S.A.

First Part

Fundamentals for printed surface assessment

Chapter 1 Spatial image attributes

Nowadays, image is everywhere, as it is confirmed in our everyday life by new digital technologies or even in the industry with the development of artificial vision. Image processing and computer vision sciences have been developed in parallel to meet the increasing need of automated image understanding. The main objective of these techniques is to produce new technologies able to recover semantic information from a simple digital image. But human vision, probably the smartest in this world, is difficult to reproduce artificially. A veritable semantic gap is drawn up between the input of a simple digital image capture from a camera, and the Grail of image understanding by a machine. This idyllic objective meets the one of artificial intelligence science. Three main levels of processes are commonly listed [8]: At a low level side, the *image processing* covering the concepts of image filtering, contrast enhancement, or image sharpening. In practice, the input and output are images. Then, there is an intermediate level named *image analysis*, gathering the disciplines of segmentation, shape descriptors, or point detectors. Here, the input is a digital image, and the output corresponds to numerical attributes. Finally, the high level, *image understanding*, corresponds to pattern recognition, and semantic approaches, where an output verdict is expected at the end. The main question relies on the desire to know on which criteria our “recognition” is based. A panel of image tools is available to reach our objectives at the end in terms of image classification through attributes such as shape, segmentation, color, or texture.

1.1 Texture

Texture is usually considered in two different fields: image synthesis, and image analysis. In image synthesis, the texture is an image corresponding to a surface, which is mapped to 3D mesh in order to improve the visual aspect after rendering of the scene. This is not the scope of this work. *Image analysis* focuses on image processing on a given image in order to extract some features. This notion of texture in the image analysis sense is difficult to define. An intuitive description of the context is explained in the following lines: Until now, we were defining a region as a homogeneous area, and an edge as an intensity variation. A texture could be characterized as a region with intensity variations. There is also an importance in the spatial pixels organisation. There is no mathematical definition universally recognized. In 1979, in *Statistical and Structural Approaches to Texture*, Haralick gives the following definition: “An image texture is described by the number and types of its primitives and the spatial organization or layout of its primitives” [9]. In 1981, Zucker et al. come back to the difficulties for proposing a correct definition. “Texture is an apparently paradoxical notion. On the one hand, it is commonly used in the early processing of visual information, especially for practical classification purposes. On the other hand, no one has succeeded in producing a commonly accepted definition of texture”. According to Maître, mathematical definitions for texture are either too general or imprecise, either too restrictive to fit the diversity of encountered cases. Nevertheless, we notice a high connexion with the human vision. In “Le traitement des images”, Hermes Science Publications [10], 2003, Maître gives the following definition: « A texture is a field of the image that appears as a coherent and homogeneous domain, i.e. forming a whole for an observer. ».

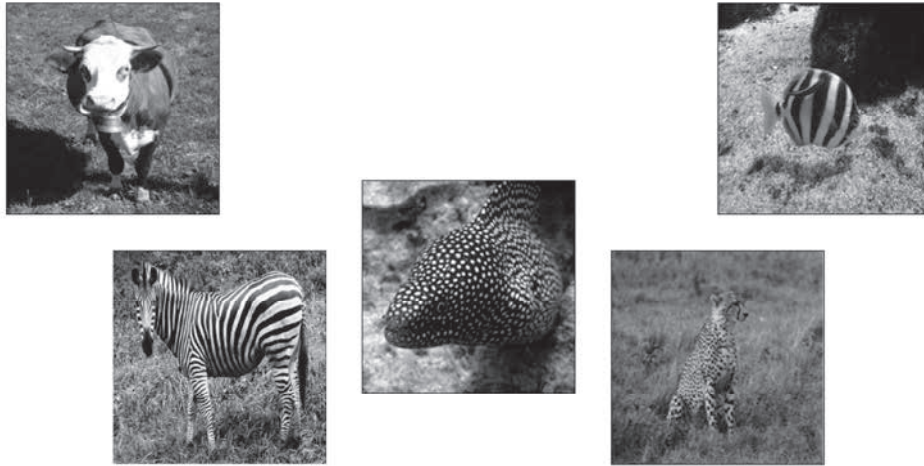


Figure 1. Examples of natural textural objects.

The capacities of the human visual system to distinguish the different textures are remarkable but very poorly explained. Figure 2 shows an example of “natural” interpretation.

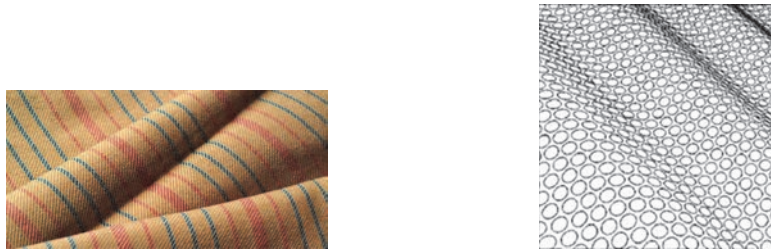


Figure 2. “Natural” interpretations of textures.

Textures can however be characterised by a common property of a set of pixels known under the denomination of “primitive”. They can be classified into two groups, regular textures or random textures, corresponding to different approaches for description.

A periodical texture is characterized by a periodicity of a pattern which is invariant by translation. Most of the time, it corresponds to artificial textures or human made constructions. Spectral approaches are appropriated.



Figure 3. Example of periodical texture, containing Repetitive Texture Elements (Texels).

In contrast with such a periodicity, random textures present intensity distribution without any apparent regularity. It is a mess, with however a certain visual homogeneity. Usually, probabilistic approaches are appropriate.

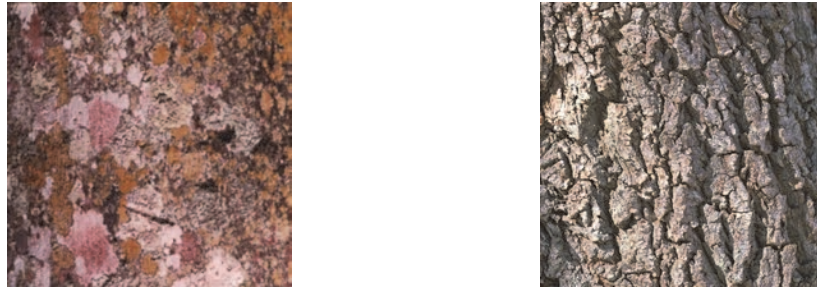


Figure 4. Example of random texture with homogeneous statistical properties.

Nevertheless, the boundary between these two categories is not always clear. Some textures are never strictly periodical, neither completely random.



Figure 5. Between random and periodical textures.

Either the pattern or the repetition law is random, and the other is not. The pattern can vary according to the position, while keeping the same characteristics, or the repetition law can change. This nevertheless gives an impression of apparent homogeneity.

In the study of textures, different scale levels should be considered. At low scale, we focus on small details, and at high scale, on coarse areas. Most of the time, a texture is composed of micro textures, with pixel-size primitive pattern, and macro textures, with extractible clusters. The difficulty lies in the separation of the texture and the primitive itself, as well as in the layout of these primitives.



Figure 6. Notion of scale in Texture analysis.

As the definition of a texture is not precise, the community brought some reference databases. One of the famous one is the Brodatz database [11], published in 1966 by P. Brodatz, and created for art and design. Let us cite some others created for research applications as VisTex database [12], which intends to provide free high quality textures. The Outex database provides both surfaces and natural scene textures dedicated to texture analysis algorithms, and for help in their development and empirical evaluation, [13, 14]. The CuRRET database, proposed by Columbia and Utrecht Universities groups three databases of reflectance and texture.

The two main operations with textures are classification, and segmentation. Classification aims at assigning a texture to the nearest texture in a database. There is no need to recognize primitives, but just look which image is the closest. Classification is made with respect to reference textures, and segmentation with respect to referenced criteria. The goal in both cases is to obtain a verdict on similarity/non-similarity for a given texture with other ones. There is no universal method, and as in image processing, the method has to be selected according to the objectives and the context (robustness to rotations, to a change in lighting, etc...).

1.1.1 Statistical methods

The general scheme of statistical methods is summarized as follows. A certain neighbourhood of “appropriate” size and shape is defined around a pixel (i, j) of the image I . Features are computed on each neighbourhood of I . Pixels are classified, using eventually a dimensionality reduction. Several approaches are proposed in the literature, from the study of histograms, to Local Binary Patterns [15, 16], passing through Co-occurrence matrices [17], and Run-Length matrices [18].

First, the histogram tool is the simplest. It represents the gray level repartition in the image. The shape of the histogram is characteristic of some components in the image as the background, some particular object, or also image noise. For an image encoded on B bytes, the histogram size is 2^B .

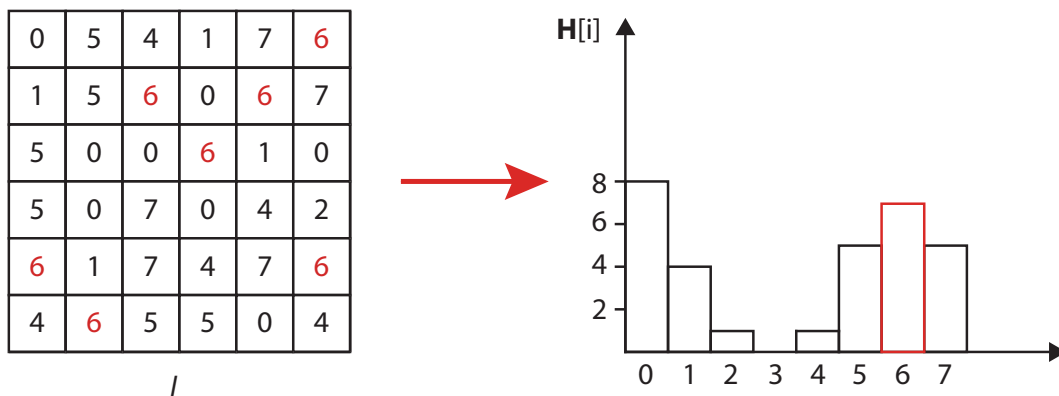


Figure 7. An Histogram: A graphical representation of the gray level distribution.

The histogram can be assimilated to a probability distribution. Quantifications are possible. The histogram is thereafter used to calculate distances between various histograms, by histogram intersection (normalized or combined histograms), or by Manhattan distance [19, 20]. However, it should be noticed that often the only histogram is not enough. Very different textures are sometimes characterized by very similar his-

tograms. The histogram is only representative of the distribution of pixels in the image without regard to their spatial arrangement. We can try to go to local histograms, but often this is insufficient and problematic: a window size has to be specified. Often statistics from the histogram are unreliable. When applied to texture, we can encounter some special cases where we see the histogram limits, for example in Figure 8.

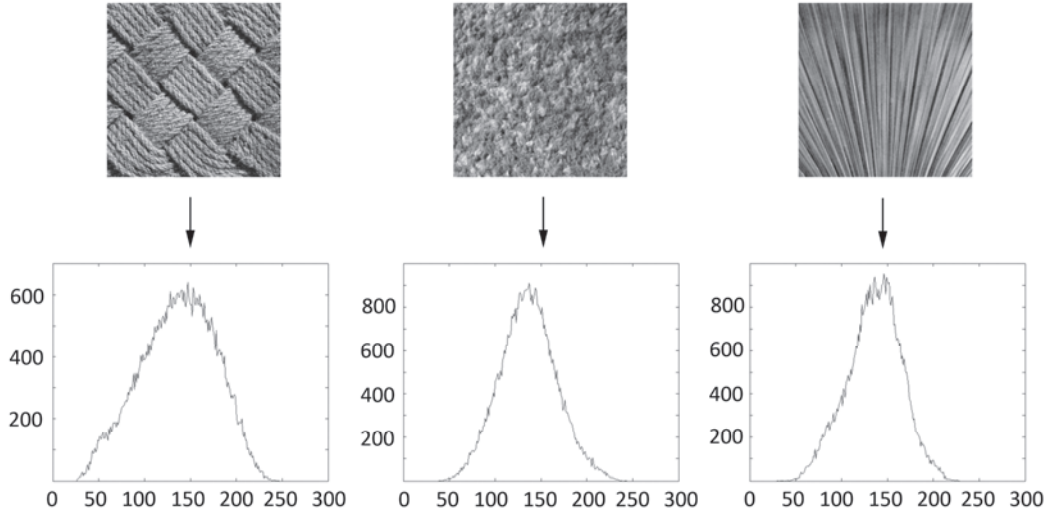


Figure 8. Different textures presenting close histograms.

We can deduce that the histogram, alone, is not sufficient to discriminate textures. Some attempts on local histograms can be tested, but let's continue the study with more powerful tools.

The histogram is a first-order statistic tool. By definition, it takes into account only one pixel at a time.

The moment of order k (not centred) is defined as follow:

$$\mu_k = \sum_{i=0}^{255} i^k p(i), \quad (1.1)$$

where $p(i)$ corresponds to the probability of occurrence of pixel value i in the image. The famous one is the average denoted μ_1 . By centering the data, we obtain

$$\tilde{\mu}_k = \sum_{i=0}^{255} (i - \mu_1)^k p(i), \quad (1.2)$$

leading to the well-known variance: $\sigma^2 = \tilde{\mu}_2$.

But these two first moments are insufficient to describe textures. For example, the two very different images displayed in Figure 9 have the same average and standard deviation.



Figure 9. Two different images presenting exactly the same two first statistical moments.

The literature proposes the skewness, indicator of symmetry around the average:

$$\gamma_1 = \frac{\tilde{\mu}_3}{\sigma^3} \quad (1.3)$$

Another attribute called kurtosis is defined as:

$$\gamma_2 = \frac{\tilde{\mu}_4}{\sigma^4} - 3, \quad (1.4)$$

and corresponds to a measure of flattening of the distribution of a real random variable.

Then, the energy, or uniformity criterion defined as:

$$E = \sum_{i=0}^{255} p^2(i). \quad (1.5)$$

It is maximal when all pixels are equal.

Entropy, a measure of disorder, is defined as:

$$Ent = - \sum_{i=0}^{255} p(i) \log(p(i)) \quad (1.6)$$

But these statistics are not really reliable. Indeed, if the area of interest is too small, the statistics are not very significant any more. These statistics still present the same drawback by representing only the gray level pixels distribution in the image without taking into account the spatial arrangement.

To improve these tools, it has been proposed to compute statistics on particular sets of points. Histogram of gradients is an example [21]. The method relies on edge detection by Canny edge detector, then the number of bits is chosen, each bit representing an angular sector. For each edge point, one weights the bit to the corresponding angle by the magnitude value.

In image processing, a classical tool in texture characterization relies on Haralick's parameters derived from the gray-level co-occurrence matrix (GLCM) also called gray-tone spatial-dependence matrix, first presented in [17]. In contrast with first-order statistic tools (histogram, mean, standard deviation, skewness, and kurtosis), the GLCM is a statistic tool of the second order [22]. First-order statistics are representative of gray-level distribution of the pixels in the image regardless of their spatial arrangement, whereas second-order statistics involve two pixels simultaneously by accounting for their relative position in the image.

The construction of the GLCM $\mathbf{H}_{\mathbf{t}}$ is defined as:

$$\mathbf{H}_{\mathbf{t}} = (h_{\mathbf{t}}(i, j))_{i \in \llbracket 0, 2^{n_b}-1 \rrbracket, j \in \llbracket 0, 2^{n_b}-1 \rrbracket}, \quad (1.7)$$

with

$$h_{\mathbf{t}}(i, j) = \text{Card} \left\{ (p, p + \mathbf{t}) \in I^2; f(p) = i \text{ and } f(p + \mathbf{t}) = j \right\}, \quad (1.8)$$

where I is a rectangular image encoded on n_b bits, f is an application from I to $\llbracket 0, 2^{n_b}-1 \rrbracket$, Card denotes the cardinality of the set, \mathbf{t} is a given translation vector, and $(p, p + \mathbf{t})$ is a pair of pixels in image I , cf. Figure 10. The vector \mathbf{t} may be specified by a unit vector \mathbf{w} and a distance D :

$$\mathbf{t} = D \cdot \mathbf{w} \quad (1.9)$$

Starting from an initialization to the zero matrix, $\mathbf{H}_{\mathbf{t}}$ is incrementally built by considering in turn every pair of pixels $(p, p + \mathbf{t})$ in image I , and incrementing by one the value $h_{\mathbf{t}}(f(p), f(p + \mathbf{t}))$ of the entry $(f(p), f(p + \mathbf{t}))$ (see fig).

After normalization of this matrix (by dividing it by the number of analyzed pair of pixels), each value $h_{\mathbf{t}}(i, j)$ of entry (i, j) represents the normalized frequency to shift, according to a vector \mathbf{t} , from a pixel with value i to a pixel with value j (cf. Figure 11):

$$p_{\mathbf{t}}(i, j) = \frac{h_{\mathbf{t}}(i, j)}{\text{Card} \{I \cap T_{-\mathbf{t}}(I)\}}, \quad (1.10)$$

with $T_{\mathbf{x}}$ means the translation operator of vector \mathbf{x} .

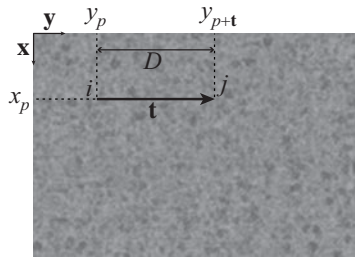


Figure 10. A pair of pixels coordinates $((x_p, y_p), (x_p + D, y_p + D))$ designated by the vector \mathbf{t} , with respective values i and j ; involving the entry (i, j) of the gray level co-occurrence matrix to be incremented.

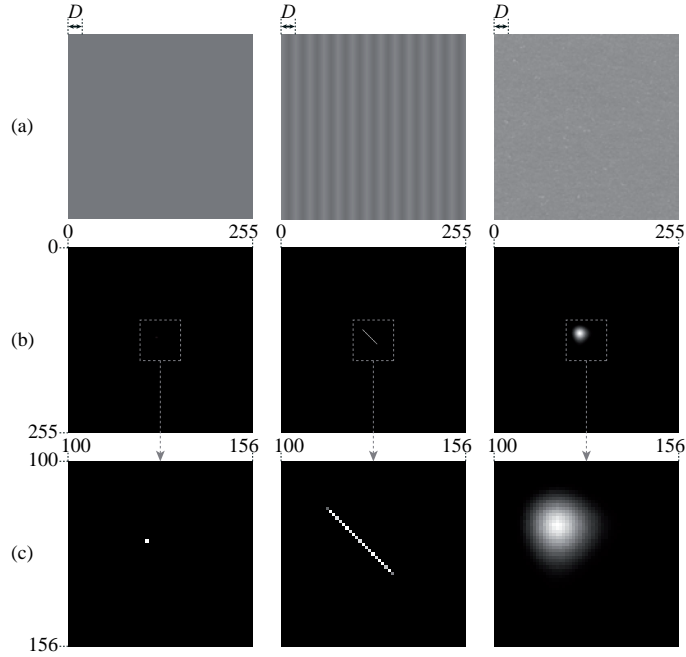


Figure 11. (a) Three original gray level images. (b) Gray level representation of the corresponding GLCM where the white color means the max value. (c) Zoom on the center of images (b).

The GLCM are usually never used directly, because of a weak robustness as their very sparse characteristic. Quantifications (regular or adaptative) could be proposed to reduce the number of gray levels, which results in a diminution of the size of the GLCM matrix. The matrix could also be made symmetrical to fill it more. Several directions of vector \mathbf{t} can be summed.

Texture attributes are usually computed from the GLCM. 14 historical attributes have been defined by Haralick, in particular the following second-order ones: the entropy, the energy, the contrast, the variance, the homogeneity:

The entropy is a disorder indicator; reflecting the image complexity:

$$Ent = \sum_{i=0}^{2^{n_b}-1} \sum_{j=0}^{2^{n_b}-1} p_{\mathbf{t}}(i, j) \times \log(p_{\mathbf{t}}(i, j)). \quad (1.11)$$

The energy or second angular moment measures the global image homogeneity:

$$Ene = \sum_{i=0}^{2^{n_b}-1} \sum_{j=0}^{2^{n_b}-1} p_{\mathbf{t}}(i, j)^2. \quad (1.12)$$

The contrast is high when the GLCM entries far from the diagonal are high, and low if the texture is rather uniform:

$$Con = \sum_{i=0}^{2^{n_b}-1} n^2 \sum_{|i-j|=n} p_{\mathbf{t}}(i, j). \quad (1.13)$$

The variance attribute is defined as follow:

$$Var = \sum_{i=0}^{2^{n_b}-1} \sum_{j=0}^{2^{n_b}-1} (i-j)^2 p_t(i, j). \quad (1.14)$$

It can be shown that the variance outcome from the GLCM corresponds to the mean square deviation between the image and its transpose:

Indeed, Eq. (1.14) can be rewritten using Eq. (1.10) as follows:

$$Var = \frac{1}{Card\{I \cap T_{-\mathbf{t}}(I)\}} \sum_{i=0}^{2^{n_b}-1} \sum_{j=0}^{2^{n_b}-1} (i-j)^2 h_t(i, j).$$

Then Eq.(1.8) can be rewritten as follows:

$$h_t(i, j) = Card\{(p, p + \mathbf{t}) \in I \cap T_{-\mathbf{t}}(I); f(p) = i \text{ and } f(p + \mathbf{t}) = j\},$$

which yields to:

$$h_t(i, j) = \sum_{p \in \{I \cap T_{-\mathbf{t}}(I)\}} \delta_{f(p), i} \times \delta_{f(p+\mathbf{t}), j},$$

and

$$Var = \frac{1}{Card\{I \cap T_{-\mathbf{t}}(I)\}} \sum_{p \in \{I \cap T_{-\mathbf{t}}(I)\}} \sum_{i=0}^{2^{n_b}-1} \sum_{j=0}^{2^{n_b}-1} (i-j)^2 \delta_{f(p), i} \times \delta_{f(p+\mathbf{t}), j}.$$

This finally yields to the variance attribute expressed as:

$$Var = \frac{1}{Card\{I \cap T_{-\mathbf{t}}(I)\}} \sum_{p \in \{I \cap T_{-\mathbf{t}}(I)\}} \sum_{i=0}^{2^{n_b}-1} \sum_{j=0}^{2^{n_b}-1} (f(p) - f(p + \mathbf{t}))^2. \quad (1.15)$$

The homogeneity attribute is defined as follows:

$$Hom = \sum_{i=0}^{2^{n_b}-1} \sum_{j=0}^{2^{n_b}-1} \frac{1}{1 + (i-j)^2} \times p_t(i, j). \quad (1.16)$$

It is higher and higher when we can find, in the image, many couples of same pixels value, which is the case when the texture is uniform or periodical. This indicator is a measurement of texture uniformity or periodicity.

Another second order tool often used in texture analysis is the run length matrix. In opposition to GLCM which considers the gray level of pairs of pixels, the Run Length Matrix (RLM) method uses pixel segments having the same gray levels in a given direction. These ranges of gray levels are defined by a set of consecutive pixels of same value and oriented in a certain direction. The method can be compared to the famous Run Length Encoding (RLE) method [23].

The construction of the RLM matrix \mathbf{L} is made as follows:

$$\mathbf{L} = (l(i, j))_{i \in \llbracket 0, 2^{nb}-1 \rrbracket, j \in \llbracket 1, M \rrbracket}, \quad (1.17)$$

where M corresponds to the larger possible section in a given direction. The lines correspond to the gray level, and the columns correspond to the length of a section. $l(i, j)$ denotes the number of section of length j having the gray level i for a given orientation. There is no need to choose a particular distance as in the GLCM method because we now count the different sections, or ranges. Only the direction (angle) remains as parameter. The information obtained is more of “primitive” type than “variation” type. Some textures attributes can be derived from this matrix, as the total number of section in an image, the percentage of section, the heterogeneity of gray level and the heterogeneity of the sections length.

1.1.2 Frequential methods

Frequential or spectral methods consist in the extraction of energy held by the signal in some various and specifics wavebands. Usually they are used for regular textures analysis.

The Fourier transform, initially introduced by Joseph Fourier [24] in 1822, gives a spectral representation of a signal, here a texture image, in 2D. A non-periodical function can be represented by a sum of sinus and cosines functions comprising all frequencies:

$$f(x) = \int_{-\infty}^{\infty} F(\nu) e^{-j2\pi\nu x} d\nu, \quad (1.18)$$

$F(\nu)$ is called the spectrum of the signal $f(x)$. The spectrum shows the frequencies present in the signal as well as their spatial offset (contained in the phase of the spectrum). $|F(\nu)|$ represents the weight of each frequency ν in the signal, and $f(x)$ is expressed as a weighted sum of sinusoidal signals.

In 2D, the Fourier transform is written as follow:

$$TF(f(x, y)) = \int_{-\infty}^{\infty} \int_{-\infty}^{\infty} f(x, y) e^{-j2\pi\nu_x x} e^{-j2\pi\nu_y y} dx dy. \quad (1.19)$$

The frequency features extraction is based on energy computation on various part of the spectrum, by considering either frequency rings, either particular directions in the 2D frequency representation (module of the Fourier transform) of the image obtained by FFT (Fast Fourier Transform).

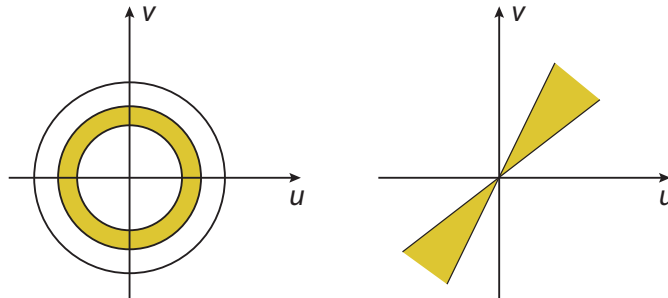


Figure 12. Frequency ring and direction sector masks to apply in the Fourier domain.

Energy evaluated on a frequency ring is an indicator of regularity, and energy evaluated along a certain direction is an indicator of directionality.

In the following, we show for a given image the result of a filtering in the frequency domain, by either keeping only a ring of the module of the Fourier transform, see Figure 13, either a set of directions (an oriented sector), see Figure 14, and reconstruct the image by returning in the spatial domain.

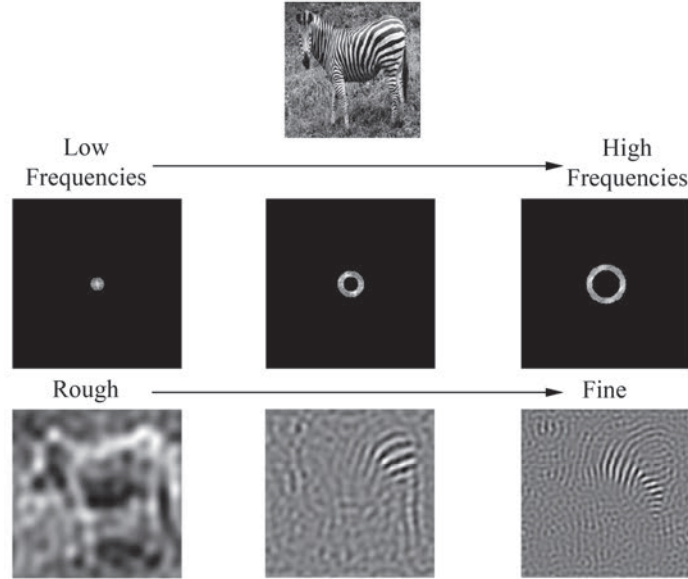


Figure 13. Frequencies features extraction by filtering in the Fourier domain with different ring sizes.

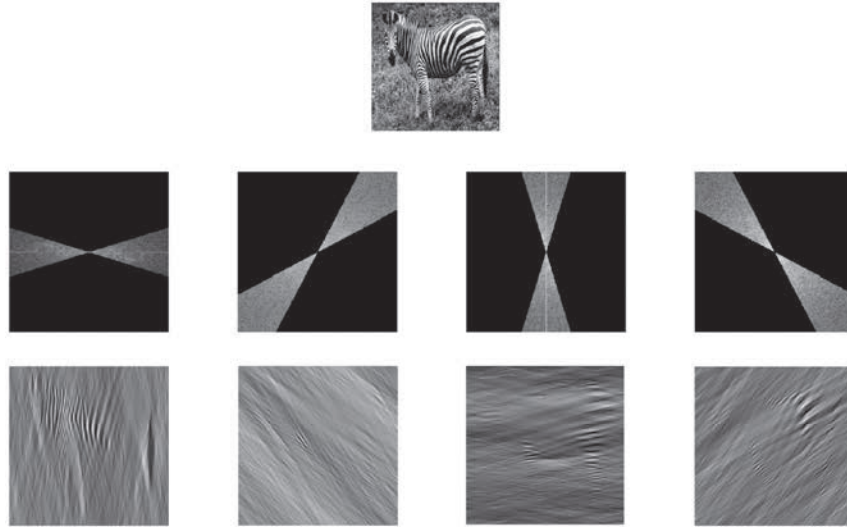


Figure 14. Frequencies features extraction by filtering in the Fourier domain with different sectors directions.

A direction in the spatial domain is recovered in the frequency domain.

But the extraction of frequency features via Fourier transform do not allow to take into account the spatial localisation information, and we will find the same issues as for first order statistical analysis.

Some new methods have been explored to reach our goals, and correspond to spatial-frequency analysis by filtering methods. They offer the possibility to highlight local properties over an area of interest centered on each point. Famous methods as Laws filters can be mentioned. The image is filtered using a set of filters. Energy computation is performed by summation of filtered images. These energies are combined to ensure invariance to rotation. A feature vector is finally obtained.

Another example is the Gabor filters. They are constructed by the convolution between a bidimensional Gaussian and a sinusoidal plane wave. They enable the analysis of a texture at various scales (frequencies), and several orientations (angles).

1.2 Edges

In contrast with the previous approach, focussed on the study of areas, and pixel groups with similar characteristics, we now focus on contours, with detection of intensity variation, and changes in characteristics. In image processing, a lot of challenges are linked to the problematic of edge detection. In this work, the study of edges quality, independently of the acquiring system is paramount; the printing system should be able to reproduce sharp edges between solid areas with different colors. In their work in 2004, C. Ducottet et al. have constructed an interesting argumentation for localization and characterization of edges relying on the wavelet transform [25]. They introduce three main contour shapes, that they call transition edge, the peak edge and the line edge.

In 1-Dimension, a transition is characterized by its derivative. The detection of an inflexion point is made by a local maximum of the first derivative, or by a zero crossing of the second derivative, with a sign change.

In 2-Dimension, let us denote $f(x, y)$ the 2-D signal. The directional derivative, along a vector

$\mathbf{u} = \begin{pmatrix} \cos(\theta) \\ \sin(\theta) \end{pmatrix}$ is given by the formula:

$$\frac{\partial f}{\partial \mathbf{u}} = \frac{\partial f}{\partial x} \cos(\theta) + \frac{\partial f}{\partial y} \sin(\theta) = \bar{\nabla} f \cdot \mathbf{u}, \quad (1.20)$$

where $\bar{\nabla}$ is the gradient operator, aligned with the contour normal direction. When \mathbf{u} is the gradient direction, then the derivative is maximal.

Let us consider now a 2-D discrete signal, such as a grid of pixel. The derivative is approximated by a difference of two successive pixels:

$$\begin{aligned} \frac{\partial f}{\partial x}(x, y) &\approx \frac{\Delta f}{\Delta j} [i, j] = f[i, j+1] - f[i, j] = f_j[i, j] \\ \frac{\partial f}{\partial y}(x, y) &\approx \frac{\Delta f}{\Delta i} [i, j] = f[i+1, j] - f[i, j] = f_i[i, j] \end{aligned} \quad (1.21)$$

The famous Prewit and Sobel gradient operators are obtained from the combination of a smoothing and a derivative following the formula:

$$\begin{aligned} f_j[i, j] &= h_j * f[i, j] \\ f_i[i, j] &= h_i * f[i, j] \end{aligned} \quad (1.22)$$

with the kernels:

$$\begin{aligned} h_j &= \begin{pmatrix} 1 \\ c \\ 1 \end{pmatrix} \begin{pmatrix} 1 & 0 & -1 \end{pmatrix} = \begin{pmatrix} 1 & 0 & -1 \\ c & 0 & -c \\ 1 & 0 & -1 \end{pmatrix} \\ h_i &= \begin{pmatrix} 1 \\ 0 \\ -1 \end{pmatrix} \begin{pmatrix} 1 & c & 1 \end{pmatrix} = \begin{pmatrix} 1 & c & 1 \\ 0 & 0 & 0 \\ -1 & -c & -1 \end{pmatrix}, \end{aligned} \quad (1.23)$$

and with $c = 1$ for Prewit filter, and $c = 2$ for Sobel filter. The module of the gradient will be given by the formula:

$$|\nabla f| = \sqrt{f_j^2 + f_i^2}. \quad (1.24)$$

But such filters are limited, especially when the signal is noisy. An example is shown below with an image of a light rectangular in a dark background, noisy, with a signal to noise ratio (SNR) of 5dB:

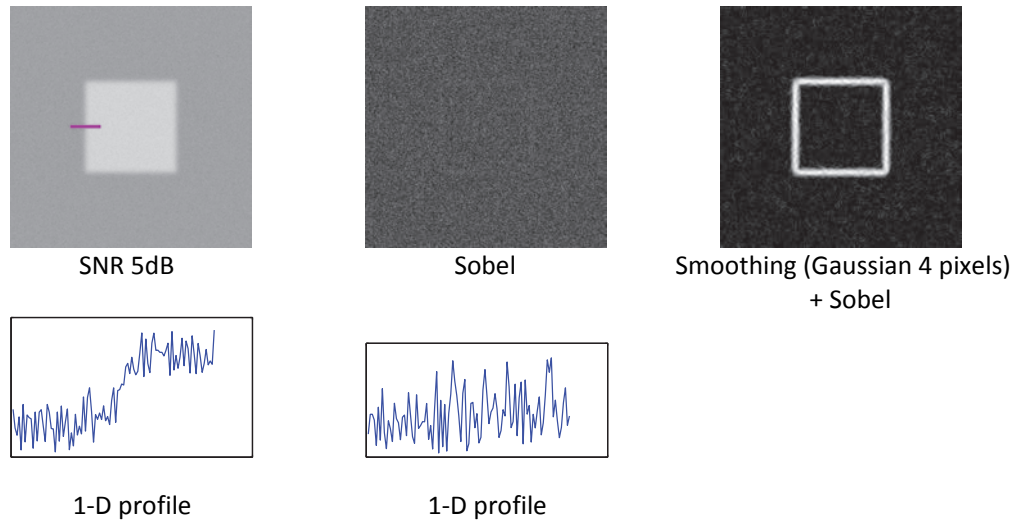


Figure 15. Need of a smoothing. A Gaussian smoothing before a Sobel filtering enables recover edges.

A classical tool in signal processing, more robust, is the derivative of Gaussian:

The Gaussian function is defined as:

$$g_{\sigma}(x) = \frac{1}{\sigma\sqrt{2\pi}} e^{-\frac{x^2}{2\sigma^2}}, \quad (1.25)$$

where σ is called the standard deviation of the Gaussian function.

A Gaussian smoothing is given by the convolution product:

$$f_s = g_{\sigma}(x) * f(x), \quad (1.26)$$

The smoothing + derivative correspond to:

$$f_s' = \frac{d}{dx}(g_\sigma * f)(x) = \left(f * \frac{d}{dx}g_\sigma\right)(x) = f * g_\sigma'(x), \quad (1.27)$$

where function $g_\sigma'(x)$ is the derivative of the Gaussian filtering function expressed as:

$$g_\sigma'(x) = -\frac{x}{\sigma^2} \frac{1}{\sigma\sqrt{2\pi}} e^{-\frac{x^2}{2\sigma^2}} = -\frac{x}{\sigma^3\sqrt{2\pi}} e^{-\frac{x^2}{2\sigma^2}}. \quad (1.28)$$

The extension for 2-D signals corresponds to the gradient of Gaussian filter, defined by:

$$\vec{\nabla} g_\sigma(x, y) = \begin{pmatrix} -\frac{x}{\sigma^4 2\pi} e^{-\frac{x^2+y^2}{2\sigma^2}} \\ -\frac{y}{\sigma^4 2\pi} e^{-\frac{x^2+y^2}{2\sigma^2}} \end{pmatrix}. \quad (1.29)$$

The associated complex filter can be written as:

$$\nabla g_\sigma(x, y) = -\frac{1}{\sigma^4 2\pi} (x + iy) e^{-\frac{x^2+y^2}{2\sigma^2}}. \quad (1.30)$$

An example of a Gradient of Gaussian (GOG) filtering is shown in Figure 16: the filtering is performed in the Fourier domain by the term-by-term product between the Fourier transform of the input image and the Fourier transform of the complex Gradient of Gaussian filter.

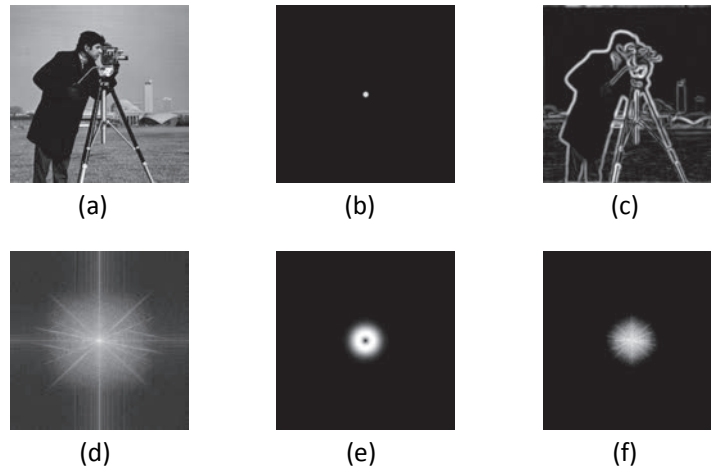


Figure 16. Gradient of Gaussian filtering, (a) is the input image, and (d) the module of its Fourier transformed; (b) the GOG filter with a standard deviation of 4 pixels, and (e) the module of its Fourier transformed; (f) is the product of (d) and (e), and (c) is the resulting filtered image obtained by taking the module of the resulting complex image after inverse Fourier transform of (f). For a better visibility, we draw the logarithm of the module for all spectrums. A zoom in (f) would show that the zero-frequency has been totally removed by the filtering, resulting in an absence of solid areas in (c).

The real part of the complex spectrum of the image represents the derivative along the x axis (vertical), the imaginary part represents the derivative along y axis (horizontal), the module represents the module of the gradient, and the phase represents the direction of the gradient.

The contour detection method that we present is based on the concepts detailed above. The idea of the method is to extract the local maximums of the gradient in the gradient direction. Let us take the module of Gradient-of-Gaussian-filtered image. The direction of the gradient \mathbf{u} is given by the vertical component (in the real part of the Fourier image) u_i , and the horizontal component (in the imaginary part of the Fourier image) u_j . We consider a pixel of the Gradient-of-Gaussian-filtered image whose module value is denoted as $M(i, j)$. We consider the neighbouring gradient points M_1 , and M_2 in the gradient direction (see Figure 17).

We consider that $M(i, j)$ is a pixel of the contour if, and only if:

$$\begin{cases} M > M_1 \\ M \geq M_2 \end{cases}, \quad (1.31)$$

with M_1 and M_2 given by the following formula (1.32), depending the sign of $u_i \times u_j$ and the orientation of the contour, and corresponding to Figure 17.

$$\begin{aligned} M_1 &= \frac{\text{abs}(u_j)}{\text{abs}(u_i)} M(i-1, j+1) + \frac{\text{abs}(u_i) - \text{abs}(u_j)}{\text{abs}(u_i)} M(i-1, j) \\ M_2 &= \frac{\text{abs}(u_j)}{\text{abs}(u_i)} M(i+1, j-1) + \frac{\text{abs}(u_i) - \text{abs}(u_j)}{\text{abs}(u_i)} M(i+1, j) \end{aligned} \quad (1.32)$$

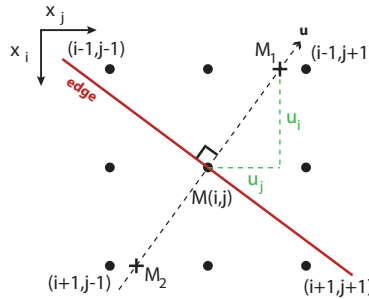


Figure 17. Contour points detection: extraction of the local maximums of the gradient in the gradient direction.

Concerning the smoothing, the σ -value is selected according to the type of contour we want to highlight: for very blur and noisy contour, a high σ is preferable, but this will generate delocalization. Conversely, a low σ will be dedicated to sharper contour.

The Laplacian operator can also detect contours. It is defined, in its continuous version, as:

$$\Delta f = \frac{\partial^2 f}{\partial x^2} + \frac{\partial^2 f}{\partial y^2}. \quad (1.33)$$

Its discrete version is defined by the simple 3x3 mask:

$$\begin{pmatrix} 0 & -1 & 0 \\ -1 & 4 & -1 \\ 0 & -1 & 0 \end{pmatrix}. \quad (1.34)$$

The Laplacian of Gaussian operator is computed in the same idea that the Gradient of Gaussian operator:

A 2-D Gaussian is defined by:

$$g_{\sigma}(x, y) = \frac{1}{2\pi\sigma^2} e^{-\frac{x^2+y^2}{2\sigma^2}}, \quad (1.35)$$

And, by using formula (1.33), the Laplacian of Gaussian filter is given by:

$$\Delta g_{\sigma}(x, y) = \frac{1}{2\pi\sigma^4} \left(\frac{x^2+y^2}{\sigma^2} - 2 \right) e^{-\frac{x^2+y^2}{2\sigma^2}}. \quad (1.36)$$

The Laplacian operator is well appropriated to detect small objects. We have better closed contour than with gradient operator, but the Laplacian is also more sensitive to noise.

Chapter 2 Perception & colorimetry

Color is a complex science, as it always question of human sensations. On the one hand, we can approach it from a scientific point of view, by defining color with some physical properties. But, in the other hand, we need physiological data, as human receptor responses present in our retina, to handle the colored stimulus in a human dimension. In the nature, we encounter other species that have other visual systems, and perceive the same world in a complete different way.

Despite a large breakthrough in the study of the perception these last decades, our knowledge on human vision is still a subject of investigation. We easily understand that we cannot separate the color definition to the study of human perception. Thus, color science remains a challenging topic, incomplete, where development and innovation have still a bright future. This chapter begins with fundamentals on the human vision, leading then to a description of color.

2.1 Human vision

The human vision, or what we usually call visual perception, differs mainly from artificial vision, computer vision, or all the recent technologies dealing with digital sensors to reproduce the act of seeing. The human being has always been interested by the perception.



Illustration by Michael Marsicano

Many centuries ago, in the ancient Greek age, two theories were proposed: the first one, corresponding to the «emission» theory, defending that the processes of vision relied on the interception of rays emanated from eye with visual objects. In parallel, another approach was explaining vision as something characterizing the object and entering into the eye.

Later, in 1021, Ibn Al-Haytham (also known as Alhazen) first demonstrated this last theory attesting that vision was brought by light coming from objects and entering into the eye. Moreover he added that the phenomenon of vision occurs in the brain, and that our experience affects visual perception. Then, in 1604, Johannes Kepler presented in «*Astronomiae pars Optica*» (The Optical Part of Astronomy) [26] a more advanced explanation of the eye functioning. He resolved the «optical part» of the eye, leaving the relationship with the subjective world that is seen. In the middle of the 17th century, René Descartes played a major role using the famous thinking of «Cartesian Dualism» distinguishing the human machine and the world that we see. The purpose was to link the observer and the observed. An interesting question was raised by John Locke, in a famous letter he wrote in 1693 [27]: «If a man, blind since birth, suddenly regained sight, could he distinguish objects (globes from cubes) by sight alone? ». Nowadays, it is well known that the answer is no, because his brain would never have learned how to process theses stimulus. In the 19th century, Von Helmholtz was one of the first to claim that the external environment cannot be immediately perceived owing to the mediocrity of the information presents in the retinal images, and that we need to

interpret these sensory data to start the construction of percepts. He defended the hypothesis that vision was led by “unconscious inferences” drawn by the visual machine. He later calls them “inductive conclusions” encouraging the idea that the perception is a process where a general conclusion is constructed by an accumulation of individual hypotheses about the world. This idea enabled explaining visual illusions.

With about 70% of all our sensory receptors, the vision is the most developed of our five common senses, owing to its 260 millions of photoreceptors. 15% of the brain is dedicated to vision, and several millions of colors are visible by humans. In the act of seeing, two successive processes are defined: the first one corresponds to a sensation. A classical definition is: “Psychophysiological phenomenon whereby an external or internal stimulation has a specific modifier effect on the conscious living being, state or change of state thus provoked with affective predominance (pleasure, pain) or representative (perception)”. The second one is the perception, which starts where the sensation stops, and which could be defined as follow: “Function whereby the mind represents objects; act by which this function is exercised; its result”. Vision relies on the measure of energy sensed by photoreceptors, but the representation that we obtain is a product of our brain. Seeing is indeed a subjective process, and the mechanism of sight requires more than a study of eyes. The connex sciences are optics for the eye, anatomy and neuroscience, psychophysics and cognition.

The eye is a transparent media containing four ocular tissues which are the only transparent materials in the human body: the cornea, the aqueous humor, the crystalline lens, and the vitreous humor.

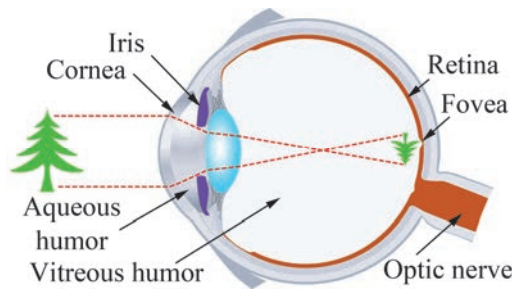


Figure 18. A Human eye scheme. Illustration from AVMD - Dr. Eberhard A.- W. Peters, Internist – Betriebsmedizin – Flugmedizin, 38102 Braunschweig, Wolfenbütteler Str. 80.

The human retina is an extension of the brain delocalized in the back side wall of the eyeball. It captures the input light, and encodes stimuli. Two different types of photoreceptors cells are present: the cones corresponding to photopic vision (vision in daylight), and the rods for scotopic vision (night vision).

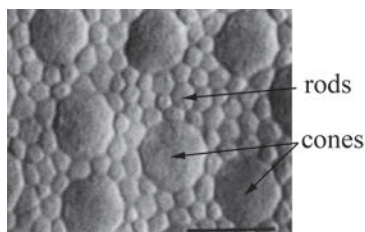


Figure 19. Cones and rods in the periphery of the fovea.
Source: Curcio et al., 1990

The human retina approximately gets five millions of cones and 125 millions of rods. Before stimulating the photoreceptors on the retina, the light crosses the plexiform layer in top of them which is constituted of a dense network of nervous fiber. The fovea is a small pit (of 5 mm of diameter) located in the center of the macula, and contains the highest density of cones, thanks to a special hexagonal mosaic disposition and fine cones. It is responsible for the capture of smallest

details and colors. Visual acuity is therefore non-uniform. In the fovea, there is no rods at all, which explains that during the night, we cannot see a small object (star for example) by watching in front of it, but we can see it by watching a little next to it. In this area, light and details are enhanced by the fact that there is no other cell layer above: they are all pushed to side.

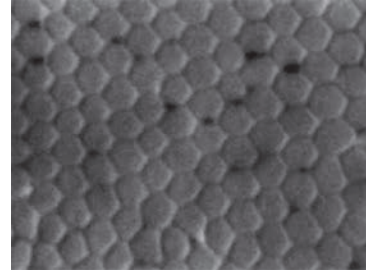


Figure 20. Cones in the fovea. Source: Curcio et al., 1990

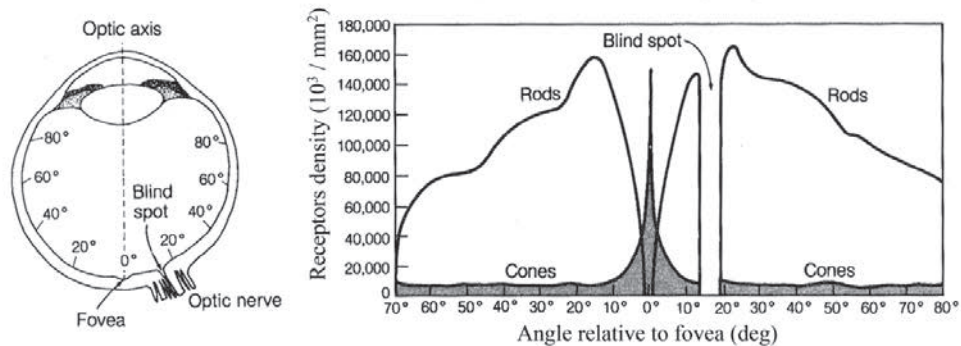


Figure 21. The distribution of rods and cones in the human retina. The left figure gives the locations on the retina of the “angle” relative to the optic axis used on the right figure (based on Lindsay & Norman, 1977).

The human retina contains 3 main layers of nervous cell tissues where neural activity occurs: first the photoreceptors, then bipolar cells, and above, ganglion cells, all three separated by synaptic connections.

The role of the photoreceptor cells is to transform the light energy into a signal dedicated to the nervous system. Rods and cones have globally the same structure: an outer segment (with stacked rhodopsin, opsin filled membranes), an inner segment (composed of mitochondria, ribosomes, and a nucleus), and ends with a synaptic terminal.

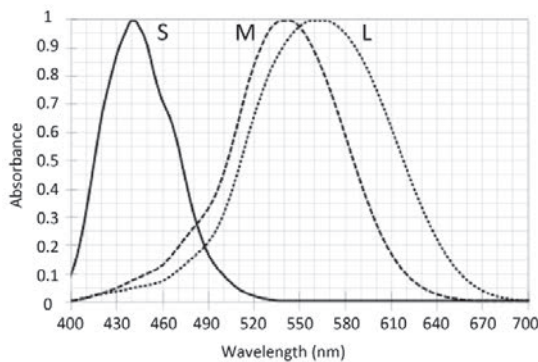


Figure 22. Absorbance curves of the three types of cones, (S), (M), (L) of a human retina.

Human retina contains one type of rod (498 nm, purple), and three types of cones (437 nm, green, 533 nm, yellow, and 564 nm, orange). Human is sometimes said to be trichomat [28] in photopic vision, but we should be careful to commonly held idea arguing that human has a RGB sight, which is false. There is an important difference between what a human perceive and digital RGB capture system. The three different types of cones present different absorption spectra. There are therefore named Short (S), Medium (M), and Long (L)

As each type of cones has a response depending on both wavelength of the input light, and its intensity, the brain would not be able to distinguish between different colors if he doesn't get input signal from more than one type of cone. Trichromatic color vision is made possible through connexions between at least two types of cones. 3 different type of coding are known to be organized into three paths. One is called the achromatic path, and two others correspond to chromatic channel by opposition of red and green, and blue and yellow.

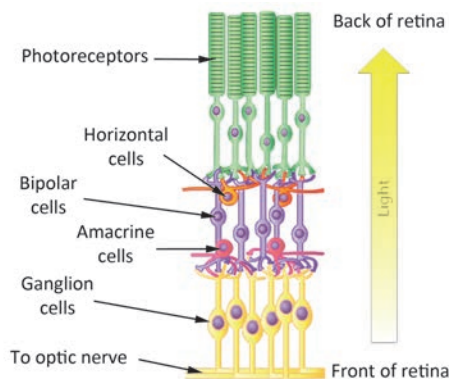


Figure 23. Photoreceptors connexions inside the retina. Light has to cross all the neuronal cells before hitting a photoreceptor.

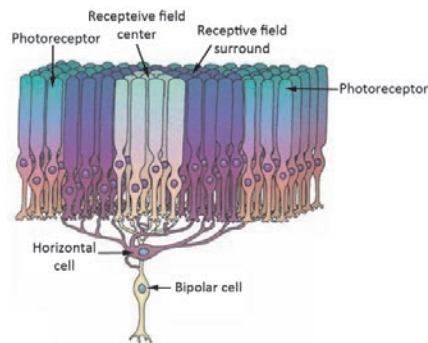


Figure 24. A "receptive field" of adjacent photoreceptors. Image from Wolters Kluwer Health, Lippincott Williams and Wilkins, 2011

The retina contains more than 130 million of receptors but only about 1.2 million fibers (axons) are available in a standard optic nerve. An important spatial encoding and decoding of signals is needed to deal with the limited bandwidth of the optic nerve. Adjacent photoreceptors are connected together forming a circular path and leading to the terminology of "receptive field". It simply denotes a set of photoreceptors that supply together a given cell in the neural system. The receptive fields of the retina have a concentric shape with a circular central area, and a surrounding ring. The signal obtained corresponds to the opposition between the center, and the surround, always antagonistic. The energy difference between the center and the surround of a receptive field is measured by the corresponding ganglion cell. A maximal response is obtained when either the center only or surround only is enlightened. All the receptive fields do not generate a mosaic of non overlapping disks, and most of the time each photoreceptor is engaged into several neighbouring receptive fields. Usually, there is overlapping of several receptive fields corresponding to neighbouring ganglion cells.

There is a trade-off between resolution (small receptive field simulated by high spatial frequencies) and sensibility (larger receptive fields, simulated by lower spatial frequencies). Ganglion cells therefore measure contrast into the retina surface. This spatial organization leads to high sensibility of edges in human vision.

The second part in the act of seeing corresponds to the perception, which can be understood as a mental construction. The perception depends greatly of our origin, culture, and education. Our brain learned hypothesis, and sometimes, in some special conditions, it can be deceived. This is commonly called visual illusions. The introduction of the notion of Simultaneous contrast in Chapter 7 is an illustration of this concept.

2.2 Around the concept of color - CIE experiments & principals laws

2.2.1 Definition of color

The world colors that we perceive are issued from interactions between three entities: a light source, an object, and our visual system. Color is the result of a physical stimulus emitted from an illuminated object, or directly a light source, and entering the eye. We call light an electromagnetic wave owned by the visible domain. Such radiations are defined by their wavelength, ranged between about 380 and 780 nm.

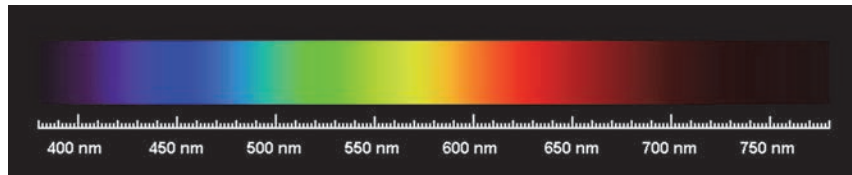


Figure 25. The visible spectrum. Illustration from www.euhou.net. Maite Lacarra et al. universit  Pierre et Marie Curie, Paris, France.

Our eyes can distinguish blue hue, below 480 nm, green between 480 and 560 nm, yellow between 560 and 590 nm, orange lies between about 590 to 630 nm, and red is perceived beyond 630 nm. Purple is a hue that we don't find in the visible spectrum. We usually see it by mixing red and blue extreme lights of the visible spectrum.

Nearly three centuries ago, Newton studied light, and shown with his famous experiment that white light can be decomposed into many visible wavelengths by using a simple prism which disperses light. A light source can therefore be characterized by the relative power for each wavelength. A source is a real, or physically possible light, with a spectral power distribution that can be obtained experimentally. Once the determination is obtained, we can speak of standard source. An important category of them is named blackbodies, whose color depends only on their temperature (black when cold and more and more brighter and whiter when heated). Their temperature, called color temperature, is expressed in Kelvins (K) and entirely defines the color of the body.

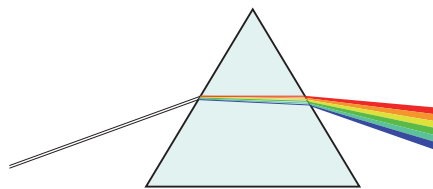


Figure 26. White light beam dispersing through a prism into a spectrum.

Various spectral power distributions of light have been recorded by the *International Commission on Illumination* (*Commission Internationale de l' clairage*, CIE) and are known as *illuminants*. An illuminant is not necessarily physically realizable as a source.

Some of them, such as blackbody radiators, have been defined with physical properties. The illuminant denoted as A corresponds to a blackbody radiator with a color temperature of 2856 K. Others are based on statistics applied to measured light. The Illuminants D series corresponds to natural daylight. Painting, plastic, and textile industries have selected the denominated D65 illuminant corresponding to a blackbody

whose color temperature would be 6500 K. Graphical arts and computer science industries prefer the use of the D50. The F illuminants series is dedicated to fluorescent lamps.

The interaction between light and an object strongly impacts color. Several phenomena may occur when light hits an object. The elements presented briefly in the following paragraph will be more detailed in Chapter 4:

First of all, transmission: When light arrives on the surface of an object, it can go cross it unless it is too much scattered or absorbed. In this case the object is said to be translucent. When entering a new medium (with a different refractive index than the initial one), a small part of light is not transmitted (about 10% for a material of refractive index near to 1.5 dipped into air and hit by a light perfectly diffuse), but reflected at the interface. At normal incidence, only 4% of light is reflected at each interface of such a material with air. This phenomenon is well observed when looking through a glass window: we can see both the outside thanks to a very good transparency of the glass material for light coming from outside to inside, and also we can distinguish our face as a shadow superposing to this image, and corresponding to the part of light going from inside to outside but reflected at the interface back to our eyes. The refractive index characterizes the speed attenuation of light when crossing a medium. Unless the material is hit at normal incidence, a change of refractive index by a change of medium will generate this reflection effect at the interface, and a change in the light direction. Note that the refractive index depends of the wavelength (see Figure 26 of the prism).

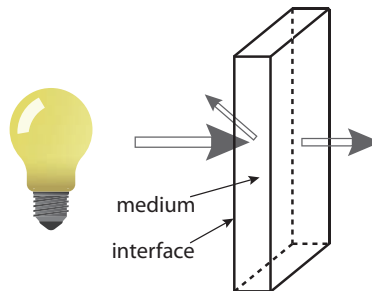


Figure 27. The transmission phenomenon of a light beam crossing a transparent object.

During the crossing of the material, light can also be absorbed. It results in a loss of a part of some visible light which is transformed into heat. When this absorption phenomenon addresses only a part of the incoming light, we speak of a colored material, still transparent, but the absorption of only a part of the input white spectrum results in a colored appearance for the material.

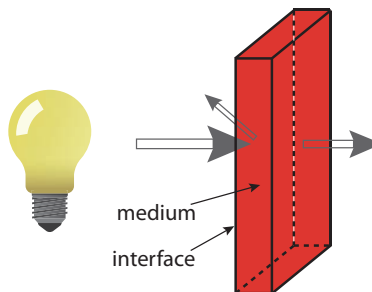


Figure 28. Absorption of input white light by a colored transparent material.

If the light is totally absorbed, and no light exits the material, it is said to be opaque. In this case, the material appears black for an observer located at the back side.

Another phenomenon that can occur is known as scattering. When light interacts with mater, it may be absorbed, and reemitted, at the same frequency, but with a new direction. It happens when light encounters small particles presenting a different refractive index than the rest of the material. The amount of scattering depends on the size of these particles. It is higher when the particle size is close to the wavelength. This phenomenon is encountered very often in the nature, as for example the blue color of the sky is due to scattering by the air molecules. When a material presents sufficiently scattering, we speak of diffuse light reflection. A material is said to be translucent when only a part of light passing through it is scattered and the remaining part is transmitted. If the scattering is too important to let light passing through it, it is said to be opaque. In the printing industry, the pigment size control and their refractive index are important to master the scattering and thus color. Very often, pigment particles size corresponds to the wavelength order of magnitude, and their refractive index is sufficiently different from the resin with which they are coated. Pigments can be chosen in such a way that their particles size is very smaller with respect to the wavelength, and that they have close refractive index with the one of the resin, leading to a small scattering and so a transparency appearance. Transparent coatings can be obtained using small pigment particles size despite the difference in refractive index.

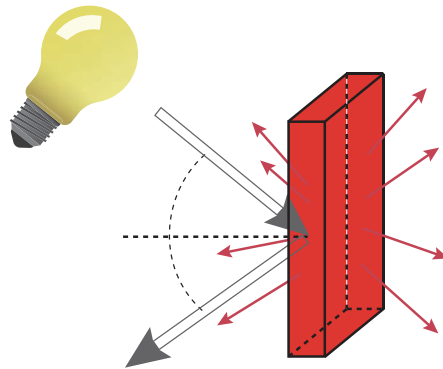


Figure 29. Light scattering by a translucent material. In such a configuration, a part of light is transmitted, and another part is diffusely reflected by scattering. Reflection at the surface occurs.

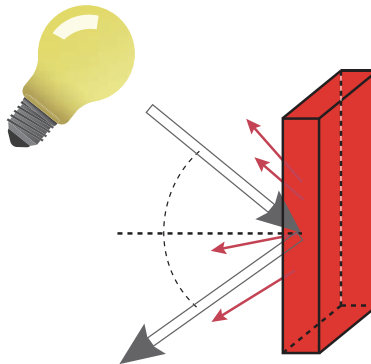


Figure 30. Light scattering by an opaque material. There is no transmitted light, but a part is diffusely reflected by scattering. Reflection at the surface occurs.

Most of the time, the light absorbed by the material is dispelled into heat. However, in presence of certain material, a part of absorbed light can be reemitted at another wavelength, and become diffuse. This phe-

nomenon is called fluorescence. Fluorescent Whitening Agents are often used in paper and textile formulation to enhance the white appearance. They absorb light around 300 to 400 nm in the ultraviolet band-width, and reemit into the visible spectrum between 400 to 500 nm.

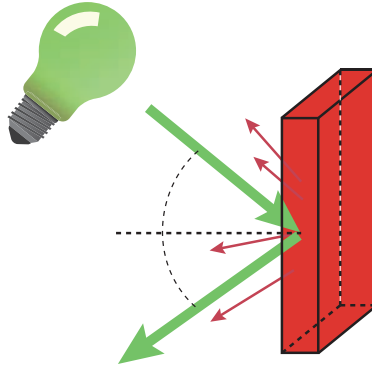


Figure 31. Light reemission by a fluorescent, opaque object. The input green light is absorbed and reemitted into red light.

Until now, we have exposed the two first pillars of the proposed color definition: the emission from a light source, of a physical stimulus, that contacts a material, and interacts with it. The third pillar, and not the least important, consists of the interpretation of this stimulus by our visual system. This part has already been exposed in the previous section, and therefore the notion of color can henceforth be identified.

The next goal consists in the description of color. Color systems rely on either color theories, either on sets of samples, either on physical measurements. In the following points, several color systems will be mentioned quickly, and the last one will be addressed in more details.

2.2.2 Color-mixing based systems

A system using color mixing is based on several main colors named primaries, and deal with their combination to produce colors. Simple examples are very common, as color Cathode Ray Tube (CRT) screens that display colors. The screen is coated with phosphors, and the color properties (brightness, hue, and persistence of illumination) depend on the choice of these phosphors. Usually they are based on three different phosphors, emitting red light, green light and blue light. They are arranged in successive stripes, red, green, and blue; or in cluster, with juxtaposed

$$\begin{bmatrix} R & G & B \\ B & R & G \\ G & B & R \end{bmatrix}$$

matrices coated on the glass screen.

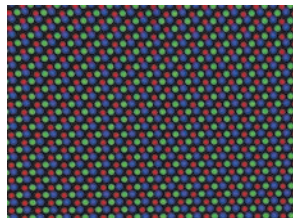


Figure 32. Shadow mask in CRT screens.

When each of the primaries are set to their minimal value, black is obtained, and when all three are at their maximal value, white results. By varying each of the primaries, we obtain a cubic arrangement of colors, often presented as the RGB cube.

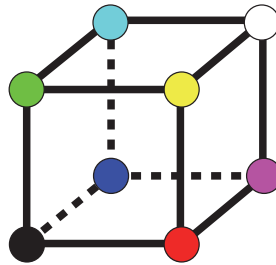


Figure 33. RGB color cube.

Many computer graphics softwares use cross-sections of this cube to represent color selection tool.

Sometimes, it is interesting to rotate this representation by moving down the black corner, and top the white one, and get a double hexcone representation of colors, with lightness as the vertical axis, hue the hexcone base periphery, and the chroma as the distance to the vertical achromatic axis. Before the age of color display screens, a more theoretical application for additive color mixing systems was the spinning disk, where different proportions of white, black and highly saturated color paper are disposed. A change in these proportions or in the colored paper generates a sampling in the color space. Ostwald, in 1931, presented such a system.

Another very common example relies in printing, where a set of primary inks is used to reproduce colors. Usually four inks as cyan, magenta, yellow, and black are sufficient. To help in the communication between colorists designers and printers, new systems are developed: A target color, or spot color is obtained by a mixing of different inks which is then printed. This ensures better consistency than quadrichromy, where the four primaries are printed, one by one, with uncertainties as to when one wants to have a very accurate rendered color. A famous example is the Pantone Matching System, based on 14 ink primaries. The set of color reachable (the color gamut) is larger than the one obtained using cyan, magenta, yellow, and black primaries. Color cards, or organized sets of color samples, are thus created, giving for each color, a recipe of ink amounts. But one must be aware that the primary amounts of ink correspond to a specification of a color, and not its results. Therefore, to ensure high consistency in the perceived color, several aspects as ink, paper and printing process have to be controlled. In general, all color mixing systems trying to reach perceptual consistency fail. There is no linear relationship between color mixing and perception leading to difficulties to interpolate between primaries amounts.

2.2.3 Color perception based systems

In contrast with color-mixing systems, those based on color perception rely on our vision. As those systems do not require any samples, they require although a correct consistency between the different persons and a perception without any ambiguity. In comparison to color-mixing systems where primaries are selected in order to sample regularly the set of visible colors, in perceptual systems we will focus on sampling evenly the perceptions. Visual interpolations between colors will be led. The viewing conditions and the lighting environment will be the main issues.

We continue by the presentation of such conceptual systems based on color perceptions that are called: color order systems.

In the early twentieth century, Professor Albert H. Munsell marked a turning point in the way of representing colors by proposing a 3-Dimensional system that separates the hue, the lightness and the chroma with perceptual and equal visual spacing. This HSV system corresponds to a volume where the vertical Axis holds a variable ranging from black to white (Value channel, or luminance channel). The distance between a given color point and this axis corresponds to the chromaticity of the color (or its saturation), and the hue is indicated by the horizontal angle with a reference color.

The hue represents a shade of color. The Munsell system is based on five main chromatic basis shades of color denoted as: Red (R), Yellow (Y), Green (G), Blue (B), Purple (P). The intermediate shades are also considered, giving the: Orange (YR), Green-Yellow (GY), dark Cyan (BG), Blue-Purple (PB), dark Magenta (RP). These 10 shades constitute the 10 principal hues. Each one is then divided into 10 sectors numbered such that the figure 5 marks the middle of the tone and 10 the boundary between a color and the next. For example, the Red (R) is divided into 10 sub-hues: 1R, 2R, ..., 5R (corresponding to the introduced R), ... 9R, and 10R. The basis of five principal hues has been proved to be visually fairer than systems based on 4 colors (Red, Green, Yellow, and Blue) as the painted globe experiment of Munsell, in 1931: He was led by

the feeling that those five hues, at the same level of chroma, and mixed together with a spinning disk should result in a neutral color. He demonstrated this principle by painting a globe with these five hues at different chroma levels.



Figure 34. Munsell's painted globe designed to the definition of the five principal hues, in 1905.

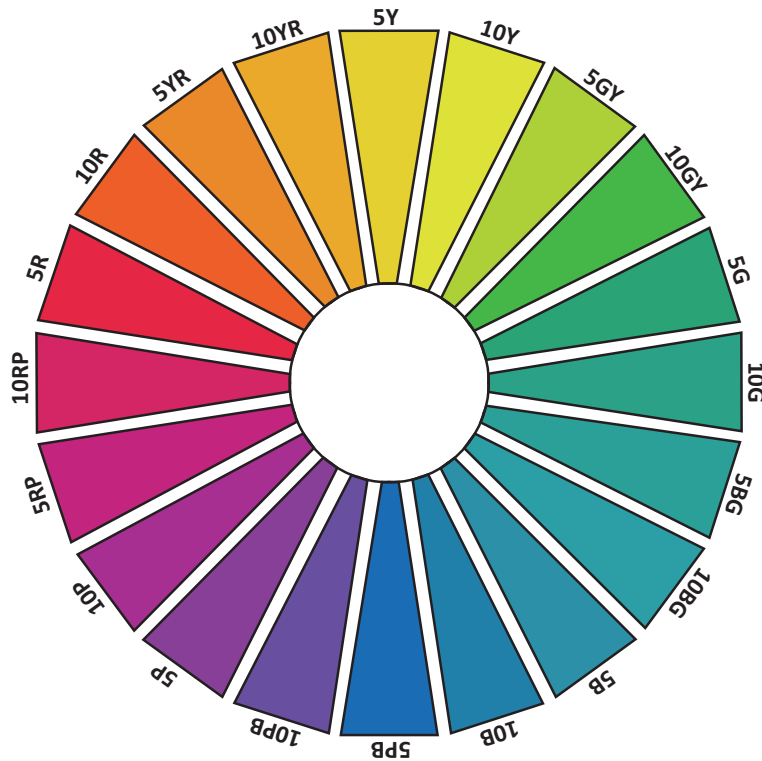


Figure 35. Representation of the ten principals hues, and some intermediates.

The Value channel, ranges from black (0) to white (10), and are visually equally spaced by a visual instrument designed by Munsell. Non-Chromatic colors are therefore situated along this vertical black/white axis, and are denoted with the “N” prefix as: N0, N1, ..., N10.

For a given hue and value, Munsell split the colors along a third dimension called chroma, or saturation. A color with low chroma is close to a neutral gray, and when the chroma is augmented, the color becomes more and more pure. At the origin, Munsell plan to sample its color space using a sphere, but the limitation would have been to straightforward, because for a given hue/value couple, several maximum chroma values exist depending on pigments used.

The Munsell color solid Atlas followed. Then, after the 1930s, the Atlas was improved.

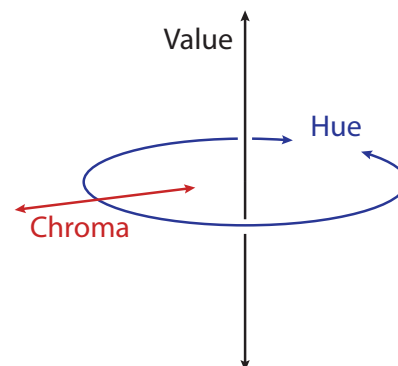


Figure 36. The cylindrical HSV (Hue, Saturation or Chroma, and Value) representation.

A Munsell color is given by the notation: H V/C, where H is one of the ten main hues, supplemented by a number for the subhue information, V represents the value, and C is the chroma.

2.2.4 Color matching based systems – The CIE experiments

The color specification issue raised in this chapter can be greatly simplified when considering color matching. Indeed, the systems based only on our perception, without physical attributes, can lead to accuracy problems to the color specification. Perceptual accuracy, viewing and illuminating conditions will be the main actors. The principle of such color matching systems lies in the attempt to match a color to be reproduced with a color of a sample presented in some specific viewing conditions. When the colors of two materials are compared, they are put side by side under the same viewing conditions. When comparing a colored light (produced by a display for instance) and a material sample, we verify that the light emitted from the display is the same that the reflectance of the material. First color matching experiences date back to several centuries, when Newton discovered that different stimuli, for instance one being constitute of every wavelengths, and the other being a superposition of yellow and blue wavelengths can produce the same visual white color light. The visual colorimetry concept, the science of the measurement of color, was born. It was based on the metamerism concept, for which different spectral stimuli are not distinguishable for an observer. The consequence is that two different people can have different conclusion regarding the matching of two colors. The use of a visual colorimeter, in various conditions it is not designed to, can lead to serious metamerism issues. The purpose would be to replace any individual observer by a kind of average observer, which would limit this greatly this phenomenon due to statistics. If such an observer could be standardized, then this standard observer would enable universal color specification, without dependencies to any particular one. This has been first done by the CIE in 1931, and was a start to the modern color measurement systems [29, 30].

We have introduced in Section 2.1 that two input stimuli are seen as equal in terms of color when their respective cone responses match. Considering this assumption, it would seem that the color specification system could be simplified by the use of cone responses directly.

For a given stimulus, the cone response is obtained by integration, with the multiplication of the spectral power distribution of the stimuli by each of the three spectral sensitivities of the cones, and this for each wavelength, and then all the products are summed. In a first attempt, we can consider an ideal observer with ideal cone spectral sensitivities as presented in Figure 37. When the stimulus is an object, we consider the product of the spectral reflectance of this object and the spectral power of the illuminant source, c.f. Figure 38.

The colorimeter we want to develop here should use three lamps in order to be able to display a color matching every stimulus perceived by the ideal observer. We consider three monochromatic lights at 450 nm, 550 nm, and 650 nm for optimal primaries for our ideal observer, c.f. Figure 37. As for 450 nm the relative sensitivity for the middle wavelength and long wavelength receptors is null, then varying the power of the 450 nm lamp will result only in a change in the response of the short wavelength receptors. In the same reasoning, varying the 550 nm lamp will only interact with the middle wavelength receptors of the ideal observer. And by varying only the 650 nm lamp, only the long wavelength receptors are solicited. So, any stimulus seen by this ideal observer can be matched by adjusting the amounts of the three 450 nm, 550 nm, and 650 nm primary lights.

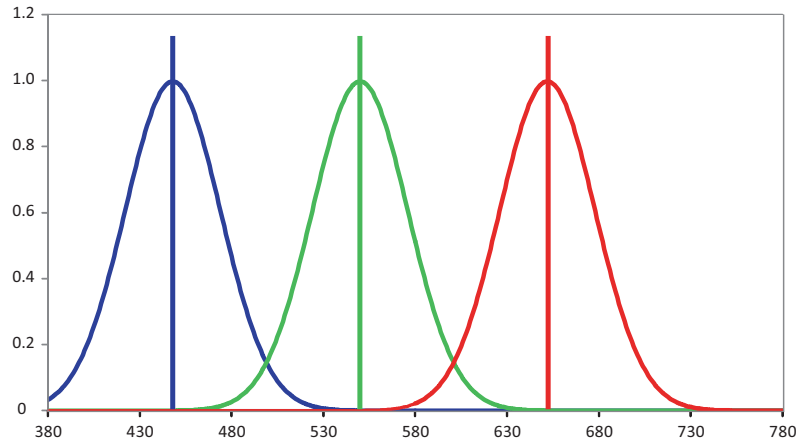


Figure 37. Relative sensitivity curves for an ideal observer, and optimal primaries to develop a colorimeter at 450 nm, 550 nm, and 650 nm, corresponding with the maxima sensitivity of each observer cone receptors for maximal efficiency.

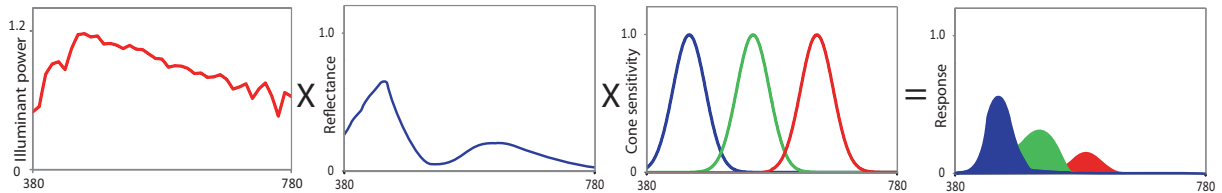


Figure 38. Computation of observer/colorimeter responses (right) by integration: For each wavelength, the stimulus's spectral power distribution (obtained by the product of the source light power with the object reflectance curves) is multiplied by each of the three cone's spectral sensitivities, and the products are summed.

We can now wonder what would be the result if we apply this methodology to a real observer. In the same idea that we done for an ideal observer, we would like to find three primary lamps that can manage independently each cone responses of the real observer. The spectral sensitivities of a real observer's cones show us that it is not possible to reach this goal, see Figure 39. Even if, for short wavelength and long wavelength the choice of a light simulating only one receptor type is obvious, for middle wavelength, it is not possible to choose a wavelength that is independent of the two other receptors spectral sensitivity. This leads to the consequence that every visual colorimeter based only on three primaries cannot simulate every stimulus seen by a real observer.

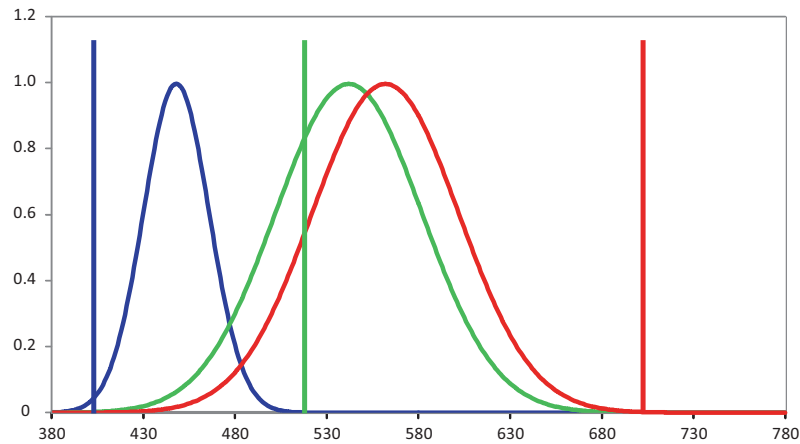


Figure 39. Optimal primaries of 400 nm, 520 nm, and 700 nm for maximization of the independence of the real observer cone responses.

The following is about the color matching experiment: In the 1930s, two scientists named W. David Wright (1928, 1929) and John Guild (1931) separately carried out experiments on the human vision. They realized color matching experiments, using a circular screen of an angular size of 2 degrees, corresponding to the size of the human fovea. The screen was split in two equal parts. On one side, a test field, where a test color is projected, and on the other side, the reference field, presenting adjustable color mixture of three primary colors by an observer. See Figure 40.

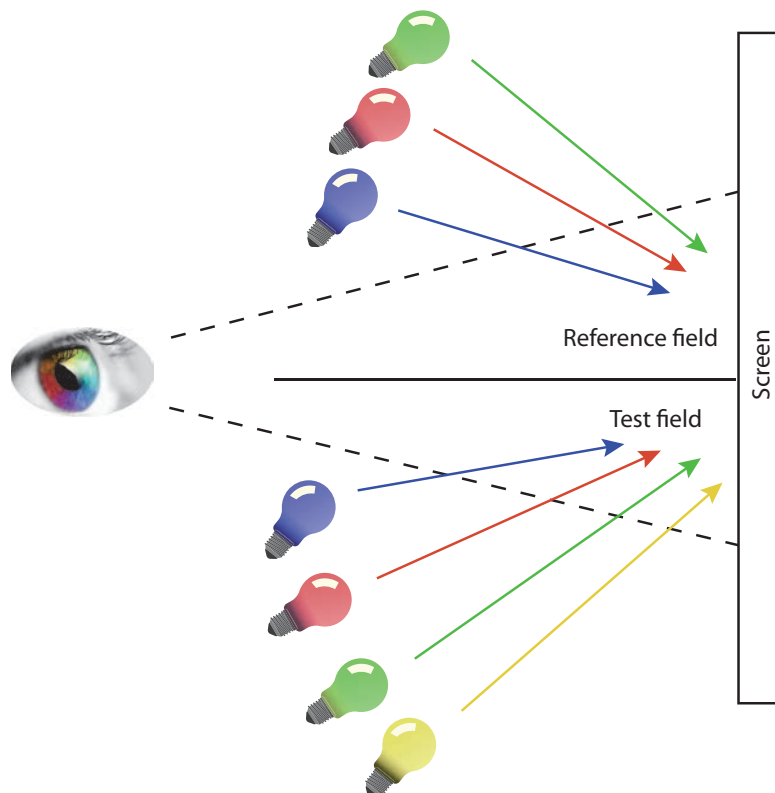


Figure 40. A color-matching experiment. The reference field presents three monochromatic lamps. The test field presents also the same three primaries, and includes another test light (shown in yellow).

Each of the three primaries has a fixed chromaticity, but an adjustable brightness. After the verification of Grassmann's law, the experience consists in the determination of each primary needed to make the reference field visually match the test field, for a given color displayed in the test field. The assessor is invited to modify the brightness of each primary until a match between the reference field and the test field is observed. But this methodology is not suitable to all colors. When this is the case, one of the three primary used in the reference field can be added to the test lamp, and a matching to the two remaining primaries in the reference field is looked for. The amount of the primary added in the test field is considered as a negative value in the reference field. For each wavelength of the visible spectrum, a plot is drawn presenting the amount of each primary intensity selected as a function of the wavelength, c.f. Figure 41. Note that the curves have been normalized in order to have a constant value for the area under them. These three curves denoted \bar{r}_λ , \bar{g}_λ , and \bar{b}_λ are known as the *color matching functions* for the 1931 standard observer, and define the tristimulus values for each wavelength of the spectrum colors. The three primaries used in these experiments were monochromatic lights at 435.8 nm, 546.1 nm (easily reproducible as they correspond to two mercury emission lines), and 700 nm (chosen to simulate only the long wavelength receptors). Please note that in Figure 41, the \bar{r}_λ and \bar{g}_λ are null at 435.8 nm, \bar{r}_λ and \bar{b}_λ are null at 456.1 nm, and \bar{g}_λ and \bar{b}_λ are null at 700 nm. These three color matching function are reported in detailed in Annex A in Table 5.

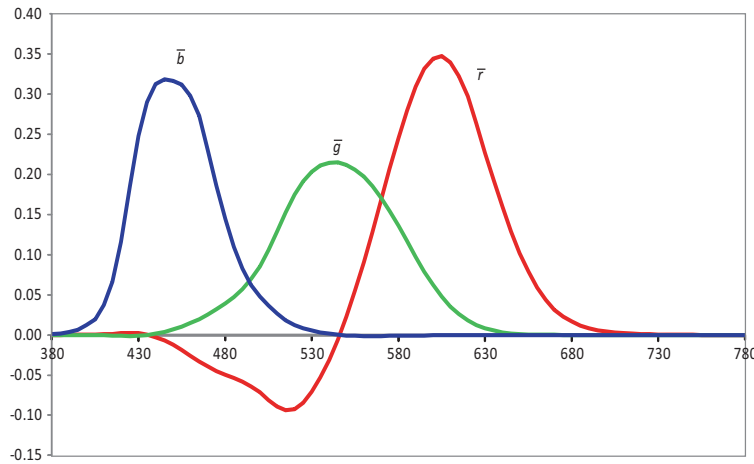


Figure 41. Plot of the CIE RGB color matching functions for the 1931 CIE Standard observer.

In the same period, the General Electric Company is building a new device to enable the acquisition of analog spectra of the reflectance or transmittance of an object [31, 32]. It was envisaged that this analog signal of this instrument could be converted to interface with mechanical or electrical devices, in order to compute tristimulus values, increasing colorimetry science from a level of visual system to a new level of computation system. However, the \bar{r}_λ , \bar{g}_λ , and \bar{b}_λ functions being both positive and negative, the devices would have need six channels, complexifying greatly the project. The idea of a new set of color matching functions, all positive, began to rise. This concern led to the development of a new set of primaries, in a way that their corresponding color matching functions are always positive, and that one of them corresponds to the standard photometric observer function of the CIE, 1924. These high requirements impose a none-physically realizable primaries set, obtained by a transformation of primaries, and leading to the CIE XYZ system, with new color matching functions denoted \bar{x}_λ , \bar{y}_λ , and \bar{z}_λ . This system is well known under

the denomination of the 1931 standard observer, or equivalently the 2° observer, and is supposed to correspond to the color matching values of an average human population, of normal sight. The Table 6 in Annex B presents these \bar{x}_λ , \bar{y}_λ , and \bar{z}_λ color matching functions for each wavelength with a 5nm step, and three main standard illuminant power distribution.

After having presented the CIE standard observers, we describe now the process to compute tristimulus values from the spectral data of an object. For an emissive source (as for example a screen) the spectral power distribution $P(\lambda)$ is multiplied with the CIE standard observer functions $\bar{x}(\lambda)$, $\bar{y}(\lambda)$, or, $\bar{z}(\lambda)$, and then summed to give the tristimulus values as defined in the Eq. (2.1):

$$\begin{cases} X = \int_{\lambda} P(\lambda) \bar{x}(\lambda) \\ Y = \int_{\lambda} P(\lambda) \bar{y}(\lambda) \\ Z = \int_{\lambda} P(\lambda) \bar{z}(\lambda) \end{cases} \quad (2.1)$$

But in practice, the CIE standard observer functions are defined for a discrete set of wavelength, as they are obtained from empirically experiment, and discrete summations replace the integrals. In a general case, involving a reflective or transmissive object, the spectral power distribution $P(\lambda)$ is replaced by the spectral reflectance (or transmittance) of the sample $R(\lambda_i)$, multiplied wavelength by wavelength with the illuminant spectral power distribution $I(\lambda_i)$. Then this resulting spectra is multiplied with $\bar{x}(\lambda_i)$, $\bar{y}(\lambda_i)$, or, $\bar{z}(\lambda_i)$ to give for each wavelength a product: $R(\lambda_i)I(\lambda_i)\bar{x}(\lambda_i)$, $R(\lambda_i)I(\lambda_i)\bar{y}(\lambda_i)$, and $R(\lambda_i)I(\lambda_i)\bar{z}(\lambda_i)$, as presented in Figure 38. These products are then summed (on all the wavelengths, which corresponds to compute the area under the curves) to yield the tristimulus values X , Y , and Z , describing the XYZ color space, as defined by the CIE:

$$\begin{cases} X = k \sum_{i=1}^n R(\lambda_i) I(\lambda_i) \bar{x}(\lambda_i) \\ Y = k \sum_{i=1}^n R(\lambda_i) I(\lambda_i) \bar{y}(\lambda_i) \\ Z = k \sum_{i=1}^n R(\lambda_i) I(\lambda_i) \bar{z}(\lambda_i) \end{cases} \quad (2.2)$$

where λ_i denotes the different n wavelengths in the spectral range, $\bar{x}(\lambda)$, $\bar{y}(\lambda)$, $\bar{z}(\lambda)$ are standard observer color matching functions defined by the CIE, $R(\lambda)$ is the measured spectral reflectance of a sample, $I(\lambda)$ is the spectral power distribution of a reference illuminant, and k is a normalizing constant defined by:

$$k = \frac{100}{\sum_{i=1}^n I(\lambda_i) \bar{y}(\lambda_i)} \quad (2.3)$$

The previous color system described proposes colorimetry standards to specify colors with tristimulus values, and enable their representation in a three-dimensional space. An interesting natural concept consists in the comparison of the distances between colors in this color space to the perceptual differences between them. A classical tool to quantify perceived color differences relies on the Just Noticeably Difference (JND) for stimuli. Several people have used this notion to analyse the CIE XYZ color space uniformity [33-37]. This leads to the conclusion that the most important disadvantage of the CIE XYZ tristimulus system is its non-uniformly spaced characteristic. But in fact there is no reason that it should be, because the primaries have originally been chosen arbitrary, being given the technical limits of the 1930s. Perhaps if the tristimulus values have better match the cone responses, we would have expected a better visual resemblance. Since 1931, the color science has been developed by scientists in order to reach new color spaces, aiming to uniform visual spacing. Following Munsell lightness scale, Glasser first used in 1958 a cube-root function to approximate the complex 5th order polynomial of Newhall in 1943. Then, the CIE also adopted this approximation, and leads to the common CIELAB 1976 color system.

The definition for CIE 1976 $L^*a^*b^*$ (CIELAB) is:

$$\begin{cases} L^* = 116 \times f\left(\frac{Y}{Y_n}\right) - 16 \\ a^* = 500 \times \left[f\left(\frac{X}{X_n}\right) - f\left(\frac{Y}{Y_n}\right) \right] \\ b^* = 200 \times \left[f\left(\frac{Y}{Y_n}\right) - f\left(\frac{Z}{Z_n}\right) \right] \end{cases} \quad (2.4)$$

with X_n, Y_n, Z_n the tristimulus values of the considered reference white; and f a function such that:

$$\begin{cases} f(x) = x^{1/3}, \text{ if } x > \left(\frac{6}{29}\right)^3 \\ f(x) = \frac{1}{3} \times \left(\frac{29}{6}\right)^2 \times x, \text{ if } x \leq \left(\frac{6}{29}\right)^3 \end{cases} \quad (2.5)$$

The cylindrical coordinates are then defined as $L^*C_{ab}^*h_{ab}$ by:

$$\begin{cases} L^* = L^* \\ C_{ab}^* = \sqrt{(a^*)^2 + (b^*)^2} \\ h_{ab} = \tan^{-1}\left(\frac{b^*}{a^*}\right) \end{cases} \quad (2.6)$$

A particular attention should be made to the computation of h_{ab} when a^* is null: a classical function denoted as atan2 enables to avoid the ambiguity.

Other color space conversions are all referenced in the Bruce Lindbloom website [38]. For example, color spaces conversions such as sRGB, or Adobe RGB 1998 (which are important because used by many digital devices) from the CIELAB are detailed.

2.2.5 Color tolerancing

When speaking of color tolerancing, we understand the computation of a metric scale corresponding to visual perception for color differences. Therefore, the color space in which this metric will be computed is paramount. We intend a nearly uniform visual spacing color space, in which some color transformations are optimized. CIELAB is commonly used and recommended, since 1976. In such a color space where visual uniformity has been achieved, CIELAB differences should correspond to visual differences in every part of the space.

The color difference, denoted ΔE_{ab}^* , is then proposed to be computed in the CIELAB color space as the Euclidian distance between the tristimulus of the two stimuli: the reference one, and a test one, see Figure 42.

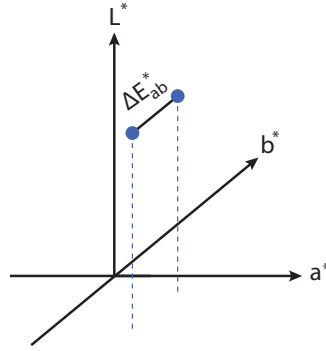


Figure 42. Color difference ΔE_{ab}^* in the CIELAB color space can be computed by the Euclidian distance between two stimuli.

$$\Delta E_{ab}^* = \left[(\Delta L^*)^2 + (\Delta a^*)^2 + (\Delta b^*)^2 \right]^{1/2}, \quad (2.7)$$

with ΔL^* , Δa^* , and Δb^* computed as follows:

$$\begin{cases} \Delta L^* = L_{sample}^* - L_{ref}^* \\ \Delta a^* = a_{sample}^* - a_{ref}^* \\ \Delta b^* = b_{sample}^* - b_{ref}^* \end{cases} \quad (2.8)$$

Even if the CIELAB is supposed to be visually uniformly spaced, it is not exactly the case, and in some parts of the color space, the visual differences are not equal. Nevertheless, the goal would be to obtain a single value representing the same perceptual distance between all pair of colors. It is recognized that the lightness, the hue, and the saturation have an influence on the visual color difference perceived. That is why, more recently, in the 1990s, new approaches have emerged. In 1995, the original Delta-E distance have

evolved, henceforth denominated as ΔE_{94} , by taking into account the location of the reference in the color space and by dynamically rescaling the score in function of this location:

$$\Delta E_{94} = \left[\left(\frac{\Delta L}{K_L S_L} \right)^2 + \left(\frac{\Delta C}{K_C S_C} \right)^2 + \left(\frac{\Delta H}{K_H S_H} \right)^2 \right]^{1/2}, \quad (2.9)$$

with ΔL , ΔC , and ΔH computed as follows:

$$\begin{cases} \Delta L = L_{ref} - L_{sample} \\ \Delta C = C_{ref} - C_{sample} \\ \Delta H = \sqrt{(\Delta a)^2 + (\Delta b)^2 - (\Delta C)^2} \end{cases}, \quad (2.10)$$

with $C_{ref} = \sqrt{(a_{ref})^2 + (b_{ref})^2}$, $C_{sample} = \sqrt{(a_{sample})^2 + (b_{sample})^2}$, $\Delta a = a_{ref} - a_{sample}$, $\Delta b = b_{ref} - b_{sample}$.

The constants are chosen as following: $S_L = 1$, $S_C = 1 + K_1 C_{ref}$, $S_H = 1 + K_2 C_{ref}$, $K_L = \begin{cases} 1, \text{ default} \\ 2, \text{ textiles} \end{cases}$,

$K_C = 1$, $K_H = 1$, $K_1 = \begin{cases} 0.045, \text{ graphic arts} \\ 0.048, \text{ textiles} \end{cases}$, $K_2 = \begin{cases} 0.015, \text{ graphic arts} \\ 0.014, \text{ textiles} \end{cases}$.

Be careful on the computation of ΔH . The value inside the square root might be, in rare cases, negative, and the computation would fail. Bruce Lindbloom proposed in his web site (see ref) a solution: the value of ΔH is in fact not necessary, we just need $(\Delta H)^2$. So a solution would be to remove the square root, and compute directly: $(\Delta H)^2 = (\Delta a)^2 + (\Delta b)^2 - (\Delta C)^2$.

The constants K_L , K_C , and K_H enable the user to adjust respectively the lightness channel, the chroma channel, and the hue channel. Moreover, as this metric dynamically adjust the tolerance in function of the location of the reference, the “role” of the sample and the one of the reference cannot be reversed, as this metric do not verify the symmetric property of a distance: In the computation of S_C and S_H , only the chroma of the reference color is used. An inversion of the sample and the reference would result in a change in the score, because the tolerance would be assessed at the location of the “new” reference (formerly having the role of the sample). This is an important limitation to note of this ΔE_{94} metric. It would be more understandable that the color difference between a pair of colors be the same regardless which one correspond to the reference. To address this issue, an extension have been proposed at the end of the 1990s, called ΔE_{2000} . It is a much more complex formula, using trigonometry formulas, and centring the tolerance on the middle of the segment connecting the two color points. This new metric enable to compare any pair of colors without having to specify which one is a sample and which one is the reference. Nevertheless, the use of this last metric is sometimes controversial, and is not recommended in industrial processes where a batch of samples has to be compared to a single reference target.

For our applications, we propose an intermediate between the complex ΔE_{2000} , and the simple ΔE_{94} metrics: We propose to start from the ΔE_{94} formula presented in Eq. (2.9), and to change the computation of S_C and S_H , by making them symmetrical:

$$\begin{cases} S_C = 1 + K_1 \sqrt{(C_{ref})^2 + (C_{sample})^2} \\ S_H = 1 + K_2 \sqrt{(C_{ref})^2 + (C_{sample})^2} \end{cases} \quad (2.11)$$

Chapter 3 Measurement of colored surfaces

The previous chapter showed that color is based on three entities. A source of light, an illuminated object, and a human eye and brain, who acquires the signal and converts it into a response then converted into a color by the brain.

If we were able to assign digital values to this response, it would be very useful, for example to define accurately a color by another person, in another place. Color perception is naturally and continuously done by our visual system, but it is difficult to reproduce by digital instruments. Most of the time, the measuring instrument records quantities of light, and a digital processing tends to reproduce human visual sensations. In this chapter we present, and characterize, two different measuring tools that we used in our work: a color flatbed scanner, and a spectrophotometer.

3.1 Flatbed color image scanner

3.1.1 Introduction

The purpose of this study is to characterize a measuring instrument used for the digitalization of the samples for which we want to assess the print quality. The measuring instrument that we consider here is a flatbed scanner-type with CCD (Coupled Charge Device). A study of the color rendering and the reproducibility of measures will be held following a pre-study on a similar scanner performed by the Newtowne Technologies company based in Lyon, France. An analysis of the spatial characteristics will also be conducted in order to validate the stability of the resolution on the entire sample acquisition surface.

The flatbed scanner used in our experiments is a EPSON PERFECTION V700 Photo, using the EPSON Dual Lens System with a Color Epson MatrixCCD™ line sensor of an optical resolution of 4800 ppi (for reflection), and a hardware resolution of 4800 x 9600 ppi (horizontal x vertical). The color bit depth is 48-bits per pixel (3x16 bits), with an optical density of 4 Dmax. The light source is a white cold cathode fluorescent lamp.

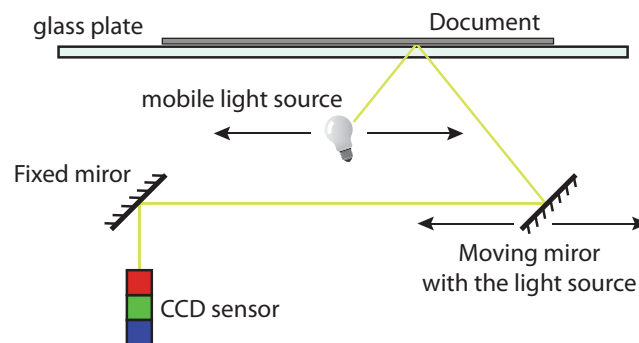


Figure 43. Scanner principle diagram.



Figure 44. EPSON PERFECTION V700 Photo scanner. cf. Epson web site for more details.

Regarding optical density, some recalls can be given: Depending on the used materials (film or paper) one uses a densitometer in transparency or reflection. In both cases the device measures the amount of light transmitted by the document based on the received light.

The reflectance at any point of a surface is the ratio of the luminous flux reflected on this surface to the luminous flux falling on the surface.

$$R = L_r / L_i . \quad (3.1)$$

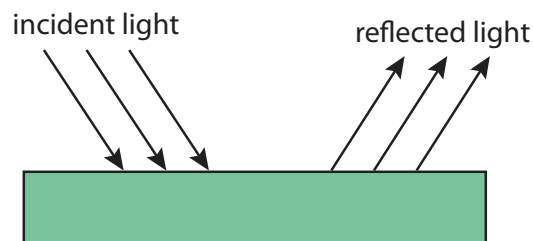


Figure 45. Reflection of light by a surface.

The transmittance of a film is the ratio of the transmitted light flux through this film to the incident flux.

$$T = L_t / L_i . \quad (3.2)$$

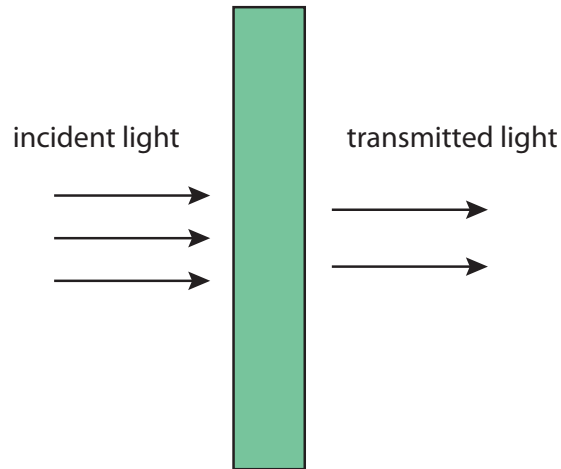


Figure 46. Transmission through a slice of material.

The opacity of a given point is equal to the inverse of the transmittance (transparency): $O = 1/T$. The values of the opacity will therefore be between 1 and infinity, while those of the transmittance are between 0 and 1.

Let us assume a filter that would let through only 1/10 of the light, its transmission would be 1/10 and its opacity 10. If we put two identical filters side by side, it is not 2 times less light that we let pass as might be supposed, but 100 times less ($1/10 \times 1/10$). If we add a third filter, the total combination will transmit only 1/1000th ($1/10 \times 1/10 \times 1/10$) of the emitted light. These numbers increase or decrease exponentially and it is not easy in practice to handle such numbers and logarithms are used: We determine the optical density on the basis of the logarithm of opacity so as to obtain more convenient values.

$$D = \log_{10}(O) = \log_{10}(1/T) . \quad (3.3)$$

Density	$D = \log_{10}(O)$	0	0.3	1	1.3	2	3	3.3	4
Opacity	$O = 1/T$	1	2	10	20	100	1000	2000	10000
Transmission	T	100%	50%	10%	5%	1%	0.1%	0.05%	0.01%
Reflectance	R	100%	50%	10%	5%	1%	0.1%	0.05%	0.01%

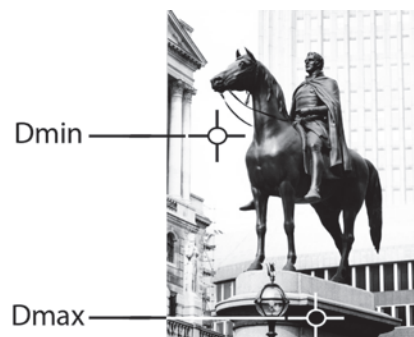


Figure 47. Black ink density in an example of a photo from Public Monuments & Sculpture association web site, <http://www.pmsa.org.uk/pmsa-database/632/>.

3.1.2 Colorimetric characteristics of the system

In order to analyze the accuracy of the color digitalization, we use a Kodak Q-60 color chart provided with nominal colorimetric CIEXYZ values depending on the date of manufacture. These data are very accurate.

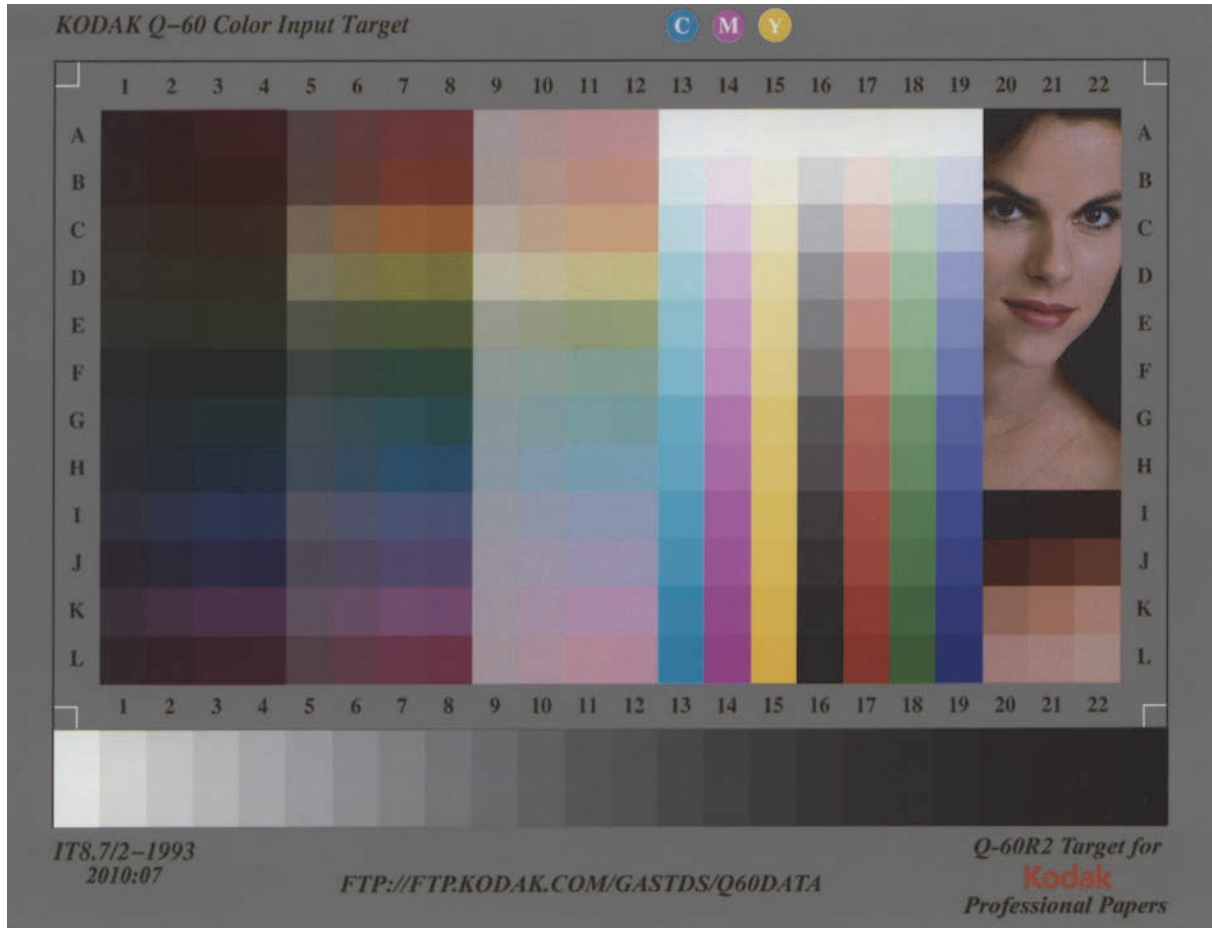


Figure 48. KODAK Q-60R2 Color Input Target.

We scanned this color target with the EPSON PERFECTION V700 Photo scanner. The automatic color correction of the EPSON Scan software was disabled. Moreover, all the adjustment parameters (such as sharpness, descreening, color restoration, dedusting etc.) were also deactivated. After having digitalized the target, we defined a mask for each color patch of the target and calculate a RGB value for each patch as the average of the RGB value of all pixels of the corresponding mask. Theses digitalized RGB values were transposed into the CIELAB color space, considering a 2° standard observer and a D65 illuminant, with the absolute white as reference white. The color target presenting some high saturated colors, it was judicious to consider the scanned image in the AdobeRGB color space as it is wider than the sRGB. A short explanation of this remark is made in the following paragraph. Theses measured colors are compared to the theoretical ones using the CIE DeltaE94 color metric. The average difference on the whole 264 patches target is 6.18 units in DeltaE94. The histogram of the DeltaE94 differences for the entire target is presented Figure 52.

The ground truth color values are obtained by measuring the spectral reflectance of each patches and then converting to Lab color space considering a 2° standard observer with a D65 illuminant and the absolute white as reference white. A preview of these colors in an RGB color space is presented in Figure 49 by considering the Lab to sRGB color conversion (a) and the Lab to AdobeRGB1998 color conversion (b). We can easily understand our initially stated wish to consider the AdobeRGB1998 color space rather than the sRGB color space: Indeed, the color points of the target in the sRGB color space are too much saturated, and several colors are outside the sRGB gamut (especially the four more saturated cyan, the two more saturated yellow, and two oranges points). In a wider RGB gamut (b) corresponding to AdobeRGB1998, only the two much saturated yellow are outside. These two gamuts are represented Figure 50 in the xy chromaticity diagram.

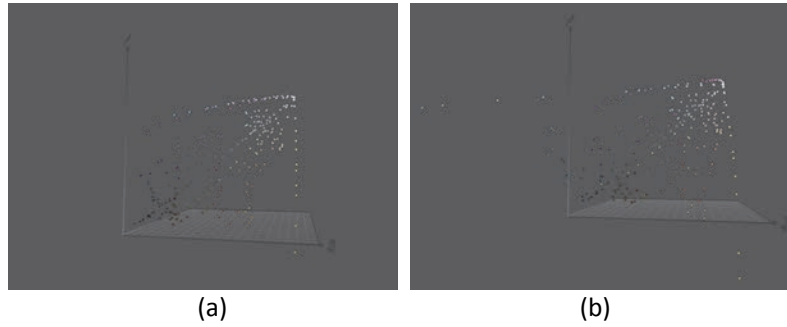


Figure 49. 3D view of the 385 color patches of the KODAK Q-60 Color Input Target in (a) sRGB color space, and (b) AdobeRGB color space.

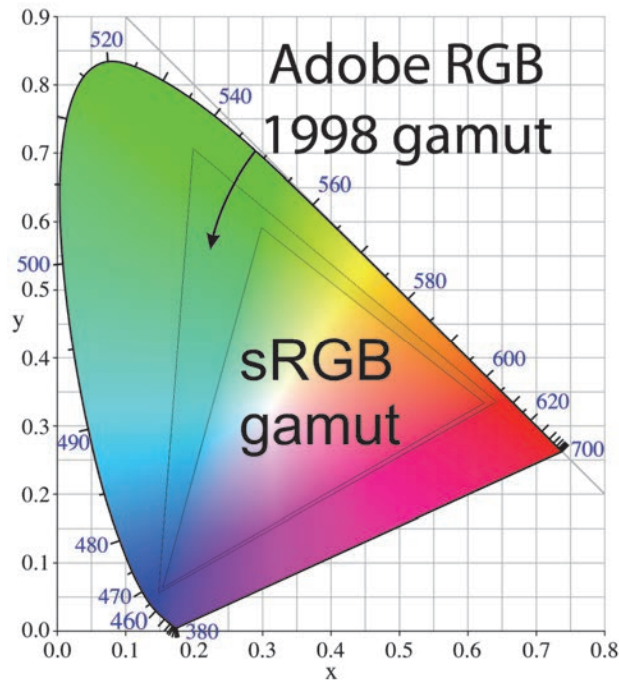


Figure 50. Comparaison of sRGB and AbodeRGB color spaces.

Considering now the scanned values, we compare the performances depending on the input RGB color space considered. On Figure 51, we represent the Euclidian distance between ground truth values and

scanned values of all color points projection in the (a^*b^*) plan by considering either a scanner in the sRGB color space or in AdobeRGB color space. We notice that in the AdobeRGB color space, the distance is globally smaller than in sRGB. The gamut of the scanner is a bit enlarged if we consider the AdobeRGB color space, and better match the target than in the sRGB color space.

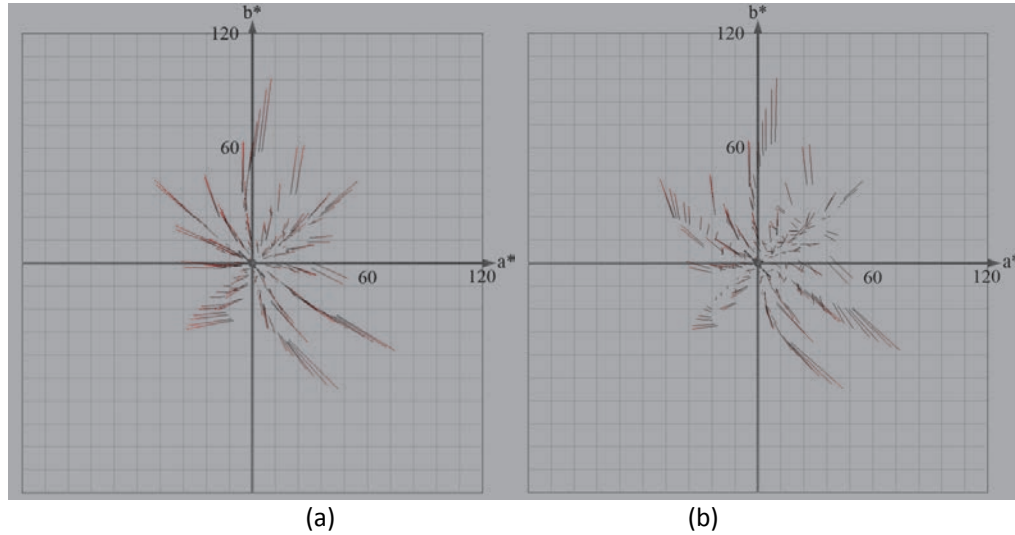


Figure 51. Visualization in (a^*b^*) plan of the deviation between ground truth values (red side of lines) and digitalized values (black side of lines) for color patch of KODAK Q-60 Color Input Target, considering scanned values in sRGB color space (a) or AdobeRGB color space (b).

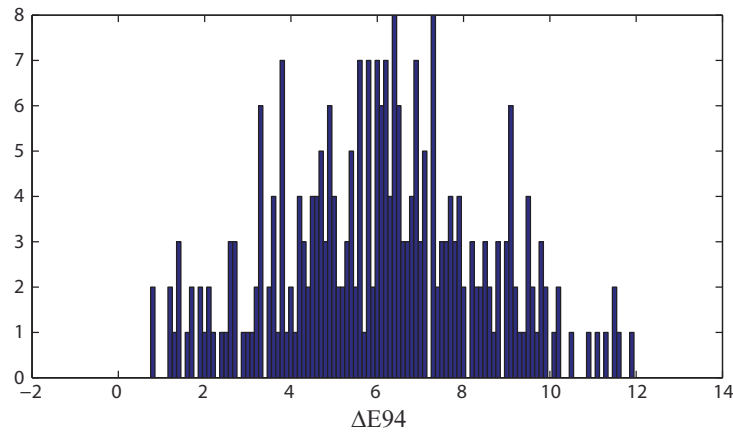


Figure 52. Histogram of color differences of the digitalized KODAK Q-60 Color Input Target (AdobeRGB) compared to the ground truth values.

Regarding the reproducibility of colors, we digitalized the color target 10 times, and changed each time the target position on the scanner glass. The RGB values for each of the 264 patches were converted into CIELAB color space, and we analyse their L^* , a^* , b^* values. We note a standard deviation for L^* value of 0.18, 0.12 for a^* , and 0.13 for b^* . We thus notice relatively low standard deviation values on the three channels L^* , a^* , b^* .

Another path of investigation was how the scanning resolution influences the color values. We analysed the variations of color values of the 264 patches of the target due to the resolution of scan. For

each patch of the target scanned 10 times for 3 different resolutions we compute the average of L values, a^* values, and b^* values. Then we compute the standard deviation of these values for the 3 resolutions (600 ppi, 1200 ppi, and 2400 ppi). The average of the standard deviations on the 264 patches is 0.40 for the L, 0.24 for a^* , and 0.23 for b^* . The resolution therefore doesn't have an excessive effect on the color values.

We also analysed the influence of resolution on the reproducibility of colors by studying the hue variation for each patch for 10 successive scans at the 3 resolutions. The average of the standard deviation of the 10 scans of each patches are computed. We obtained respectively for L, a^* , and b^* values: 0.18, 0.12, and 0.13 at 600 ppi, 0.17, 0.11, 0.12 at 1200 ppi, and 0.39, 0.20, 0.18 at 2400 ppi. This shows us that the reproducibility of measures in terms of color is similar for 600 and 1200 ppi, but it decreases a bit for 2400 ppi.

In order to highlight the presence of chromatic aberrations, we scanned a white and black pattern at 1200 dpi (Figure 53). We observe chromatic aberrations in the direction of movement of the sensor with red bottom and blue top. They are lower in the horizontal direction.



Figure 53. Digitalization of a black and white pattern at 1200 ppi for chromatic aberrations identification.

Following the analyses carried out to study the various color drifts of the acquisition system, one can draw the main conclusions. The system reproducibility is correct. There is no significant drift for color values or reproducibility depending on the resolution. The gamut of the acquisition system is compact, but a bit enlarge if we consider the color values in the AdobeRGB space rather than in sRGB color space. The optical system presents some slight chromatic aberrations, mainly in the vertical direction.

3.1.3 Spatial characteristics of the system

First of all, we verify the accuracy of the requested resolution. The scan of this target at an intended 600 ppi resolution will be evaluated. The horizontal "V" pattern present on this Kodak target has an exactly 0.13 inch opening. We measure at the extremity of the pattern 78 pixels, which corresponds to a perfect 600 ppi resolution.

To study in more details the local variations of resolution, we digitalized a sheet of graph paper at 600 ppi. By measurement of the position of scanned lines in the image, we can deduce the spatial aberrations over the entire acquisition area.

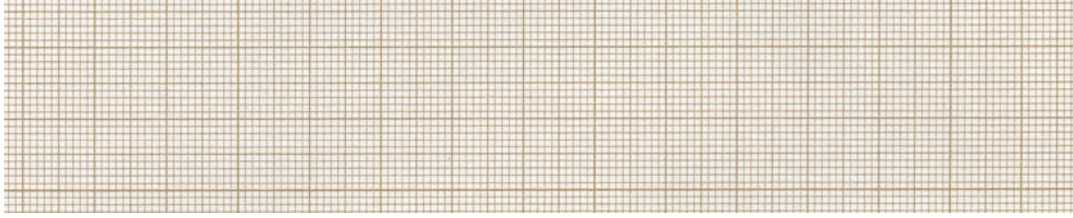


Figure 54. Example of acquisition of a graph paper sheet for spatial calibration.

One can study the evolution of resolution depending on the horizontal, Figure 55 (a), and vertical, Figure 55 (b), position.

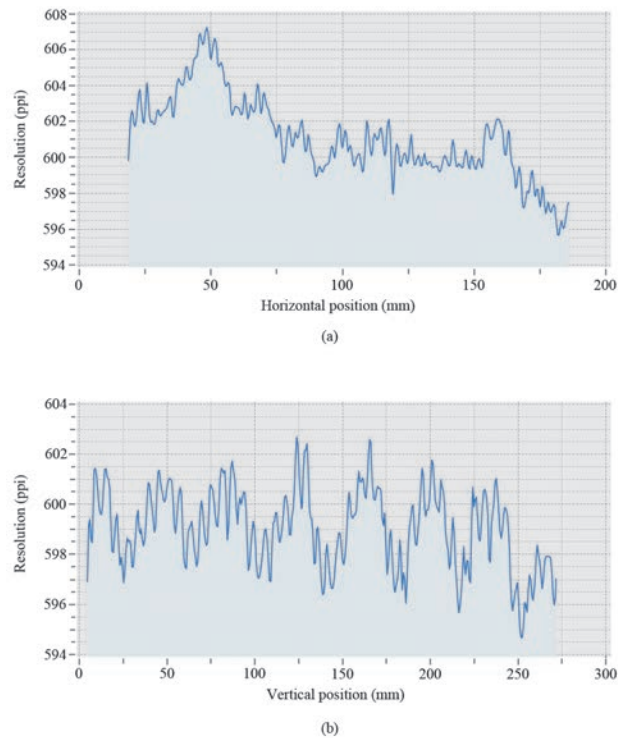


Figure 55. Study of the horizontal and vertical resolution drift.

We observe that there is a significant drift in horizontal direction. It seems that the positioning of lenses or sensors along the array of acquisition is not uniform. Thus, on the right side of the field, the lenses are less close to each other than on the left side where they are closer. This drift can be corrected by adjusting the position of the pixels by polynomial interpolation or spline on each line of the captured image. But such treatment would create a change in the value of certain pixels on each line, the most affected by this drift being on the edges of each line, and would lead to a loss of the native resolution of the image as well as local color unwanted distortions. It is preferable to analyze the scanner profile derives and place the sample on the scanner glass in an area where the drifts are minimal, as presented in the following 3.1.4 section. Regarding the vertical spatial drift, the engine displacement looks pretty good with low regular drifts of ± 2 ppi. It will therefore be important to pay attention to the placement of the measurement sample, if pos-

sible prefer the center of the field to have the more uniform resolution possible, and limit the horizontal spatial drifts.

In order to study the spatial performances of our scanner, we used, firstly, a specific Kodak target, see Figure 137 in Annex. C. A classical measure for the determination of the precision of an optical-imaging system is the computation of its modulation transfer function (MTF). With recent revolution of the digitalization, we can wonder how the MTF can still be defined in this new world of sampling systems. A rigorous method for measuring the MTF of a sampled imaging system has been presented by Sitter et al. in 1995 with simple bar patterns imaging. This method is reliable since the fundamental frequency component does not overlap with an aliased harmonic component. An optimal set of bar-pattern measurement frequencies derives from this method and led us to choose the best special frequencies in the following ones of our Kodak target, see Figure 56, that avoid errors due to aliasing.

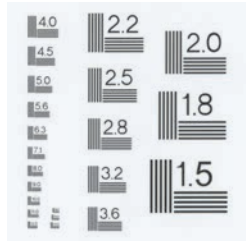


Figure 56. Scan at 600 ppi of a Bar-target chart from Kodak target for measurement of the MTF of our scanner.

Numerals indicate the number of cycles (one black plus one white line) per millimeter.

We choose a scan at 600 ppi. The special frequency therefore ranges from 0 to $\frac{1}{2\Delta}$, with Δ representing the sample spacing ($42 \mu\text{m}$ in our example for a 600 ppi scan). The authors build an equation connecting the number k of cycles of the bar pattern and the number N of samples for the analysis: To avoid aliasing effects, one may choose frequencies (fundamental frequency denoted as $1/d$) that are equally distant from the aliased m^{th} harmonic and the aliased $(m+1)^{\text{th}}$ harmonic.

This leads to

$$\frac{1}{d} = \frac{2}{(2m+3)\Delta},$$

with m being an even integer strictly positive. In a discret application,

$$\frac{1}{d} = \frac{k}{N\Delta}$$

yields to

$$k = \frac{2N}{2m+3}, \text{ and then}$$

$$N = km + \frac{3}{2}k.$$

By choosing k as an even integer (we chose two cycles of the bar pattern for our analysis) and varying m we obtain a list of N values that avoid aliasing effect.

In the Kodak target we used for this experiment, we selected the bar period that match best this list: 1.5, 2.0, 2.2, 2.5, 2.8, 3.2, 3.6, 4.5, 5.0, 6.3, 8.0, 9.0 cycles per millimeter.

The system MTF is given by the following equation:

$$H\left(\frac{1}{d}\right) = \left| \frac{d\bar{I}[k]}{NaL\text{sinc}\left(\frac{L}{d}\right)} \right| \quad (3.4)$$

With $a = (a+c) - c$, $(a+c)$ is obtained by averaging a white pixel area in the target, and c is estimated by averaging a black pixel area (in the text of figure "5" on the bar pattern chart for example).

$$\bar{I}[k] = \sum_{n=0}^{N-1} \bar{i}[n] \exp\left(-j2\pi \frac{k}{N}\right),$$

with $\bar{i}[n]$ is a one dimensional vector of data taken in the direction of the periodicity of the chosen bar pattern.

$\frac{L}{d}$ is the duty cycle of the bar pattern, and is defined by

$$\frac{L}{d} = \frac{\bar{I}[0]/N - c}{a}.$$

The obtained curves for both horizontal and vertical frequencies are displayed below.

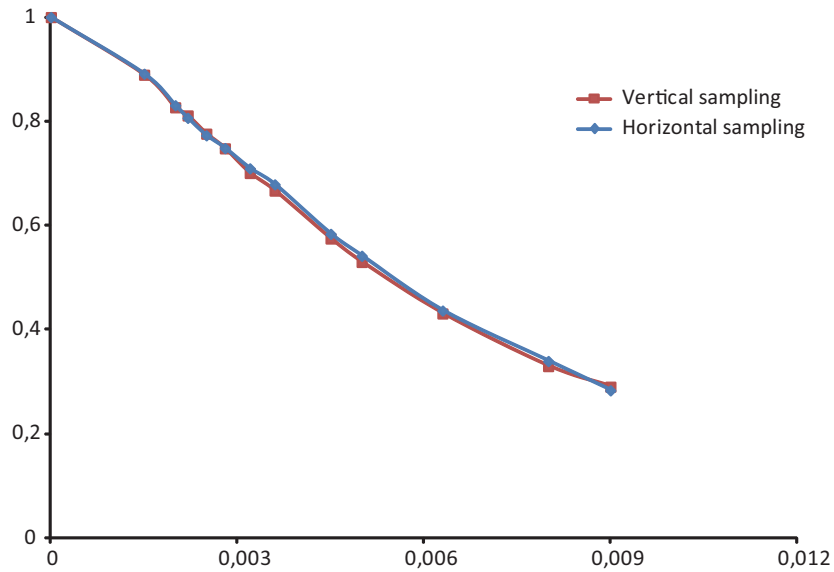


Figure 57. Plot of the computed MTF in vertical and horizontal directions of our EPSON PERFECTION V700 Scanner computed with the bar pattern chart on Figure 56.

3.1.4 Correction of color drifts of the acquisition system

As we showed in the previous sections, the flatbed scanner, a useful tool, very common nowadays, enables acquiring color pictures with a certain trustworthiness, thanks to control lighting, and geometrical distortions quite low. But it is also obvious that the colors obtained by a scanner will not be the same that the ones obtained from another acquisition device, or with the same device but with different settings, and may also be perceived differently by our visual system. The reason is that the RGB color coordinates given by the scanner are device dependent, which means that they depend on the spectral responses of the sensors. And these responses are also different of the responses of our brain cells [28].

The color calibration of the scanner requires finding the correspondence between the RGB device-dependent coordinates given by the scanner, and color values depending only on the surface property and the illuminant [39, 40]. For that purpose, acquisition of images presenting color patches of well-known spectral reflectances values will be addressed. By using techniques, as interpolation or polynomial regression as in [41], discussed later, we can compare the data given by the scanner to the ground truth color values, and a color transformation can be derived. Standards defining colour targets for input scanner calibration are proposed in ISO 12641.

The KODAK Q-60 Color Input Target, displayed in Figure 48, has been designed according to some specific aspects of both ANSI and ISO 12641 standards. The target is based on the use of twelve hue angles (from row A to row L) and three lightnesses at each hue angle, providing rather uniform sampling of the CIELAB color space. It is defined in detail in ANSI standard IT8.7/2 (for reflection materials). For each pair of hue angle and lightness there are four chroma (saturation) levels. The first three of these at each lightness level (columns 1-3, 5-7, and 9-11) are specifically defined in the ANSI and ISO standards and are referred to as the common gamut area. The values of these patches are based on paper color gamut information provided by Agfa, Fuji, Kodak, and Konica. The patches are defined such that they are able to be produced on all the sensitized products included in the gamut comparison. The fourth chroma (columns 4, 8, and 12), represents the maximum chroma (colorfulness) that the specific product can produce at that hue angle and lightness level. Following columns (13-19) presents cyan, magenta, yellow, grey, red, green and blue gradients characteristics of the target dye set. The grey gradient is defined to start at D-min (white) and end at D-max (black) in twelve steps with equal lightness increments. The cyan, magenta, and yellow gradients are based on the amount of each of those dyes contained in the column 16 neutral grey gradient. The red, green, and blue gradients are made of appropriated combinations of the cyan, magenta, and yellow gradients. At the bottom, there is another twenty two step neutral grey gradient, surrounded by D-min and D-max patches. Steps 1 to 22 are defined according to L^* values specified in the standards documents. Moreover, the additional columns 20-22 of the target have been left undefined for each manufacturer to include a personalised area. Kodak has included 12 flesh patches in this area recognizing the importance of flesh tone reproduction in professional applications. Kodak targets also include a portrait image which will be useful in subjective confirmation of input scanner calibration.

The ANSI and ISO standards define the format for reflection targets which is 5x7 inch, and some specifications and tolerances for colorimetric aim values. About the numerical target data, the standards specify that for all targets the batch-specific CIEXYZ tristimulus mean value and standard deviation for each patch should be available.

Although data is available via a direct FTP access from KODAK website, we choose to measure the target with a spectrophotometer to get the entire reflectance data, which will enable us to convert into tristimu-

lus values considering any illuminant we want: the data provided by Kodak being for a two degree standard observer, and D50 illuminant, whereas we are working rather with D65 illuminant. The spectrophotometer captures light from a quite small surface, for instance a disk with a few millimeters diameter, and integrates all surface heterogeneities. The measuring geometry may have a strong influence if the surface of the color chart is glossy (which is the case with Q-60 target). For our measurement, we use the X-Rite i1 Pro spectrophotometer based on $45^\circ:0^\circ$ geometry, where light comes at 45° and reflected light is captured in the normal direction to the surface. The KODAK Q-60 Color Input Target being glossy, the $45^\circ:0^\circ$ geometry enables avoiding specularly reflected light.

The first step for calibrating the scanner is the spectral measurement of the color target to get color values for each patch. A color space needs to be selected to represent the color in a tristimulus form. We selected the CIELAB color space for its better visual linearity than an RGB color space for example. The conversion from spectrum to CIELAB requires defining an illuminant, and a standard observer. We choose to work with the D65 illuminant which corresponds to a daylight illuminant, with the 2° standard observer. The CIELAB color components are computed in the following way; first, the spectrum is converted into XYZ color space, as defined by the CIE (presented in Chapter 2.4), and then converted into CIELAB values. The $L^*a^*b^*$ values obtained are considered as the ground truth color values of the color chart.

The second step is the imaging of the target with the acquisition system. According to the previous study on the scanner, the target is located on the glass surface of the scanner, in an area where the distortions are minimal. For that purpose, we home-build a kind of angle bracket enabling scanning a sample always at the same best position on the glass surface of the scanner (see Figure 58).

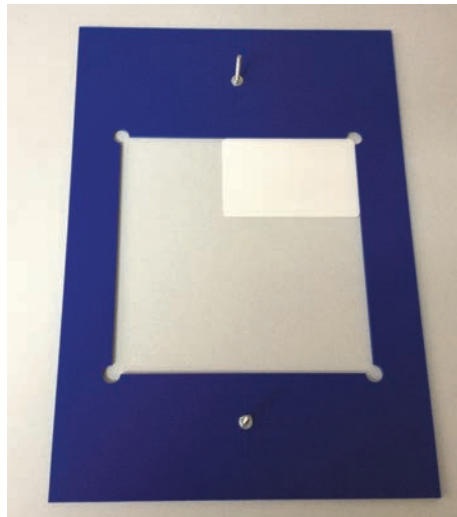


Figure 58. Home-made angle bracket laid on the scanner glass for constant sample scanning location.

The scanner acquires the image of the target at a resolution of 600 ppi. We manually locate the coordinates of the first top left patch, and then, by considering a horizontal and vertical offset we compute a mask for each patch (see Figure 59). A 100×100 pixel area is averaged for each patch to get the color values of this considered patch.

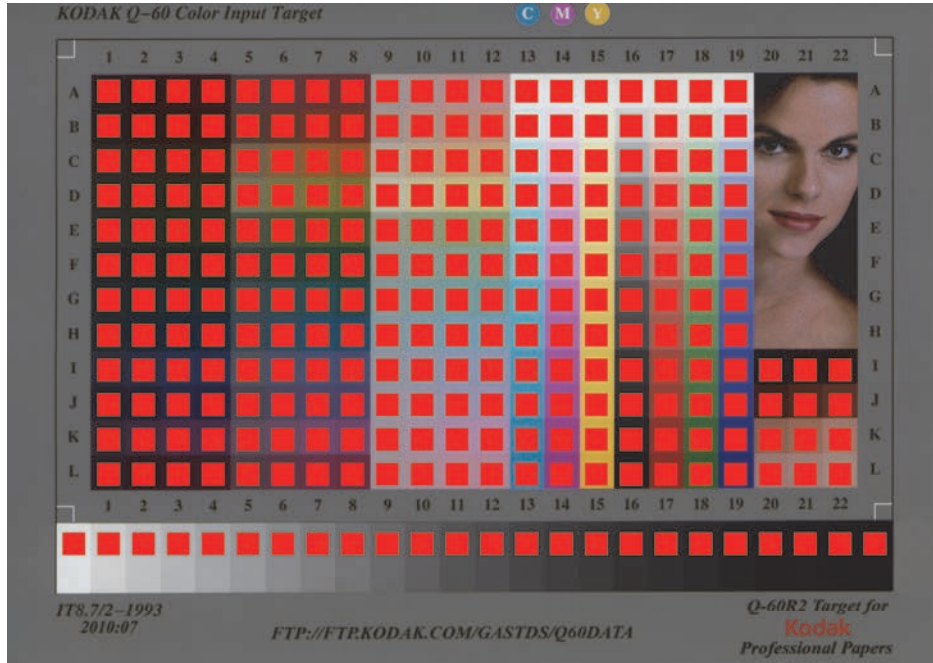


Figure 59. Target mask for the automatic computation of the color values of each patch.

Images are acquired using the EPSON Scan v3.81FR software. Every automatic color correction tool or enhancement option has been disabled in order to be sure that digitalization settings are the same for all patches. The scanner provides an image of 4100*3000 pixels, corresponding to the size of the target digitalized at 600 ppi. See Figure 48.

The color calibration aims to provide colors closed to those that would be obtained by a spectral measurement. It means determining a transform between RGB sources colors (given by the non-calibrated scanner), and the target ones. A pre-processing of the colors issued from the scanner device can be performed in order to help the future color calibration. This step is optional, but should be mentioned because the performances are a little better including this pre-processing. It consists in a gamma correction on the L channel.

The principle of this pre-processing is simple to set up: First we study the relationship between the luminance of patches scanned and then converted into CIELAB assuming that RGB scanner colors are in Adobe RGB color space $L^{scanned}$, the source, and the luminance of the reference patches (the target) L^{ref} . We first visualize this relationship considering the 24 gray patches on the Kodak target Figure 48.

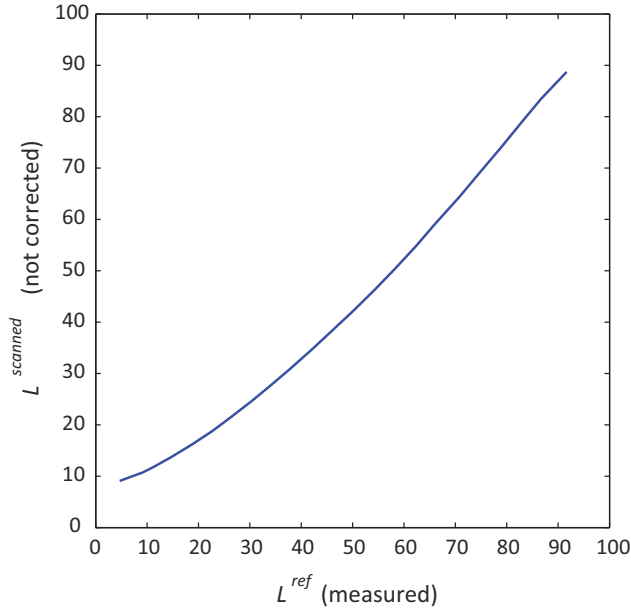


Figure 60. Correspondence between the luminance obtained on the scanned image and the one of the ground truth, for the 24 gray patches of the Kodak target.

As we observe a non-linear relationship, we understand the need to correct this first drift.

For each patch i of the Kodak color target, the luminance channel L_i^{ref} corresponding to the ground truth (the measure) is plotted versus the luminance $L_i^{scanned}$ of the uncorrected scanner color. The 264 points are then fitted by a second-order polynomial function, see Figure 61.

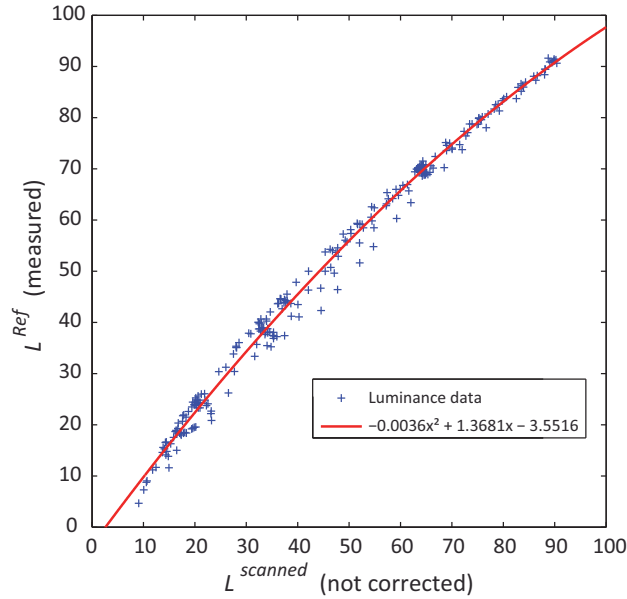


Figure 61. Fitting of the relationship between the luminance channel of reference image, and the luminance obtained from the scanned image. The polynome kept is: $-0.0036X^2 + 1.3681X - 3.5516$.

The pre-processing of the lightness consists in applying this polynomial function to the L channel of the scanner colors, rendering the luminance closer to the corresponding ground truth color we would get by a

spectral measure. See Figure 64 presenting the input target after pre-processing correction only, in contrast to Figure 63 corresponding to the raw scanned image.

Once this is done, we can compute the color transform T from the scanner-gamma-corrected colors to the ground truth ones.

The color transformation T we are looking for is supposed to convert a source vector corresponding to the color obtained by the uncalibrated scanner, after gamma correction, to a new color vector as close as possible to a target color vector (the ground truth). For any patch i , we denote as $\mathbf{c}_i^{\text{source}} = (L_i, a_i, b_i)$ the source vector, and as

$$\mathbf{c}_i^{\text{target}} = (L_i^{\text{measured}}, a_i^{\text{measured}}, b_i^{\text{measured}})$$

the target vector. The transformation T aims to correct the color distortions generated by the scanner device and therefore to provide colors that are not device-dependent any more, but that characterize only the considered sample reflectance properties and its illuminant. We choose a polynomial transformation as we have sufficiently patches in our color target. The main thing we have to be careful is the possible divergence of the polynomial between the training colors. An increase in the order of the polynomial will result in better fitting to the target colors, but in the same time, in higher drift between those training points. Considering our 264 color patches, we found that the third order is a good trade-off, as it is shown for digital colour camera by Cheung et al. in 2004 [42]. \mathbf{T} is the matricial representation of the third-order transform T . We can write:

$$\mathbf{c}_i^{\text{corrected}} = \mathbf{v}_i^{\text{source}} \cdot \mathbf{T}, \quad (3.5)$$

with \mathbf{T} a 20×3 matrix, $\mathbf{c}_i^{\text{corrected}}$ a vector of size three close to $\mathbf{c}_i^{\text{target}}$, and $\mathbf{v}_i^{\text{source}}$ a vector of size 20 obtained from the values of $\mathbf{c}_i^{\text{source}}$, L_i , a_i , and b_i issued from the scanner after the gamma correction of the Luminance, and defined as:

$$\mathbf{v}_i^{\text{source}} = (1, L_i, a_i, b_i, L_i^2, L_i a_i, L_i b_i, a_i^2, b_i^2, a_i b_i, L_i^2 a_i, L_i^2 b_i, L_i^3, L_i a_i^2, L_i b_i^2, L_i a_i b_i, a_i^2 b_i, a_i b_i^2, a_i^3, b_i^3). \quad (3.6)$$

This vector construction is obtained following the tree in Figure 62.

\mathbf{T} is defined as:

$$\mathbf{T} = \begin{bmatrix} t_1^L & t_1^a & t_1^b \\ t_2^L & t_2^a & t_2^b \\ \dots & \dots & \dots \\ t_{20}^L & t_{20}^a & t_{20}^b \end{bmatrix}. \quad (3.7)$$

The 20×3 entries of the matrix \mathbf{T} are obtained from a learning of the 264 patches, by solving the following matrix equation in the least-mean square sense with the *mldivide* function or the \backslash operator in Matlab:

$$\begin{bmatrix} \mathbf{c}_1^{\text{target}} \\ \mathbf{c}_2^{\text{target}} \\ \dots \\ \mathbf{c}_{264}^{\text{target}} \end{bmatrix} \equiv \begin{bmatrix} \mathbf{v}_1^{\text{source}} \\ \mathbf{v}_2^{\text{source}} \\ \dots \\ \mathbf{v}_{264}^{\text{source}} \end{bmatrix} \cdot \mathbf{T}, \quad (3.8)$$

where each row of the matrices bordering the \equiv symbol is a line vector attached to one of the 264 color patches of the calibration set. The vectors $\mathbf{c}_i^{\text{target}}$ are obtained by spectral measurement of the target, and CIELAB color conversion, and the $\mathbf{v}_i^{\text{source}}$ vectors are obtained by Eq. (3.6).

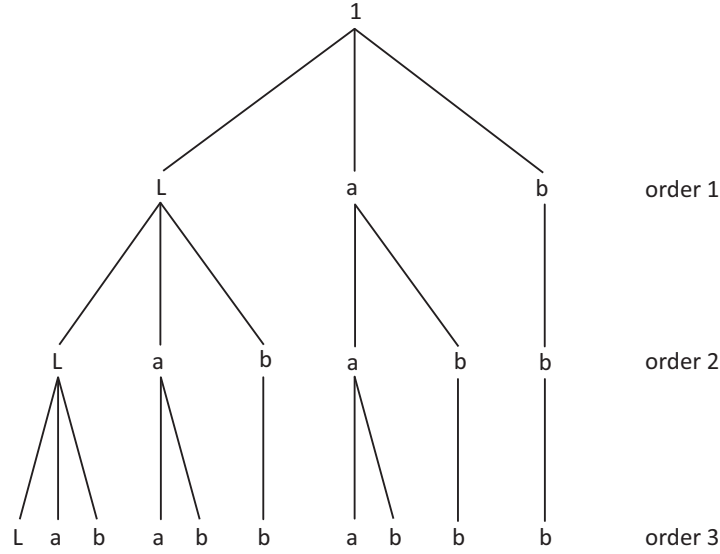


Figure 62. The construction of first, second, and third polynomial orders.

A Look Up Table (LUT) file is build to register the whole 256^3 RGB color transformations in order to quickly correct a new input image without having to compute for each pixel the entire algorithm. See Figure 65 presenting the input target after pre-processing correction and color transform T . In order to assess the performance of the method, we compute the ΔE_{94} color distance between every $\mathbf{c}_i^{\text{corrected}}$ color vector and the corresponding $\mathbf{c}_i^{\text{target}}$ color vectors. Firstly, we perform such a comparison on the training samples, i.e., on the target used for learning, and then, on new target with different colors than the ones used for training in order to verify that the algorithm remains valid with colors different from the training ones. The average ΔE_{94} values computed on each set of patches are compared with those given by the software developed by Newton Technologies, Virtual Proofer ©. Its last version 1.0.2 fixes some issues concerning the D50 illuminant used for color conversions in the former version, 1.0.1. Please note that VirtualProofer works in the sRGB color gamut, whereas our method works in AdobeRGB color gamut, which is wider than the sRGB one, and therefore subject to wider distortions. Our input not-corrected image target is therefore further away from the ground truth than the sRGB-not-corrected one, but in the same time, the number of « in gamut » patches will be higher using AdobeRGB color space rather than sRGB. The results are presented in Table 1 to Table 3 below. Table 1 corresponds to test on the Kodak Q60R2-07-2010 target (the learning target), Table 2 corresponds to test on the Patch_Dav_03 target (an home-made target, presenting different colors than the learning target), and Table 3 that corresponds to another test target, cf. Annex D.

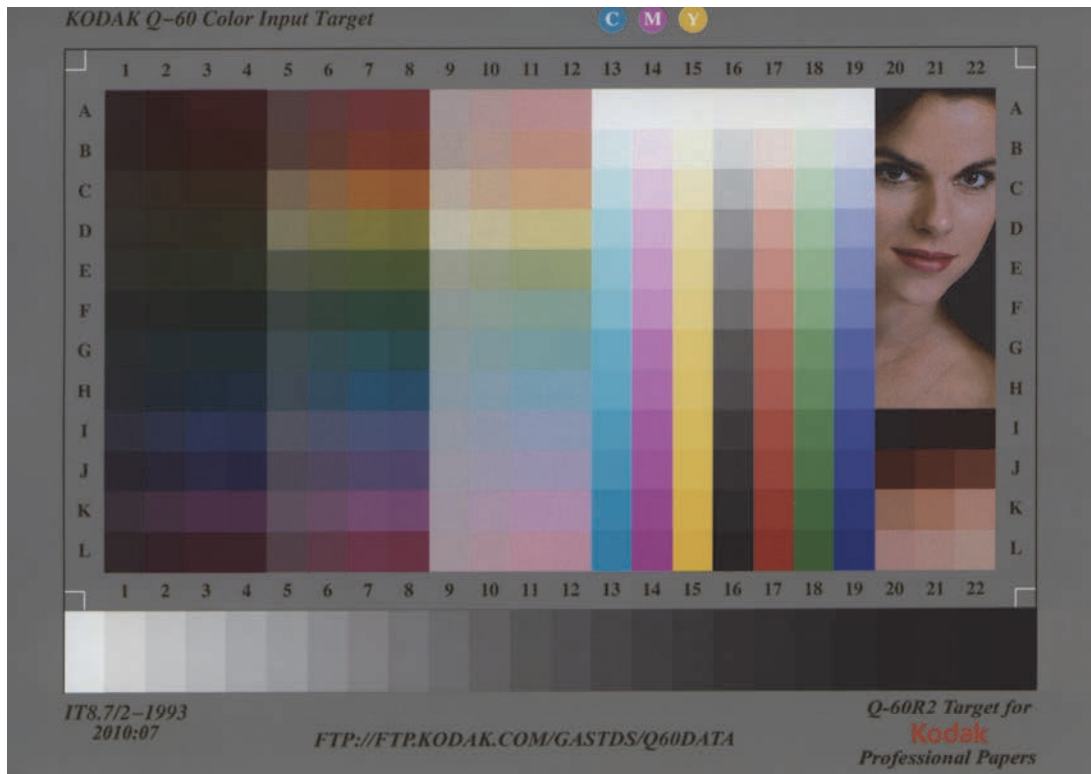


Figure 63.The Kodak Q60R2-07-2010 target image obtained after scan without any correction.

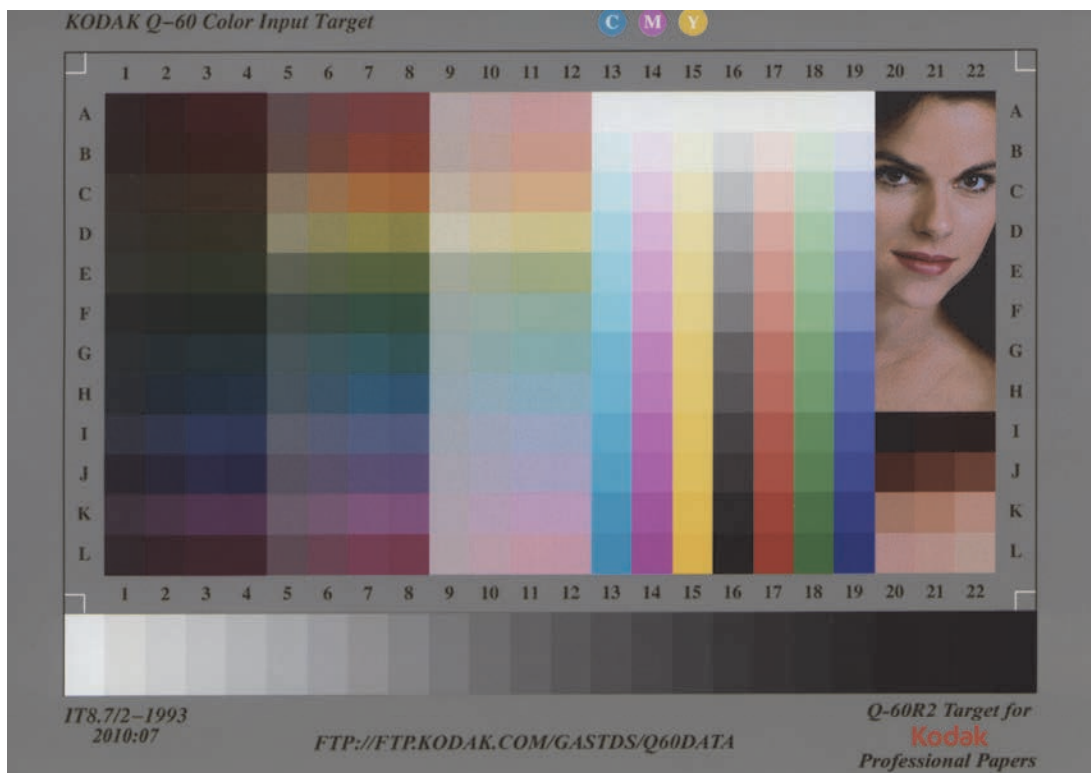


Figure 64. The Kodak Q60R2-07-2010 target image obtained after scan and gamma correction.

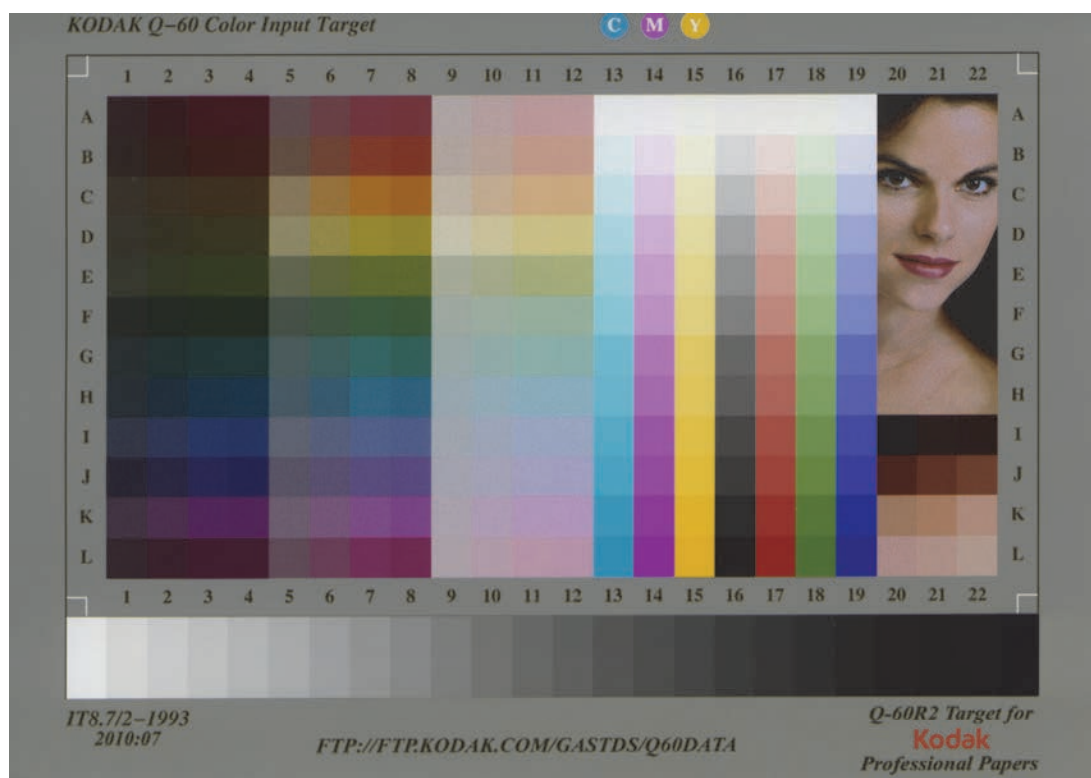


Figure 65. Kodak Q60R2-07-2010 target image obtained after scan, gamma correction, and color transform.

Table 1. Performance of the color calibration on the Kodak Q60R2-07-2010 target – Mean and 95% of the ΔE_{94} metric.

DeltaE94(ref, scanned)	Scanned with correction		Scanned without correction	
On all the 264 target color patches	μ	95%	μ	95%
Virtual Proofer v1.0.1	-	-	-	-
Virtual Proofer v1.0.2	0.692	2.08	3.78	9.04
L.S. 3 rd & γ -corrected	0.605	1.24	6.08	9.81
On «in gamut» patches only				
Virtual Proofer v1.0.1	-	-	-	-
Virtual Proofer v1.0.2 (243)	0.508	0.95	3.39	7.42
L.S. 3 rd & γ -corrected (262)	0.600	1.23	6.06	9.81

Table 2. Performance of the color calibration on the Patch_Dav_03 target – Mean and 95% of the ΔE_{94} metric.

DeltaE94(ref, scanned)	Scanned with correction		Scanned without correction	
On all the 149 target color patches	μ	95%	μ	95%
Virtual Proofer v1.0.1	4.59	12.77	5.60	13.79
Virtual Proofer v1.0.2	4.15	11.98	5.65	14.00
L.S. 3 rd & γ -corrected	3.33	8.30	7.16	12.56
On «in gamut» patches only				
Virtual Proofer v1.0.1 (99)	2.91	7.24	3.52	8.30
Virtual Proofer v1.0.2 (99)	2.68	7.83	3.53	8.03
L.S. 3 rd & γ -corrected (118)	2.84	7.62	6.39	10.46

Table 3. Performance of the color calibration on the Eye-One ScanTarget 1.4 target – Mean and 95% of the ΔE_{94} metric.

DeltaE94(ref, scanned)	Scanned with correction		Scanned without correction	
On all the 288 target color patches	μ	95%	μ	95%
Virtual Proofer v1.0.1	-	-	-	-
Virtual Proofer v1.0.2	1.99	5.42	5.06	11.64
L.S. 3 rd & γ -corrected	1.47	3.12	6.94	11.65
On «in gamut» patches only				
Virtual Proofer v1.0.1	-	-	-	-
Virtual Proofer v1.0.2 (215)	1.33	2.84	3.83	8.91
L.S. 3 rd & γ -corrected (254)	1.37	3.07	6.54	10.73

In Table 3, we obtain an average score in ΔE_{94} of 1.47 units, and when considering only “in-gamut” patches (which means only patches which color is inside the AdobeRGB color gamut that we use), a score of 1.37 units is obtained. This is close to the visual limit of 1.0 unit to conclude that the results are good enough to validate our method. A new scanned image can now be color corrected, provided that it is printed on a support close to the one used for learning (a Kodak glossy photo paper). This approach can be generalized to other color flatbed scanners provided that each device is separately calibrated.

3.2 Spectrophotometer

A spectrophotometer is an instrument delivering the spectral reflectance or transmittance factor of a material depending to the wavelength. They work only in the visible spectra range, that we presented in 2.2.1, and usually give values between 380 and 730 nm.

The principals sub-systems composing a spectrophotometer are first, a source of light, an optical system to guide the light to the sample defining the optical condition of the measure, a mean of dispersing the light after its reflection on the sample in order to separate the different wavelengths, then a detector, to capture the energy of each wavelength band, and a signal processing system to convert the light intensity into the expecting signal for analysis.

The reflectance and the transmittance both depend on the incident light, thus enabling the use of any source of light in theory. But in particular cases, especially when the sample is fluorescent, an adaptation of the optical system design is required because the light source spectral properties influence the final measurement. Ideally, the light source should be the same as the viewing condition, but this is often very difficult to reproduce the same condition, that is why the light source is often chosen to simulate a classical standard illuminant in the studied waveband. The spectrum of the source is also often constraints by cost factors or congestion factors, or power supply.

Once this input light as interacted with the sample, it enters the dispersing system. Historically, a prism was used. Then a slit combined to a scanning device were used in front of the detector to resulting, for each position of the slit, in monochromatic light, captured by the detector. Another dispersing system that used to be present in first spectrophotometers was an interference filter wheel. Today, most of the spectrophotometer systems prefer the use of diffraction gratings. Other instruments use a prism with a detector-array

to convert each wavelength to a signal. This electrical signal is then amplified and digitalized for numerical processing. In the case of the X-rite instruments that we use, the spectrophotometer delivers a 10 nm sampling. Using equation (2.2) we can compute CIEXYZ coordinates easily for any illuminant.

Different geometries exist, to enable or disable the specular reflection component. In our case, we use either a X-rite i1Pro (Eye-One Pro) spectrophotometer or a X-rite SpectroEye whose optical geometry is $45^\circ/0^\circ$ DIN 5033, which means that there is an annular light source illuminating the sample at 45° , and the detector is located at 0° , thus avoiding any specular reflection if the surface is flat.

We present on Figure 67 the certification of our GretagMacbeth SpectroEye we used for many measurements.



Figure 66. The i1Pro (left) and the SpectroEye (right) spectrophotometers we used.

	GretagMacbeth™	Gretag-Macbeth AG Althardstrasse 70 8105 Regensdorf Switzerland
		Phone: +41 (0)1 842 24 00 Fax: +41 (0)1 842 22 22

Certificate

Model: GretagMacbeth SpectroEye

Serial No: 3.264 – 12155

This notification serves to certify that the unit described above has been inspected and tested to be in accordance with the specifications published by Gretag-Macbeth AG.

Specifications

Inter instrument agreement:	Typically $0,3 \Delta E^*_{CIE,lab}$ (D50, 2°) average based on 12 BCRA tiles Maximally $0,8 \Delta E^*_{CIE,lab}$ (D50, 2°) on 12 BCRA tiles
Short term repeatability:	$0,02 \Delta E^*_{CIE,lab}$ (D50, 2°), mean value of 10 measurements every 10 seconds on white
White reference:	Ceramic tile based on barium sulfate according to DIN 5033 certified by PTB (Physikalisch Technische Bundesanstalt, Germany)

Regensdorf, 21. January 2002


Quality Assurance Manager



GretagMacbeth 98.50.23 en Printed in Switzerland

Figure 67. Our SpectroEye specifications.

Chapter 4 Color prediction

The goal of this chapter is to expose the fundamental principles of the interaction between incoherent white light with matter, which are at the base of the prediction models for the color rendering of printed surfaces. The more advanced approaches available today rely on optical models describing the selective attenuation of the wavelengths reflected by the print, combined with a model for the ink spreading, and calibrated using a small set of printed patches. The calibration requires to print about twenty full-tone and halftone color patches and to measure their spectral reflectance. For paper prints, such models generally have good prediction accuracy for a large panel of papers and inks deposition techniques [43].

4.1 Absorption in non scattering media

Following the study by Pierre Bouguer, Johann Heinrich Lambert cited Bouguer's "Essai d'Optique sur la gradation de la lumière" [44] published in Paris in 1729 in his book "Photometria", in 1760 [45]. According to Lambert-Bouguer's law, in a homogeneous isotropic non-scattering medium, the absorbance of a slice of medium is proportional to its thickness. One century later, August Beer extended the law to the chemical field asserting that absorbance is proportional to the concentration of the attenuating entities in a solution.

Considering I_0 the incident light intensity on such an absorbing media with a surface area A , and a concentration C of absorbing molecules, cf. Figure 68. The absorbance of the medium is related to the cross section σ of the absorbing atoms or molecules. In a slice of infinitesimal thickness dx , we can write the flux attenuations as:

$$i(x+dx) = i(x) - \frac{\sigma CA}{A} dx \times i(x), \quad (4.1)$$

or equivalently,

$$\frac{di}{i} = -\sigma C dx,$$

and by integration we obtain:

$$i(x) = I_0 \times e^{-\sigma C x}. \quad (4.2)$$

The usual Beer-Lambert-Bouguer law gathers the two laws by relating absorbance to both the concentration of attenuating entities, and the thickness of the media.

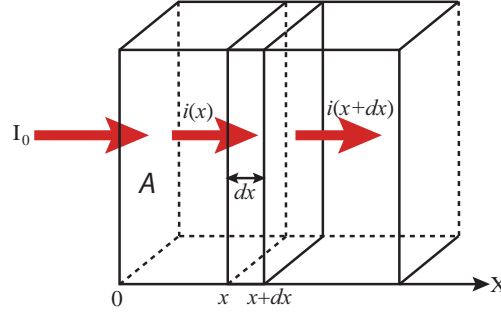


Figure 68. Absorbing media illustrating the Beer-Lambert-Bouguer law.

Usually, we present the law as:

$$i(x) = I_0 \times e^{-Kx}, \quad (4.3)$$

which leads to the transmittance of the material:

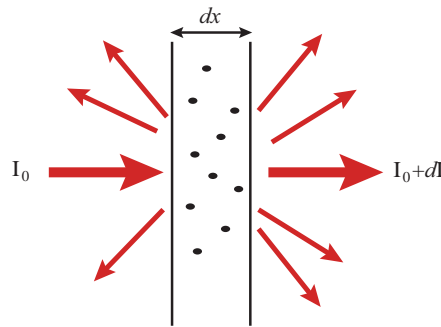
$$t(x) = \frac{i(x)}{I_0} = e^{-Kx}, \quad (4.4)$$

with $K = \sigma \cdot C$ being proportional to the concentration in absorbing substance.

In an absorbing medium, doubling the thickness of the material means that its transmittance is squared.

4.2 Highly scattering media

When the material is not perfectly transparent, Beer-Lambert-Bouguer's absorption law does not hold any more because of scattering. The light scattering corresponds to any phenomenon modifying the trajectory of a photon in a given medium, cf. Figure 69. It is mainly due to variations of the local refractive index of the medium.

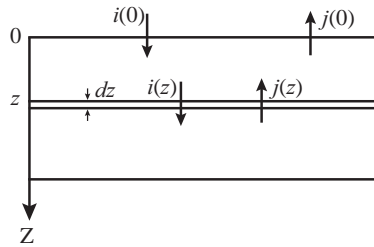
Figure 69. Light scattering by an infinitesimal layer of thickness dx .

In a similar approach as the one proposed for absorption, we consider a flux variation dI proportional to the incident flux and the thickness of the scattering crossed media:

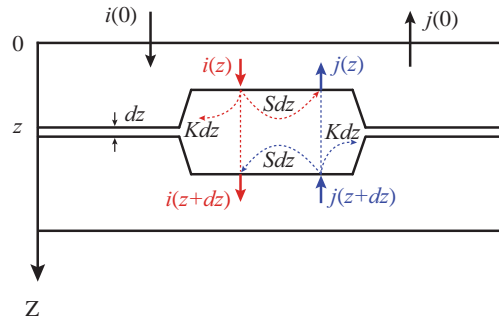
$$dI = -\beta(\lambda) I dx. \quad (4.5)$$

At this step, the particles responsible for the scattering are sufficiently distant to consider that a photon is not diffused more than once during the crossing of the medium. But this assumption fails when considering thick media or high particles density media where multiples diffusions occur. The resolution of such a problem requires a high mathematical process to solve the radiative transfer equation (RTE). For a practical approach, we can use simplified models.

In 1931, Kubelka and Munk proposed a scattering model to predict the luminance of a white overlay layer on top of a plane surface. It is a simplified version of the RTE where only two Lambertian fluxes are considered, propagating in opposite directions. The main assumption in Kubelka-Munk theory is that light is completely diffuse in the material. In theory, the illumination should be Lambertian and the whole exiting flux should be collected, requiring ideally an integrating sphere spectrophotometer. This theory does not apply to metallic or pearlescent inks that change the polarization of the light.



Let us consider an infinitesimal slice of material of thickness dz , the others dimensions being sufficiently large to avoid edge effects. We denote as K the part of the light flux which is absorbed (linear absorption coefficient), and S the part which is back diffused (linear scattering coefficient). Here is supposed that K and S are constant in the studied medium. The Kubelka-Munk theory considers: one downward flux, denoted $i(z)$, and another upward flux, denoted $j(z)$, where z denotes the propagation direction, perpendicular to the layer of medium.



We perform a fluxes balance in the infinitesimal slice. Getting through this slice, the entering flux $i(z)$ is reduced by a factor Kdz due to absorption, and by a factor Sdz due to scattering. The remaining flux is however increased by a factor Sdz due to the back scattering of the opposite flux $j(z)$. The balance gives

$$i(z+dz) = i(z) - Kdz \times i(z) - Sdz \times i(z) + Sdz \times j(z),$$

and finally we obtain a first differential equation:

$$\frac{di}{dz} = -(K + S)i + Sj. \quad (4.6)$$

Similar reasoning for upward flux $j(z)$ leads to a similar equation, with opposite sign:

$$\frac{dj}{dz} = (K + S)j - Si \quad (4.7)$$

Equations (4.6) and (4.7) lead to the following differential system:

$$\begin{cases} \frac{di}{dz} = -(K + S)i + Sj \\ \frac{dj}{dz} = (K + S)j - Si \end{cases} \quad (4.8)$$

To solve it, one can use the Laplace transform [46].

The Laplace transform of a causal function noted $f(z)$ is:

$$F(p) = \int_0^\infty f(t)e^{-pt} dt \quad (4.9)$$

The derivative of f in the Laplace domain is given by:

$$pF(p) - f(0).$$

The Laplace transform of differential system of Eq. (4.8) gives:

$$\begin{cases} pI(p) - i(0) = -(K + S)I(p) + SJ(p) \\ pJ(p) - j(0) = (K + S)J(p) - SI(p) \end{cases} \quad (4.10)$$

By solving Eq. (4.10), we have:

$$\begin{cases} I(p) = \frac{(p - aS)i(0) + Sj(0)}{p^2 - b^2S^2} \\ J(p) = \frac{(p + aS)j(0) - Si(0)}{p^2 - b^2S^2} \end{cases} \quad (4.11)$$

with $a = (K + S)/S$, and $b = \sqrt{a^2 - 1}$ ($a^2 - 1$ being positive).

As $p/(p^2 - K^2)$ is the Laplace transform of $\cosh(Kz)$, and $K/(p^2 - K^2)$ is the Laplace transform of $\sinh(Kz)$, we can conclude that $I(p)$ is the Laplace transform of:

$$i(z) = i(0)\cosh(bSz) + \frac{1}{b}(j(0) - ai(0))\sinh(bSz), \quad (4.12)$$

and that $J(p)$ is the Laplace transform of:

$$j(z) = j(0)\cosh(bSz) + \frac{1}{b}(aj(0) - i(0))\sinh(bSz). \quad (4.13)$$

By denoting as I_0 the incident flux entering a layer of thickness h without any interface, the reflectance corresponds to the ratio $j(0)/I_0$, and the transmittance corresponds to $i(h)/I_0$. Evaluation at the boundaries gives $i(0) = I_0$, and $j(h) = 0$.

By injecting boundary condition in Eq. (4.13) at height of $z = h$, we have:

$$\rho_h = \frac{j(0)}{I_0} = \frac{\sinh(bSh)}{b \cosh(bSh) + a \sinh(bSh)}, \quad (4.14)$$

and

$$\tau_h = \frac{i(h)}{I_0} = \frac{b}{b \cosh(bSh) + a \sinh(bSh)} \quad (4.15)$$

If we now consider a layer with infinite thickness. We compute the limit in Eq. (4.14) when h become infinite, and get:

$$\lim_{h \rightarrow \infty} \rho_h = \lim_{h \rightarrow \infty} \frac{1}{a + b \coth(bSh)} = \frac{1}{a + b} = a - b. \quad (4.16)$$

We denote as ρ_∞ this limit, and obtain the most famous equation of Kubelka-Munk theory:

$$\frac{K}{S} = \frac{(1 - \rho_\infty)^2}{2\rho_\infty}. \quad (4.17)$$

The model presented here does not take into account any interface. The incident flux I_0 is in fact both partly transmitted in the material, and partly reflected by the air/material interface. The output flux j_0 undergoes the same phenomenon. In 1942, Saunderson introduced a correction [47], famously known as Saunderson correction, taking into account theses reflections, cf. Figure 70. We denote as R the reflectance of the material as the ratio of the outgoing flux J_0 over the incoming flux I_0 , ρ internal reflectance given by the Kubelka-Munk theory considering no interface, which is obtained by Eq. (4.14) at depth 0 by the upward over downward fluxes ratio j_0/i_0 . We denote as T_{in} the transmitted component of the incoming flux I_0 , and r_e the external reflectance. In the same way, J_0 is split into a transmitted component denoted as T_{out} , and an internally reflected component denoted as r_i .

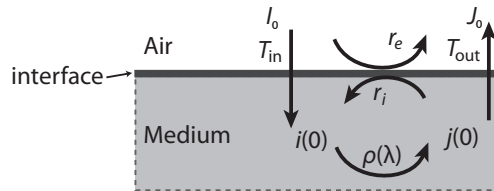


Figure 70. Illustration of Saunderson correction.

We write the fluxes conservation for the crossing of light in the material:

$$i(0) = T_{in}I_0 + r_i\rho i(0), \quad (4.18)$$

and

$$J_0 = r_eI_0 + T_{out}\rho i(0). \quad (4.19)$$

Saunderson combined these two equations (4.18) and (4.19) to build his correction formula:

$$R = r_e + \frac{T_{in}T_{out}\rho}{1 - r_i\rho}. \quad (4.20)$$

The quantities r_e , r_i , T_{in} , and T_{out} are related to the refractive index of the material, and the illumination and/or observation geometries. They are independent of wavelength in most practical cases.

Some fundamentals on radiometry have to be mentioned now to get these parameters.

Physical value managed in radiometry is the radiance. Snell's laws make the relationship between incident reflected and refracted radiances.

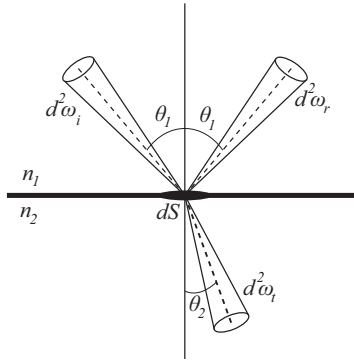


Figure 71. Reflection and refraction of a radiance at the interface between two media.

The ratio of the incoming flux $d^3\phi_i(\theta, \varphi)$ in direction (θ, φ) over the solid angle $d^2\omega_i$ and the illuminated surface element dS of apparent area $dS \cos(\theta)$ lead to the incident radiance:

$$L_i(\theta, \varphi) = \frac{d^3\phi_i(\theta, \varphi)}{dS \cos(\theta) d^2\omega_i}. \quad (4.21)$$

The solid angle of a pencil of light propagating in a given direction specified by the spherical coordinates (θ, φ) is:

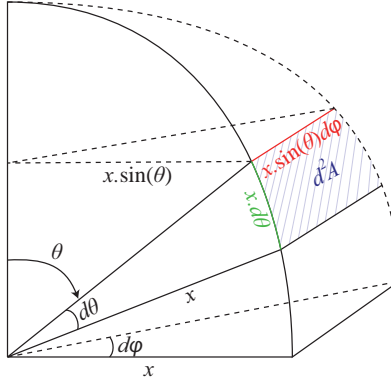


Figure 72. Definition of infinitesimal solid angle.

$$d^2\omega = \frac{d^2A}{x^2} = \frac{x^2 \sin(\theta) d\theta d\varphi}{x^2} = \sin(\theta) d\theta d\varphi. \quad (4.22)$$

Finally, Eq. (4.21) and (4.22) lead to:

$$L_i(\theta, \varphi) = \frac{d^3\phi_i(\theta, \varphi)}{dS \cos(\theta) \sin(\theta) d\theta d\varphi}. \quad (4.23)$$

In our application, the incident flux is Lambertian, i.e. the incoming radiance is the same in every direction; hence $L_i(\theta, \varphi)$ is a constant. We thus have to consider the incoming flux $d^3\phi_i(\theta, \varphi)$ in all directions:

$$d\phi_i^L = \int_{\varphi=0}^{2\pi} \int_{\theta=0}^{\pi/2} d^3\phi_i(\theta, \varphi) = dS \int_{\varphi=0}^{2\pi} \int_{\theta=0}^{\pi/2} L_i(\theta, \varphi) \cos(\theta) \sin(\theta) d\theta d\varphi,$$

and so we have:

$$d\phi_i^L = dS \cdot L_i \int_{\varphi=0}^{2\pi} \int_{\theta=0}^{\pi/2} \cos(\theta) \sin(\theta) d\theta d\varphi = dS \cdot L_i \cdot \pi. \quad (4.24)$$

Considering now the reflected flux $d\phi_r$, we have for each direction (θ, φ) the relation:

$$d^3\phi_r(\theta, \varphi) = R_{12}(\theta) d^3\phi_i(\theta, \varphi).$$

This leads to:

$$d\phi_r(\theta, \varphi) = dS \int_{\varphi=0}^{2\pi} \int_{\theta=0}^{\pi/2} R_{12}(\theta) L_i \cos(\theta) \sin(\theta) d\theta d\varphi = dS \cdot \pi \cdot L_i \int_{\theta=0}^{\pi/2} R_{12}(\theta) \sin(2\theta) d\theta.$$

The Lambertian reflectance of an interface, denoted as r_{12} for light coming from medium 1 and entering in medium 2 of respective indices n_1 and n_2 with $n_2 > n_1$, is:

$$r_{12} = \frac{d\phi_r}{d\phi_i^L} = \int_{\theta=0}^{\pi/2} R_{12}(\theta) \sin(2\theta) d\theta, \quad (4.25)$$

with the reflectivity $R_{12}(\theta)$ obtained by the average of the two components of polarization respectively named “parallel” and “perpendicular” and denoted R_{s12} for s-polarized light, and R_{p12} for p-polarized light. r_{12} depends only on the relative index of the interface denoted as $n = n_2/n_1$. An analytical formula can be obtained for Eq. (4.25) by integration of the two components of polarization [48]:

$$r_{12} = \frac{1}{2} + \frac{(n-1)(3n+1)}{6(n+1)^2} - \frac{2n^3(n^2+2n-1)}{(n^4-1)(n^2+1)} + \frac{8n^4(n^4+1)\ln(n)}{(n^4-1)^2(n^2+1)} + \frac{n^2(n^2-1)^2}{(n^2+1)^3} \ln\left(\frac{n-1}{n+1}\right) \quad (4.26)$$

This reflectance equation is dedicated to Lambertian light coming from medium of lowest refractive index and entering a medium of higher refractive index. In the opposite side, the reflectance is higher because all incident light with incident angle higher than the critical angle $\theta_T = \arcsin(n_1/n_2)$ will be totally reflected in the medium 2, and $R_{21}(\theta_2) = 1$. Thus, let us divide the integral expressing the reflectance r_{21} of Lambertian light coming from medium 2 into two integrals:

$$r_{21} = \int_{\theta_2=0}^{\pi/2} R_{21}(\theta_2) \sin(2\theta_2) d\theta_2 = \int_{\theta_2=0}^{\theta_T} R_{21}(\theta_2) \sin(2\theta_2) d\theta_2 + \int_{\theta_T}^{\pi/2} \sin(2\theta_2) d\theta_2 \quad (4.27)$$

Snell's law $n_1 \sin(\theta_1) = n_2 \sin(\theta_2)$, and its differential $n_1 \cos(\theta_1) d\theta_1 = n_2 \cos(\theta_2) d\theta_2$ lead to:

$$n_1^2 \sin(\theta_1) \cos(\theta_1) d\theta_1 = n_2^2 \sin(\theta_2) \cos(\theta_2) d\theta_2,$$

and finally:

$$n_1^2 \sin(2\theta_1) d\theta_1 = n_2^2 \sin(2\theta_2) d\theta_2.$$

For $\theta_2 \in [0, \theta_T]$, we have $\theta_2 = \arcsin(n_1 \sin(\theta_1)/n_2)$

and we have

$$R_{12}(\theta_1) = R_{21}(\theta_2)$$

independently of polarization, giving:

$$\left(\frac{n_1}{n_2}\right)^2 R_{12}(\theta_1) \sin(2\theta_1) d\theta_1 = R_{21}(\theta_2) \sin(2\theta_2) d\theta_2.$$

We can rewrite Eq. (4.27) as: $r_{21} = \left(\frac{n_1}{n_2}\right)^2 r_{12} + \int_{\theta_T}^{\pi/2} \sin(2\theta_2) d\theta_2$, which leads to:

$$1 - r_{21} = \left(\frac{n_1}{n_2}\right)^2 (1 - r_{12}). \quad (4.28)$$

According to notations introduced in Figure 70, and in case of diffuse/diffuse geometry, we have $r_e = r_{12}$ given by (4.26), $r_i = r_{21}$ given by (4.28).

Energy conservation at the interface imposes that, if the incident flux is Lambertian:

$$T_{in} = t_{12} = 1 - r_{12}, \quad (4.29)$$

and, if the whole exiting flux is collected:

$$T_{out} = t_{21} = 1 - r_{21}. \quad (4.30)$$

4.3 Williams-Clapper model

In 1953, in “Multiple Internal Reflections in Photographic Color Prints” [49], Williams and Clapper introduced an optical model for predicting the color of a nonscattering layer on top of a diffusing background. It was originally dedicated to glossy photographs and oil paintings made of a diffusing paper-type substrate coated with a non scattering ink layer in optical contact with the background, which means there is no interface between them. It is derived from a description of the multiple reflections of light between the diffusing background and the air-print interface through the coloring layer. The nonscattering layers and the diffusing background are assumed to have same refractive index n . By denoting as $\rho(\lambda)$ the internal reflectance of the background, and $t(\lambda)$ the internal transmittance of the coloring layer under normal incidence, the spectral reflectance factor of the print, illuminated at angle θ_i and observed at angle θ_r . ($\theta_i : \theta_r$ geometry) is given by

$$R(\lambda) = r_s + \frac{T_{in} T_{out} \rho(\lambda) t^{1/\cos(\theta'_i) + 1/\cos(\theta'_r)}}{1 - r_i(t, \lambda) \rho(\lambda)} \quad (4.31)$$

where θ'_i denotes the orientation of the incident beam after refraction in the coloring layer, and θ'_r the orientation of the exiting beam before refraction in air:

$$\begin{aligned} \theta'_i &= \arcsin(\sin(\theta_i)/n), \\ \theta'_r &= \arcsin(\sin(\theta_r)/n) \end{aligned} \quad (4.32)$$

r_s is the specularly reflected light component captured by the observer (which is zero if $\theta_i \neq \theta_r$). T_{in} denotes the Fresnel transmittance of the print-air interface for the incident light:

$$T_{in} = T_{12}(\theta_i), \quad (4.33)$$

T_{out} is the Fresnel transmittance of the interface for the exiting light accounting for the change of geometrical extent due to the refraction in air,

$$T_{out} = \frac{T_{21}(\theta'_r)}{n^2} = \frac{T_{12}(\theta_r)}{n^2}, \quad (4.34)$$

and $r_i(t, \lambda)$ is the spectral reflectance of the diffuse light that is internally reflected by the interface through the coloring layer:

$$r_i(t, \lambda) = \int_{\theta=0}^{\pi/2} t^{2/\cos\theta}(\lambda) R_{21}(\theta) \sin(2\theta) d\theta. \quad (4.35)$$

The refractive index is generally assumed to be $n = 1.5$. For a reflectance factor based on the $45^\circ : 0^\circ$ geometry, we have $T_{in} = 0.95$, $T_{out} = 0.96 / 1.5^2$, $r_s = 0$, and $r_i = 0.6$ that are constants attached to the reflections and transmission of light by the air-print interface depending only on the refractive index of the layers [50].

4.4 Berns' equation

A simplified version of the Williams-Clapper equation is to consider that the coloring layers have an effective internal transmittance $T(\lambda)$ independent of the orientation and angular distribution of light. The Clapper-Yule reflectance model for halftone prints [51], as well as Bern's reflectance model [52] for con-tone prints rely on this « non-orientational » internal transmittance which is often suitable when the colorant is slightly scattering. The Williams-Clapper equation thus simplifies into the following equation, equivalent to a Saunderson correction [47], see Eq. (4.20) for colored diffusing background of reflectance $\rho(\lambda)T^2(\lambda)$ (see Figure 73):

$$R(\lambda) = r_s + \frac{T_{in} T_{out} \rho(\lambda) T^2(\lambda)}{1 - r_i \rho(\lambda) T^2(\lambda)} \quad (4.36)$$

with

$$r_i = \int_{\theta=0}^{\pi/2} R_{10}(\theta) \sin(2\theta) d\theta \quad (4.37)$$

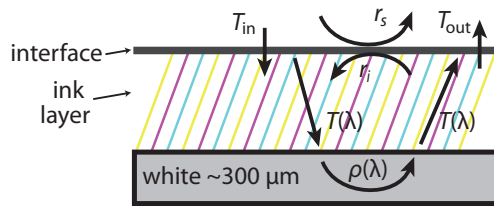


Figure 73. Structure comprising a white diffusing background coated with non-scattering ink layer.

According to Beer-Lambert-Bouguer law [39], doubling the thickness of the coloring layer or doubling the concentration in the absorbing substance is equivalent [53]: the internal transmittance $t_i(\lambda)$ of the original layer becomes $t_i^2(\lambda)$, the factor 2 being the *relative optical thickness* of the coloring substance. In the case where the coloring layer contains a mixture of three colorants, e.g. cyan, magenta and yellow, with respective relative optical thicknesses ε_c , ε_m and ε_y , the internal transmittance of the coloring layer is

$$T(\lambda, \varepsilon_c, \varepsilon_m, \varepsilon_y) = t_c^{\varepsilon_c}(\lambda) t_m^{\varepsilon_m}(\lambda) t_y^{\varepsilon_y}(\lambda) \quad (4.38)$$

and the reflectance of the print, according to Berns' model, becomes:

$$R(\lambda, \varepsilon_c, \varepsilon_m, \varepsilon_y) = r_s + \frac{T_{in} T_{out} \rho(\lambda) t_c^{2\varepsilon_c}(\lambda) t_m^{2\varepsilon_m}(\lambda) t_y^{2\varepsilon_y}(\lambda)}{1 - r_i \rho(\lambda) t_c^{2\varepsilon_c}(\lambda) t_m^{2\varepsilon_m}(\lambda) t_y^{2\varepsilon_y}(\lambda)} \quad (4.39)$$

The diffusing background reflectance $\rho(\lambda)$, and the internal transmittances of the three colorants, $t_c(\lambda)$, $t_m(\lambda)$ and $t_y(\lambda)$, can be deduced from measured data. Since the spectral reflectance factor of the print without ink ($T(\lambda) = 1$) depends only on $\rho(\lambda)$, we have

$$R_0(\lambda) = r_s + \frac{T_{in} T_{out} \rho(\lambda)}{1 - r_i \rho(\lambda)}, \quad (4.40)$$

therefore,

$$\rho(\lambda) = \frac{R_0(\lambda) - r_s}{T_{in} T_{out} + r_i [R_0(\lambda) - r_s]}. \quad (4.41)$$

Then, the spectral reflectance factor of the card with a layer of colorant j , with internal transmittance $t_j(\lambda)$ and unit optical thickness, is given by:

$$R_j(\lambda) = r_s + \frac{T_{in} T_{out} \rho(\lambda) t_j^2(\lambda)}{1 - r_i \rho(\lambda) t_j^2(\lambda)}. \quad (4.42)$$

Knowing $R_j(\lambda)$ and $\rho(\lambda)$, we can deduce the colorant's internal transmittance:

$$t_j(\lambda) = \sqrt{\frac{1}{\rho(\lambda)} \cdot \frac{R_j(\lambda) - r_s}{T_{in} T_{out} + r_i [R_j(\lambda) - r_s]}}. \quad (4.43)$$

This can be repeated for every colorant.

Second Part

Attributes for printed images quality assessment

Chapter 5 Tone homogeneity index

This chapter introduces a homogeneity assessment method, compliant with human visual perception, for the printed versions of uniform color images. This parameter has been specifically selected as one of the relevant attributes of printing quality. The method relies on image processing algorithms from a scanned image of the printed surface, especially the computation of gray level co-occurrence matrices and of objective homogeneity attribute inspired of Haralick's parameters. The viewing distance is also taken into account when computing the homogeneity index. Resizing and filtering of the scanned image are performed in order to keep the level of details visible by a standard human observer at short and long distances. The combination of the obtained homogeneity scores on both high and low resolution images provides a homogeneity index, which can be computed for any printed version of a uniform digital image. We tested the method on several hardcopies of a same image, and compared the scores to the empirical evaluations carried out by non-expert observers who were asked to sort the samples and to place them on a metric scale. Our experiments show a good matching between the sorting by the observers and the score computed by our algorithm. This work follows our contribution in [54].

5.1 Introduction

The present work focuses on the homogeneity of tones, i.e., the homogeneity of any surfaces on which an originally uniform digital color image is printed. This attribute, considered as relevant, is tackled through two indices dedicated to particular defaults in the standard ISO 13660:2001, the only international standard describing a wide range of attributes of image quality dedicated to quality assessment for binary or monochrome printing systems [55]. In this standard, both mottling and graininess are defined as a type of homogeneity default of paper-like surfaces and two indices are suggested in the spatial domain. Our purpose here is first to define a more generic index able to take into account any factor altering homogeneity. A second objective is to get a normalized index, which is not the case of mottling and graininess indices whose normalization is not straightforward. A pass-band method was proposed [56] as an alternative able to better take into account the sensitivity of the human visual system. A pass-band assessment based on wavelets, followed by a second-order statistics calculation on the gray-level co-occurrence matrix was achieved in [57] to form an homogeneity index. In 1999, in his studies of "Optical homogeneity of prints" [58], Johansson raised the importance of the confrontation between instrumental measurement and subjective quality evaluation. Our aim here is to integrate human vision characteristics into both the filtering step and the second-order statistics calculation. As in [56], our approach first consists in the digitalization of the printed surface using a high resolution flatbed office scanner, the scanned image being then processed in order to compute an homogeneity index which is consistent with the perception of human observers. This method is based on color images whereas the previously mentioned works are limited to gray level images. Moreover, for several versions of a same digital image printed on different supports with different printing techniques, we compare the scores given by our method with those given by the observers during a sensory metrology experiment.

In the next sections, we first explain how the surfaces are digitalized and which tool of image processing we use before developing in details our method and its tunable parameters. We finally compare the score provided by the method with empirical assessment by observers on four sets of samples.

5.2 Digitalization of the prints

For the digitalization of the samples, a scanner is used. An initial study on scanners presented in 3.1 have led to the conclusion that it is a reliable tool for image acquisition due to its remarkable reproducibility, owing to a uniform illumination, and a good geometry that avoids specular reflections when the surface is flat. However, spatial and color distortions induced by the acquisition systems should be taken into account when assessing quality from scanned image.

The color gamut of the human visual system is much larger than the gamut of the scanner, which is unknown but can be assumed to be quite close to sRGB. Because of this, the color distortion problem is twofold: Firstly, the so-called "seen by the scanner" colors are displaced within the very gamut of the scanner; and secondly, it may also appears that different printable colors are out of the gamut of the scanner, but perceived by the scanner as having the same color. A color calibration would seem necessary to solve at least the first issue, using color characterization for an imaging system such as presented in [40, 59]. However, we noticed that some color corrections may add noise. As part of our work (the assessment of homogeneity), we discarded color correction in order to prevent degradation of our homogeneity measurement.

Regarding the spatial distortions, there is a significant horizontal drift. In the vertical direction, we do not notice geometric drift: the position of the motor is properly controlled. This drift can be corrected by adjusting the position of the pixels by polynomial interpolation or spline on each line of the captured image. But such treatment would create a change in the value of certain pixels on each line, the most affected by this drift being on the edges of each line, and would lead to a loss of the native resolution of the image as well as local color unwanted distortions. It is preferable to analyze the scanner profile derives and place the sample on the scanner glass in an area where the drifts are minimal. We recommend scanning samples at a high resolution (e.g. 2400 dpi), and then reducing to 1200 dpi, the initial resolution of our method, in order to perform controlled down-sampling.

5.3 Background: Image homogeneity analysis

On the GLCM, introduced in Section 1.1.1, Haralick defined several texture attributes among which a homogeneity attribute comprised between 0 and 1, defined as:

$$Hom = \sum_{i=0}^{2^{n_b}-1} \sum_{j=0}^{2^{n_b}-1} \frac{1}{1+(i-j)^2} \times p_t(i, j). \quad (5.1)$$

If the GLCM \mathbf{H}_t of image I is computed on a uniform image (top left image on Figure 11) or on a periodical image with period t (top middle image), then for every pair of pixels $(f(p), f(p+t))$, we have $f(p) = f(p+t)$. Therefore, only entries in the diagonal of \mathbf{H}_t are incremented, and Hom is 1. In the other cases, as for example for the top right image of fig, \mathbf{H}_t is not diagonal, and Hom ranges in $]0, 1[$.

Formula (5.1) may be replaced with other ones, defined so as to give different weight to entries more distant from the diagonal. For example, we may generalize Eq. (5.1) by defining the following function weighting the shifting probability $p_t(i, j)$ (measured by the normalized frequency (1.10)):

$$w_{a,b} : x \mapsto \frac{1}{1 + a \times x^b}, \quad (5.2)$$

where a and b are tunable real values (see Figure 74), and $x = |i - j|$.

Using $w_{a,b}$ with different a and b values than the ones used in Eq. (5.1), we can tune the response of the homogeneity score to variations of the pixel values in the image.

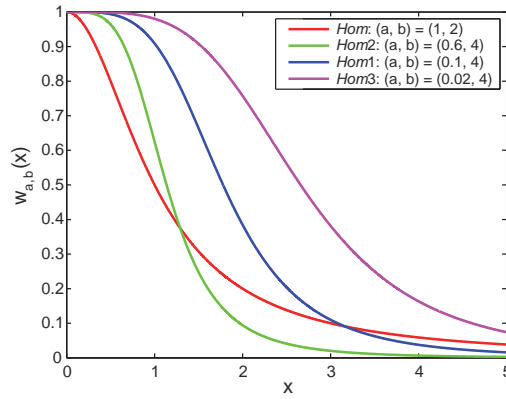


Figure 74. $w_{a,b}$ function for three different sets of (a, b) values. Original Haralick's attribute (denoted as *Hom*) corresponds to the $w_{1,2}$ function plotted in red line. $w_{0.1,4}$ and $w_{0.6,4}$ functions, respectively denoted as *Hom1* and *Hom2*, are plotted in blue, respectively green lines.

5.4 Overview of the method

The Homogeneity assessment method that we propose relies on the following steps (summarized in Figure 75):

- A printing and digitalization as detailed in Section 5.2;
- After some basic image registration, a pre-processing, including image resizing and filtering in order to simulate near vision at High Resolution (HR), and far vision at Low Resolution (LR). We work on two channels (lightness and hue) on both HR and LR images (see Figure 76);
- The application of the Image Homogeneity Analysis method described in Section 1.1.1 and in Section 5.3, and the score computation from the GLCM on both HR and LR images (see Sections 5.6 and 5.7);
- In parallel to all of this, a comparison with psycho-visual assessment (see Section 5.9) is recommended to verify whether the used parameters are optimal for the considered application (see Section 5.8).

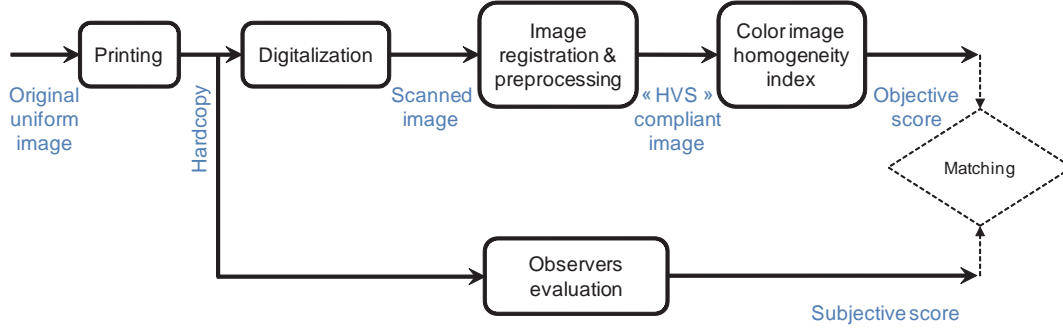


Figure 75. Our main algorithm flowchart.

5.5 Pre-processing

This section intends to modify the raw scanned image into several new ones, filtered and resized, in order to render the human vision performance at different viewing distances. It also considers different channels of the color images in order to focus on lightness and hue inhomogeneities. A three steps pre-processing of the scanned images is performed (see Figure 76): First, changes the size of the image in order to get a HR one and a LR one. Then, one creates custom color channels from the initial RGB channels, and leads to one gray level image per each new custom channel. Finally one filters them in order to take account of human visual resolution. Optionally, one may quantize.

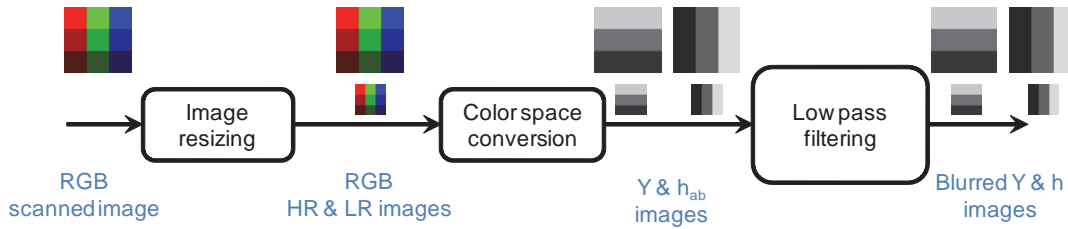


Figure 76. Image registration and pre-processing: the RGB input image is converted into four gray level images according to human vision.

For the HR image, a 1200 pixel per inch (ppi) image is recommended. A bicubic interpolation (scale of 1/2 if the input image is 2400 ppi) with antialiasing method is selected to perform image resizing.

The first step is to change the color space. The scanner yields R,G,B values for each pixel. We could process the R, G, and B channels each ones as a grayscale image, but they do not contain the optimal information. In order to be more consistent with human perception, we choose to convert the RGB values into CIELAB values by considering that the input RGB values are represented in the Adobe RGB (1998) color space, then converting into CIE1931XYZ for a 2° standard observer, and finally converting in CIELAB by selecting the D65 illuminant. CIELAB color space is chosen because it is a color appearance model [28] (pages 160 - 161). We analyze the L^* (lightness) channel, and the h_{ab} (hue) channel. The a^* and b^* Cartesian coordinates are transformed into cylindrical coordinates C_{ab}^* and h_{ab} , respectively defined as

$$C_{ab}^* = \sqrt{a^{*2} + b^{*2}}, \quad (5.3)$$

$$h_{ab} = \tan^{-1} \left(\frac{b^*}{a^*} \right). \quad (5.4)$$

Note that the $\text{atan}(y/x)$ function yields an angle in $\left[\frac{-\pi}{2}, \frac{\pi}{2} \right]$ which is not defined if $x=0$. Alternative function is available in most computation softwares, often denoted as $\text{atan2}(y,x)$, yielding an angle in $[-\pi, \pi]$, defined for every y and x .

Regarding the lightness image, it is also possible to define it directly from RGB values, using the NTSC luminance (Y) formula, first presented in Ref. [60]:

$$Y = 0.299 \times R + 0.587 \times G + 0.114 \times B. \quad (5.5)$$

The second step corresponds to the simulation of the modulation transfer function of the human visual system. According to Hermann von Helmholtz's observations [61], we consider the definition of the "normal visual acuity" as the ability to resolve a spatial pattern separated by a visual angle α of one minute of arc. Thus, giving an observation distance d (in cm) and a scan resolution of the image r_s (in ppi), we can define the convolution kernel of the blurring filter (Figure 77). The size s of the kernel depends on the standard deviation σ used for the Gaussian profile:

$$\sigma = d \times \tan \left(\frac{1}{60} \right) \times \frac{r_s}{2.54}, \quad (5.6)$$

$$s = 6 \times \sigma + 1 \quad (5.7)$$

We choose to simulate the HR images as viewed at a short distance ($d = 15$ cm), near the human punctum proximum, which corresponds to $\sigma = 2.06$ pixels, i.e., $s = 13$.

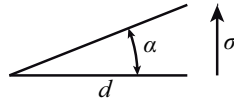


Figure 77. Definition of σ knowing the visual angular resolution $\alpha = 1' = \frac{1}{60}$ degree at the viewing distance d .

Lastly, a quantization step (e.g. on $n_b \leq 8$ bits for each channel), can eventually be performed, with the consequence to decrease the size of the GLCM but also to lose the least significant bits (i.e. small gray-level variations in the image).

For the low resolution images, we perform the same 3 steps with a 240 ppi resolution image (scale of 1/10 if the input is 2400 ppi), with $\sigma = 1.03$ pixels and $t = 7$, which corresponds to the image viewed by an observer at about 40 cm.

The pre-processing step leads to 4 images, denoted as $Y^{(HR)}, Y^{(LR)}, h_{ab}^{(HR)}, h_{ab}^{(LR)}$.

5.6 Application of the image homogeneity analysis method

We apply the method presented in Section 5.3 and Section 1.1.1 on the four images $Y^{(HR)}, Y^{(LR)}, h_{ab}^{(HR)}, h_{ab}^{(LR)}$ obtained in the pre-processing step.

For each of the two HR images, we choose the following translation vectors \mathbf{t}_1 and \mathbf{t}_2 to compute respectively GLCMs \mathbf{M}_1 and \mathbf{M}_2 :

$$\mathbf{t}_1 = D^{(HR)} \cdot \mathbf{u}_1 \quad (5.8)$$

$$\mathbf{t}_2 = D^{(HR)} \cdot \mathbf{u}_2 \quad (5.9)$$

with $D^{(HR)} = 25$ pixels (corresponding to a physical displacement of about 0.5 mm on 1200 ppi image), and $\mathbf{u}_1 = \mathbf{y}$, $\mathbf{u}_2 = \mathbf{x}$ the horizontal, respectively vertical unit vectors (see Figure 10).

We then compute a GLCM \mathbf{M} as the average of \mathbf{M}_1 and \mathbf{M}_2 :

$$\mathbf{M} = \left(\frac{\mathbf{M}_1 + \mathbf{M}_2}{2} \right) \quad (5.10)$$

We also compute a chroma value on the HR image, denoted as $c^{(HR)}$ and defined as the average of the chroma values computed from Eq. (5.3) on each pixel of the image. From matrix \mathbf{M} , we compute the homogeneity attribute $Hom1$ according to Eq. (5.2) with a value of a denoted $a^{(HR)}$ depending on $c^{(HR)}$ and given in Figure 78.a, and $b = 4$.

For each of the two LR images, we perform similar processing as above with $D^{(LR)} = 35$ pixels (corresponding to a physical displacement of about 0.37 cm on 240 ppi images), and compute the $Hom2$ attribute using the $w_{a^{(LR)},4}$ function defined by Eq. (5.2), where $a^{(LR)}$ is given by Figure 78.b as a function of $c^{(LR)}$ computed as $c^{(HR)}$ on the chroma values of the LR image.

These values for D , a , and b , have been chosen because they seem the most relevant in our study according to physical and empirical considerations.

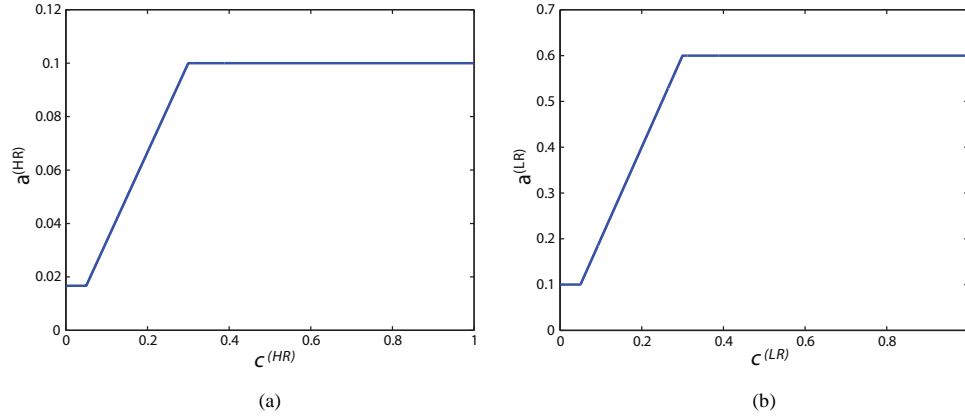


Figure 78. Variation of the $a^{(HR)}$ and $a^{(LR)}$ values as a function of the chroma values $c^{(HR)}$, respectively $c^{(LR)}$, for HR and LR images.

5.7 Construction of the objective Score

The computation of homogeneity attribute on the GLCM of $Y^{(HR)}, Y^{(LR)}, h_{ab}^{(HR)}, h_{ab}^{(LR)}$ yields four values to be combined in order to obtain the final homogeneity score. Let's denote these four values as $H_{Y^{(HR)}}, H_{h_{ab}^{(HR)}}, H_{Y^{(LR)}}, H_{h_{ab}^{(LR)}}$.

Our experience shows that relevant homogeneity score in respect to human perception is given by the following empirical formula:

$$\min \left(\frac{H_{Y^{(HR)}} + c^{(HR)} \times H_{h_{ab}^{(HR)}}}{1 + c^{(HR)}}, \frac{H_{Y^{(LR)}} + c^{(LR)} \times H_{h_{ab}^{(LR)}}}{1 + c^{(LR)}} \right). \quad (5.11)$$

Notice that the chroma is taken into account in this formula through the parameters $c^{(HR)}$ and $c^{(LR)}$ computed in Section 5.6 because we noticed that the influence of the homogeneity parameter on the hue image is lower when the colors are not saturated. The weight attributed to the luminance channel is higher than the one attributed to the hue channel ($0 \leq c \leq 1$, and in practice, on prints, it is rather $0 \leq c \leq 0.6$) as it is commonly done in video compression for digital television video encoding where the luminance channel has a double bandwidth than the chromatic ones (See for example [62]).

5.8 Referenced parameters of the method

The referenced parameters of our method are:

- *Quantization* (images encoded on n_b number of bits): The less is quantization, the more careful details are kept. It seems better to keep all the details. Instead of decreasing n_b below the usual value of 8 bits, we prefer adjusting the a and b parameters in formula (5.2).

- *Size of blurring kernel*: it is set by the considered viewing distance d , which is about 15 cm for near vision, and 40 cm for far vision.
- *Scan resolution*: The size of one pixel in HR images is about $21 \mu\text{m}$ after downsampling original 2400 ppi scanned image to 1200 ppi. This appears sufficiently accurate in comparison to the human vision and to the finest commercial printing systems available today.
- *Parameters $D^{(HR)}$ and $D^{(LR)}$* : They must be representative of the characteristic size of the inhomogeneities that we wish to highlight, in respect to near sight and far sight observations.
- *Vectors \mathbf{t}_1 and \mathbf{t}_2* : horizontal and vertical vectors used to compute the GLCM. These two directions have been selected because they coincide to the orientation of classical defects of most printing systems, because defaults often occur in the printing direction (vertical) and in the perpendicular direction of it.

5.9 Experimental testing and comparison with psycho-visual assessment

In order to verify the relevance of the proposed score in respect to human observer evaluation, we carried out the following experiment: Four uniform color images have been printed with various printers (laser, inkjet, retransfer) and on various supports (office paper, glossy photograph paper, APCO paper, white polymer). This yielded four sets of samples. For the digitalization step, all samples were scanned at 2400 ppi in TIFF format, 24 bits, by the EPSON Scan Ver. 3.81 FR, 2002 driver, with a EPSON Perfection V700 PHOTO scanner. The “No color correction” option was selected. An overview of some samples is presented in Figure 79.

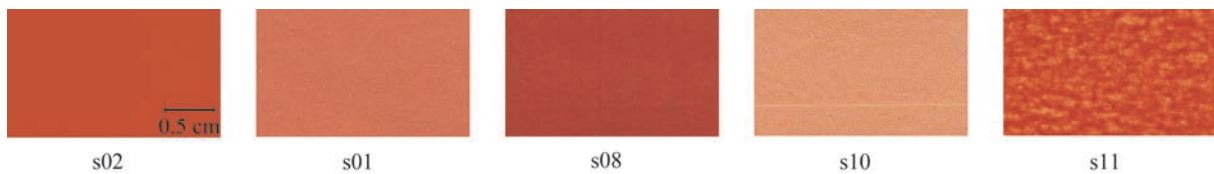


Figure 79. An overview of some scanned samples (in lower resolution than the original ones). s_{02} is printed on glossy photograph paper, s_{01} and s_{08} on office paper, s_{10} and s_{11} on APCO paper. All patches have same size.

The assessors were submitted to a ranking test, using an ordinal, unstructured scale, according to the method recommended by François Sauvageot in [63]. A panel of 8 assessors made the experiment on the four sets of samples. Despite a larger panel of assessors would have probably ascertain a highest accuracy in the sensorial measurement, we preferred using a reduced panel in order to be more representative of the type of measurement that can be achieved in practice in the industry. Nevertheless, the relative low standard deviation over the 8 assessors displayed in Figure 80 shows that we already have, with this small panel, a good estimation of observers’ perception. The assessors were presented randomly the samples to sort in respect to their perceived homogeneity, and then were asked to place them on a one meter scale, in order to measure the intensity of the sensorial quantity. The light conditions were not fixed, but we pay attention in every experiences of having a room sufficiently lit by daylight (and / or artificial light). The distance between the assessors and the samples was not fixed and the assessors were free to look at them

from short and/or far distance. The positions (in meter) given by all the observers are indicated in Figure 80 by their average (with black dots) and standard deviation (with error bars) for each sample. Note that here no rescaling of the positions has been performed: the dispersion of the positions of the samples partly comes from the different scaling adopted by the observers in their evaluation. The continuous red line in Figure 80 represents the score computed with our method by formula (5.11), using adapted weighting functions (5.2). The blue line is computed using the original weighting function (5.1) proposed by Haralick. And the green line corresponds to the evaluation of the print mottle (using the lightness channel only since the standard [55] is designed for monochrome prints), and is plotted according to the right axis. We see that the scores given by our method follows fairly well the positioning of the samples by the observers on the metric scale, and that the adaptation of the original weighting function (5.1) was relevant. For example, we can notice that the original weighting function provides low scores on the set of low saturated samples (experiment (d)) compared to the three other sets presenting more saturated colors. Regarding to the mottling-based score, there are two drawbacks: its scale is non-normalized, and the curves show that it cannot render the various kinds of homogeneity printing defects presents in our four sets.

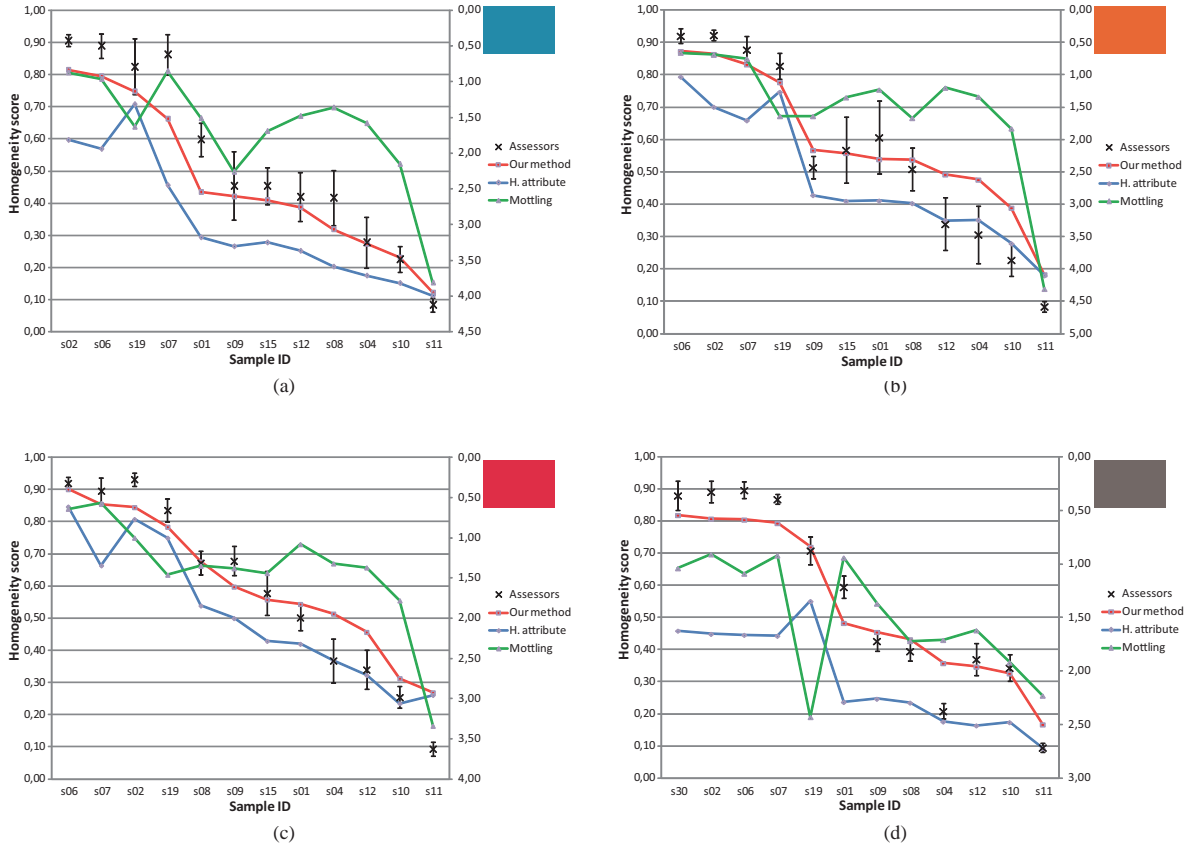


Figure 80. Comparison between objective and subjective evaluations for (a): a blue set of samples, (b): an orange set of samples, (c): a red set of samples, and (d): a gray set of samples.

In Figure 81, we can see the influence of rescaling the scores given by observers on the ones given by our method. For each experience (a), (b), (c), or (d) presented on Figure 80, we choose s_{\max} and s_{\min} the samples giving respectively the maximum and the minimum score of our algorithm. Then, for each observer

having participated to the experiments, we adjust linearly its scale on the one given by the objective method by using the two reference points s_{\max} and s_{\min} . This rescaling was motivated by both the desire to let assessors scoring each set of samples without any recommendation (that would give them some a priori); and also by the fact that it is difficult to obtain an absolute score from observers: we thus preferred to let them using their own sub-scale and to use this rescaling operation afterwards in respect to our algorithm whose scale is mathematically fixed between 1 (perfect homogeneity) and 0.

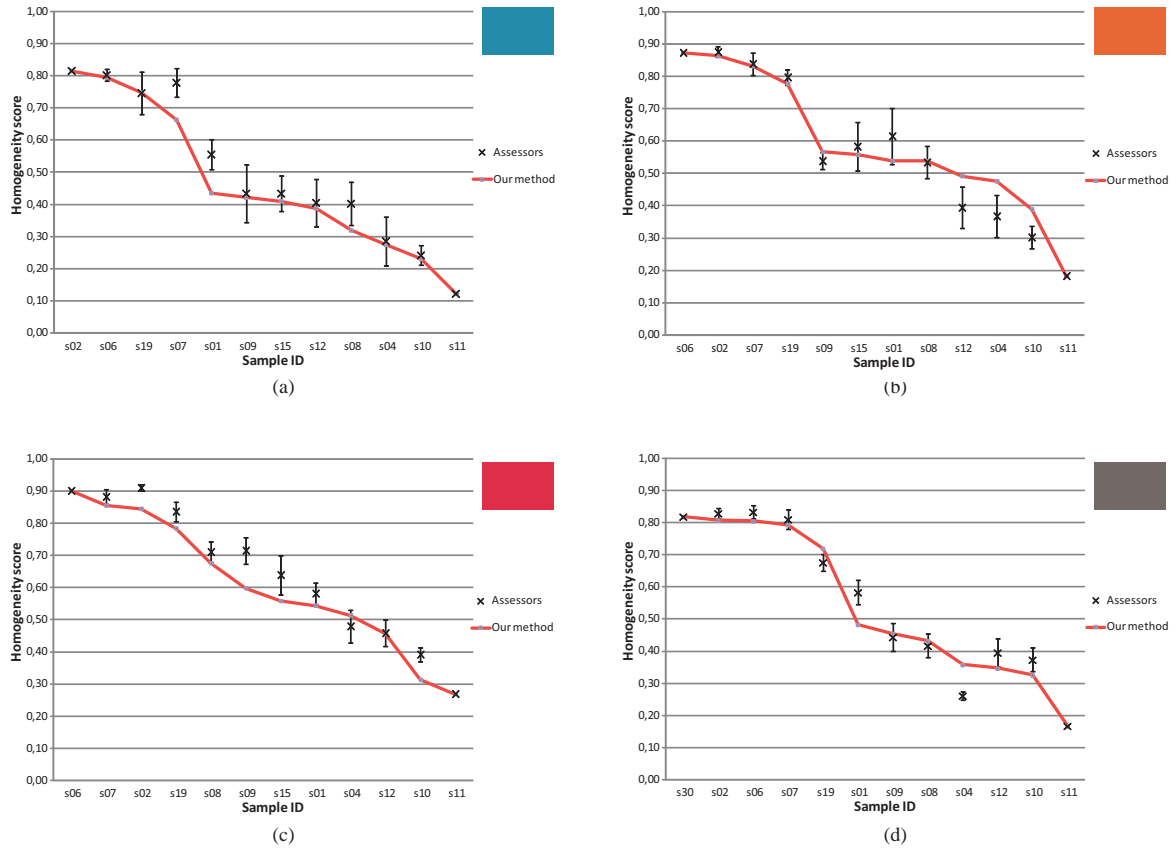


Figure 81. Comparison between objective and rescaled subjective evaluations for (a): a blue set of samples, (b): an orange set of samples, (c): a red set of samples, and (d): a gray set of samples.

In order to assess the performance of our method, six different classes are defined by selecting six threshold values of the objective score scale (0.8, 0.7, 0.6, 0.52, 0.3, 0). Assessors' scorings are also quantified into this six grades classification by clustering. The matching of the classes given by observers and by our method is presented in Figure 82: In more than 70% of the cases our method and the assessors give the same class, and only in 5% our method is mistaken by two classes.

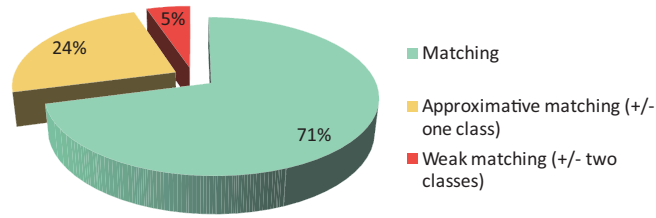


Figure 82. Percentage of samples classified in the same of six categories by assessors (subjective evaluation) and by our scoring method for homogeneity attribute.

5.10 Influence of the size of the studied area

We have not yet discussed the required size of the samples. Our experiments used rather large areas of 24 x 35 mm to assess homogeneity, which corresponds to a HR image of 1134 pixels by 1654 pixels, and a LR image of 227 pixels by 331 pixels. Using $D^{(LR)} = 35$ pixels, we have 63552 usable pairs of pixels in the LR image to compute the GLCM \mathbf{M}_l . If the size of the LR image is smaller than 35 pixels, we cannot compute the score (with the proposed parameters used in section 5.6). Moreover, we find out that for a LR image size close to 35 pixels, the algorithm computation is not relevant because the number of pairs of pixels to increment into the GLCM is not sufficient, and the statistics here are not relevant anymore. Thus, we recommend computing only images of at least 1 cm by 1 cm (corresponding to LR images of 95 pixels by 95 pixels). Nevertheless, if only small patches are available for evaluation in a given application, we propose an adaptation for the algorithm based only on the HR image. This makes sense to discard the LR image since it was initially used for its low frequency information, which is not significant anymore in a too small patch. Hence, the computation of a score on two levels of detail is no more motivated, and homogeneity can be assessed only on the high frequencies information presents in the HR image of a small patch. An overview of results for different printing technologies on polycarbonate is proposed in Figure 83.

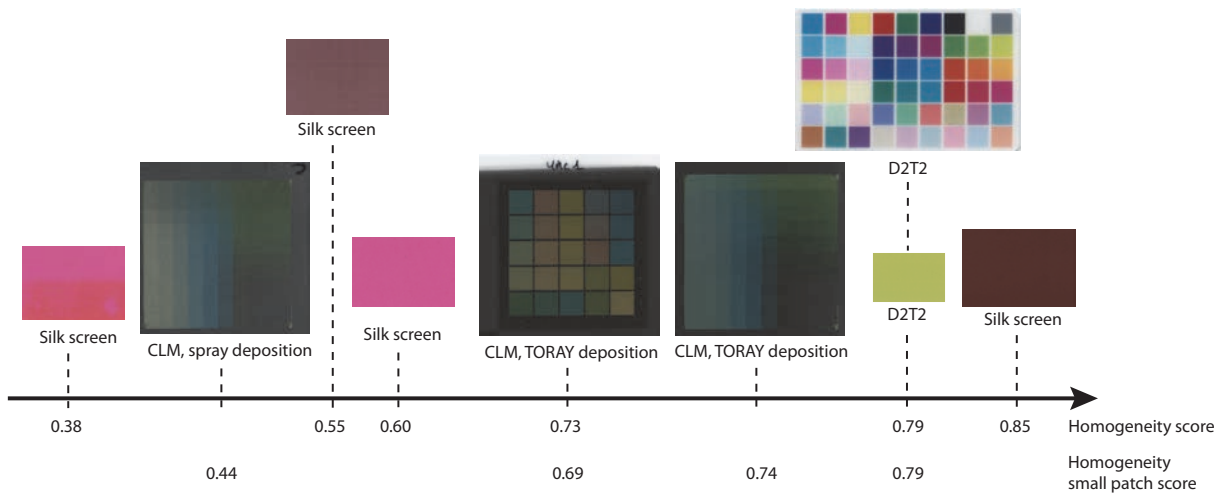


Figure 83. An overview of some scanned samples of prints on polycarbonate with different printing systems, and their corresponding homogeneity score given by our method for large patch (homogeneity score) or small patch (homogeneity small patch score).

5.11 Conclusion

We proposed a method for assessing automatically the homogeneity of printed surfaces, an attribute known to contribute to the visual quality of prints. This method is based on a high resolution scanned color image of the surface, which is then processed by computing a gray-level co-occurrence matrix on a lightness channel and a hue channel of the color image and a variant of Haralick's parameter. The index computed according to our method is in accordance with the empirical assessment by a small panel of non-expert observers. The fact that the observers can freely observe the samples from far or short distance justifies the use of high resolution and low resolution images in our method. We recommend using samples of at least 1 squared centimeter, and to compare, either with the algorithm or in sensorial experiment, patches having all the same size. If only small patches are available, the score can be computed from the HR images since we can assume that only near sight is relevant for evaluation. Recently, a work on a color version of co-occurrence matrices working in the CIELAB color space to comply with human perception have been proposed, and it would be worth to be tested [64]. Another idea of improvement of the method proposed here would be to extend the measure for natural image with the detection, in the original image, of an area nearly homogeneous, and to compute the score on this area. In the context of color model calibration, Brichon et al. proposed such a method in [65]. Our homogeneity index is a first attribute which should be combined with other attributes in order to get a global quality score for printed natural images. It may also help to compare the performances of different printing systems in terms of visual quality.

Chapter 6 Edge sharpness index

In printing, an important attention should be addressed to edges. An edge can be defined as a transition from a high density to the paper white. In terms of quality, we focus on the abruptness or steepness of such a transition, and the resulting visual appearance of that edge sharpness.

The sharpness is computed by scanning the printed copy at high resolution: (2400 ppi) to capture fine details and filter it order to remove noise. Filtering is also a way to measure sharpness with similar performance as the human visual system (a Gaussian filter reproduction the acuity of the visual system is thus used: GOG & LOG filtering). Then, using a Laplacian operator, the contours are highlighted in the luminance channel of the images in both the original digital image and in the scanned printed copy. We measure the edge thicknesses, and the phases of the gradient operator to assess the angle delocalization.

6.1 Introduction

Edges constitute an important part of our perception. Our visual system relies on contrast, as the mechanism of receptive field presented in Figure 24 in Section 2.1. In the nature, we encounter a lot of animal species with high contrasted shapes on their skin or around their eyes to impress their own kind, or intimidate their prey. A recent study on development of assistance for visual impaired led to the conclusion that the contours constitute visual indices important for human vision, and are an important source of help to a scene analysis [66]. The measure of sharpness of natural images using Gaussian model was presented in [67] by Dijk et al. Then another study to assess local blur in an image using both its spectral and spatial properties have been proposed by Vu et al. [68]. In 2005, HP Laboratories proposed a measure of sharpness based on an analysis of localized frequency content in a feature-based context [69], taking into account advantages of a study in a frequency domain, but not limiting it to similar scenes where those methods traditionally fail when the scene changes.

6.2 Digitalization of the prints

Following the study of the scanner in the First Part, we pay attention to the spatial distortions, even more in this case because we are focussing here on edges, a very precise area, where we cannot afford to more uncertainties in the pixels position. We use the device presented in section 3.1.4 to correct sample registration on the scanner glass. A scan at high resolution is used to ensure the recording of very small details (very high frequencies): we use 2400 pixel per inch sampling, which is a true sampling from our scanner (not an interpolation image generated by the scanner driver).

6.3 Overview of the method

The Edge Sharpness assessment algorithm we developed, summarized in Figure 84, presents the following steps:

- A printing of a sample, and its digitalization as detailed in Section 6.2;

- In parallel to this digitalization, an image upscale for the reference image to the same resolution as the scanned one;
- The scanned image is then color corrected and some basic preprocessings are performed on the luminance image to recover the original markers position in the scanned image;
- The original image is then registered on the corrected scanned image;
- The application of Edge detection described in First Part in Section 1.2 on the original and scanned image, and the computation of the score by the measure of the edge thickness enlargement, and the angle delocalization (see Section 6.6);
- In the same way as we proceeded for the homogeneity criterion, we recommend to verify the used parameters with a comparison to psycho-visual assessment (See Section 6.7).

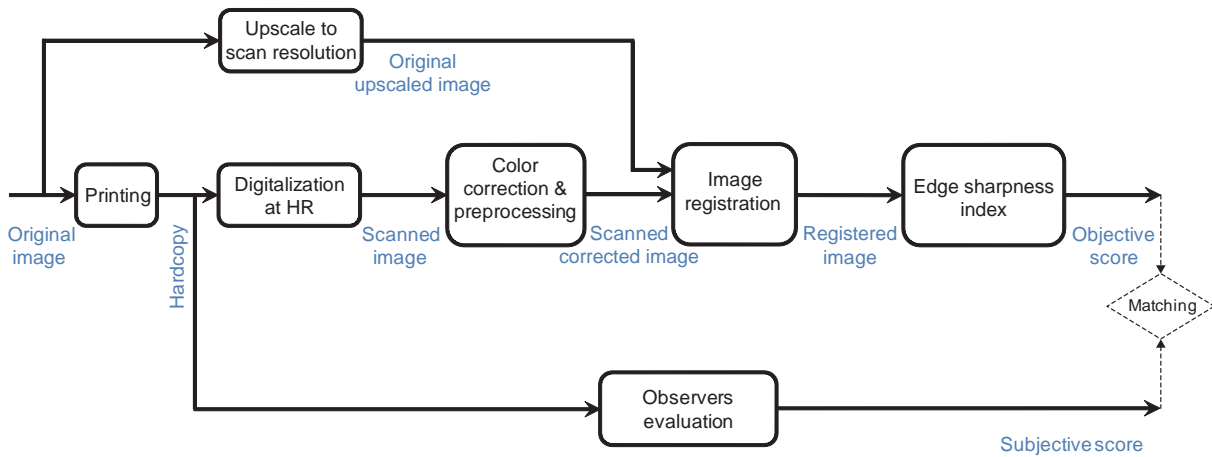


Figure 84. Our Main algorithm flowchart for the assessment of Edge Sharpness.

6.4 Color correction & Pre-processing

As this part focuses on edge, and not on homogeneous areas anymore, we assumed that a color correction (susceptible to bring noise in solid areas) should not disturb too much the signal we want to analyse. We therefore start by correcting the raw scanned image with the method we presented in First Part, in Section 3.1.4.

The picture to analyse is layout in a rectangular pattern, with four cyan markers in the edges that will be used to the image registration. An overview of these original, scanned, and color-corrected scanned images are presented below:

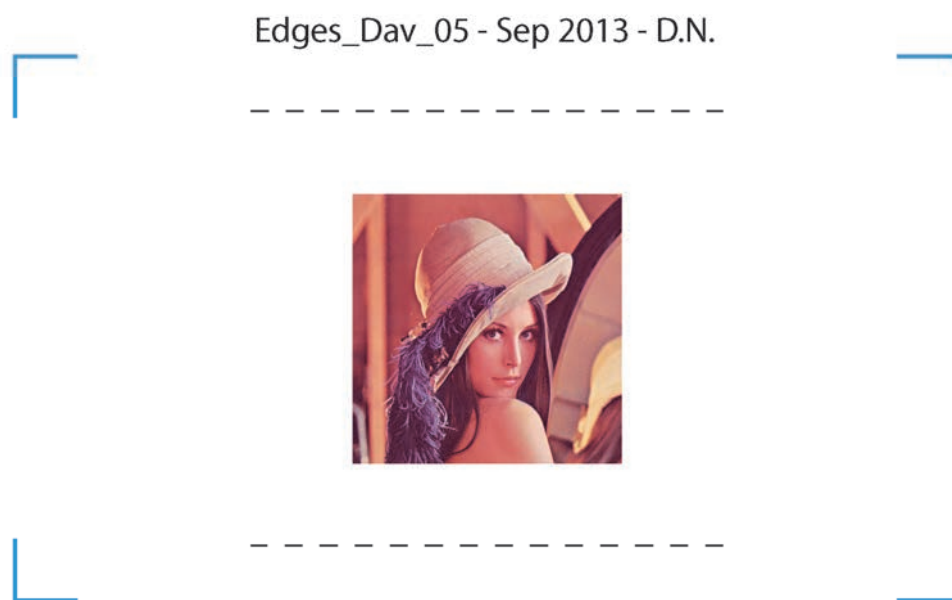


Figure 85. The original digital layout.

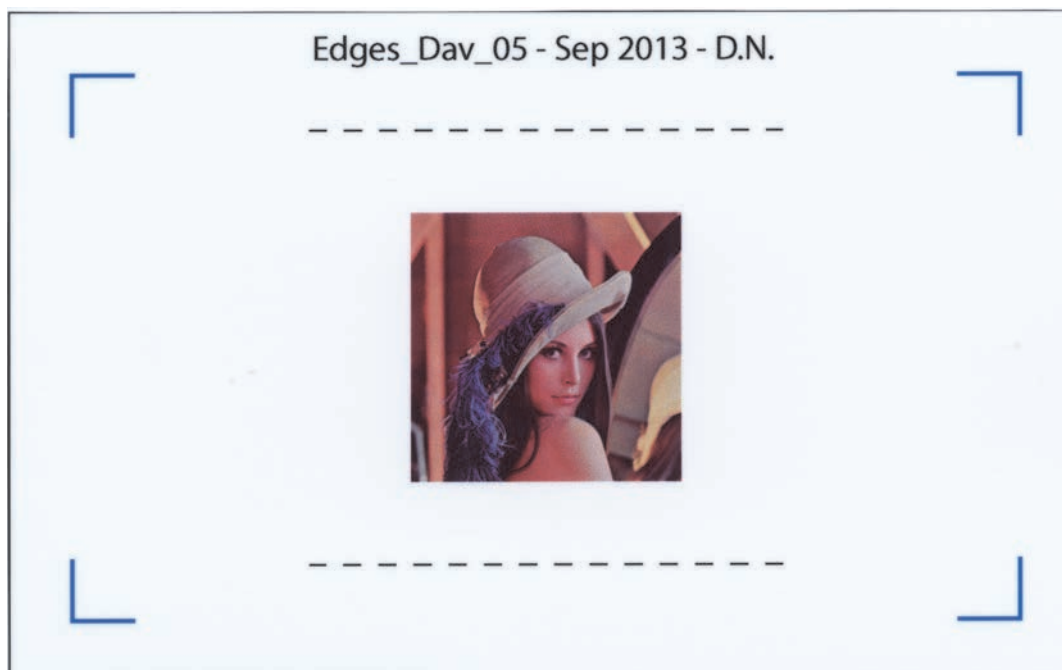


Figure 86. Scanned, not color-corrected image of a printed sample of the original image.

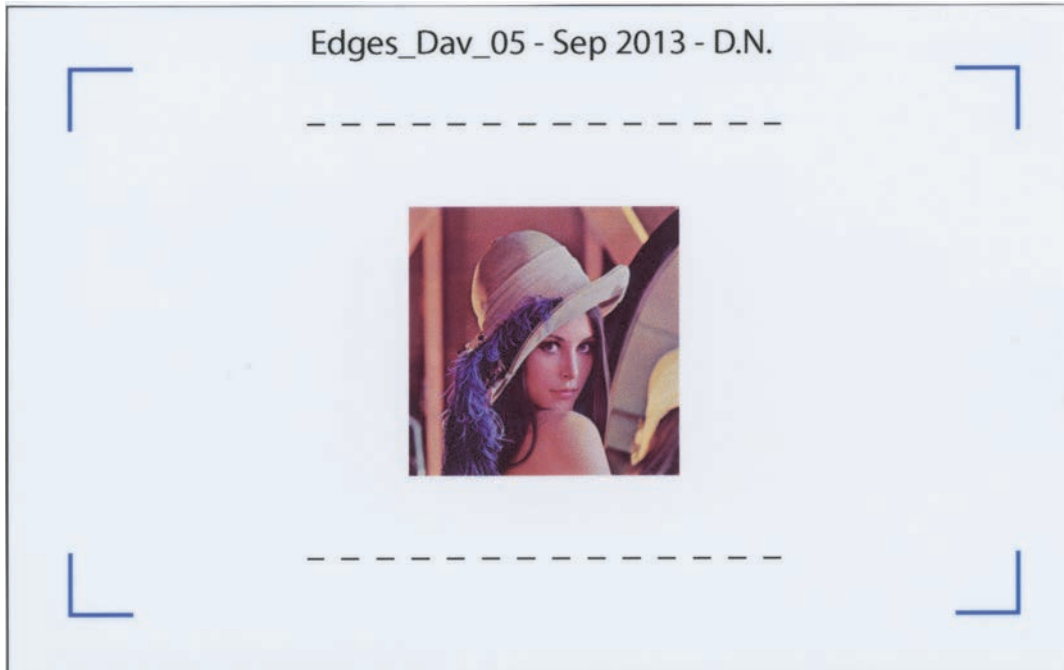


Figure 87. Scanned image, including color correction, of a printed sample of the original image.

The next steps correspond to the pre-processing necessary to prepare the image registration. First, on the original image, we apply several basic image processing tools to recover the coordinates of the four edge markers.

The image is first converted into a luminance image using the formula (5.5) presented in the previous Chapter 5 using the standard formula corresponding to the luminance of the NTSC space. This image is then binarized to obtain a logical mask, where white (value 1) corresponds to an “object”, and black (value 0) corresponds to the background, see Figure 88.

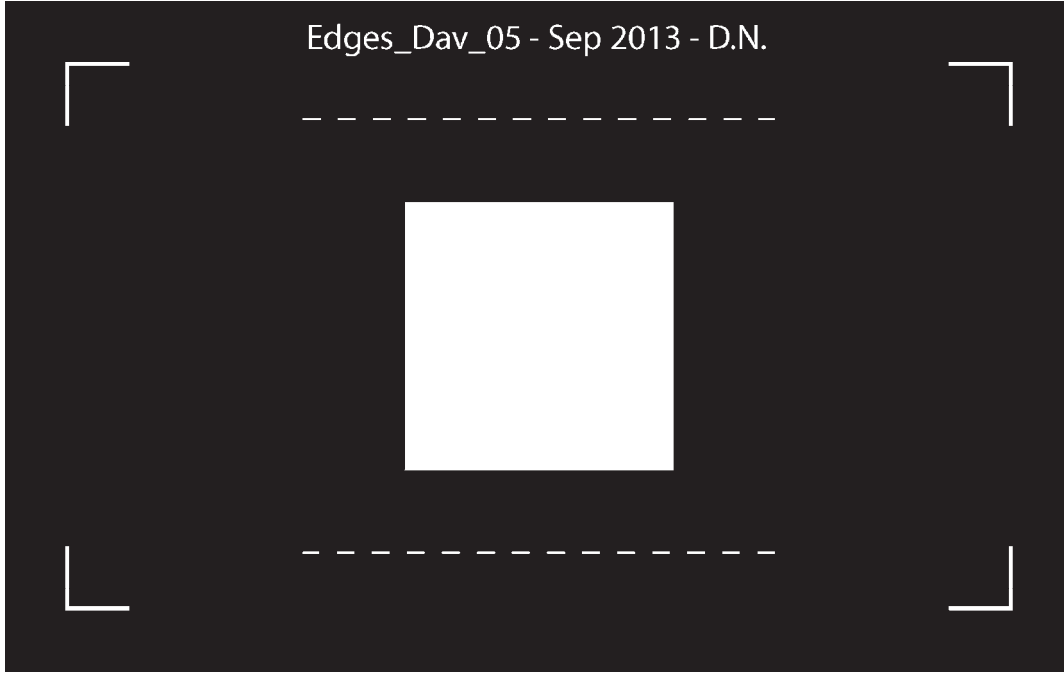


Figure 88. Logical mask, with “objects” in white, and background in black.

The “objects” we are focusing here are the four edge markers. Mathematical morphology operators [70, 71], first imagined by Georges Matheron et Jean Serra in 1964 in the Laboratory of the Ecole nationale supérieure des mines de Paris, are used to “clean” this image in order to keep only the markers. We use two image opening operators (in the sense of the mathematical morphology) with a well-chosen structural element: an horizontal line to keep the horizontal patterns, and a vertical line to keep the vertical pattern. The size of the line will define the elements that will be kept, and the elements that will be removed: in the case of an opening, a connected pattern that cannot include this line will be removed. We intend to keep the edge markers, and remove the other objects, and we choose the length (in pixel) of the line structural element as following: knowing the size of the markers denoted as *marker_size* (in mm), and those of the image width denoted as *image_size* (in mm), and the image width size (in pixel) denoted as *image_width*, we choose a size for our structural elements as three quarters of the size of the marker to keep the marker, but remove all that is smaller than it, as the following formula:

$$l_{SE} = \text{floor} \left(\frac{\text{marker_size}}{\text{image_size}} * \frac{3}{4} * \text{image_width} \right). \quad (6.1)$$

A logical OR function between the two resulting images leads to the following image, cleaned:



Finally, in order to obtain the marker coordinates, a simple hit-or-miss operator is applied. This operator uses two different structural elements, a first one that need to “hit” the object, and a second one that need to “miss” the object. Once these two conditions are satisfied, the corresponding pixel is detected by the hit-or-miss operator. We recover the marker coordinates using for example for the top left corner, the two following structural elements:

$$SE_1 = \begin{bmatrix} 0 & 0 & 0 & 0 & 0 & 0 & 0 & 0 & 0 & 0 & 0 \\ 0 & 0 & 0 & 0 & 0 & 0 & 0 & 0 & 0 & 0 & 0 \\ 0 & 0 & 0 & 0 & 0 & 0 & 0 & 0 & 0 & 0 & 0 \\ 0 & 0 & 0 & 0 & 0 & 0 & 0 & 0 & 0 & 0 & 0 \\ 0 & 0 & 0 & 0 & 0 & 0 & 0 & 0 & 0 & 0 & 0 \\ 0 & 0 & 0 & 0 & 0 & 1 & 1 & 1 & 1 & 1 & 1 \\ 0 & 0 & 0 & 0 & 0 & 1 & 0 & 0 & 0 & 0 & 0 \\ 0 & 0 & 0 & 0 & 0 & 1 & 0 & 0 & 0 & 0 & 0 \\ 0 & 0 & 0 & 0 & 0 & 1 & 0 & 0 & 0 & 0 & 0 \\ 0 & 0 & 0 & 0 & 0 & 1 & 0 & 0 & 0 & 0 & 0 \\ 0 & 0 & 0 & 0 & 0 & 1 & 0 & 0 & 0 & 0 & 0 \end{bmatrix} \quad (6.2)$$

$$SE_2 = \begin{bmatrix} 0 & 0 & 0 & 0 & 0 & 0 & 0 & 0 & 0 & 0 & 0 \\ 0 & 0 & 0 & 0 & 0 & 0 & 0 & 0 & 0 & 0 & 0 \\ 0 & 0 & 0 & 0 & 0 & 0 & 0 & 0 & 0 & 0 & 0 \\ 0 & 0 & 0 & 0 & 0 & 0 & 0 & 0 & 0 & 0 & 0 \\ 0 & 0 & 0 & 0 & 0 & 0 & 0 & 0 & 0 & 0 & 0 \\ 0 & 0 & 0 & 0 & 0 & 0 & 0 & 0 & 0 & 0 & 0 \\ 0 & 0 & 0 & 0 & 0 & 0 & 1 & 1 & 1 & 1 & 1 \\ 0 & 0 & 0 & 0 & 0 & 0 & 1 & 1 & 1 & 1 & 1 \\ 0 & 0 & 0 & 0 & 0 & 0 & 1 & 1 & 1 & 1 & 1 \\ 0 & 0 & 0 & 0 & 0 & 0 & 1 & 1 & 1 & 1 & 1 \\ 0 & 0 & 0 & 0 & 0 & 0 & 1 & 1 & 1 & 1 & 1 \end{bmatrix}. \quad (6.3)$$

On the scanned image, the same algorithm cannot be used because the background cannot be so easily segmented from the rest of the image. The image is also first converted into a luminance image using the same formula (5.5). Then a threshold is computed to binarise the image. We use Otsu method [72], implemented in Matlab. The threshold is computed on a thumbnail of a marker because we only want to segment the marker from the background.

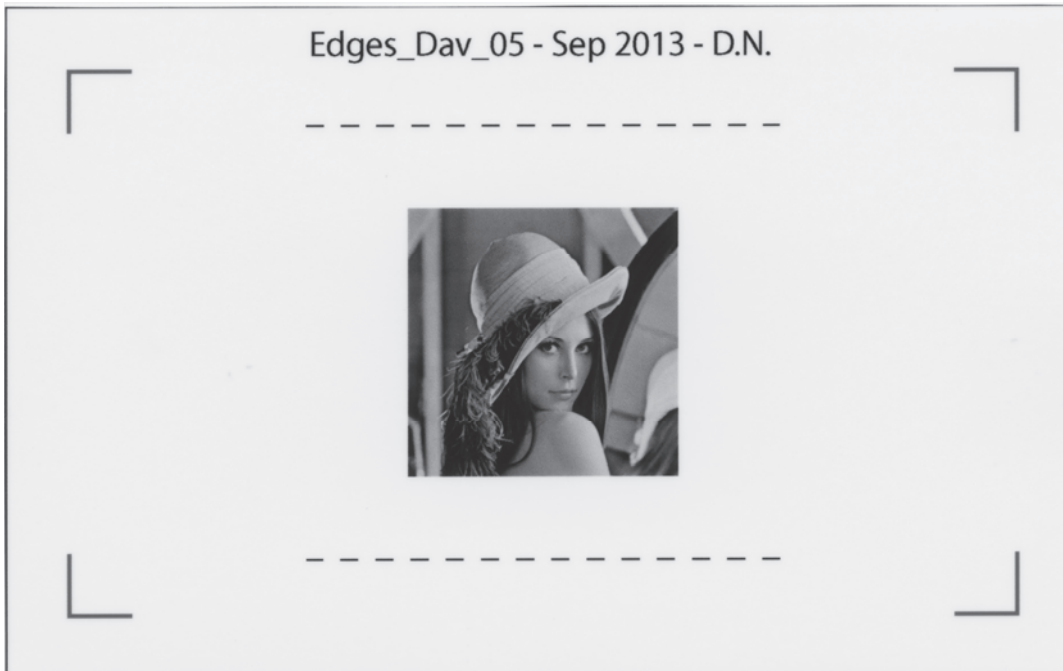


Figure 89. Gray-level image of the printed-scanned version of a picture to assess edge sharpness.

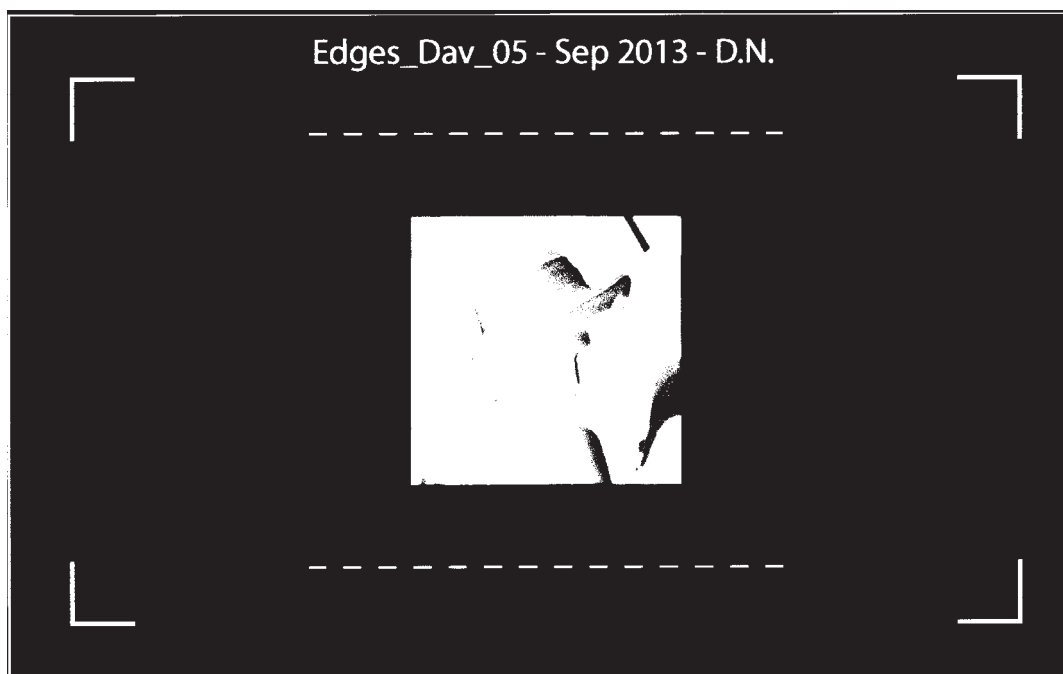


Figure 90. Black-and-white image obtained from gray-level image after binarization.

In the same reasoning than in the original image, an opening is performed to remove all the other “objects” to keep only the markers.



Figure 91. “Cleaned” black-and-white image.

Then, the method used to recover the coordinates of the marker in the scanned image is the correlation. We extract in the original image (around the coordinates of each of the four marker found) a thumbnail of the marker pattern to recover in the scanned image. The correlation method requires that the scanned image is not too distorted. Correlation may fail for example if one image is slightly rotated. This thumbnail is now searched in the scanned image, leading to a correlation image where the maximum of correlation is searched. The location gives the coordinates of the marker. This is repeated for the three other markers.

The next step is the image registration. To avoid inappropriate interpolation on the scanned image, we prefer registering the original image onto the scanned one. A first issue appears: the scanned image is at high resolution (2400 ppi), but the input original one, dedicated to printing, is usually only at 600 ppi. The input image is therefore primary upscaled to the scanned resolution by bicubic interpolation. From the four markers coordinates, we compute a 2-D projective transformation that maps the quadrilateral formed by the original image markers onto the quadrilateral formed by the scanned image markers. The *maketform* function is used in Matlab. Then the transformation is applied to the original picture to do the registration.

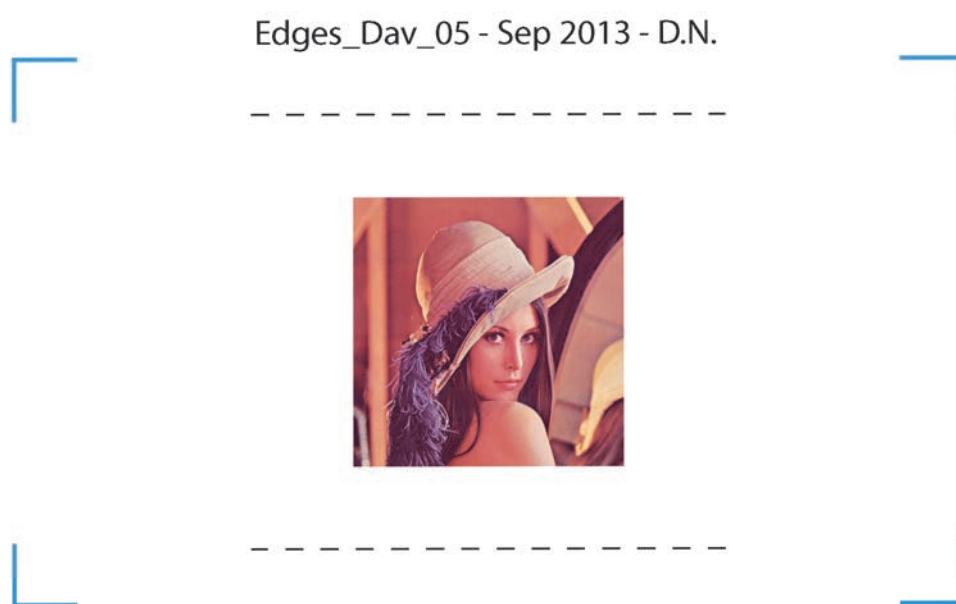


Figure 92. Registered original image.

A better visualisation between original and registered original image is done on Figure 93 and Figure 94.

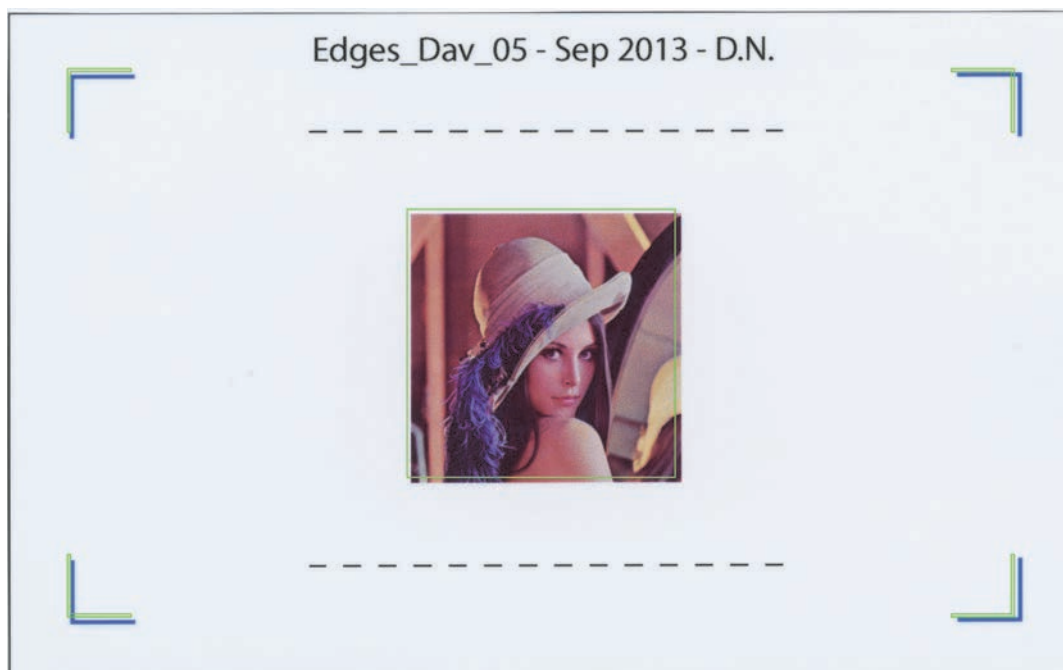


Figure 93. Before image registration. Green lines corresponds to the original image contours.

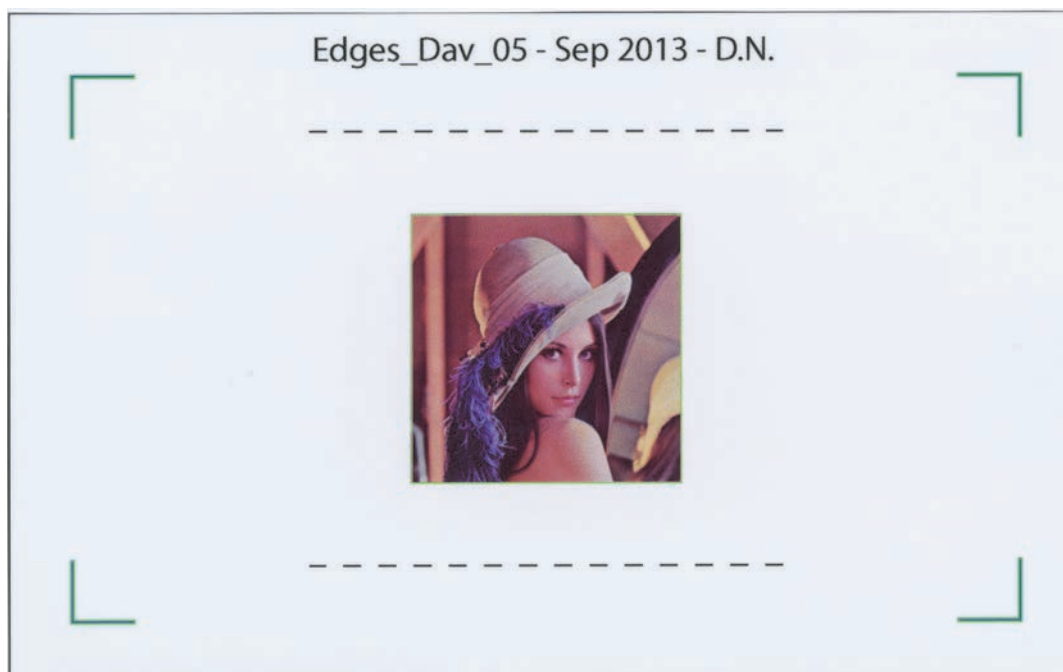


Figure 94. After image registration. Green lines corresponds to the original image contours.

6.5 Application of the edge detection method

We apply the edge detection method presented in Section 1.2 on both the original image and the scanned image. We start by the computation of the Gradient of Gaussian filtering, with a standard deviation parameter σ of 4 pixels, requiring a filter of size 25 pixels (about 265 μm at 2400 ppi). A threshold is selected for keeping only the most important contours in the original image based on the amplitude of the gradient. In the scanned image, a lower threshold is selected because we want to be sure that all the contours detected in the original image can be recovered in the detected contours present in the scanned image. The module of the resulting images is presented below in Figure 95:

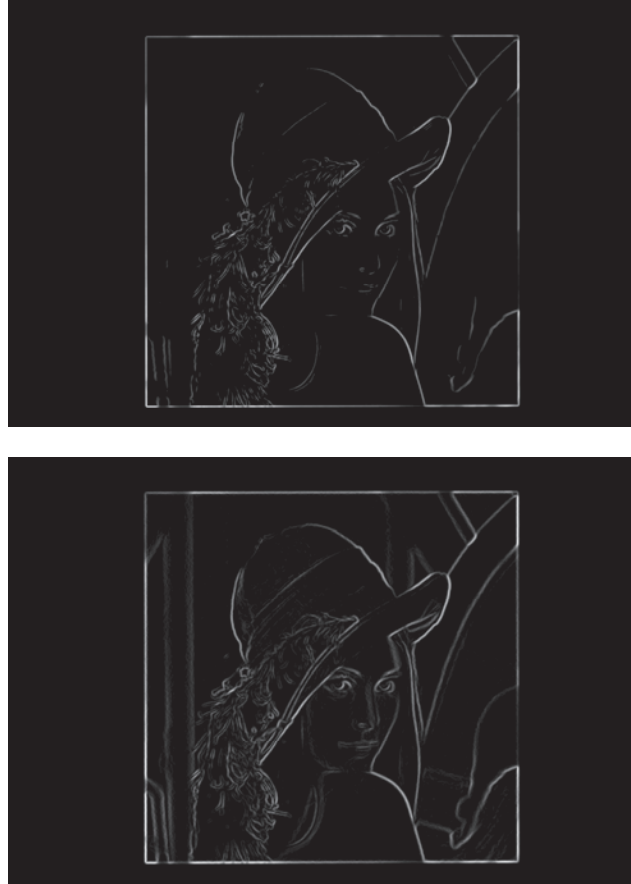


Figure 95. Module of the Gradient of Gaussian filtering, on the registered original image (top) and the scanned image (bottom).

Next step consists in the edge point detection by extracting gradient local maximums in the gradient direction, for the two images. We look for finding the position of the pixels of the edge central line.

We apply the method presented in Section 1.2, Eqs. (1.31) and (1.32), by considering the four different possible cases, depending of the sign of $u_i \times u_j$, and the sign of $\text{abs}(u_i) - \text{abs}(u_j)$. The computation of M_1 , and M_2 of formula (1.31) needs the study of the resulting four different cases, represented Figure 96 (a), (b), (c), and (d), and leading to respectively the four formulas (6.4), (6.5), (6.6), (6.7).

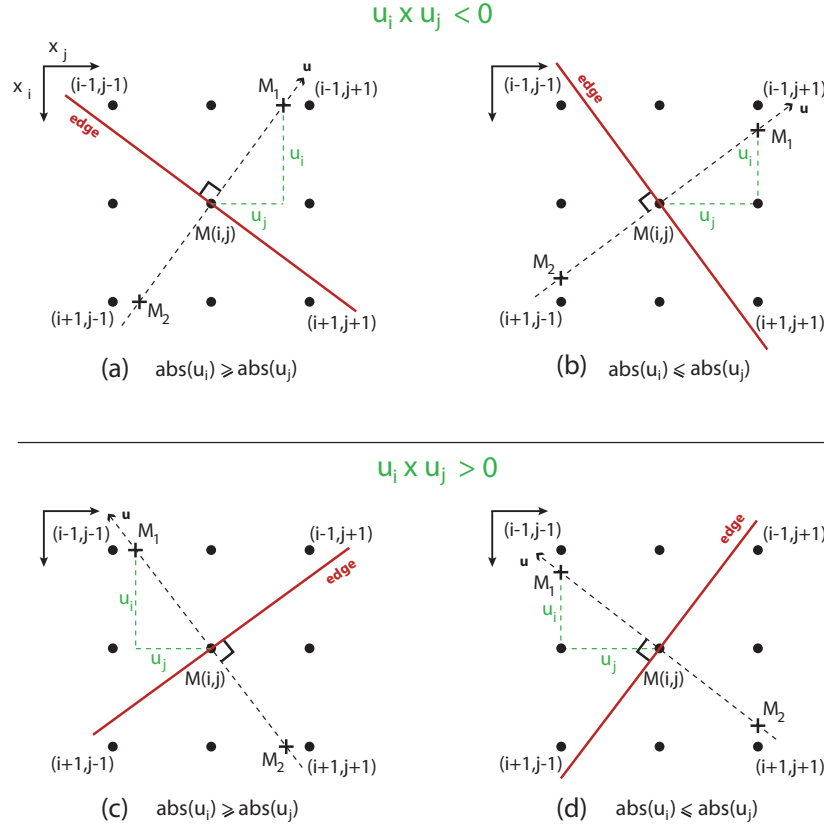


Figure 96. The four different cases for the decision to select the point M on a contour (in red line on the figure), depending on the direction of the gradient (in dashed arrow on the figure).

In the case where $u_i \times u_j < 0$ and $\text{abs}(u_i) \geq \text{abs}(u_j)$ we have:

$$\begin{aligned} M_1 &= \frac{\text{abs}(u_j)}{\text{abs}(u_i)} M(i-1, j+1) + \frac{\text{abs}(u_i) - \text{abs}(u_j)}{\text{abs}(u_i)} M(i-1, j) \\ M_2 &= \frac{\text{abs}(u_j)}{\text{abs}(u_i)} M(i+1, j-1) + \frac{\text{abs}(u_i) - \text{abs}(u_j)}{\text{abs}(u_i)} M(i+1, j) \end{aligned} \quad (6.4)$$

In the case where $u_i \times u_j < 0$ and $\text{abs}(u_i) \leq \text{abs}(u_j)$ we have:

$$\begin{aligned} M_1 &= \frac{\text{abs}(u_i)}{\text{abs}(u_j)} M(i-1, j+1) + \frac{\text{abs}(u_j) - \text{abs}(u_i)}{\text{abs}(u_j)} M(i, j+1) \\ M_2 &= \frac{\text{abs}(u_i)}{\text{abs}(u_j)} M(i+1, j-1) + \frac{\text{abs}(u_j) - \text{abs}(u_i)}{\text{abs}(u_j)} M(i, j-1) \end{aligned} \quad (6.5)$$

In the case where $u_i \times u_j > 0$ and $\text{abs}(u_i) \geq \text{abs}(u_j)$ we have:

$$\begin{aligned}
M_1 &= \frac{u_j}{u_i} M(i-1, j-1) + \frac{u_i - u_j}{u_i} M(i-1, j) \\
M_2 &= \frac{u_j}{u_i} M(i+1, j+1) + \frac{u_i - u_j}{u_i} M(i+1, j)
\end{aligned} \tag{6.6}$$

In the case where $u_i \times u_j > 0$ and $\text{abs}(u_i) \leq \text{abs}(u_j)$ we have:

$$\begin{aligned}
M_1 &= \frac{u_i}{u_j} M(i-1, j-1) + \frac{u_j - u_i}{u_j} M(i, j-1) \\
M_2 &= \frac{u_i}{u_j} M(i+1, j+1) + \frac{u_j - u_i}{u_j} M(i, j+1)
\end{aligned} \tag{6.7}$$



Figure 97. Localization of the contours in the original image (center) and in the printed copy (right).

6.6 Computation of the objective sharpness score

Our strategy to assess sharpness is first to be independent of the original image quality. It is easily understandable that an initial poor image quality will result in a poor edge sharpness quality after printing, especially if the input photo is blurred. We thus need a reference quality, and this will be the edge sharpness measurement of the original image. Both images (reference and scanned) will be simultaneously assessed. As the scanned image usually presents very complex edge location (see right image in Figure 97) due to the printing and scan processes which can affect contours, we prefer assessing only the edges detected in the original image (central image in Figure 97).

We want to measure the thickness of the contours in the scanned image and to compare them to have those in the original image. Due to the blurring or halftoning by the printer, which are low pass filtering, the contours are thicker in the printed-then-scanned image, to an extent that we will evaluate and convert into a measure of sharpness degradation due to the printer. For that purpose we analyse the contours thickness by using the Laplacian operator with the contour location obtained previously with the gradient operator. A criteria based only on the gradient operator would be correlated to amplitude and contrast, which is not our objective.

For a classical transition edge, the Laplacian presents two maxima around the edge central line which has been localized previously by the gradient method. The distance between this edge location and one of the Laplacian maximum line, in the gradient direction will correspond to our edge sharpness measurement. Indeed, the sharper is the transition, the closer will be the Laplacian maximum line to the Gradient maximum line. In the contrary, the less sharp is the edge transition, the farther will be the Laplacian maxima.

We thus apply the Laplacian of Gaussian method presented in section 1.2, with a standard deviation parameter σ of 8 pixels.

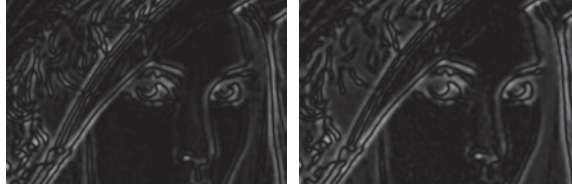


Figure 98. Sharpness evaluation by measurement of the edge thickness in the Laplacian of Gaussian filtering applied to the original (left side) and printed-then-scanned (right side) images.

Our algorithm aims at looking for the correspondent edge pixels in the scanned image. The two edges images of Figure 97 are reported on Figure 99.

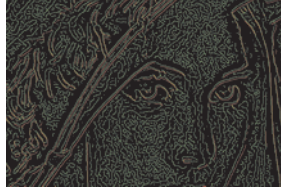


Figure 99. Localization of the contours in the original image (in red) and in the scanned image (in green).

Using this red pixel mask, for each of the edge pixel in the original gradient image denoted $e_{ref}(i, j)$, our algorithm first try to localize an edge pixel in the scanned image of gradient (green pixel mask) denoted $e_{scanned}(i + n_i, j + n_j)$ in a certain neighbourhood (n_i, n_j) . If, for a red pixel edge in original image we can find a green pixel edge of the scanned image in a neighbourhood of a maximum of 10 pixels, then our algorithm select the closest one and consider the pair of pixel as a correspondence between the two images. Then, we study the Laplacian of Gaussian images in the direction of the original gradient image (see Figure 100). In the original image, the direction of the gradient

$$\mathbf{g}_{ref}(i, j) = \begin{pmatrix} g_x(i, j) \\ g_y(i, j) \end{pmatrix}$$

at pixel $e_{ref}(i, j)$ is given by the two entities:

$$\begin{cases} g_x(i, j) = \text{imag}(e_{ref}(i, j)) \\ g_y(i, j) = \text{real}(e_{ref}(i, j)) \end{cases}, \quad (6.8)$$

where imag and real denote respectively the imaginary part and the real part of the gradient image at the pixel $e_{ref}(i, j)$. From Eq. (6.8) we define the normalized gradient direction vector as:

$$\mathbf{g}_{ref}^{norm}(i, j) = \begin{pmatrix} dx \\ dy \end{pmatrix} = \begin{pmatrix} g_x / \sqrt{g_x^2 + g_y^2} \\ g_y / \sqrt{g_x^2 + g_y^2} \end{pmatrix}. \quad (6.9)$$

On the original Laplacian of Gaussian image $L_{ref}(i, j)$, we study a line profile defined by a direction and a length given by the normalized vector $\mathbf{g}_{ref}^{norm}(i, j)$, whose points coordinates are given by:

$$profil_{ref}^L(l) = \begin{pmatrix} x \\ y \end{pmatrix} = \begin{pmatrix} i \\ j \end{pmatrix} + l \times \begin{pmatrix} dx \\ dy \end{pmatrix}, \quad (6.10)$$

with $l \in \mathbb{N}$.

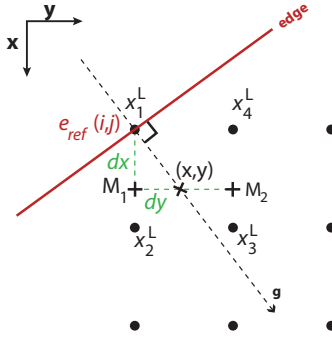


Figure 100. Study of a line profile (in red line), in the Laplacian image, defined by the direction of the gradient (specified by the dashed arrow).

For each obtained point $profil_{ref}^L$ in the Laplacian of Gaussian image, we compute its value by interpolation. Let us denote $(x_1^L, y_1^L), (x_2^L, y_2^L), (x_3^L, y_3^L), (x_4^L, y_4^L)$ the four bounding pixels in the image, the value of $profil_{ref}^L$ is given by:

$$profil_{ref}^L = (y_4^L - y) \times M_1 + (1 - (y_4^L - y)) \times M_2, \quad (6.11)$$

where M_1 and M_2 are given by:

$$\begin{cases} M_1 = (x_2^L - x) \times L_{ref}(y_1^L, x_1^L) + (1 - (x_2^L - x)) \times L_{ref}(y_2^L, x_2^L) \\ M_2 = (x - x_4^L) \times L_{ref}(y_3^L, x_3^L) + (1 - (x - x_4^L)) \times L_{ref}(y_4^L, x_4^L) \end{cases}. \quad (6.12)$$

We look for a local maximum, where the following conditions are satisfied:

$$\begin{cases} profil_{ref}^L(l+1) < profil_{ref}^L(l) \\ profil_{ref}^L(l) > profil_{ref}^L(l-1) \end{cases}. \quad (6.13)$$

We deduce the local contour "width" $w_{ref}(x, y)$ with the formula:

$$w_{ref}(x, y) = \sqrt{(x-i)^2 + (y-i)^2} = l \times \sqrt{dx^2 + dy^2} . \quad (6.14)$$

We can also note the angle of the local contour point as:

$$a_{ref} = -\text{atan2}(\text{real}(e_{ref}(i, j)), \text{imag}(e_{ref}(i, j))) \times \frac{180}{\pi} . \quad (6.15)$$

Then, we proceed exactly in the same way in the scanned image at the pixel $e_{scanned}(i + n_i, j + n_j)$ found. We get the two quantities $w_{scanned}(x, y)$ and $a_{scanned}$ using the same formulas as for the original image, (6.14) and (6.15).

Then a ratio between the original width and the scanned width is locally computed, which gives the sharpness score for this pixel:

$$score_{width}(i, j) = \frac{w_{scanned}(x, y) - w_{ref}(x, y)}{w_{scanned}(x, y)} . \quad (6.16)$$

It can happen that $score_{width}(i, j)$ is negative, in this particular case where it seems that the print is sharper than the original layout, we follow the rule: If $score_{width}(i, j) > -0.5$ then we choose to consider that the local edge are of same width, and we give the best score to this local contour by choosing $score_{width}(i, j) = 0$. In other cases, if $score_{width}(i, j) \leq -0.5$, then we consider that either the pair of points cannot be associated, or that the algorithm failed at this particular location, so we put the worst score by choosing: $score_{width}(i, j) = 1$.

A score on the angle difference between the original and scanned image can also be computed:

$$score_{angle}(i, j) = \text{abs}(a_{ref}(x, y) - a_{scanned}(x, y)) , \quad (6.17)$$

with the condition that if $score_{angle}(i, j) > 180^\circ$, then we choose $\text{abs}(score_{angle}(i, j) - 360^\circ)$.

An example of the obtained scores for the image Figure 89, is presented on Figure 101:

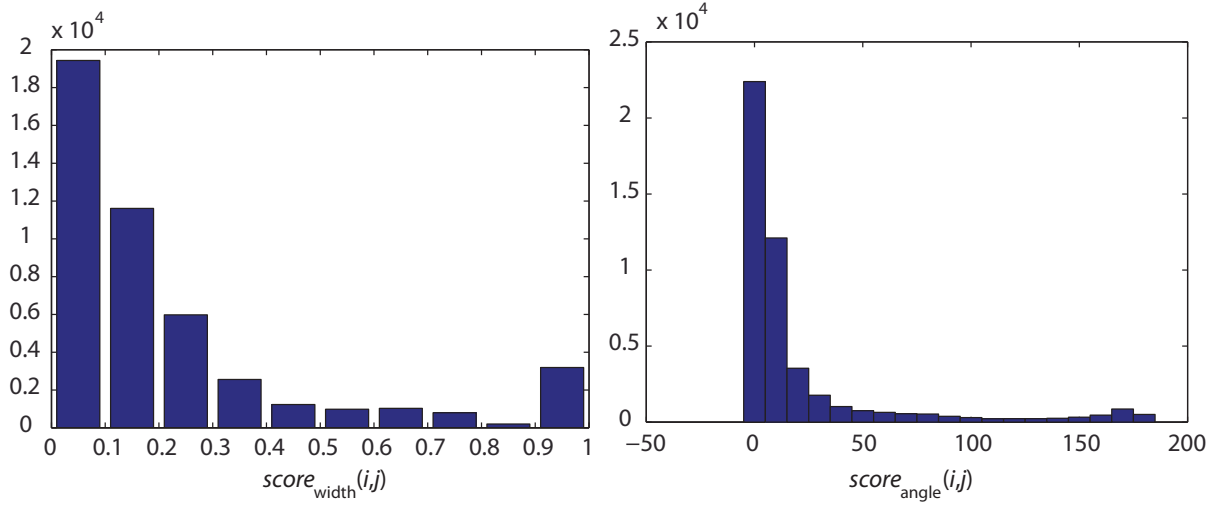


Figure 101. Histogram corresponding of our “width” and “angle” delocalisation score for the sample image in reference to the original layout image.

Finally, the last rule concerns the case where no edge point is found in a neighbourhood (n_i, n_j) of $+/-$ 10 pixels from the edge pixel. We thus consider than the edge has totally disappeared in the print process and we thus choose maximum penalty: $score_{width}(i, j) = 1$, and $score_{angle}(i, j) = 180^\circ$.

The final score for the image is obtained by computing the average of those local score for each pixel $e_{ref}(i, j)$, and we have the formula:

$$score_{sharpness} = mean_{i,j}(score_{width}(i, j)). \quad (6.18)$$

The angle delocalisation introduced in (6.17) could also have been used, but we empirically decided that the width information was sufficient for our application. Another indicator we tested was the percentage of pairs of edge pixels $(e_{ref}(i, j), e_{scanned}(i + n_i, j + n_j))$ leading to a gradient-angle difference lower than 20° .

6.7 Experimental testing and comparison with psycho-visual assessment

Psycho-visual experiment was carried out from several copies of three images shown in Figure 102. In the same idea that what was proposed in section 5.9 for tone homogeneity, assessors were asked to sort the copies in terms of sharpness quality and to place them on a metric scale (0 m = very blurred, 1 m = perfectly sharp), see Figure 104. The position is then converted into a ranking in 6 classes A, A-, B, B-, C, C-. The scores given by the algorithm, between 0 (blurred) and 1 (perfectly sharp), are also converted into a similar ranking. The matching of the classes given by observers and by our method is presented in Figure 105: The algorithm and the assessor rank more than 60% of the samples in the same class, and only 6% of the samples are ranked in non-neighbouring classes. 100% of the best and worst samples are ranked in the same extreme classes.

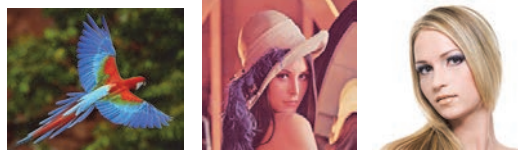


Figure 102. Three images used in our experiments to assess edge sharpness criteria.

In the same manner as suggested in the previous chapter, in section 5.9, we propose to rescale the assessors scores linearly in the same range that the scores given by the algorithm for a given set of samples. For our three sets of three images presented Figure 102 and printed with different parameters and conditions, we perform this rescaling. The maximum and minimum scores given by the assessors are thus readjusted to the same value of the algorithm. The results are presented in Figure 103.

We also propose to select six different classes, defined by selecting six threshold values of the objective score scale (0.74, 0.68, 0.6, 0.5, 0.45, 0), in order to assess the performance of our method. Assessors' scorings are also quantified into this six-grade classification by clustering.

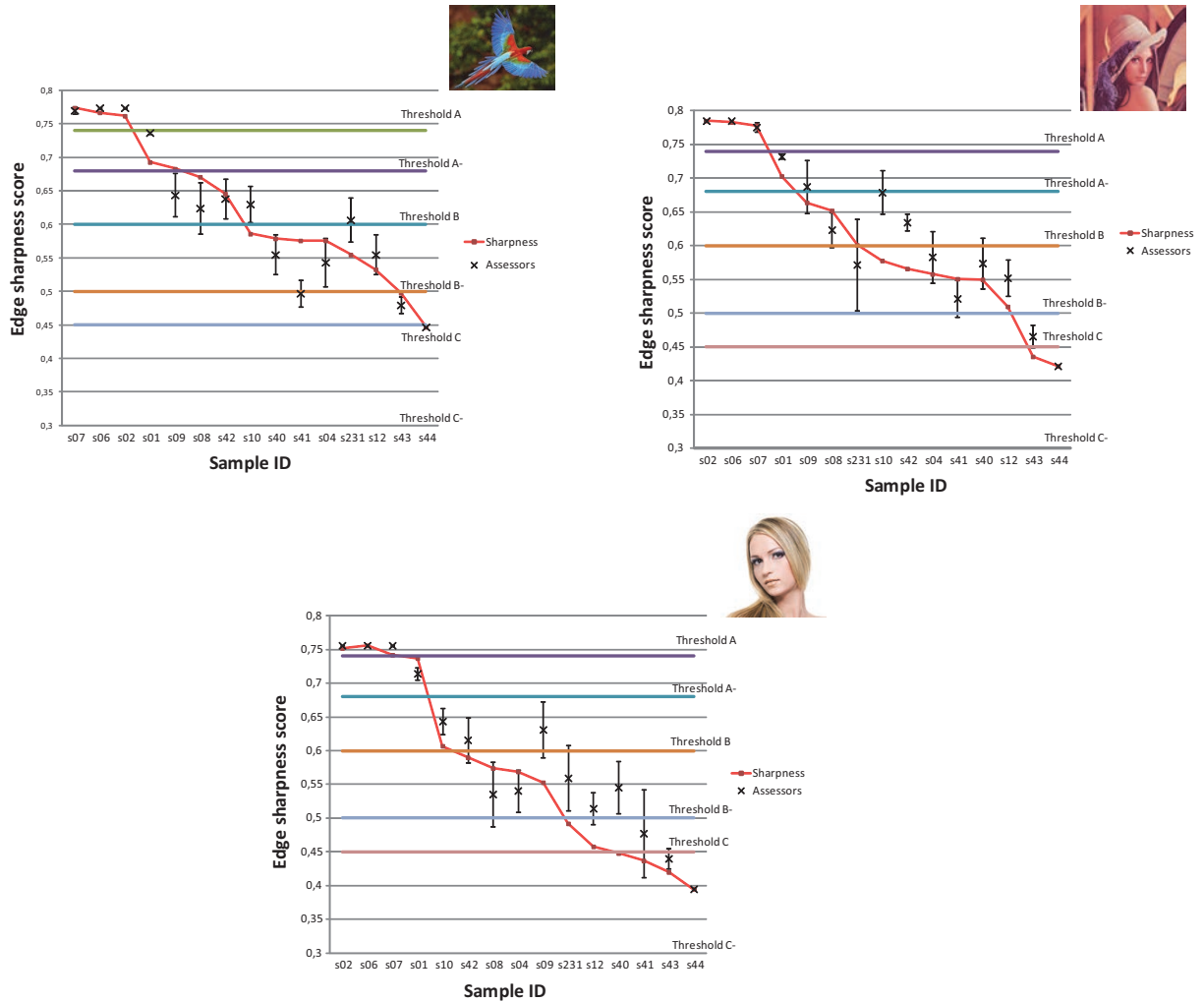


Figure 103. Comparison between objective and subjective evaluations for three images for the edge sharpness criteria.



Figure 104. Sharpness scores computed on 5 printed copies of a same digital layout.

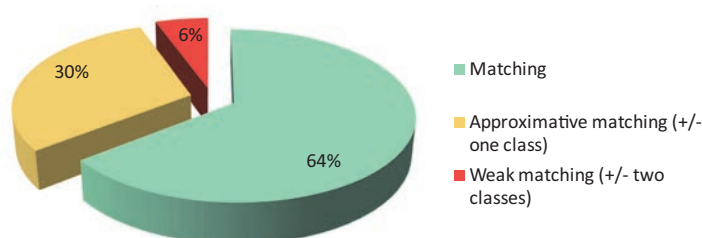


Figure 105. Percentage of samples classified in the same of six categories by assessors (subjective evaluation) and by our scoring method for edge sharpness attribute.

The two first classes and the last class are always correctly recovered. We can note the possibility to improve the rate of correctly recovered classes by reducing the number of classes (three or four classes only).

6.8 Conclusion

We proposed a method for assessing automatically, through the attribute of edge sharpness, the blurring of a printed natural image introduced by the printing system. This attribute is known to mainly contribute to the visual quality of prints, as, despite a fine tone reproduction, the printing system should also be able to reproduce sharp edges between areas with different colors. This method is based on a high resolution scanned color image of the print, which is then processed by computing the Laplacian of Gaussian filter to measure locally, on each contours pixel, its width, and compare it to the locally width of the same pixel of contours in the reference digital image. The index computed according to our method is in accordance with the empirical assessment by a small panel of non-expert observers. This edge sharpness index is, following the tone homogeneity, a second attribute which should be combined with other attributes in order to get a global quality score for printed natural images. Here again, the performances of different printing systems, in terms of visual quality, may also be compared by the use of this index.

Chapter 7 Colorfulness index

The colorfulness of a picture corresponds to the quantity of color present in the image. Typically, a black and white photo, or a gray level image, should obtain the lowest score with this criterion, and a very shiny colored picture, with very saturated colors, should obtain a high score.

At the very beginning of the study, such a criterion didn't appear as a prior feature to assess, as the very essence of this work was to assess print quality, and that one can judge of the quality of a photo print even if it is in black and white. But recent improvement in the secure printing field (see Color Laser Marking technology introduced in the following Part, in Chapter 8) led us to revise our opinion, and include the study of color reproduction in the print quality assessment study.

7.1 Introduction

The color assessment, realized by our human visual system, needs the introduction of the simultaneous contrast notion. This phenomenon, not always well known is however crucial in the color perception of objects by an observer in a colored scene.

Simultaneous contrast is a perceptual phenomenon explaining the fact that a same image may be perceived differently according to its surrounding. It is due to the fact that the human visual system has a global interpretation of its field of view, and emphasizes contrasts between neighbouring colors, or textures.

A famous illustration of this phenomenon is presented in Figure 106 with the checker shadow illusion. The image presents a checkerboard with light and dark squares. On the left part of the Figure 106 (a), the area of the image labelled A appears to be darker than the area of the image labelled B. However, they are actually exactly the same color, as it is confirmed in Figure 106 (b) with an homogeneous gray rectangle linking the "A" box to the "B" box.

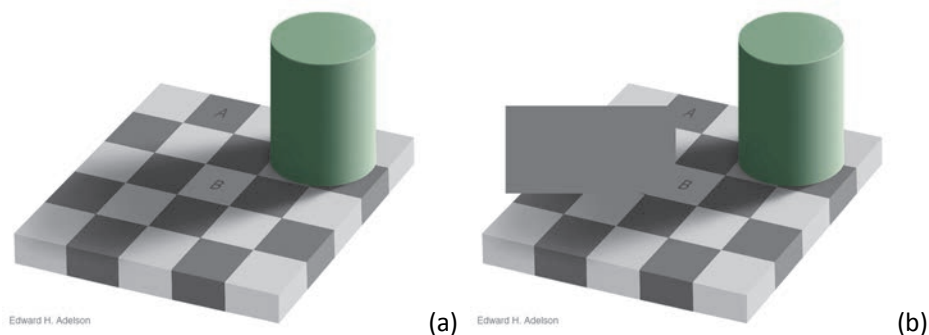


Figure 106. "Checkers shadow Illusion" by Adelson Edward H. (1995): (a) original image, and (b): image with uniform rectangle showing that A and B boxes have the same color.

In a similar way, the following picture presents an image in three different contexts. The simultaneous contrast is illustrated here from a commonly called “lightness constancy” to a “color constancy”. On these three examples, the girl’s eyes have the same color.

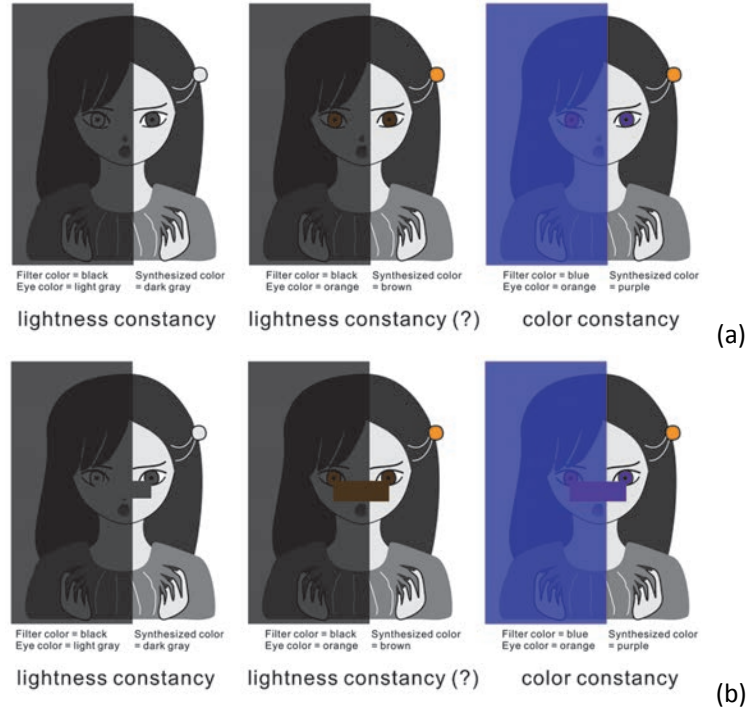


Figure 107. From lightness constancy to color constancy, by Akiyoshi Kitaoka (2009). (a) original image, and (b): image with uniform rectangle showing that the girl have not mismatched eyes.

7.2 Digitalization of the prints

Following the methodology used in Sections 5.2 and 6.2, we use the same acquisition system for the digitalization of prints: a flatbed scanner. In contrast with the previous chapter, this criteria focussing on the colorfulness aspect of the printing, high spatial resolution of the scanning is not mandatory. We therefore select a classical scanning resolution of 600 ppi.

7.3 Overview of the method

The Colorfulness, our is proposed to be assessed following the steps summarized in Figure 108:

- Printing and digitalization steps as detailed in Section 7.2;
- A pre-processing step, including image resizing in order to simulate the blurring of human vision, and avoid the study and characterization of very small and not resolvable printed details. The color of a print being most of the time a juxtaposition of their inkables dots, this image size reduction models the low pass filtering performed by our visual system;
- The application of the color prediction model presented in Section 4.4, dedicated to a simulation of D2T2 print, in the field of non scattering ink layers in top of a white diffusing plastic background;

- In parallel to all of this, a comparison with psycho-visual assessment (see Section 7.7) is conducted to verify whether the used parameters are optimal for the considered application (see Sections 7.4 and 7.6).

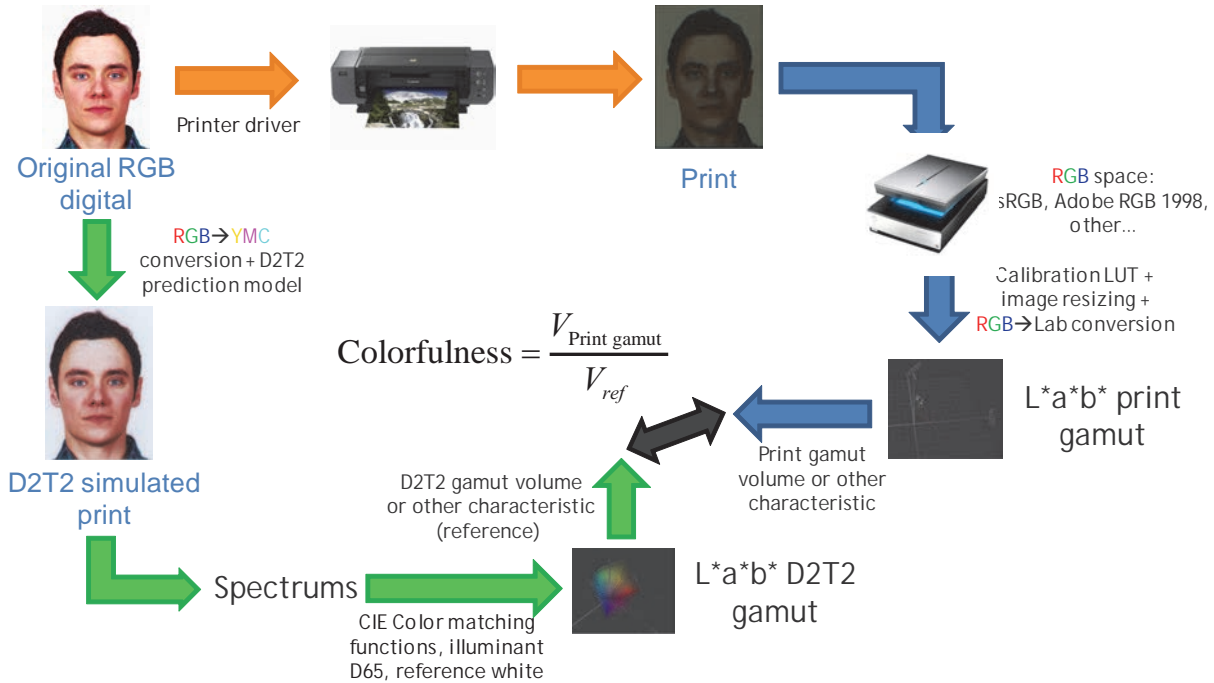


Figure 108. Main algorithm flowchart for the assessment of Colorfulness.

7.4 Pre-processings

As this part focuses on color, color management is important, and we need a color correction for the scanner acquisitions. We therefore start by correcting the raw scanned image with the method we presented in Section 3.1.4.

Then an image size reduction is performed so that the color in the reduced image is the average of several pixels in the scanned image, thus reducing the color noise. The original digital image and the printed-then-scanned image having both a resolution of 600 ppi, we apply the same reduction factor to the two images. Using different values for this reduction factor we can personalize the criterion, and adapt the analysis on larger or smaller areas. Of course, the reduction factor value can be chosen regarding the size of the image. In our applications, we used images of size 35x45 mm, and we empirically conclude that for such a picture, a reduction factor of $\frac{1}{4}$ leads to a new image containing the useful information. An image reduction using bicubic interpolation is used, and applied to both the original image and the scanned one.

7.5 Application of the color prediction models

For the targeted colorfulness score, we need here again a reference image, to normalize the measure performed within the scanned image only. A trivial reference, the simplest expected, would be to choose the original image itself, rescaled to the same size as the assessed one. But this would mean to

compare very different colors, as the original image is in the digital world, and the scanned image we aim to assess is in the physical world. We well know that the gamut of the RGB digital layout is far from the one of a printing, even when the printer is dedicated to high gamut printing. It is therefore obvious that the gap would be too large, and the reference image, being too high in a colorfulness scale, would drop the final score of the assessed image. We need another point of comparison. We therefore propose to consider the Dye Diffusion Thermal Transfert (D2T2) printer as reference for color reproduction, and colorfulness of a printing system will be assessed by its capacity to reproduce colors “as well as” D2T2. We chose the D2T2 printing system as the reference for our colorfulness attribute because it is one standard in the card industry, and was easily available at Gemalto for tests. We take benefit of the color prediction model for D2T2 that we present in section 4.4, and illustrate more precisely in the following, third and last Part: Section 8.2, to simulate the colors rendered by the D2T2 printer which prevent having to print images physically.

An example of an image simulated by this method and physically printed in D2T2 then scanned is presented in Figure 109. The color calibration of the scanner is performed according to the method explained in Section 3.1.4.

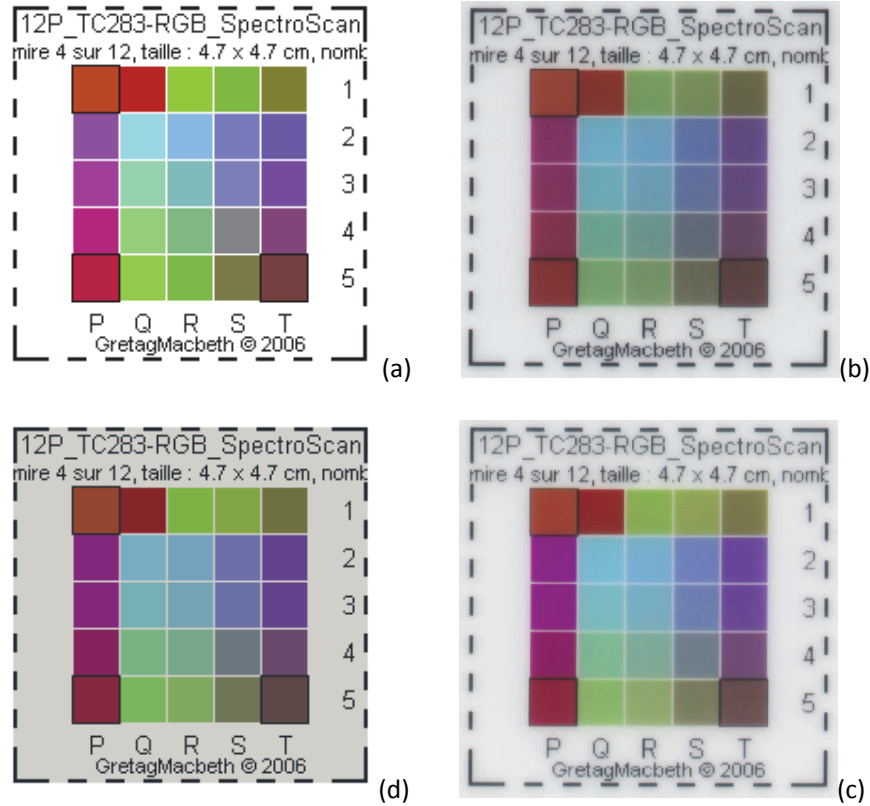


Figure 109. Comparison between (a) the original layout, (b) a print in D2T2 redigitalized by scanner, (c) a color correction of this scan, and (d) the simulation of the printed version with Berns' equation.

7.6 Computation of the objective colorfulness score

In our application, the goal is to assess the colorfulness of typically an ID photo.

Let's take as example the original layout in Figure 110 (a) and a printed-then-scanned version Figure 110 (b), using an ink jet printer with low quality settings and a basic office paper.

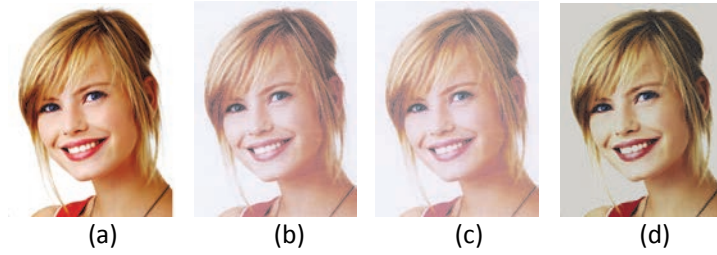


Figure 110. (a) Original digital image, (b) scanned printed image in inkjet on office paper, (c) scanned image after calibration of the scanned, and (d) D2T2 simulated image (considered as reference)).

The evaluation is based on the study of the two color gamuts of both the reference image simulated as if printed in D2T2, and the printed-then-scanned image. The score is expected to be independent of the original image.

The first task is the evaluation of the reference gamut. The D2T2 simulated image from the original layout is selected. The simulation of the D2T2 leads for each color to a spectra that can then be converted into CIE-LAB color space. At the beginning, a list of all pixels present in the image is computed, and be considered only their chrominance values a^* and b^* .

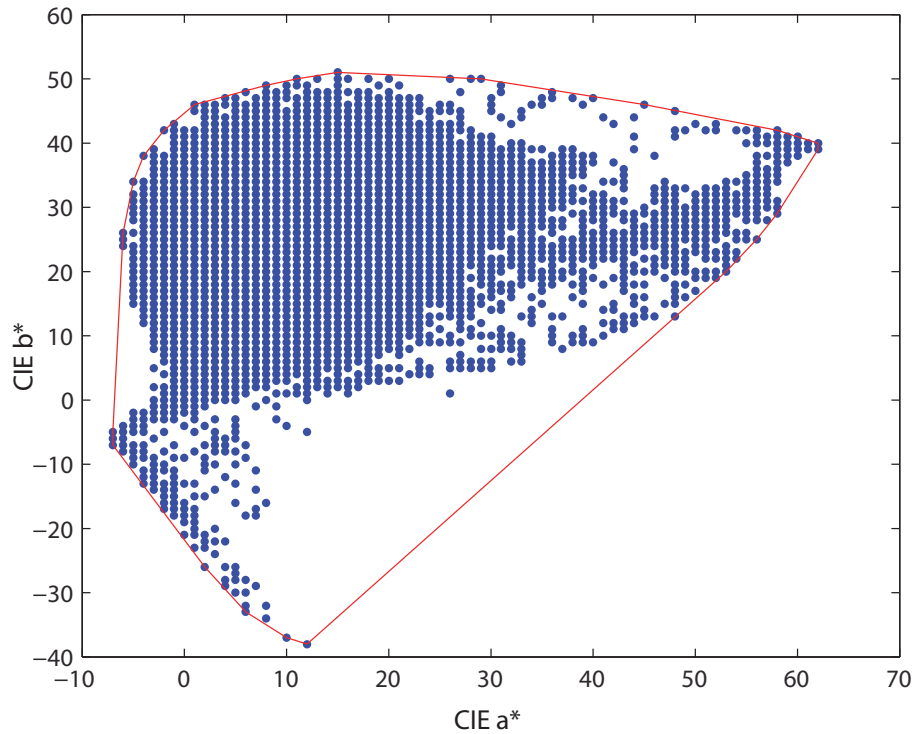


Figure 111. Projection on the CIELAB (a^*, b^*) plane of the pixel colors of the reference image, and its convex hull plotted in red solid line.

This chrominance dot diagram is then triangularized using the Delaunay method [73]. The 2-D Delaunay triangulation of a set of point in a plane is a triangulation such that no point is inside the circumscribing

circle of any triangle. Thus, the Delaunay triangulation avoids too much elongated triangles. An overview of the Delaunay triangulation applied on the set of points shown in Figure 111 is drawn in Figure 112.

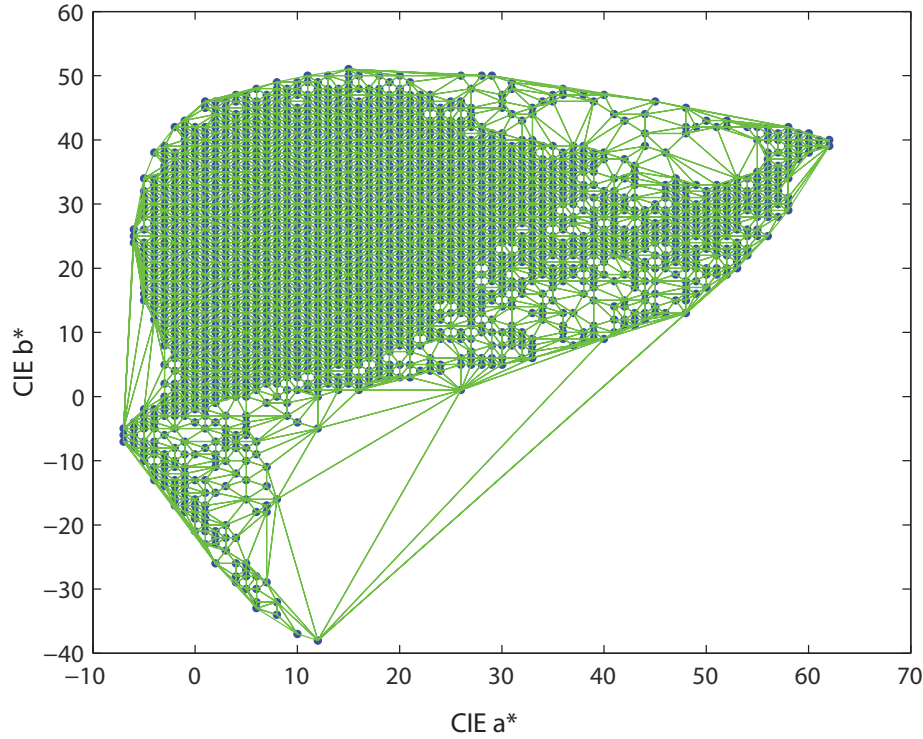


Figure 112. Delaunay triangulation of the set of color points of the reference image in the CIELAB 2-D (a^*, b^*) plane.

We recover the property stating that the union of all simplexes of a triangulation is the convex hull of the points.

Our goal being the representation of the color space filled by the pixels of the considered image, we choose to measure the area of the surface covered by those points. We understand that the large triangles are not representative of the colors present in the image since a large triangle means not sufficiently color points in the neighbourhood to ensure a locally finer cutting. In order to “clean” this cloud of points, we will study the distribution of the size of those triangles, set a threshold on the size of them, and remove triangles whose size is too large. The triangle size is measured by its area, computed according to the formula, for a given ABC triangle:

$$A_{ABC} = \frac{1}{2} \begin{vmatrix} x_B - x_A & x_C - x_A \\ y_B - y_A & y_C - y_A \end{vmatrix}, \quad (7.1)$$

where (x_A, y_A) , (x_B, y_B) , and (x_C, y_C) are the Cartesian coordinates of the three apexes of the ABC triangle.

The threshold is chosen according to the following methodology: we first identify the most represented triangle size in the histogram of triangle size. The distribution decreases very rapidly, so we decide to place a threshold very near to this maximum:

$$\text{threshold} = 2 \times \text{bincenter}_{\max} . \quad (7.2)$$

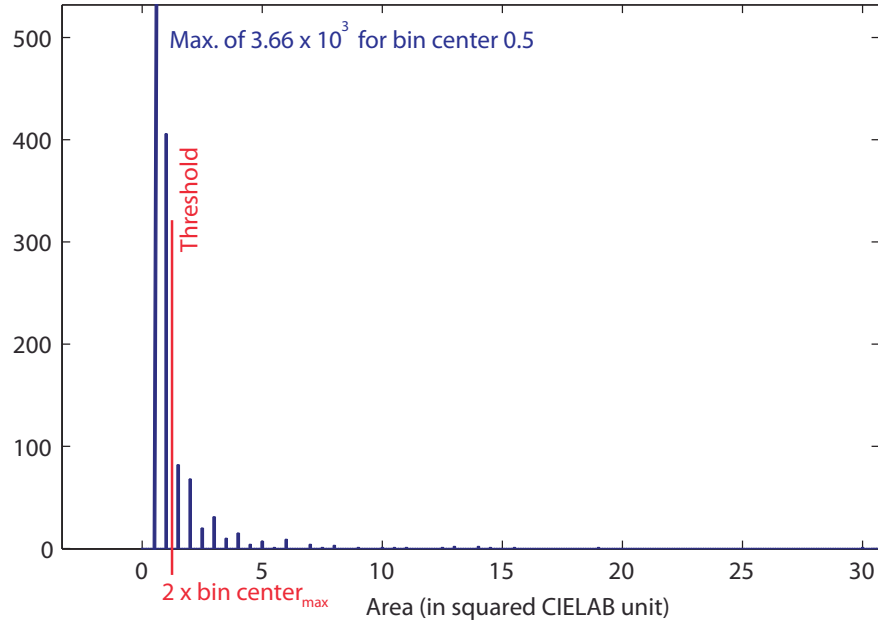


Figure 113. Histogram of the triangle size of the Delaunay triangulation of the reference image.

An “area filtering” is then performed on the triangulation of Figure 112, to remove all triangles smaller than this threshold, yielding the set of triangles displayed in Figure 114.

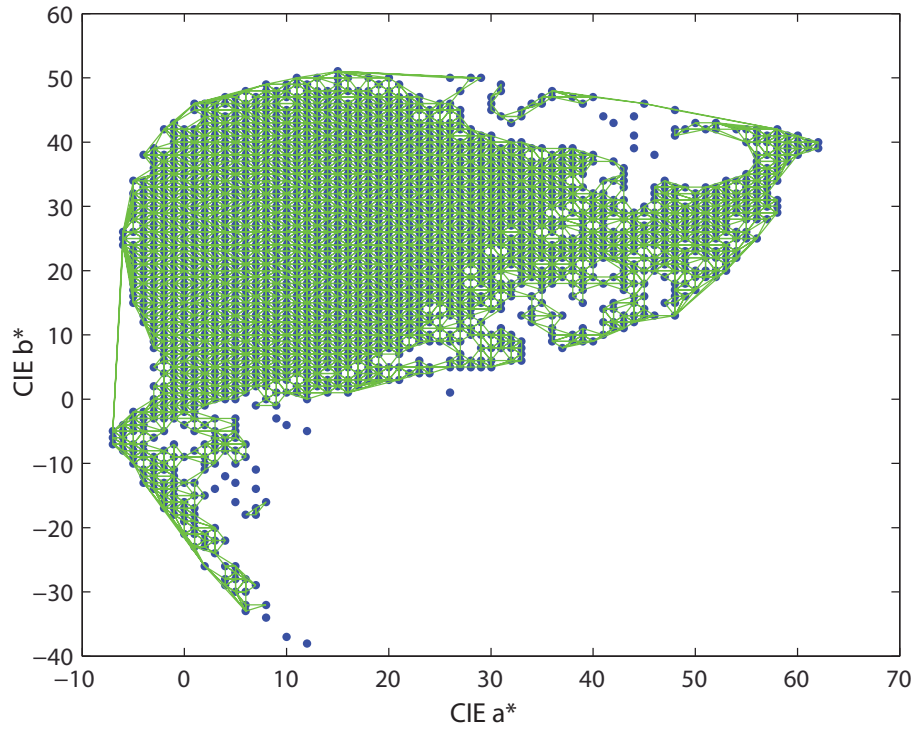


Figure 114. “Area-filtered” Delaunay triangulation of the set of color points of the reference image in the CIELAB (a^*, b^*) plane.

All areas of the remaining triangles t_i for the reference image I_{ref} are summed so as to form the reference score:

$$A_{ref} = \sum_{t_i \in I_{ref}} A_{t_i}. \quad (7.3)$$

Similar reasoning line is followed on the scanned color corrected image. First a color conversion is done in order to obtain the scanned image pixel in CIELAB, considering input RGB as AdobeRGB 1998 color RGB, the D65 illuminant, and an absolute white reference. The calibration of the scanner being performed in the CIELAB color space and then reconverted into RGB color for display, we use in our experiment the CIELAB color image before this conversion back to RGB.

The chrominance dot diagram is computed, still considering only the two chrominance channels a^* and b^* , shown in Figure 115.

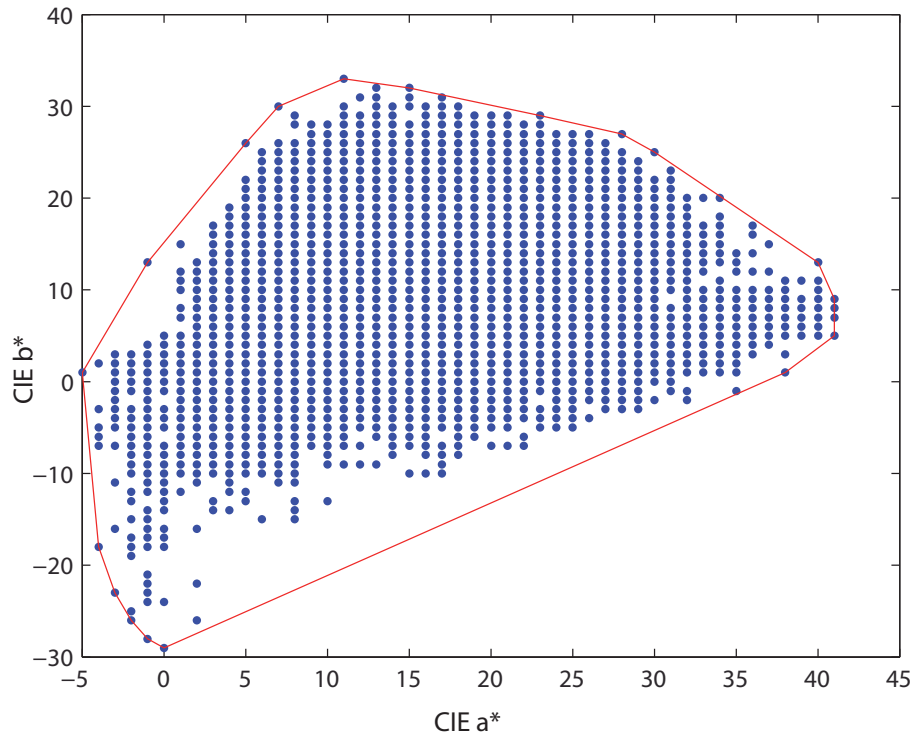


Figure 115. Projection on the CIELAB (a^*, b^*) plane of the pixel colors of the printed-then-scanned image, and its convex hull plotted in red solid line.

The Delaunay triangulation applied on the diagram of Figure 115 is drawn in the Figure 116.

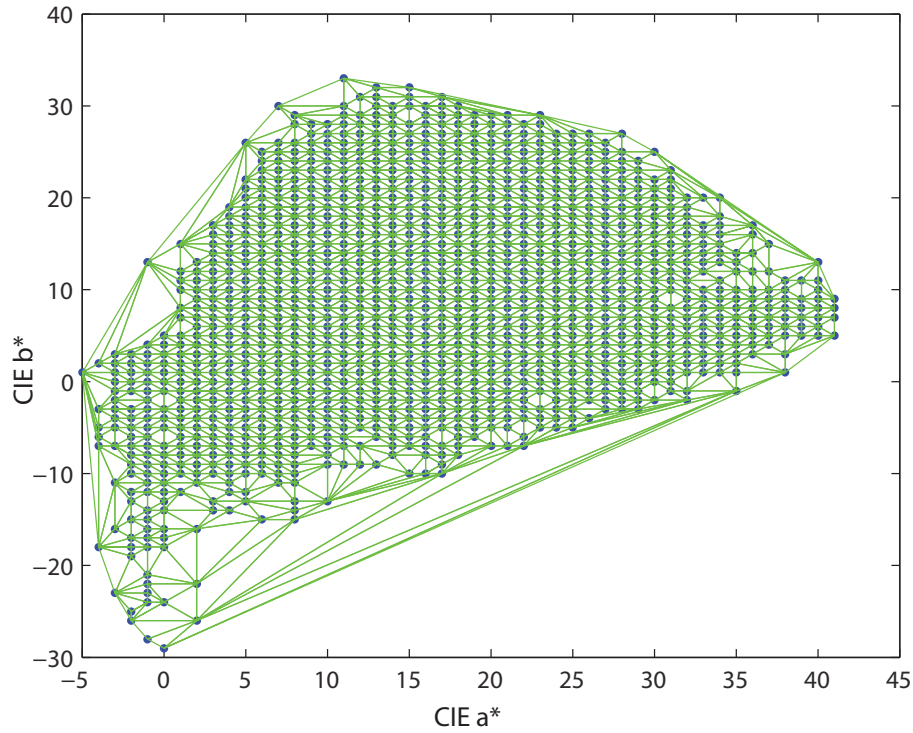


Figure 116. Delaunay triangulation of the set of color points of the reference image in the CIELAB 2-D (a^*, b^*) plane.

A new threshold is computed in order to keep only the smallest triangles, from the histogram displayed in Figure 117, and the filtering is performed in the same manner as for the D2T2 reference image.

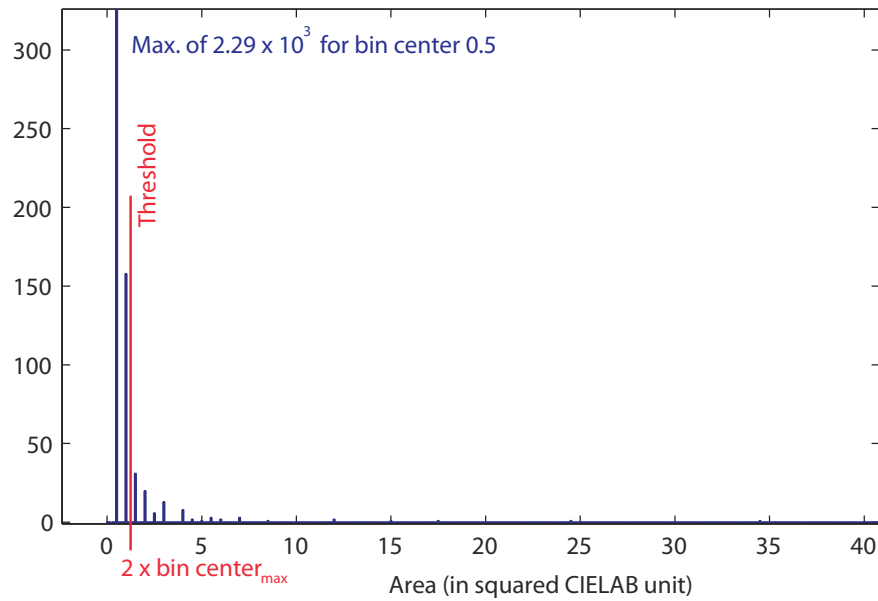


Figure 117. Histogram of the triangle size of the Delaunay triangulation of the scanned image.

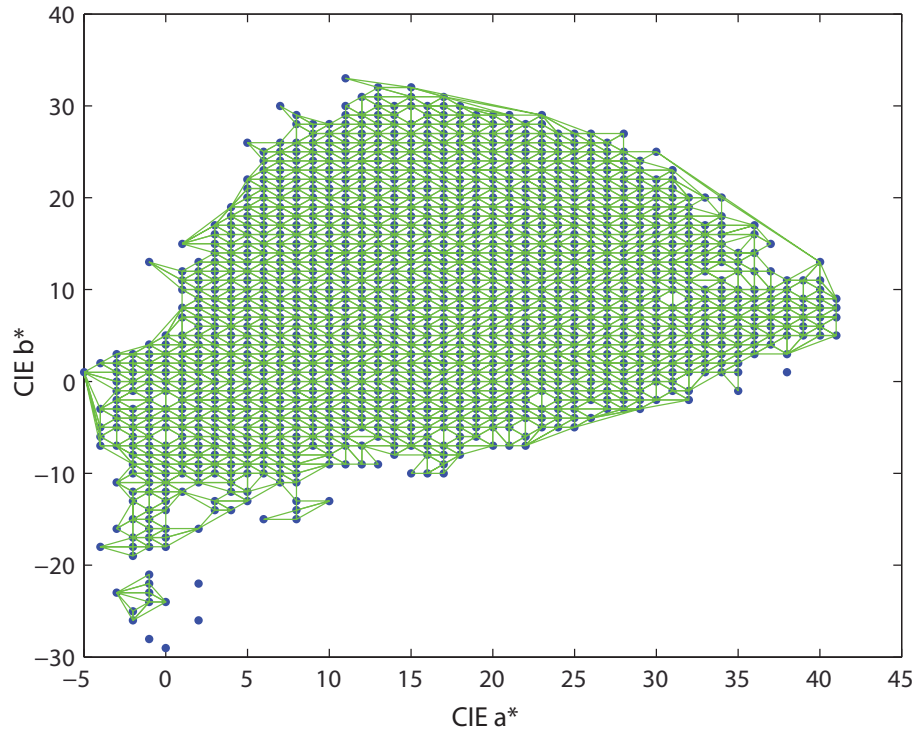


Figure 118. “Area-filtered” Delaunay triangulation of the set of color points of the printed-then-scanned image in the CIELAB (a^*, b^*) plane.

We compute the score of the printed-then-scanned image $I_{scanned}$ as the sum of all the remaining triangles t_i :

$$A_{scanned} = \sum_{i \in I_{scanned}} A_{t_i}. \quad (7.4)$$

Then, the colorfulness score is the ratio of $A_{scanned}$ to A_{ref} :

$$A_{scanned} / A_{ref}. \quad (7.5)$$

With such a definition, the colorfulness score can be higher than 1, when the colorfulness of the scanned image is higher than the one of the D2T2-simulated image.

7.7 Experimental testing and comparison with psycho-visual assessment

Psycho-visual experiment was carried out from several copies of four images (see Figure 119). According to similar idea that what was proposed in section 5.9, assessors were asked to sort the copies in terms of colorfulness and to place them on a metric scale (0 m = absence of chromaticity, 1 m = presence of very saturated colors). The position is then converted in a ranking in 6 classes: A, A-, B, B-, C, C-. The scores given by the algorithm is in this case not limited to 1 as the reference is the D2T2 printing, and several samples can have a better score than this technology. They are however also converted in similar ranking.

The matching of the classes given by observers and by our method is presented in Figure 121. The algorithm and the assessor rank nearly 60% of the samples in the same class, and only 1% of the samples are ranked in non-neighbouring classes.



Figure 119. The four images used for testing our colorfulness attribute.

As that was suggested in the precedent chapter, in section 5.9, we propose to rescale the assessors scores linearly in the same range that the scores given by the algorithm for a given set of samples.

We perform this rescaling with the four sets of the four images presented in Figure 119 and printed with different parameters and conditions. The maximum and minimum scores of the assessors are set to the maximum and minimum values given by the algorithm. The results are presented in Figure 120.

In order to assess the performance of our method, six different classes are defined by selecting six threshold values of the objective score scale (1.25, 1.15, 0.9, 0.7, 0.35, 0). Assessors' scorings are also quantified into this six grades classification by clustering.

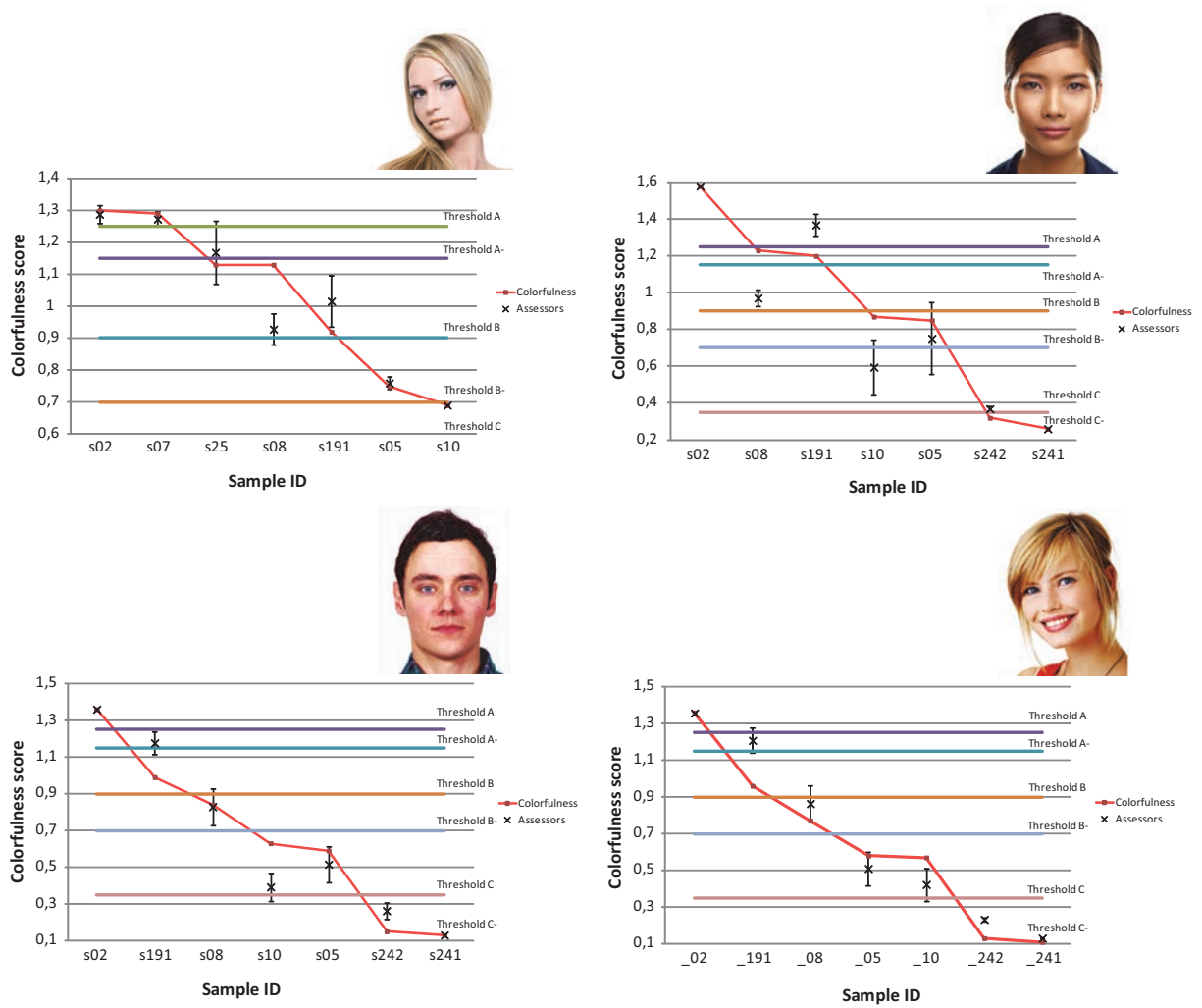


Figure 120. Comparison between objective and subjective evaluations for three images for the colorfulness criteria.

We verify with these four experiments, yielding to similar performances, that the colorfulness score does not depend on the input image chosen for the assessment.

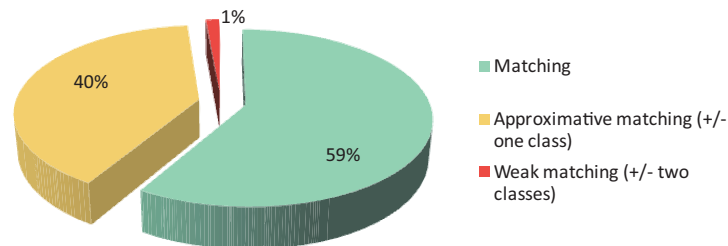


Figure 121. Percentage of samples classified in the same of six categories by assessors (subjective evaluation) and by our scoring method for colorfulness attribute.

Once again, we can note the possibility to improve the rate of correctly recovered classes by reducing the number of classes (three or four classes only).

7.8 Conclusion

We proposed a method for assessing automatically the colorfulness of a printed natural image, corresponding to the quantity of color well reproduced by the printing system. This attribute is considered as optional, as we still can observe a high photo quality for a black and white print, without any color. Nevertheless, our world, full of colors, tends to make us revise our first opinion, and suggest that the color reproduction quality is also an important factor to take into account when assessing a printing quality, mainly due to visual expectation for color quality of prints. The method is based on a scanned color image of the print, which is then processed and analysed in terms of quantity of colors in comparison to a reference. The reference is constructed according to a simulation of a printing system known to provide a high color gamut that we take as reference: the Dye Diffusion Thermal Transfert (D2T2) printing system. The comparison of the two gamuts is done in the (a^*, b^*) chromaticity plane of CIELAB color space, by comparing the two areas of the surfaces defined by the color coordinates present in the two images. The index computed according to our method is in accordance with the empirical assessment by a small panel of non-expert observers.

This criterion is dedicated to the chromaticity of the color. Another aspects would have also be possible to analyse, such as the contrast regarding the lightness axis, or a matching in the gravity center of the cloud of points in the CIELAB color space providing information about a global color drift in the printing.

Third Part

Color prediction models for innovative printing technologies

Chapter 8 Prediction of the spectral reflectance of laser-generated color prints

Recent color printing technologies based on the principle of revealing colors on pre-functionalized achromatic supports by laser irradiation offer advanced functionalities, especially for security applications. However, color prediction is more challenging for these technologies than for classic ink-transfer printing systems. The spectral properties of the coloring materials modified by the lasers are not precisely known and may strongly vary, depending on the laser settings, in a nonlinear manner. We show in this chapter, through the example of the Color Laser Marking technology based on laser-bleaching of a mixture of pigments, that the combination of an adapted optical reflectance model and learning methods to get the model's parameters enables predicting the spectral reflectance of any printable color with rather good accuracy. Even though the pigment mixture is formulated from three colored pigments, an analysis of the dimensionality of the spectral space generated by CLM printing, thanks to a Principal Component Analysis decomposition, shows that at least four spectral primaries are needed for accurate spectral reflectance predictions. A polynomial interpolation is then used to relate RGB laser intensities with virtual coordinates of new basis vectors. By studying the influence of the number of calibration patches on the prediction accuracy, we can conclude that a reasonable number of 130 patches are enough to achieve good accuracy in this application. This work has been the subject of one of our recent contribution [74].

8.1 Introduction

The usual definition for printing as application of inks on a support in order to transmit information [1] is still valid for most printing systems but is becoming too narrow for certain printing processes under development. Owing to the progress in photonics and chemistry, the transfer of photo-active substances on the support and the revelation of information can be made in two separate steps. This is the case for the laser-induced color marking based on silver nanoparticles in crystalline matrices [75] where, for example, a clear TiO₂/Ag layer is coated on the support, and then colored under laser irradiation [76]. The Color Laser Marking (CLM) technology studied in the present work is a second example dedicated to the card printing industry [77]. The colored components, which form a sublayer of the card, are selectively bleached when exposed to laser irradiation, i.e., their spectral transmittances are modified. Since the color of every printable pixel can be modified, the system enables continuous-tone printing, i.e., without halftoning, similar to silver photograph printing. Compared to the Dye Diffusion Thermal Transfer (D2T2) technology which also enables continuous-tone printing on cards [1], the interest in CLM is that printing can be processed after lamination of the card, and the production of color is made below the protection overlay to ensure security, whereas the D2T2 approach involves printing on the card surface and coating it with a protection patch: varnish or thin hot laminated overlay. Moreover, CLM is a more advanced technology that can add security features such as Kinegram® on the printing photo area and new ones specific to this technology. The structure of the card is more robust to attacks such as delamination of the card and ID photo replacing or modification thanks to irreversible color changes [78]. Selectively bleaching pigments by laser

sources as a means of secure printing is practically not investigated and is only found as a subject of patents [79, 80].

In the CLM technology, the photosensitive layer is a dark grey mixture (named CMYart) involving three pigment-type colorants: cyan, magenta and yellow, coated onto a transparent polycarbonate film, which is then laminated together with the other polycarbonate films constituting the final card. Figure 122 shows an area of white card where this mixture is deposited. Three lasers of different wavelengths are used to bleach the targeted pigments and “reveal” colors inside the polycarbonate card: a red laser bleaches the cyan pigments in the mixture, a green laser the magenta pigments, and a blue laser the yellow pigments. As the laser power increases, the dark dye mixture is more bleached and the resulting color is brighter. The laser beam diameter is around 30 to 35 μm with a Gaussian irradiance profile and a variable input power encoded on 8 bits, which can therefore produce 256 irradiance values on the surface. The printing resolution is around 600-800 dpi and, by tuning the power of the three lasers in each pixel, coloration of the surface can be achieved in an almost continuous way in contrast to halftoning in classic printing, as shown in Figure 123.



Figure 122. The CMYart ink containing a mixture of cyan, magenta and yellow pigments (dark area) deposited on polycarbonate substrate (white area).

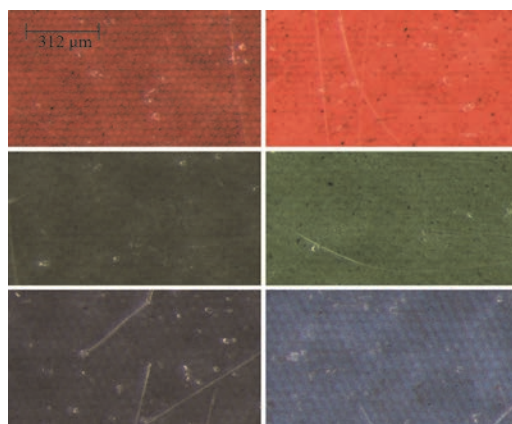


Figure 123. Microscopic images of areas printed in red, green, blue obtained by irradiation with, respectively, red laser, green laser and blue laser at relative power 0.5 (left) or 1 (right). The coloring layer is nearly continuous, no halftoning is needed. Higher laser power gives brighter color.

The purely physical aspects of color are characterized by the means of the reflectance/absorption spectroscopy. Within organic dyestuffs, the observed relatively narrow absorption bands in the visible region correspond to their lowest electronic excitation energies and are most often explained in terms of the

molecular orbital (MO) approach [81]. Empirically, the relatively low excitation energy is observed when the corresponding molecule includes a chain of conjugated double bonds connecting donor and acceptor moieties. The light-induced excitation (HOMO-LUMO electronic transition) is of the charge transfer type, and results in redistribution of electron density along the conjugation chain [82]. For organic pigments (as compared to dyes), another major factor affecting the initial color is the energy of the crystal lattice and intermolecular interactions.

The idea of creating colored images in a pre-deposited pigment mixture consists in trying to selectively bleach the cyan, magenta and yellow colorants by applying strong monochromatic sources of light (such as lasers) of the wavelengths corresponding to their absorption maxima. Electronic excitation of the colorant molecules can give rise to photochemical transformations breaking the bond conjugation and thus leading to the disappearance of the corresponding absorption band. This is the common mechanism of the general color fading (non-selective pigment bleaching) observed under sunlight for textiles or museum paintings [83]. The basic requirement to the choice of colorants for CLM printing is the possibility to bleach them selectively in a mixture. In practice, however, selective addressing is difficult owing to overlapping absorption bands, and even if bleaching takes place, the remaining molecular fragments are not completely colorless. Most often, the residual absorbance is not limited to the near UV region, but exhibits broad bands, infringing into the visible, which results in a dull yellowish tint, sometimes intensified by the degradation of the medium.

Using dye solutions as the primary colored components has some advantages, namely better mastering the selectivity owing to the presence of narrower absorption bands, and lower required light energies for monomolecular reactions. Among existing common applications of selectively addressing organic dyes by the light of the corresponding wavelengths, dye sensitizers for silver-salt based color photography [84], or in photodynamic therapy of cancer [85] can be mentioned. Another example is presented by Lume-Jet company in Ref. [86]. For security applications in polycarbonate cards, pigments are preferable over dyes, due to their higher aging resistance. Pigments are colorants that are applied into a medium by a dispersion process and remain as solid particles held in place mechanically, usually in a matrix of a solid polymer [87]. They are characterized by high energies of intermolecular bonding (crystalline lattice), and their observed color depends on both light absorption and light scattering components, affected also by their crystalline modification and physical conditioning. Thus, exciting pigment molecules compared to similar dyes requires generally much higher energies (such as those reached by monochromatic laser sources), broadens the corresponding spectral absorption bands, which complicates selective addressing of the colored components, and generates a significant amount of heat that can drastically decrease the reaction selectivity in terms of the product formation, or cause degradation/burning of the surrounding materials.

Calibrating a printing system means establishing the look-up table from RGB values of the original digital layout and the command parameters for the three lasers yielding the targeted printed colors. For that purpose, the exhaustive method consists in varying incrementally all the laser command parameters, measuring the obtained colors with a spectrophotometer, and creating an ICC profile. As an advantage, this method accounts for all optical, chemical, thermal, mechanical phenomena whose influence on the printed color is complex and strongly non-linear. However, it is tedious and time consuming, and needs to be repeated every time when any component within the system is modified, including slight variations in the pigment ratio. Instead, we want to print a small selection of colors, and then be able to predict all other ones as it is now permitted for traditional halftone prints (as offset or inkjet) by the last generation of spectral reflectance prediction models [43].

However, these models are not directly transposable to the CLM printing because there is no half-tone. From an optical point of view, a card printed by CLM has comparable structure to a card printed by Dye Diffusion Thermal Transfer (D2T2), with a white, opaque layer in the center of the card and, on the top of it, nonscattering films with similar optical indices which can be considered as one absorbing layer. The model proposed by Berns et al. for D2T2 prints [52] will therefore be explored with CLM prints, as it relies on the spectral reflectance of the white opaque layer, the spectral transmittance of the coloring layer and the Fresnel reflectance of the air-overlay interface. In D2T2, for every printable color, the spectral transmittance of the coloring layer can be related to the spectral transmittances of the different dyes and their respective optical thicknesses according to Beer-Lambert-Bouguer law [39]. We will show that for CLM, the assumption that the coloring layer remains a mixture of the same three primary colorants is not satisfied after laser irradiation. In order to obtain a set of primaries and determine, for each color patch, their respective spectral transmittances and optical thicknesses, we thus propose to use learning methods from the measurement of a large but reasonable set of printed colors. A Principal Component Analysis (PCA) provides the spectral transmittances of “virtual” primaries. Then a non-linear regression enables linking their respective optical thicknesses to the input RGB values. The comparison between D2T2 and CLM printing will be developed in detail in this study because it seems important to show which elements of Berns model, known to provide accurate predictions in D2T2, are still valid for the CLM, and which ones need to be revised.

The optical equation predicting the spectral reflectance of a diffusing background in optical contact with a nonscattering coloring layer on the top of it was introduced by Williams and Clapper (introduced in 4.3) for photograph prints [49]. Since both the D2T2 and CLM printed cards have this structure, the Williams-Clapper equation applies. It is derived from a description of the multiple reflections of light between the diffusing background and the air-print interface through the coloring layer. The nonscattering layers and the diffusing background are assumed to have same refractive index n . By denoting as $\rho(\lambda)$ the internal reflectance of the background, and $\tau(\lambda)$ the internal transmittance of the coloring layer under normal incidence, the spectral reflectance factor of the print, illuminated at angle θ_i and observed at angle θ_r ($\theta_i : \theta_r$ geometry) is given by equations presented in Section 4.3 and 4.4.

8.2 Application of Berns’ equation to D2T2- and CLM-printed cards

In this Section, the goal is to verify if the model expressed by Eq. (4.39) is suitable for predicting reflectances of laser-bleached colorants. The spectral reflectance of color patches in which the (nonscattering) coloring layer is a mixture of the three colorants with the respective optical thicknesses ε_c , ε_m and ε_y is given by Eq. (4.39). Usually, these optical thicknesses are not precisely known. For example, in D2T2 printing, color corrections by the driver and the back diffusion effect [52] are not precisely known. That is why a calibration of the model is necessary to get the effective optical thicknesses corresponding to the amount of dyes actually present on the support, which may significantly differ from the nominal ones. The first question is to know whether they can be deduced from the measured spectral reflectances of the color patches, and whether the predicted reflectances with these obtained optical thicknesses correspond to the measured ones. We consider here a coloring layer made of three primary colorants. For a given patch, the relative optical thicknesses of these primary colorants are deduced by using the Levenberg-Marquardt minimization algorithm [88-90] from the following objective function based on the measured reflectance $R_m(\lambda)$ and predicted reflectance $R(\lambda, \varepsilon_c, \varepsilon_m, \varepsilon_y)$ expressed by Eq. (4.39):

$$(\varepsilon_c, \varepsilon_m, \varepsilon_y) = \underset{\hat{\varepsilon}_c, \hat{\varepsilon}_m, \hat{\varepsilon}_y}{\operatorname{argmin}} \sum_{\lambda} \left(R_m(\lambda) - R(\lambda, \hat{\varepsilon}_c, \hat{\varepsilon}_m, \hat{\varepsilon}_y) \right)^2. \quad (8.1)$$

The initial optical thickness values considered in the algorithm are related to the RGB values of the original digital layout, r , g and b , expressed in the range $[0,1]$:

$$(\varepsilon_c^0, \varepsilon_m^0, \varepsilon_y^0) = (1-r, 1-g, 1-b). \quad (8.2)$$

In the following, to assess the agreement between measured and predicted spectra, we will use the equivalent color difference CIELAB 1994 DeltaE metric ΔE_{94} [39], obtained by converting the predicted and measured spectra into CIE-XYZ tristimulus values, and calculated with a D65 illuminant and in respect to the 2° standard observer; then we will convert the CIE-XYZ values into CIELAB color coordinates using as a white reference the white point of the D65 illuminant.

Let us consider the case of CLM. Three white polycarbonate cards coated separately with the three primary pigmented layers (cyan, magenta and yellow) were obtained from the colorant manufacturer. The layer thicknesses and pigment concentrations were not communicated but we attributed a unit optical thickness to each individual pigment layer before bleaching. From the measured spectral reflectance of these samples, we could deduce according to Eq. (4.43) the spectral internal transmittances of the cyan, magenta and yellow colorants, respectively $t_c(\lambda)$, $t_m(\lambda)$, and $t_y(\lambda)$. Then, from the measured spectral reflectance of a card coated with a mixture of the three colorants, we could evaluate the relative optical thicknesses of the cyan, magenta, and yellow colorants, respectively $\varepsilon_c = 1.026$, $\varepsilon_m = 0.872$, and $\varepsilon_y = 0.751$. If the three single-colorant samples provided by the manufacturer have the same layer thickness and the same pigment concentration, the relative optical thicknesses mentioned above would correspond to the proportions of each colorant in the mixture. Figure 124 shows that the spectral reflectance predicted by Eq. (4.39) with these ε_j values agrees with the measured one but does not coincide perfectly: the ΔE_{94} between the two spectra is 1.08 unit, therefore above the just noticeable difference. This might be due to slight variations of pigment conditioning between the single-colorant sample and the colorant mixture coated in the studied cards.

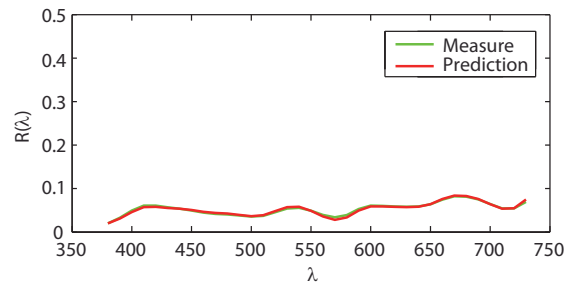


Figure 124. Predicted and measured spectral reflectances of the non-irradiated colorant mixture on polycarbonate card in CLM with fitted optical thickness values deduced from Eq (8.1).

A similar operation was performed with 570 CLM color patches printed on 24 cards using fixed laser setup (wavelengths, focal distance, frequency, min and max powers, gamma correction function, and other spe-

cific parameters). For comparison, it was also performed with 54 D2T2 color patches. For each patch, the set of optical thicknesses $\{\varepsilon_c, \varepsilon_m, \varepsilon_y\}$ was computed according to Eq. (8.1) by considering the corresponding primaries. The computed ΔE_{94} between the predicted spectra and the measured ones are displayed as histograms in Figure 125.

Regarding the D2T2 printing, the average ΔE_{94} value of 0.43 unit is low. This shows that once the spectral parameters $\rho(\lambda)$, $t_c(\lambda)$, $t_m(\lambda)$, and $t_y(\lambda)$ are known, the spectral reflectance of any color patch can be accurately predicted once the correct optical thicknesses values $\{\varepsilon_c, \varepsilon_m, \varepsilon_y\}$ are specified. This is not true in CLM printing for which a high average ΔE_{94} value of 4.2 units was obtained, with a maximum of 7.1 units. Even by fitting the optimal $\{\varepsilon_c, \varepsilon_m, \varepsilon_y\}$ values, the predicted spectral reflectances still deviate significantly from the measured ones, which so far does not enable validation of the model for CLM prints.

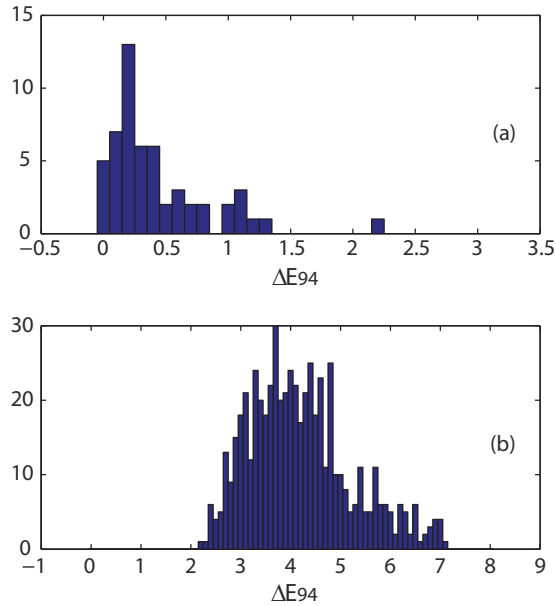


Figure 125. Distributions of the ΔE_{94} values computed between measured and predicted spectral reflectances, given by Berns equation with fitted optical thickness of the three dyes, a) for D2T2 printed cards and b) for CLM printed cards.

By way of illustration, we analyzed the “red”, “green” and “blue” patches shown in the right column of Figure 123, obtained by irradiating the card with, respectively, the red laser alone, the green laser alone, and the blue laser alone, at maximal power. Their measured spectral reflectances are plotted in Figure 126 in green line. With an ideal bleaching process, one colorant would be fully bleached under the laser irradiation, and the two other ones would not be modified. The spectra predicted according to this assumption, plotted in blue line, are very far from the measured ones (green line) especially in the long wavelength domain for the irradiation by the red laser (660 nm), in the middle wavelength domain for the irradiation by the green laser (532 nm) and in the short wavelength domain for the irradiation by the blue laser (440 nm). By fitting the optical thicknesses of the three dyes using Eq. (8.1), the predicted spectra (red lines) are closer to the measured ones but significant deviation is still observed. We must conclude that the spectral reflectance of these patches cannot be expressed in terms of a combination of three primary transmit-

tances $t_c(\lambda)$, $t_m(\lambda)$, $t_y(\lambda)$, probably because the colorant mixture after irradiation does not contain the same absorbing substances as before irradiation. In addition to targeted photobleaching, laser-induced local increases in temperature may result also in thermal decomposition of all the materials present in the substrate. Thus, apart from the initial colored components, the final image includes dull-colored decomposition products of both the initial pigments and the polymer medium. Their contribution is strongly dependent on the particular materials and the bleaching technique. The conclusion is that the model proposed by Berns and based on three primary colorants with varied optical thicknesses applies for D2T2 printing, but not for CLM printing. Therefore, the next questions are whether we can consider for CLM printing more primary colorants, how many are necessary, and how they can be determined.

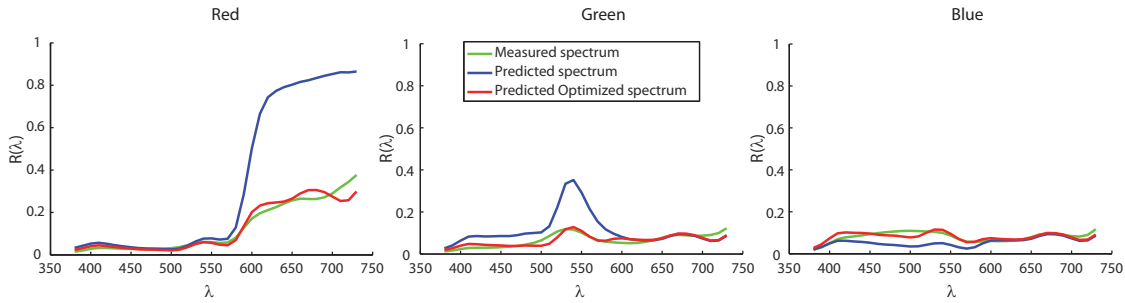


Figure 126. Measured and predicted spectral reflectances of three CLM printed patches. The predicted spectra in blue line assume that one colorant has an optical thickness 0 and the other two colorants have an optical thickness 1. Those in red line were obtained with fitted optical thickness of the three colorants.

8.3 Application of the method on virtual primaries obtained by PCA

The set of spectral reflectances which can be obtained with a given printing technology forms a vector space whose effective dimension depends on the number of colorants or inks, but also on the support and possibly on optical phenomena taking place within the print. One method to determine the dimensionality of such a spectral space is the Principal Component Analysis (PCA) [91-93], applied on a set of measured spectral reflectances of patches.

Consider discrete spectra containing N values. For instance, $N = 36$ for spectra measured between 380 and 730 nm in steps of 10 nm. Every spectrum $S(\lambda)$ can be written as a weighted sum of N base spectra $S_i(\lambda)$, called primaries:

$$S(\lambda) = \sum_{i=1}^N a_i S_i(\lambda), \quad (8.3)$$

where (a_1, a_2, \dots, a_N) represent the coordinates of the spectrum in this basis $\{S_1, S_2, \dots, S_N\}$ which are the projection of the spectrum $S(\lambda)$ onto the basis $S_i(\lambda)$, therefore given by the dot product, denoted $\langle \cdot | \cdot \rangle$, of $S(\lambda)$ and $S_i(\lambda)$:

$$S(\lambda) = \sum_{i=1}^N \langle S(\lambda) | S_i(\lambda) \rangle S_i(\lambda). \quad (8.4)$$

Alternatively to PCA, we can use the Singular Value Decomposition (SVD) [91-94]. Let us consider p spectra and form a matrix \mathbf{P} of size $p \times N$ whose rows are the different spectra. The SVD decomposes \mathbf{P} as:

$$\mathbf{P} = \mathbf{U} \cdot \mathbf{V} \cdot \mathbf{W}^T, \quad (8.5)$$

where \mathbf{U} is a $p \times p$ unitary matrix, \mathbf{V} a $p \times N$ rectangular diagonal matrix with non-negative real diagonal entries (the singular values σ_i in decreasing order), and \mathbf{W} is a $N \times N$ unitary matrix. The primaries $S_i(\lambda)$ correspond to the N columns of matrix \mathbf{W} .

In practice, the set of spectra produced by a printing technology is a subset of the N -dimensional space whose dimension is much lower than the number of wavebands in the spectra. This can be easily observed through the singular values (see Table 4): most of them are close to zero, thus meaning that the corresponding singular vectors (our primaries) can be ignored. Hence, a number $M < N$ of primaries is sufficient to accurately approximate the spectrum, which, therefore, can be written

$$S(\lambda) = \sum_{i=1}^M \langle S(\lambda) | S_i(\lambda) \rangle S_i(\lambda) + e(\lambda), \quad (8.6)$$

where $e(\lambda)$ is a spectral error that we consider sufficiently small to have no impact on the perceived color.

Two versions of the PCA are permitted according to whether we compute it directly from the spectral reflectances of the patches (in this case the spectra incorporate the influence of the diffusing support and the multiple reflections of light within the print) or from the coloring layer's internal transmittances deduced according to Eq. (4.43) from the measured spectral reflectances of the print. Tzeng and Berns [92], following the studies [95] and [96], showed that a PCA performed on the logarithm of internal transmittances of the coloring layers (or, their spectral absorbances, or their optical densities) is more relevant than a PCA performed on measured reflectances of prints, especially when the learning set is small. Furthermore,, through the logarithm of the internal transmittances, we can get a linear equation similar to Eq. (8.6). The PCA dimensionality reduction method is based, therefore, on the logarithm of spectral internal transmittances.

The i th column of matrix \mathbf{W} in Eq. (8.5), denoted $W_i(\lambda)$, corresponds to the logarithm of the transmittance of the i th primary, and we thus have

$$W_i(\lambda) = \log(t_i(\lambda)), \text{ or equivalently, } t_i(\lambda) = \exp(W_i(\lambda)).$$

For any other patch of internal transmittance $t(\lambda)$, we define:

$$\langle \log(t(\lambda)) | W_i(\lambda) \rangle = \varepsilon_i, \text{ and we can write}$$

$$\log[t(\lambda)] = \sum_{i=1}^M \varepsilon_i \log[t_i(\lambda)] + e(\lambda). \quad (8.7)$$

The M primaries with internal transmittances $t_i(\lambda)$ form the new set of “virtual” primaries. The internal transmittance of a dye mixture is written in terms of these primary transmittances as:

$$T(\lambda) = \prod_{i=1}^M \left(t_i^{\varepsilon_i}(\lambda) \right), \quad (8.8)$$

and the spectral reflectance of the patch with this mixture is given by Eq. (4.36). Obviously, only the more significant primaries are to be considered.

According to our experiments carried out with 54 D2T2 printed patches, the first ten singular values in decreasing order, issued from the SVD, are presented in Table 4. We see that the three first ones are much higher than the following ones, which indicates that the dimensionality of spectral space generated by D2T2 printing is 3. This conclusion could also be drawn from the computation of the cumulative percentage variance as it exceeds 99.9 % with three primaries. This is consistent with the fact that three dyes are mixed and that the printing of each ink does not modify the spectral transmittance of the other inks.

The first ten singular values obtained from 130 CLM printed patches are also given in Table 4. The dimensionality of the spectral space generated by CLM is higher than the one generated by D2T2 since the fourth singular value is higher and still significant. Once again, being given the cumulative percentage variance, the whole space (beyond 99.9%) is recovered using, this time, four primaries.

Table 4. Comparison of the dimension of the vector space for D2T2 and CLM printing technologies

i th singular value	1	2	3	4	5	6	7	8	9	10
D2T2 printing (computation on 54 color patches)										
σ_i	23.00	12.10	10.30	0.35	0.33	0.17	0.10	0.09	0.05	0.04
$(\sigma_i - \sigma_{i+1})/\sigma_i$	0.47	0.15	0.97	0.06	0.48	0.41	0.10	0.44	0.20	-
Variance	529	146.41	106.09	0.1225	0.1089	0.0289	0.0100	0.0081	0.0025	0.0016
% Variance	67.67	18.73	13.57	0.02	0.01	0	0	0	0	0
Cumulative % variance	67.666	86.394	99.964	99.98	99.993	99.997	99.998	99.999	100	100
CLM printing (computation on 130 color patches)										
σ_i	49.00	8.10	3.80	2.00	0.61	0.55	0.18	0.15	0.11	0.07
$(\sigma_i - \sigma_{i+1})/\sigma_i$	0.83	0.53	0.47	0.70	0.10	0.67	0.17	0.27	0.36	-
Variance	2401	65.6100	14.4400	4.0000	0.3721	0.3025	0.0324	0.0225	0.0121	0.0049
% Variance	96.59	2.64	0.58	0.16	0.01	0.01	0	0	0	0
Cumulative % variance	96.589	99.228	99.809	99.970	99.985	99.997	99.998	99.999	100	100

The first six virtual primary transmittances, used in Eq. (8.8) corresponding to the exponential of vectors $W_i(\lambda)$ issued from the PCA dimensionality reduction method, are plotted in Figure 127. As often with PCA, the basis vectors have rather a mathematical than physical meaning: here, the transmittances are higher than 1. We tested the spectrum reconstruction accuracy with 2 to 10 primaries issued from Eqs. (4.36) and Eq. (8.8) for the 570 printed colors in CLM, and plotted the average ΔE_{94} value as a function of the number of primaries (Figure 128). In order to study the influence of the number of spectra used to compute the SVD on the reconstruction accuracy, we computed it from either 294, 130, 98, 62, or 12 patches. In either case, the reconstruction based on 3 primary spectra is poor (average of 3.3 units), as already noticed in Figure 125, but it significantly drops from 4 primary spectra, which confirms that CLM generates a 4-dimensional space. It is interesting to notice that beyond 62 patches, the reconstruction accuracy remains unchanged. By refining the approximation with 6 primaries, the average value for ΔE_{94} over the 570 patches is de-

creased to 0.10 unit and its maximum to 0.39 unit. This is sufficient to ensure good reconstruction of spectral reflectances of CLM printed colors.

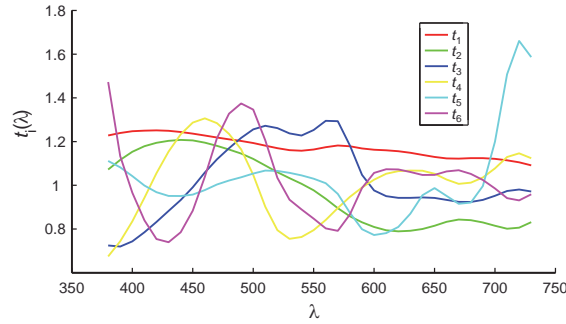


Figure 127. Virtual primary transmittances corresponding to the exponential of the first six basis vectors issued from the PCA.

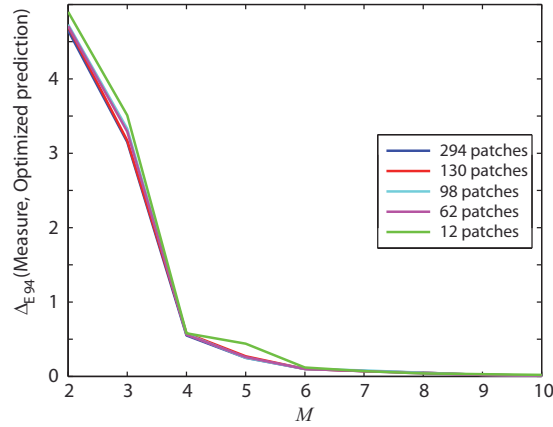


Figure 128. Spectral reconstruction accuracy of CLM prints, tested over 570 printed colors, as a function of the number M of primary spectra obtained by SVD computed from various numbers of color patches.

8.4 From RGB color to spectral reflectance

With the “virtual” primaries obtained from the SVD in the previous section, we pursue the calibration of the model by associating their respective optical thicknesses in the printed card for every RGB color of the digital layout used as command for the lasers.

Let us denote as M the number of ‘virtual’ primaries. A third order polynomial regression is used, according to a simplified method presented in Ref. [97], in order to find a transformation \mathbf{P} , containing the polynomial regression coefficients, that maps the input R, G, B values to the M optical thicknesses of primaries. At the third order, the matrix \mathbf{P} representing the calibration of the predictive model is a $20 \times M$ matrix:

$$\mathbf{P} = \begin{bmatrix} p_1^{\varepsilon_1} & p_1^{\varepsilon_2} & \dots & p_1^{\varepsilon_M} \\ p_2^{\varepsilon_1} & p_2^{\varepsilon_2} & \dots & p_2^{\varepsilon_M} \\ \dots & \dots & \dots & \dots \\ p_{20}^{\varepsilon_1} & p_{20}^{\varepsilon_2} & \dots & p_{20}^{\varepsilon_M} \end{bmatrix}. \quad (8.9)$$

For a given color patch j originally defined by its RGB values (r_j, g_j, b_j) , converted in CMY values according to Eq (8.2) $(C_j, M_j, Y_j) = (1 - r_j, 1 - g_j, 1 - b_j)$, we define the following 20-dimensional vector

$$\mathbf{d}_j = (1, C_j, M_j, Y_j, C_j^2, C_j M_j, C_j Y_j, M_j^2, Y_j^2, M_j Y_j, C_j^2 M_j, C_j^2 Y_j, C_j^3, C_j M_j^2, C_j Y_j^2, C_j M_j Y_j, M_j^2 Y_j, M_j Y_j^2, M_j^3, Y_j^3) \quad (8.10)$$

and then obtain the set of optical thicknesses $\boldsymbol{\varepsilon}_j^{cal} = (\varepsilon_{1,j}^{cal}, \varepsilon_{2,j}^{cal}, \dots, \varepsilon_{M,j}^{cal})$ (representing the M calibrated input parameters to predict patch j) from the following matrix product:

$$\boldsymbol{\varepsilon}_j^{cal} = \mathbf{d}_j \cdot \mathbf{P}. \quad (8.11)$$

The $20 \times M$ entries of the matrix \mathbf{P} are obtained from a learning set of N printed color patches, by solving the following matrix equation in the least-mean square sense by using for example the operator \ or the `mldivide` function with Matlab:

$$\begin{bmatrix} \boldsymbol{\varepsilon}_1^{projected} \\ \boldsymbol{\varepsilon}_2^{projected} \\ \dots \\ \boldsymbol{\varepsilon}_N^{projected} \end{bmatrix} \equiv \begin{bmatrix} \mathbf{d}_1 \\ \mathbf{d}_2 \\ \dots \\ \mathbf{d}_N \end{bmatrix} \cdot \mathbf{P}, \quad (8.12)$$

where each row of the matrices bordering the \equiv symbol is a line vector attached to one of the N color patches of the calibration set. For a calibration patch i , the optical thicknesses vectors $(\boldsymbol{\varepsilon}_{1,i}^{projected}, \boldsymbol{\varepsilon}_{2,i}^{projected}, \dots, \boldsymbol{\varepsilon}_{M,i}^{projected})_{i=1..N}$ are obtained according to the method presented in the previous section, with Eq. (8.7) by ignoring $e(\lambda)$, for a set of N patches ($N \geq 20$). The vectors \mathbf{d}_i ($i = 1..N$) are given by Eq. (8.10).

The capacity of the third-order regression represented by \mathbf{P} to provide accurate optical thickness values for every input RGB values depends on the smoothness of relationship between these input and output values. When small variations of the RGB values induce strong variations of the optical thickness values, the accuracy of the method might be poor. However, it is possible to split the RGB space into several subspaces in which the variations of optical thicknesses are more reasonable, and to define a matrix \mathbf{P} in each subspace. A similar idea was proposed by Zhang, not for the computation of a transformation matrix but for the computation of the PCA [98]. In our experiments with CLM, we observed that the RGB-to-optical-thicknesses (RGB-to-E) transform is very different according to the power of the blue laser (denoted as b). We therefore splitted the RGB space into two subspaces: a first one corresponding to the low power range of the blue laser ($b \in [0, 85]$ on 8 bits in our experiments), and a second one to the high power range of

this laser ($b \in \llbracket 86, 255 \rrbracket$ on 8 bits). The influence of blue laser power on color gradients is illustrated in Figure 129 by a representation of the corresponding colors in the CIELAB (a^*, b^*) -plane: with low blue laser power, more saturated but darker colors are obtained, whereas with high blue laser power, higher luminance is achieved, but chroma is lower and strong color drifts are observed. It would be possible to split the RGB space into more than two subspaces, but more patches would be needed to calibrate the model in each subspace. The two subspaces described above seemed optimal in our application.

Two learning sets were selected in these two RGB subspaces, and we obtained two transformation matrices \mathbf{P}_1 and \mathbf{P}_2 . For each transformation, $N = 65$ appeared a good tradeoff between the number of patches to print, and the performances. Actually, these two sets of 65 patches are those constituting the set of 130 patches used to compute the SVD in the previous section. The same basis vectors issued from these 130 patches are used for the two sub-spaces.

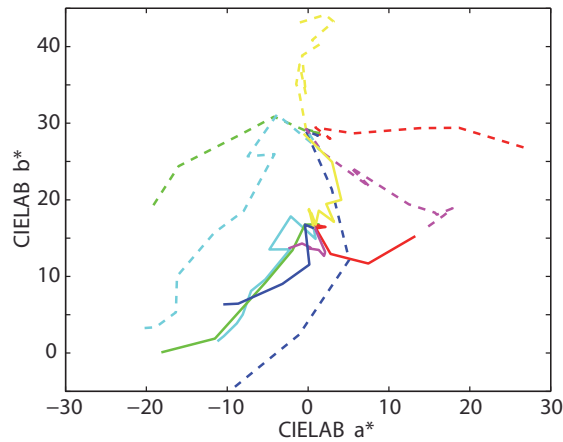


Figure 129. Red, Green, Blue, Yellow, Magenta, and Cyan color gradients obtained with low (dashed line) and high (solid line) blue laser power.

It seems important to discuss the selection of the patches to print for the calibration of the model for the important impact it may have on the final prediction accuracy. It is possible to select them manually by following the intuitive idea that good learning is achieved when they are well distributed over the RGB subspace, a usual approach in traditional CMYK printing [92] or in applications where odd chips patches in Munsell Atlas are used for learning [98]. However, due to strong non-linearity of the color variations as the laser powers increase (see Figure 129), it looks better to make the selection in the output CIELAB color space. Indeed, in the brightest part of the gamut, slight power variations of lasers can induce strong color variations, certainly reproducible, but difficult to render correctly with a polynomial regression. We represented in the CIELAB (a^*, b^*) plane all the colors that we printed. First, we arbitrarily subtracted a subset of them which will be used for testing. Among the remaining patches, we manually selected the set of patches for learning by including those with highest saturation, and those located in the border of the gamut volume, especially the patches contained in the red, green, and blue gradient wedges. Alternatively, we can randomly select the learning patches with an automated routine. By way of illustration, Figure 130 gives an overview of the printed colors obtained in the subset corresponding to the low blue laser power. We applied several times the automated selection routine in order to verify that the similar prediction accuracy is achieved at every run of the routine. Indeed, the average CIELAB ΔE_{94} value computed 40 times between the predicted colors of the testing set and the measured ones was 1.27 unit with a standard de-

viation of only $9.39 \cdot 10^{-2}$ unit. Note that the color gamut is not centered on the grey level axis, i.e. the point $(0,0)$ in the (a^*, b^*) plane. We might expect that further development of the technology could achieve a more centered gamut.

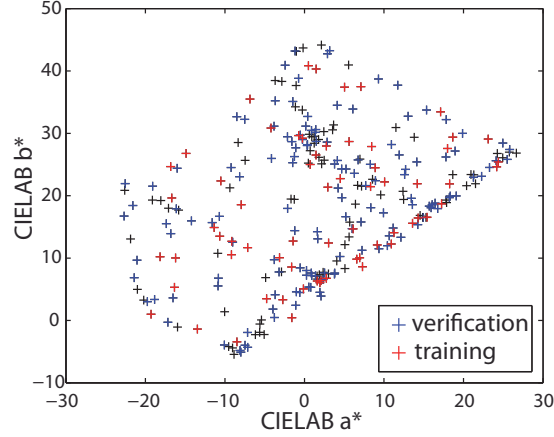


Figure 130. Printed patches colors represented in the CIELAB (a^*, b^*) plane, among which those used for the learning of the RGB to optical thicknesses transform, and for the verification of the model.

8.5 Performances & accuracy testing

A verification set containing 276 CLM-printed patches, different from the ones used for learning, was selected (this time corresponding to colors in the whole RGB space) in order to evaluate the global performance of the calibration, including the determination by SVD of the 6 more relevant primaries and the computation of their respective optimal thicknesses by using the transformation matrix \mathbf{P}_1 , or accordingly \mathbf{P}_2 with overall 130 learning patches selected by our automatic routine. The histogram of the CIELAB ΔE_{94} values computed between the measured and predicted spectra is displayed in Figure 131. We obtained an average ΔE_{94} value of 1.18 unit, and a maximum of 3.13 units, which is a fairly good accuracy for this strongly non-linear color printing system. The difference between this score of 1.18 unit and the one of 0.10 unit mentioned in Section 8.3 corresponds to the imprecision of the matrix transformations \mathbf{P}_1 and \mathbf{P}_2 relating the RGB input laser intensities with the optical thicknesses of the virtual primaries. In comparison to the model based on Berns equation presented in Section 8.2, the gain in prediction accuracy, which clearly appears by comparing the histograms of Figure 125 (b) and Figure 131, is remarkable.

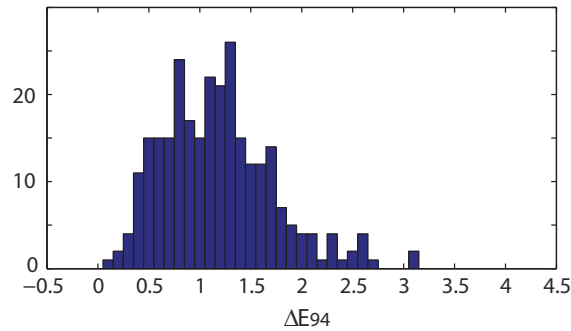


Figure 131. Histogram representing the distribution of ΔE_{94} values computed from the measured reflectance of the 276 CLM verification patches and the reflectance predicted by our method.

The variations of the prediction accuracy (i.e., the average CIELAB ΔE_{94} value over the testing patch set) according to the number of primaries selected after the PCA and the number of learning patches used for the calibration of the model were assessed. The curves plotted in Figure 132 indicate that at least 4 primaries are necessary, but more than 4 primaries do not improve much the prediction. This is true whatever is the number of learning patches. This is probably due to the fact that the RGB-to-E transform, which maps the 3-dimensional RGB space onto the M -dimensional optical thicknesses space, is more imprecise when M increases, thus compensating the gain in prediction accuracy observed in Section 8.4 with up to 6 primaries.

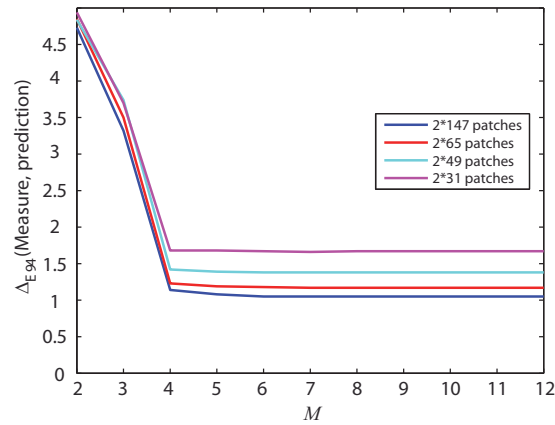


Figure 132. Performances of the prediction according to the number of learning patches and the number of considered primaries.

Regarding the number of learning patches, increasing them improves the global accuracy but to a rather small extent: using 394 patches (197 in each RGB subspace) instead of 130 decreases the average ΔE_{94} value by only 0.15 unit. Using 62 patches (31 in each RGB subspace) increases it by 0.5 unit, which is a significant loss of accuracy, but still acceptable if the number of calibration patches needs to be limited. 130 patches is rather reasonable compared to the 44 color patches required for the calibration of classic predictive models for traditional ink-based printer, such as the Clapper-Yule or the Yule-Nielsen modified Spectral Neugebauer models, which are easier to calibrate [43]. The prediction accuracy is also satisfactory in comparison with traditional printing. This is noticeable as the CLM printing system that we used (including the ink coating system and the laser marking) is a prototype in development (which has not reached yet the optimal reliability and reproducibility of an industrial system).

8.6 Conclusion

The CLM printing system illustrates the issue of using a spectral reflectance prediction method developed for an ink-transfer printing system with surfaces printed with a laser-induced coloration technique, even when the optical equation underlying the prediction model seems adapted to these surfaces. In contrast with ink-transfer printing where the spectral properties and amounts of transferred inks can be easily deduced from a few specific printed patches, the spectral properties and amounts of coloring components are different for each combination of power settings of the three lasers and do not seem to follow simple laws. Hence, existing spectral reflectance prediction methods need several adaptations. Firstly, in contrast with halftone printing, the CLM can produce a variety of colors in each printable pixel and is therefore continuous tone printing system. The amounts of primary colorants in the coloring layer are thus ex-

pressed in terms of optical thicknesses instead of ink surface coverages. Secondly, the modification of the colorants under laser irradiation, depending on the laser power, implies that the spectral transmittances of primary colorants contained in a given printed color patch are not precisely known, whereas in traditional printing, the inks' internal transmittances (each one being possibly raised to a power ϵ) are independent of the amount of other deposited inks. Thirdly, in contrast with halftoning where the amount of each ink can be easily related to the CMYK channels of the digital layout (even in case of ink spreading or mechanical dot gain), this relation is more difficult to establish in CLM printing.

These conceptual differences led us to develop a new spectral reflectance prediction model combining an optical modelization and learning methods: Berns equation developed for continuous tone prints (D2T2) was used with spectral transmittances of "virtual" primary colorants obtained by performing a principal component analysis on a set of spectral reflectances measured on printed patches. The correspondence between the input digital RGB colors and the optical thicknesses of these primaries is obtained by computing a transformation matrix from the same set of measured spectral reflectances. Despite the strong non-linearity of the relationship between the input and output color values, a rather good prediction accuracy was achieved with 130 printed patches for the calibration of the model. This number of patches is rather acceptable in comparison with the 44 calibration patches required by the most performing spectral reflectance prediction models available today for classic printing systems [43].

Chapter 9 CLM-Print simulator

On an industrial point of view, these optical prediction models presented in the previous chapter are not directly usable. Companies are not specialist into the use of such a work bathed in an exploratory environment such as Matlab that we commonly use for quick developments and results. For the Color Laser Marking technology development purpose, by Gemalto S.A., a tool that would enable the user to simulate, roughly what would be the impact in terms of color of a change of some parameters regarding the ink mixture, the bleaching process, and some physical aspect of the card polycarbonate would be a great asset. In contrary to the model presented in the previous chapter intended to be accurate, and dedicated to one laser, ink, and card structure set-up, a new tool, more flexible, close to a physic-realist model, is targeted. For all these reasons, we propose to develop CLMviewer, a software that everybody can use to simulate and preview some CLM printed images, a simple tool that could help to the color optimization demarche of the CLM technology. The main goal here is not to focus on the accuracy of the prediction, but to give the user of the software an overview, a trend, of the color modifications that the printing system causes, and an idea of the maximum of reachable gamut.

9.1 Introduction and objectives

This development, oriented company, presents specific choices will to better fit the expectances. We choose to develop the software in C/C++ in order to take advantage of the robustness and the efficiency of the execution time. A particular attention was brought to the graphical interface, to increase the simplicity of use. All data were stored in an easily editable file, which enables the more advanced users to tune their parameters. We focussed on maximal compatibility, and the development was carried out on a multi-platform environment. Moreover, we look for a free licence to manage this task. For all those reasons, we selected the Qt framework.



Figure 133. The Qt framework logo.

Qt enables the creation of GUI (Graphical User Interface) which consists in the part of the program that is in relation with the user. It enables to interacting by the mean of a graphical display. The user can take benefit of widgets. A widget is a basic element of a graphical interface with which the user interacts.

The principal question is how to create a graphical interface. The answer is either to use a library dedicated to the considered Operating System, or the use of a multi-platform library.

Such classical library are, MFC based on Win32 API, for Windows; Cocoa (in Objective-C), for Mac OS X; and X and XLib, for Linux.

Qt is multi-platform, see Figure 134. Qt can adapt itself to Linux, Windows, or Mac OS.:



Figure 134. Qt can adapt itself to Linux, Windows, or Mac OS.

It has been developed in C++, and can be used in C++, or also in Java, Python, or in C#.

The advantages of Qt are:

- A clear documentation. The official documentation can be found here [99].
- A complete framework.
- The multi-plateform aspect.

Qt has been developed since 1991, by the Finish company Trolltech, then acquired by Nokia in 2008.

The Qt licensing is LGPL, which enables us to use it freely, for commercial or private use, as soon as the program is built in dynamic mode.

The main goal of the simulator is to give the possibility to preview a CLM print, being given parameters concerning the ink composition, the bleaching process, and other physical aspects. It is a simplification of the complex physical and chemical phenomena occurring during printing explained in Chapter 8. In contrast with the study in the previous chapter, where a predictive model was proposed for a special set of laser, card structure, ink composition conditions, we now propose a model, more opened, taking into account changes of different settings, and giving a trend of the color regarding the selected parameters. It is not the purpose to look for accuracy in prediction here as we simplify all those complex phenomenons to present an ideal aspect of color. By “ideal aspect of color” we understand an “ideal” bleaching, with linear decoloration (in the sens of the optical thickness), and this, regardless the CMYart ink (the CLM ink mixture) layer density. Also, no parasit interact of one laser to other pigments than the one expected to bleach. And no chemical reaction due to laser exposure leading to the creation of new colored elements is considered.

9.2 Development of CLMviewer

We use the model presented in Chapter 4, summarized by Eq. (4.39). The initial optical thickness values of the unbleached CLM patch are computed using similar method using Eq. (8.1) on a patch similar to the one shown in Figure 122. In the following, one hundred percent of a pigment will correspond to the value of optical thickness obtained by measurement of a raw CMYart patch.

On the industrial machine, another laser is dedicated to reinforce the contrast in the image by blacking a transparent layer located under the CMYart ink. This laser enables the printing of a black layer. With similar approach than the one described in Section 4.4, and in particular by Eq. (4.43), we compute a transparency t_k for the black layer, and consider this black layer as a fourth ink. A new parameter, ε_k will enable to adjust the “quantity” of black added, varying from 0 (black layer completely transparent), to 1.0 (black layer completely burned).

$$R(\lambda, \varepsilon_c, \varepsilon_m, \varepsilon_y, \varepsilon_k) = r_s + \frac{T_{in} T_{out} \rho(\lambda) t_c^{2\varepsilon_c}(\lambda) t_m^{2\varepsilon_m}(\lambda) t_y^{2\varepsilon_y}(\lambda) t_k^{2\varepsilon_k}(\lambda)}{1 - r_i \rho(\lambda) t_c^{2\varepsilon_c}(\lambda) t_m^{2\varepsilon_m}(\lambda) t_y^{2\varepsilon_y}(\lambda) t_k^{2\varepsilon_k}(\lambda)}. \quad (9.1)$$

9.3 First start in CLMviewer

The application starts by running the CLMviewer.exe file. By selecting “File/Open...” the user can import an image (prefer .BMP images). The menu “View” enables the user to fit the image to screen or to zoom in, or out. Then, the menu “Image/Process image...” launch the screen shown in Figure 135.

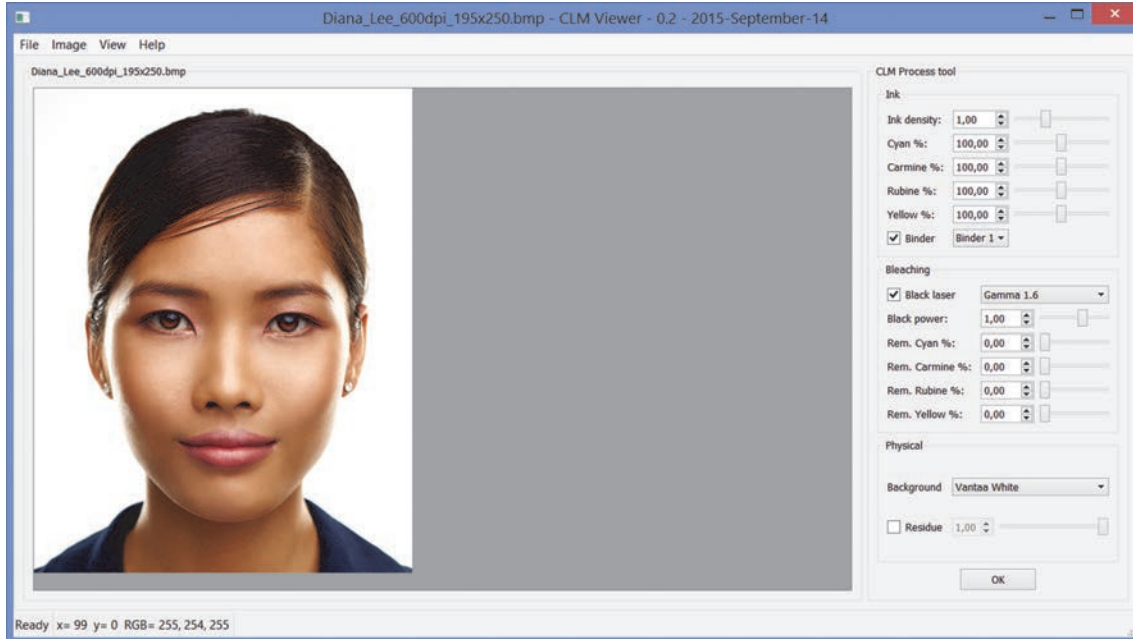


Figure 135. Graphical user interface of CLMviewer.

The Process tool is decomposed into three parts:

- The first one deals with the ink: The user can tune the ink density (relatively to the value 1.0 corresponding to the ink quantity presents in the first “Vantaa 1” deposition (denser than the current one, closer to 0.7). The proportion of each pigment can be modified according to the relative proportions measured in the “Vantaa 1” classic CYMart. The user can simulate the influence of the binder by selecting either of two possible binders, or no binder at all.
- The bleaching part is first dedicated to the settings of the added black layer, which can be simulated or not. The power of laser making black with can be tuned between 0 and 1, this latter value corresponding to usual laser power used to mark a full density of black. Finally, a simulation of remaining ink for each of the four pigments has been added to simulate an incomplete bleaching, closer to the reality.
- A part dedicated to physical attributes. The polycarbonate background may be selected among “Vantaa white” a little yellowish, and the “Standard white”, a little bluish. The simulation of residue, which adds a kind of fifth ink layer, corresponds to the residual color that appears in the area where the blue laser has strongly irradiated the ink. This point is supposed to be improved by taking into account light scattering in the coloring layer that is clearly visible for such configurations.

The user is invited to click on “OK” to run the maths. CLMviewer enjoys a multi-threading development that enables the user to continue to interact with the graphical interface during the computation of the simulation without any freezes of the application.

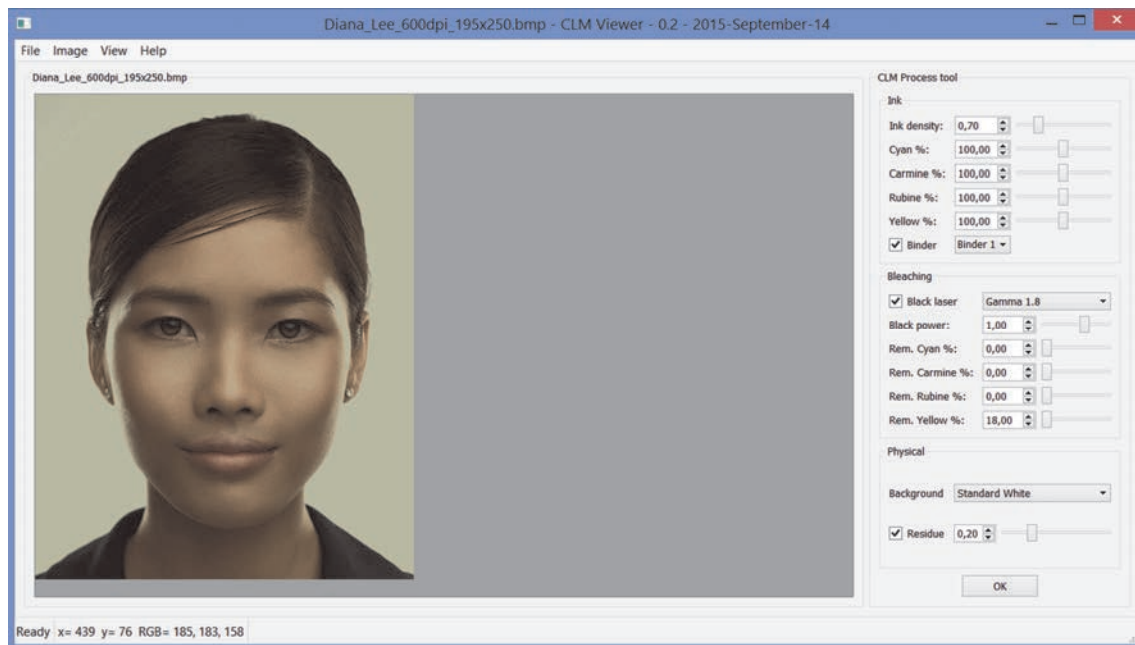


Figure 136. Simulation of a CLM printing with CLMviewer.

The image resulting can be printed (“File/Print...”), or saved (“File/save as...”).

On the image display, on the left of the screen, the user can “read” the RGB color values by moving the mouse cursor. A mouse click freezes this color values display of the location of the mouse

A text file containing all the measured spectral data is read by the software for computation of the simulation. This enables the user to modify the spectra, to consider for example new pigments for the ink, or new binder, or also new polycarbonate substrate.

Notice that the visualization always depends on the calibration of the screen.

CLMviewer has been developed with Qt framework with dynamic linking, under LGPL free license. Please report to the Qt documentation available online [99].

9.4 Conclusion

The Qt framework enabled the quick development of software, usable by professionals. It enjoys a graphical user interface, easy to create, for the benefit of the user. The approach is different from the one introduced in the previous chapter. We start again from Berns’ equation, but considered this time an ideal bleaching process, without any side effects in the color prediction encountered in Section 8.2 with CLM technology. In this sense, our target is the definition of the maximal color range, possible with the printing technology. The model remains however physically founded. We are free to tune some parameters, to preview the influence of physical modifications of the CLM set up. We added the possibility to play with the global CMYart ink density, or the proportion of each pigment in the mixture. We also have the possibility to see the influence of the binder, or the one of the white background card. An extension of the functionalities then brings the user the possibility to simulate a partial bleaching process by simulating a certain quantity of pigments remaining after a full bleaching at maximal laser power. To get closer to the visual aspect of a printed sample, we finally added some residues in areas where the blue laser has the most influence, as we noted during our experiments that the blue laser has strong impact when used at a high power, and probably responsible for the creation of new substances which pollute the expected white color. This residual coloration is added as a new pigment layer. This is a simple way to simulate what really happens, making the assumption that these materials still are purely absorbing, not scattering. In reality, we intuit that this is not the case. An extension of the model based for example on the Kubelka-Munk theory should take into account scattering in the ink layer, and more precisely, changes in scattering depending on the power of the lasers.

General Conclusion

With the initial objective to work on the quality assessment of a print, in order to measure printing quality, we came to study alternatively the digital point of view of image through indices extracted by low-level image processing algorithms, also to study the physical aspect of image through the use of color prediction models to simulate the physical interaction of light with printing materials, and finally, to study the mental image, through the conduct of psycho-visual experiments with human judgment. The main difficulties met in this work concern the relationship between these different conceptions of image. For example, an accurate measuring method available to digitalize printed samples, and a clear relationship between mental construction of quality of a print and objective quality assessment are not so trivial. The veritable challenge was to associate accurately concepts attached to these different worlds, for example matching the digital color and physical color concepts, while standard color management methods failed with the new Color Laser Marking technology developed by Gemalto S.A.

The relationship between digital and physical conceptions of what an image is has been quite widely covered, with, in the one hand, the development of various objective indices addressing tone homogeneity, edge sharpness, and colorfulness. On the other hand, the physical concept of image has been largely discussed through the color prediction models application on particularly the new color laser marking technology developed by Gemalto S.A. The relationship between these two concepts was in the heart of these thesis, with the printing process symbolized by the passage from numerical to physical images, and the scanning process, for which a color correction have also be proposed, symbolized by the passage from physical to numerical images.

The relationship between physical images and their mental representations has been studied also, for separate criteria of quality. When combining those criteria, the resulting perception of any of them is modified: the goal to reach a unique final score of quality is not trivial. The achievement of a global score incorporating and mixing all attributes would demand to gather advanced skills in sensory metrology. However, to go ahead, basic psycho-visual experiments were made for the individual attributes, by following the methodologies proposed by the state of the art.

This work can be continued and improved according the following axes.

Regarding the tone homogeneity index, an interesting area of improvement could be a reflection on how to automate such a measure on a natural image, from a research on nearly homogeneous areas in the digital image, and the assessment of the index in the same area in the printed image.

Regarding the color correction of the scanner, the average CIELAB DeltaE94 color difference that we computed between the ground truth colors measured with a spectrophotometer and the ones we measured with the computed scanner over a color chart containing 264 colors was rather good but we are sometimes disappointed regarding the visual correction of some colors, especially for white and black. These “special” colors are sometimes not very well corrected, although they are important for an ID photo because very

present in the image. We should propose and test to reinforce the weight of those colors by representing them several times in the polynomial regression.

Concerning the color prediction models, we apply a model dedicated to a non-scattering ink layer on top of a white diffusing background, which is valid before CLM ink bleaching, but becomes too narrow when laser (especially the blue one) starts to mark. It results in the creation of new particles larger than the original pigment size, and this results in an important diffusion inside the ink layer. We should therefore use another equation that takes into account this diffusion. Kubelka and Munk model should be tested if we can measure or estimate the part of light that is diffused within the coloring layer, independently of the one that is diffused by the background.

At the end, a large sensorial experiment could be carried out with many printed samples where homogeneity, sharpness and colorfulness have respectively different visual qualities. The quality scores issued from the observers' perception could be analysed thanks to learning methods in order to find the most appropriate way to combine in a global score the individual quality scores computed according to our methods. Convolutional neural networks [100] would deserve to be tested. Spatial pooling presented by Gong and Pedersen [5] may be helpful too, as they explain that the human perception being complex, weighing differently each local quality score is often more realistic than a simple average of the quality values.

Appendix

Annex A:

Table 5. CIE RGB Color matching functions using the 1931 CIE Standard Observer.

λ_i (nm)	\bar{r}_λ	\bar{g}_λ	\bar{b}_λ
380	0.00003	-0.00001	0.00117
385	0.00005	-0.00002	0.00189
390	0.00010	-0.00004	0.00359
395	0.00017	-0.00007	0.00647
400	0.00030	-0.00014	0.01214
405	0.00047	-0.00022	0.01969
410	0.00084	-0.00041	0.03707
415	0.00139	-0.00070	0.06637
420	0.00211	-0.00110	0.11541
425	0.00266	-0.00143	0.18575
430	0.00218	-0.00119	0.24769
435	0.00036	-0.00021	0.29012
440	-0.00261	0.00149	0.31228
445	-0.00673	0.00379	0.31860
450	-0.01213	0.00678	0.31670
455	-0.01874	0.01046	0.31166
460	-0.02608	0.01485	0.29821
465	-0.03324	0.01977	0.27295
470	-0.03933	0.02538	0.22991
475	-0.04471	0.03183	0.18592
480	-0.04939	0.03914	0.14494
485	-0.05364	0.04713	0.10968
490	-0.05814	0.05689	0.08257
495	-0.06414	0.06948	0.06246
500	-0.07137	0.08536	0.04776
505	-0.08120	0.10593	0.03688
510	-0.08901	0.12860	0.02698
515	-0.09356	0.15262	0.01842
520	-0.09264	0.17468	0.01221
525	-0.08473	0.19113	0.00830
530	-0.07101	0.20317	0.00549
535	-0.05316	0.21083	0.00320
540	-0.03152	0.21466	0.00146
545	-0.00613	0.21487	0.00023
550	0.02279	0.21178	-0.00058
555	0.05514	0.20588	-0.00105
560	0.09060	0.19702	-0.00130
565	0.12840	0.18522	-0.00138

570	0.16768	0.17087	-0.00135
575	0.20715	0.15429	-0.00123
580	0.24562	0.13610	-0.00108
585	0.27989	0.11686	-0.00093
590	0.30928	0.09754	-0.00079
595	0.33184	0.07909	-0.00063
600	0.34429	0.06246	-0.00049
605	0.34756	0.04776	-0.00038
610	0.33971	0.03557	-0.00030
615	0.32265	0.02583	-0.00022
620	0.29708	0.01828	-0.00015
625	0.26348	0.01253	-0.00011
630	0.22677	0.00833	-0.00008
635	0.19233	0.00537	-0.00005
640	0.15968	0.00334	-0.00003
645	0.12905	0.00199	-0.00002
650	0.10167	0.00116	-0.00001
655	0.07857	0.00066	-0.00001
660	0.05932	0.00037	0.00000
665	0.04366	0.00021	0.00000
670	0.03149	0.00011	0.00000
675	0.02294	0.00006	0.00000
680	0.01687	0.00003	0.00000
685	0.01187	0.00001	0.00000
690	0.00819	0.00000	0.00000
695	0.00572	0.00000	0.00000
700	0.00410	0.00000	0.00000
705	0.00291	0.00000	0.00000
710	0.00210	0.00000	0.00000
715	0.00148	0.00000	0.00000
720	0.00105	0.00000	0.00000
725	0.00074	0.00000	0.00000
730	0.00052	0.00000	0.00000
735	0.00036	0.00000	0.00000
740	0.00025	0.00000	0.00000
745	0.00017	0.00000	0.00000
750	0.00012	0.00000	0.00000
755	0.00008	0.00000	0.00000
760	0.00006	0.00000	0.00000
765	0.00004	0.00000	0.00000
770	0.00003	0.00000	0.00000
775	0.00001	0.00000	0.00000
780	0.00000	0.00000	0.00000

Annex B:

Table 6. CIE XYZ Color matching functions using the 2° 1931 CIE Standard Observer, and Spectral Power Distributions of the common D50, D65, A Illuminants.

λ_i (nm)	$\bar{x}(\lambda_i)$	$\bar{y}(\lambda_i)$	$\bar{z}(\lambda_i)$	$I_{D50}(\lambda_i)$	$I_{D65}(\lambda_i)$	$I_A(\lambda_i)$
380	0.001368	0.000039	0.006450	24.4875	49.97550	9.795100
385	0.002236	0.000064	0.010550	27.1791	52.31180	10.899600
390	0.004243	0.000120	0.020050	29.8706	54.64820	12.085300
395	0.007650	0.000217	0.036210	39.5894	68.70150	13.354300
400	0.014310	0.000396	0.067850	49.3081	82.75490	14.708000
405	0.023190	0.000640	0.110200	52.9104	87.12040	16.148000
410	0.043510	0.001210	0.207400	56.5128	91.48600	17.675300
415	0.077630	0.002180	0.371300	58.2733	92.45890	19.290700
420	0.134380	0.004000	0.645600	60.0338	93.43180	20.995000
425	0.214770	0.007300	1.039050	58.9257	90.05700	22.788300
430	0.283900	0.011600	1.385600	57.8175	86.68230	24.670900
435	0.328500	0.016840	1.622960	66.3212	95.77360	26.642500
440	0.348280	0.023000	1.747060	74.8249	104.86500	28.702700
445	0.348060	0.029800	1.782600	81.0360	110.93600	30.850800
450	0.336200	0.038000	1.772110	87.2472	117.00800	33.085900
455	0.318700	0.048000	1.744100	88.9297	117.41000	35.406800
460	0.290800	0.060000	1.669200	90.6122	117.81200	37.812100
465	0.251100	0.073900	1.528100	90.9902	116.33600	40.300200
470	0.195360	0.090980	1.287640	91.3681	114.86100	42.869300
475	0.142100	0.112600	1.041900	93.2383	115.39200	45.517400
480	0.095640	0.139020	0.812950	95.1085	115.92300	48.242300
485	0.057950	0.169300	0.616200	93.5356	112.36700	51.041800
490	0.032010	0.208020	0.465180	91.9627	108.81100	53.913200
495	0.014700	0.258600	0.353300	93.8432	109.08200	56.853900
500	0.004900	0.323000	0.272000	95.7237	109.35400	59.861100
505	0.002400	0.407300	0.212300	96.1685	108.57800	62.932000
510	0.009300	0.503000	0.158200	96.6133	107.80200	66.063500
515	0.029100	0.608200	0.111700	96.8711	106.29600	69.252500
520	0.063270	0.710000	0.078250	97.1290	104.79000	72.495900
525	0.109600	0.793200	0.057250	99.6141	106.23900	75.790300
530	0.165500	0.862000	0.042160	102.0991	107.68900	79.132600
535	0.225750	0.914850	0.029840	101.4269	106.04700	82.519300
540	0.290400	0.954000	0.020300	100.7547	104.40500	85.947000
545	0.359700	0.980300	0.013400	101.5359	104.22500	89.412400
550	0.433450	0.994950	0.008750	102.3170	104.04600	92.912000
555	0.512050	1.000000	0.005750	101.1585	102.02300	96.442300
560	0.594500	0.995000	0.003900	100.0000	100.00000	100.000000
565	0.678400	0.978600	0.002750	98.8675	98.16710	103.582000
570	0.762100	0.952000	0.002100	97.7350	96.33420	107.184000
575	0.842500	0.915400	0.001800	98.3265	96.06110	110.803000
580	0.916300	0.870000	0.001650	98.9180	95.78800	114.436000
585	0.978600	0.816300	0.001400	96.2084	92.23680	118.080000
590	1.026300	0.757000	0.001100	93.4988	88.68560	121.731000
595	1.056700	0.694900	0.001000	95.5933	89.34590	125.386000

600	1.062200	0.631000	0.000800	97.6878	90.00620	129.043000
605	1.045600	0.566800	0.000600	98.4784	89.80260	132.697000
610	1.002600	0.503000	0.000340	99.2691	89.59910	136.346000
615	0.938400	0.441200	0.000240	99.1553	88.64890	139.988000
620	0.854450	0.381000	0.000190	99.0415	87.69870	143.618000
625	0.751400	0.321000	0.000100	97.3817	85.49360	147.235000
630	0.642400	0.265000	0.000050	95.7218	83.28860	150.836000
635	0.541900	0.217000	0.000030	97.2895	83.49390	154.418000
640	0.447900	0.175000	0.000020	98.8572	83.69920	157.979000
645	0.360800	0.138200	0.000010	97.2622	81.86300	161.516000
650	0.283500	0.107000	0.000000	95.6672	80.02680	165.028000
655	0.218700	0.081600	0.000000	96.9285	80.12070	168.510000
660	0.164900	0.061000	0.000000	98.1898	80.21460	171.963000
665	0.121200	0.044580	0.000000	100.5966	81.24620	175.383000
670	0.087400	0.032000	0.000000	103.0034	82.27780	178.769000
675	0.063600	0.023200	0.000000	101.0682	80.28100	182.118000
680	0.046770	0.017000	0.000000	99.1330	78.28420	185.429000
685	0.032900	0.011920	0.000000	93.2570	74.00270	188.701000
690	0.022700	0.008210	0.000000	87.3809	69.72130	191.931000
695	0.015840	0.005723	0.000000	89.4922	70.66520	195.118000
700	0.011359	0.004102	0.000000	91.6035	71.60910	198.261000
705	0.008111	0.002929	0.000000	92.2460	72.97900	201.359000
710	0.005790	0.002091	0.000000	92.8886	74.34900	204.409000
715	0.004109	0.001484	0.000000	84.8715	67.97650	207.411000
720	0.002899	0.001047	0.000000	76.8544	61.60400	210.365000
725	0.002049	0.000740	0.000000	81.6828	65.74480	213.268000
730	0.001440	0.000520	0.000000	86.5112	69.88560	216.120000
735	0.001000	0.000361	0.000000	89.5455	72.48630	218.920000
740	0.000690	0.000249	0.000000	92.5798	75.08700	221.667000
745	0.000476	0.000172	0.000000	85.4048	69.33980	224.361000
750	0.000332	0.000120	0.000000	78.2299	63.59270	227.000000
755	0.000235	0.000085	0.000000	67.9609	55.00540	229.585000
760	0.000166	0.000060	0.000000	57.6918	46.41820	232.115000
765	0.000117	0.000042	0.000000	70.3074	56.61180	234.589000
770	0.000083	0.000030	0.000000	82.9230	66.80540	237.008000
775	0.000059	0.000021	0.000000	80.5985	65.09410	239.370000
780	0.000042	0.000015	0.000000	78.2740	63.38280	241.675000

Annex D:

The Kodak Q60R2-07-2010 target, the Patch_Dav_03 target (an home-made target, presenting different colors than the learning target), and the Eye-One ScanTarget 1.4 target we used into the scanner calibration LUT tests.

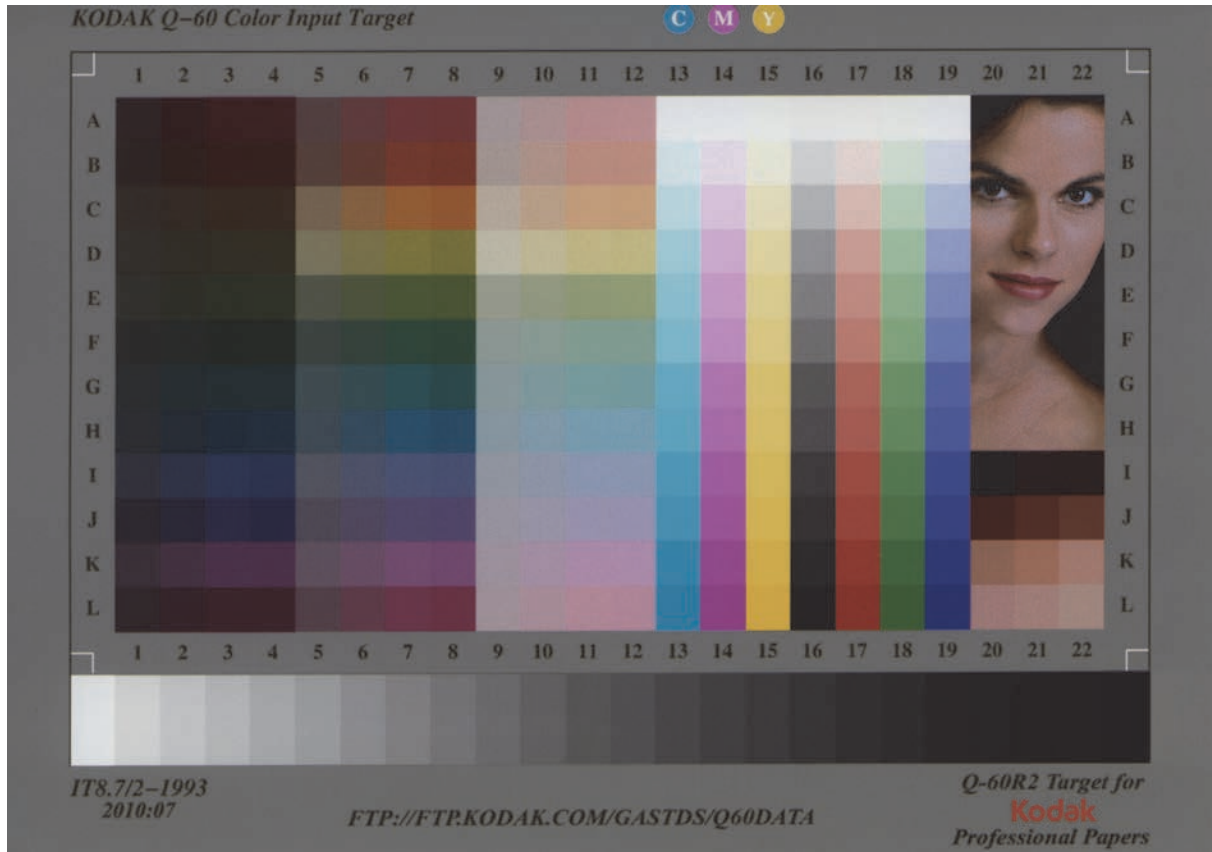


Figure 138. The Kodak Q-60R2 Target used for scanner color calibration tests.

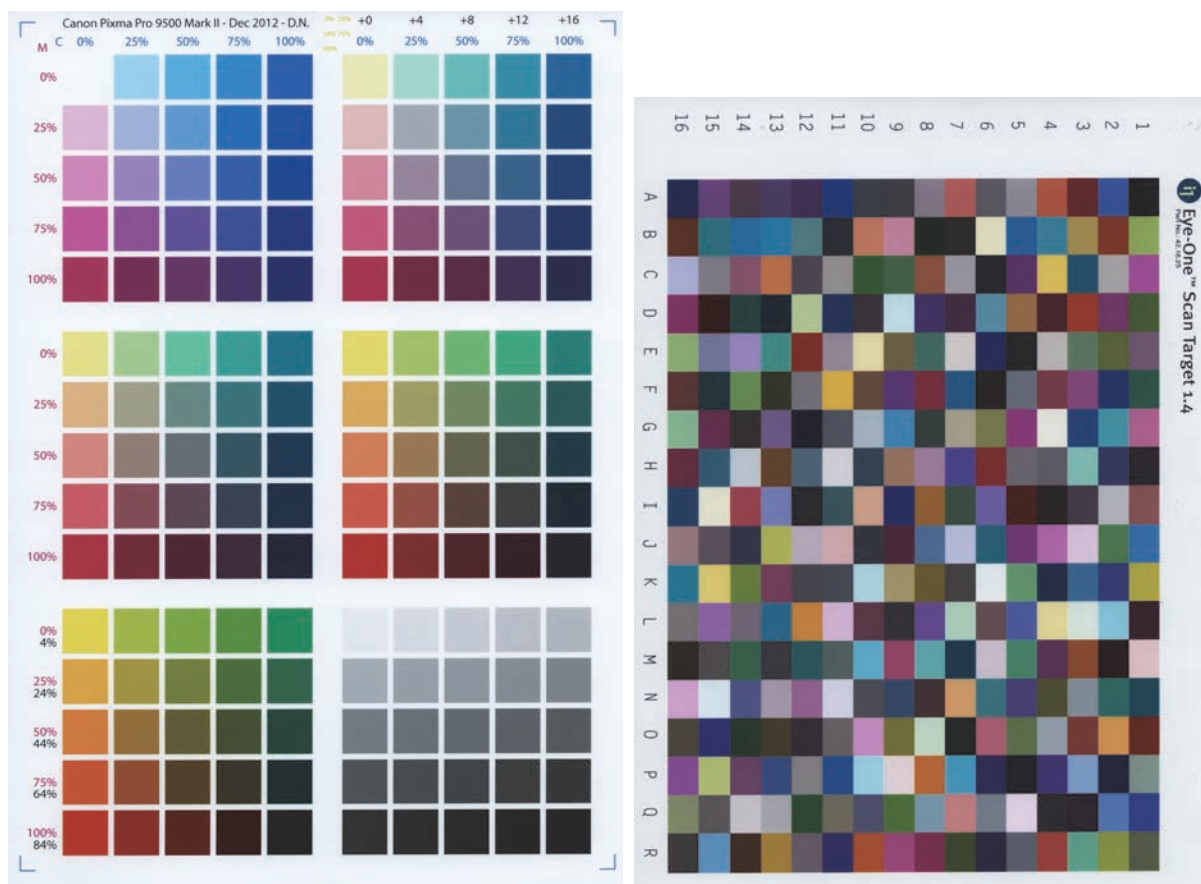


Figure 139. The Patch_Dav_03 target (left), and the Eye-One ScanTarget 1.4 target (right) used for scanner color calibration tests.

List of Figures

Figure 1. Examples of natural textural objects.	20
Figure 2. “Natural” interpretations of textures.	20
Figure 3. Example of periodical texture, containing Repetitive Texture Elements (Texels).	20
Figure 4. Example of random texture with homogeneous statistical properties.	21
Figure 5. Between random and periodical textures.	21
Figure 6. Notion of scale in Texture analysis.	21
Figure 7. An Histogram: A graphical representation of the gray level distribution.	22
Figure 8. Different textures presenting close histograms.	23
Figure 9. Two different images presenting exactly the same two first statistical moments.	24
Figure 10. A pair of pixels coordinates $((x_p, y_p), (x_p, y_p + D))$ designated by the vector \mathbf{t} , with respective values i and j ; involving the entry (i, j) of the gray level co-occurrence matrix to be incremented.	25
Figure 11. (a) Three original gray level images. (b) Gray level representation of the corresponding GLCM where the white color means the max value. (c) Zoom on the center of images (b).	26
Figure 12. Frequency ring and direction sector masks to apply in the Fourier domain.	28
Figure 13. Frequencies features extraction by filtering in the Fourier domain with different ring sizes.	29
Figure 14. Frequencies features extraction by filtering in the Fourier domain with different sectors directions.	29
Figure 15. Need of a smoothing. A Gaussian smoothing before a Sobel filtering enables recover edges.	31
Figure 16. Gradient of Gaussian filtering, (a) is the input image, and (d) the module of its Fourier transformed; (b) the GOG filter with a standard deviation of 4 pixels, and (e) the module of its Fourier transformed; (f) is the product of (d) and (e), and (c) is the resulting filtered image obtained by taking the module of the resulting complex image after inverse Fourier transform of (f). For a better visibility, we draw the logarithm of the module for all spectrums. A zoom in (f) would show that the zero-frequency has been totally removed by the filtering, resulting in an absence of solid areas in (c).	32
Figure 17. Contour points detection: extraction of the local maximums of the gradient in the gradient direction.	33
Figure 18. A Human eye scheme. Illustration from AVMD - Dr. Eberhard A.- W. Peters, Internist – Betriebsmedizin – Flugmedizin, 38102 Braunschweig, Wolfenbütteler Str. 80.	36
Figure 19. Cones and rods in the periphery of the fovea. Source: Curcio et al., 1990	36
Figure 20. Cones in the fovea. Source: Curcio et al., 1990	37
Figure 21. The distribution of rods and cones in the human retina. The left figure gives the locations on the retina of the “angle” relative to the optic axis used on the right figure (based on Lindsay & Norman, 1977).	37
Figure 22. Absorbance curves of the three types of cones, (S), (M), (L) of a human retina.	37
Figure 23. Photoreceptors connexions inside the retina. Light has to cross all the neuronal cells before hitting a photoreceptor.	38
Figure 24. A “receptive field” of adjacent photoreceptors. Image from Wolters Kluwer Health, Lippincott Williams and Wilkins, 2011	38

Figure 25. The visible spectrum. Illustration from www.euhou.net . Maite Lacarra et al. universit� Pierre et Marie Curie, Paris, France.	39
Figure 26. White light beam dispersing through a prism into a spectrum.	39
Figure 27. The transmission phenomenon of a light beam crossing a transparent object.....	40
Figure 28. Absorption of input white light by a colored transparent material.....	40
Figure 29. Light scattering by a translucent material. In such a configuration, a part of light is transmitted, and another part is diffusely reflected by scattering. Reflection at the surface occurs.	41
Figure 30. Light scattering by an opaque material. There is no transmitted light, but a part is diffusely reflected by scattering. Reflection at the surface occurs.	41
Figure 31. Light reemission by a fluorescent, opaque object. The input green light is absorbed and reemitted into red light.	42
Figure 32. Shadow mask in CRT screens.....	42
Figure 33. RGB color cube.	43
Figure 34. Munsell's painted globe designed to the definition of the five principal hues, in 1905.....	44
Figure 35. Representation of the ten principal hues, and some intermediates.	45
Figure 36. The cylindrical HSV (Hue, Saturation or Chroma, and Value) representation.	45
Figure 37. Relative sensitivity curves for an ideal observer, and optimal primaries to develop a colorimeter at 450 nm, 550 nm, and 650 nm, corresponding with the maxima sensitivity of each observer cone receptors for maximal efficiency.	47
Figure 38. Computation of observer/colorimeter responses (right) by integration: For each wavelength, the stimulus's spectral power distribution (obtained by the product of the source light power with the object reflectance curves) is multiplied by each of the three cone's spectral sensitivities, and the products are summed.....	47
Figure 39. Optimal primaries of 400 nm, 520 nm, and 700 nm for maximization of the independence of the real observer cone responses.	48
Figure 40. A color-matching experiment. The reference field presents three monochromatic lamps. The test field presents also the same three primaries, and includes another test light (shown in yellow).	48
Figure 41. Plot of the CIE RGB color matching functions for the 1931 CIE Standard observer.	49
Figure 42. Color difference ΔE_{ab}^* in the CIELAB color space can be computed by the Euclidian distance between two stimuli.	52
Figure 43. Scanner principle diagram.....	55
Figure 44. EPSON PERFECTION V700 Photo scanner. cf. Epson web site for more details.	56
Figure 45. Reflection of light by a surface.	56
Figure 46. Transmission through a slice of material.....	57
Figure 47. Black ink density in an example of a photo from Public Monuments & Sculpture association web site, http://www.pmsa.org.uk/pmsa-database/632/	57
Figure 48. KODAK Q-60R2 Color Input Target.	58
Figure 49. 3D view of the 385 color patches of the KODAK Q-60 Color Input Target in (a) sRGB color space, and (b) AdobeRGB color space.	59
Figure 50. Comparaison of sRGB and AdobeRGB color spaces.	59

Figure 51. Visualization in (a*b*) plan of the deviation between ground truth values (red side of lines) and digitalized values (black side of lines) for color patch of KODAK Q-60 Color Input Target, considering scanned values in sRGB color space (a) or AdobeRGB color space (b).	60
Figure 52. Histogram of color differences of the digitalized KODAK Q-60 Color Input Target (AdobeRGB) compared to the ground truth values.	60
Figure 53. Digitalization of a black and white pattern at 1200 ppi for chromatic aberrations identification.....	61
Figure 54. Example of acquisition of a graph paper sheet for spatial calibration.	62
Figure 55. Study of the horizontal and vertical resolution drift.	62
Figure 56. Scan at 600 ppi of a Bar-target chart from Kodak target for measurement of the MTF of our scanner.	63
Figure 57. Plot of the computed MTF in vertical and horizontal directions of our EPSON PERFECTION V700 Scanner computed with the bar pattern chart on Figure 56.	64
Figure 58. Home-made angle bracket laid on the scanner glass for constant sample scanning location.	66
Figure 59. Target mask for the automatic computation of the color values of each patch.	67
Figure 60. Correspondence between the luminance obtained on the scanned image and the one of the ground truth, for the 24 gray patches of the Kodak target.	68
Figure 61. Fitting of the relationship between the luminance channel of reference image, and the luminance obtained from the scanned image. The polynome kept is: $-0.0036X^2 + 1.3681X - 3.5516$	68
Figure 62. The construction of first, second, and third polynomial orders.	70
Figure 63. The Kodak Q60R2-07-2010 target image obtained after scan without any correction.	71
Figure 64. The Kodak Q60R2-07-2010 target image obtained after scan and gamma correction.	71
Figure 65. Kodak Q60R2-07-2010 target image obtained after scan, gamma correction, and color transform.	72
Figure 66. The i1Pro (left) and the SpectroEye (right) spectrophotometers we used.	74
Figure 67. Our SpectroEye specifications.	75
Figure 68. Absorbing media illustrating the Beer-Lambert-Bouguer law.	78
Figure 69. Light scattering by an infinitesimal layer of thickness dx	78
Figure 70. Illustration of Saunderson correction.	81
Figure 71. Reflection and refraction of a radiance at the interface between two media.	82
Figure 72. Definition of infinitesimal solid angle.	83
Figure 73. Structure comprising a white diffusing background coated with non-scattering ink layer.	86
Figure 74. $w_{a,b}$ function for three different sets of (a,b) values. Original Haralick's attribute (denoted as Hom) corresponds to the $w_{1,2}$ function plotted in red line. $w_{0,1,4}$ and $w_{0,6,4}$ functions, respectively denoted as $Hom1$ and $Hom2$, are plotted in blue, respectively green lines.	93
Figure 75. Our main algorithm flowchart.	94
Figure 76. Image registration and pre-processing: the RGB input image is converted into four gray level images according to human vision.	94
Figure 77. Definition of σ knowing the visual angular resolution $\alpha = 1' = \frac{1}{60}$ degree at the viewing distance d	95
Figure 78. Variation of the $a^{(HR)}$ and $a^{(LR)}$ values as a function of the chroma values $c^{(HR)}$, respectively $c^{(LR)}$, for HR and LR images.	97

Figure 79. An overview of some scanned samples (in lower resolution than the original ones). s_02 is printed on glossy photograph paper, s_01 and s_08 on office paper, s_10 and s_11 on APCO paper. All patches have same size.	98
Figure 80. Comparison between objective and subjective evaluations for (a): a blue set of samples, (b): an orange set of samples, (c): a red set of samples, and (d): a gray set of samples.	99
Figure 81. Comparison between objective and rescaled subjective evaluations for (a): a blue set of samples, (b): an orange set of samples, (c): a red set of samples, and (d): a gray set of samples.	100
Figure 82. Percentage of samples classified in the same of six categories by assessors (subjective evaluation) and by our scoring method for homogeneity attribute.	101
Figure 83. An overview of some scanned samples of prints on polycarbonate with different printing systems, and their corresponding homogeneity score given by our method for large patch (homogeneity score) or small patch (homogeneity small patch score).	101
Figure 84. Our Main algorithm flowchart for the assessment of Edge Sharpness.	104
Figure 85. The original digital layout.	105
Figure 86. Scanned, not color-corrected image of a printed sample of the original image.	105
Figure 87. Scanned image, including color correction, of a printed sample of the original image.	106
Figure 88. Logical mask, with “objects” in white, and background in black.	107
Figure 89. Gray-level image of the printed-scanned version of a picture to assess edge sharpness.	109
Figure 90. Black-and-white image obtained from gray-level image after binarization.	110
Figure 91. “Cleaned” black-and-white image.	110
Figure 92. Registered original image.	111
Figure 93. Before image registration. Green lines corresponds to the original image contours.	112
Figure 94. After image registration. Green lines corresponds to the original image contours.	112
Figure 95. Module of the Gradient of Gaussian filtering, on the registered original image (top) and the scanned image (bottom).	113
Figure 96. The four different cases for the decision to select the point M on a contour (in red line on the figure), depending on the direction of the gradient (in dashed arrow on the figure).	114
Figure 97. Localization of the contours in the original image (center) and in the printed copy (right).	115
Figure 98. Sharpness evaluation by measurement of the edge thickness in the Laplacian of Gaussian filtering applied to the original (left side) and printed-then-scanned (right side) images.	116
Figure 99. Localization of the contours in the original image (in red) and in the scanned image (in green).	116
Figure 100. Study of a line profile (in red line), in the Laplacian image, defined by the direction of the gradient (specified by the dashed arrow).	117
Figure 101. Histogram corresponding of our “width” and “angle” delocalisation score for the sample image in reference to the original layout image.	119
Figure 102. Three images used in our experiments to assess edge sharpness criteria.	120
Figure 103. Comparison between objective and subjective evaluations for three images for the edge sharpness criteria.	120
Figure 104. Sharpness scores computed on 5 printed copies of a same digital layout.	121
Figure 105. Percentage of samples classified in the same of six categories by assessors (subjective evaluation) and by our scoring method for edge sharpness attribute.	121

Figure 106. "Checkershadow Illusion" by Adelson Edward H. (1995): (a) original image, and (b): image with uniform rectangle showing that A and B boxes have the same color.	123
Figure 107. From lightness constancy to color constancy, by Akiyoshi Kitaoka (2009). (a) original image, and (b): image with uniform rectangle showing that the girl have not mismatched eyes.....	124
Figure 108. Main algorithm flowchart for the assessment of Colorfulness.....	125
Figure 109. Comparison between (a) the original layout, (b) a print in D2T2 redigitalized by scanner, (c) a color correction of this scan, and (d) the simulation of the printed version with Berns' equation.	126
Figure 110. (a) Original digital image, (b) scanned printed image in inkjet on office paper, (c) scanned image after calibration of the scanned, and (d) D2T2 simulated image (considered as reference)).	127
Figure 111. Projection on the CIELAB (a^*, b^*) plane of the pixel colors of the reference image, and its convex hull plotted in red solid line.....	127
Figure 112. Delaunay triangulation of the set of color points of the reference image in the CIELAB 2-D (a^*, b^*) plane.....	128
Figure 113. Histogram of the triangle size of the Delaunay triangulation of the reference image.	129
Figure 114. "Area-filtered" Delaunay triangulation of the set of color points of the reference image in the CIELAB (a^*, b^*) plane.....	129
Figure 115. Projection on the CIELAB (a^*, b^*) plane of the pixel colors of the printed-then-scanned image, and its convex hull plotted in red solid line.....	130
Figure 116. Delaunay triangulation of the set of color points of the reference image in the CIELAB 2-D (a^*, b^*) plane.....	131
Figure 117. Histogram of the triangle size of the Delaunay triangulation of the scanned image.	131
Figure 118. "Area-filtered" Delaunay triangulation of the set of color points of the printed-then-scanned image in the CIELAB (a^*, b^*) plane.	132
Figure 119. The four images used for testing our colorfulness attribute.	133
Figure 120. Comparison between objective and subjective evaluations for three images for the colorfulness criteria.	134
Figure 121. Percentage of samples classified in the same of six categories by assessors (subjective evaluation) and by our scoring method for colorfulness attribute.	134
Figure 122. The CMYart ink containing a mixture of cyan, magenta and yellow pigments (dark area) deposited on polycarbonate substrate (white area).	139
Figure 123. Microscopic images of areas printed in red, green, blue obtained by irradiation with, respectively, red laser, green laser and blue laser at relative power 0.5 (left) or 1 (right). The coloring layer is nearly continuous, no halftoning is needed. Higher laser power gives brighter color.	139
Figure 124. Predicted and measured spectral reflectances of the non-irradiated colorant mixture on polycarbonate card in CLM with fitted optical thickness values deduced from Eq (8.1).	142
Figure 125. Distributions of the ΔE_{94} values computed between measured and predicted spectral reflectances, given by Berns equation with fitted optical thickness of the three dyes, a) for D2T2 printed cards and b) for CLM printed cards.	143
Figure 126. Measured and predicted spectral reflectances of three CLM printed patches. The predicted spectra in blue line assume that one colorant has an optical thickness 0 and the other two colorants have an optical thickness 1. Those in red line were obtained with fitted optical thickness of the three colorants.	144
Figure 127. Virtual primary transmittances corresponding to the exponential of the first six basis vectors issued from the PCA.	147

Figure 128. Spectral reconstruction accuracy of CLM prints, tested over 570 printed colors, as a function of the number M of primary spectra obtained by SVD computed from various numbers of color patches.....	147
Figure 129. Red, Green, Blue, Yellow, Magenta, and Cyan color gradients obtained with low (dashed line) and high (solid line) blue laser power.	149
Figure 130. Printed patches colors represented in the CIELAB (a^*, b^*) plane, among which those used for the learning of the RGB to optical thicknesses transform, and for the verification of the model.	150
Figure 131. Histogram representing the distribution of ΔE_{94} values computed from the measured reflectance of the 276 CLM verification patches and the reflectance predicted by our method.	150
Figure 132. Performances of the prediction according to the number of learning patches and the number of considered primaries.	151
Figure 133. The Qt framework logo.	153
Figure 134. Qt can adapt itself to Linux, Windows, or Mac OS.	154
Figure 135. Graphical user interface of CLMviewer.	155
Figure 136. Simulation of a CLM printing with CLMviewer.	156
Figure 137. Kodak Test chart TL-5003	167
Figure 138. The Kodak Q-60R2 Target used for scanner color calibration tests.....	168
Figure 139. The Patch_Dav_03 target (left), and the Eye-One ScanTarget 1.4 target (right) used for scanner color calibration tests.	169

References

1. H. Kipphan, *Handbook of Print Media* (Springer Ed., 2001).
2. N. Baudet, Baudet, "Control of visual quality products - Formalization of process expertise and proposal of a robust approach to human visual inspection," (Université de Grenoble, 2012).
3. M. Pedersen, N. Bonnier, J. Y. Hardeberg, and F. Albrechtsen, "Attributes of a New Image Quality Model for Color Prints," *Color and Imaging Conference* **2009**, 204-209 (2009).
4. M. Pedersen, and S. A. Amirshahi, "Framework for the Evaluation of Color Prints Using Image Quality Metrics," *Conference on Colour in Graphics, Imaging, and Vision* **2010**, 75-82 (2010).
5. M. Gong, and M. Pedersen, "Spatial pooling for measuring color printing quality attributes," *Journal of Visual Communication and Image Representation* **23**, 685-696 (2012).
6. M. Pedersen, N. Bonnier, J. Y. Hardeberg, and F. Albrechtsen, "Attributes of image quality for color prints," *ELECTIM* **19**, 011016-011016-011013 (2010).
7. J. Lundström, and A. Verikas, "Assessing print quality by machine in offset colour printing," *Knowledge-Based Systems* **37**, 70-79 (2013).
8. M. Sonka, V. Hlavac, and R. Boyle, *Image processing, analysis, and machine vision* (Cengage Learning, 4th edition, 2014).
9. R. M. Haralick, "Statistical and structural approaches to texture," *Proceedings of the IEEE* **67**, 786-804 (1979).
10. H. Maître, "Le traitement des images," Hermes Science Publications, Paris (2003).
11. P. Brodatz, *Textures: a photographic album for artists and designers* (Dover publications, 1966).
12. The Massachusetts Institute of Technology, "The VisTex database," <http://vismod.media.mit.edu/vismod/imagery/VisionTexture/vistex.html>.
13. T. Ojala, T. Mäenpää, M. Pietikainen, J. Viertola, J. Kyllönen, and S. Huovinen, "Outex-new framework for empirical evaluation of texture analysis algorithms," in *Proceedings. 16th International Conference on Pattern Recognition*(IEEE2002), pp. 701-706.
14. The University of Oulu, "The Outex Texture Database," <http://www.outex.oulu.fi/>.
15. T. Ojala, M. Pietikainen, and D. Harwood, "Performance evaluation of texture measures with classification based on Kullback discrimination of distributions," in *Proceedings of the 12th IAPR International Conference on Pattern Recognition, Vol. 1*(1994), pp. 582-585.
16. T. Ojala, M. Pietikainen, and D. Harwood, "A comparative study of texture measures with classification based on feature distributions," *Pattern Recognition* **29**, 51-59 (1996).
17. R. M. Haralick, K. Shanmugam, and I. H. Dinstein, "Textural Features for Image Classification," *Systems, Man and Cybernetics, IEEE Transactions on* **SMC-3**, 610-621 (1973).
18. M. M. Galloway, "Texture analysis using gray level run lengths," *Computer Graphics and Image Processing* **4**, 172-179 (1975).
19. Paul E. Black, Vreda Pieterse, "Mahattan distance, in Dictionary of Algorithms and Data Structures [online],," <http://www.nist.gov/dads/HTML/manhattanDistance.html>.
20. Q. Zhang, and R. L. Canosa, "A comparison of histogram distance metrics for content-based image retrieval," (2014), pp. 902700-902700-90279.
21. N. Dalal, and B. Triggs, "Histograms of oriented gradients for human detection," in *IEEE Computer Society Conference on Computer Vision and Pattern Recognition, vol. 1*(2005), pp. 886-893.
22. G. Srinivasan, and G. Shobha, "Statistical texture analysis," *proceedings of world academy of science, engg & tech* **36** (2008).

23. E. L. Hauck, "Data compression using run length encoding and statistical encoding," (Intelligent Storage Inc., 1986), US4626829 A.
24. J. Fourier, *Theorie analytique de la chaleur* (Firmin Didot, père et fils, 1822), chap. III, sections I & II, pp. 159-177.
25. C. Ducottet, T. Fournel, and C. Barat, "Scale-adaptive detection and local characterization of edges based on wavelet transform," *Signal Processing* **84**, 2115-2137 (2004).
26. J. Kepler, *Astronomiae pars optica* (Francofurti : apud C. Marnium et haeredes J. Aubrii, 1604).
27. J. Locke, and M. Montuori, John Locke. A Letter concerning toleration : Latin and English texts revised and edited with variants and an introduction by Mario Montuori (M. Nijhoff, 1963), LII-123 p., fac-sim. h.-t. [Acq. 2240-65] ; ln-8° (22 cm).
28. G. Sharma, *Digital Color Imaging Handbook* (CRC Press, 2002).
29. T. Smith, and J. Guild, "The C.I.E. colorimetric standards and their use," *Transactions of the Optical Society* **33**, 73 (1931).
30. C. CIE, "Commission Internationale de l'Eclairage Proceedings, 1931," (Cambridge University Press Cambridge, 1932).
31. G. E. Co., "The Hardy recording spectrophotometer," *Oil Fat Ind* **6**, 31-33 (1929).
32. J. L. Michaelson, "Construction of the General Electric Recording Spectrophotometer," *Journal of the Optical Society of America* **28**, 365-365 (1938).
33. W. D. Wright, "The sensitivity of the eye to small colour differences," *Proceedings of the Physical Society* **53**, 93 (1941).
34. D. L. Macadam, "Visual Sensitivities to Color Differences in Daylight," *Journal of the Optical Society of America* **32**, 247-273 (1942).
35. W. R. T. Brown, and D. L. Macadam, "Visual Sensitivities to Combined Chromaticity and Luminance Differences," *Journal of the Optical Society of America* **39**, 808-823 (1949).
36. G. Wyszeckai, and G. H. Fielder, "Color-Difference Matches," *Journal of the Optical Society of America* **61**, 1501-1513 (1971).
37. G. Wyszecki, and G. H. Fielder, "New Color-Matching Ellipses," *Journal of the Optical Society of America* **61**, 1135-1152 (1971).
38. "Bruce Lindbloom web site," <http://www.brucelindbloom.com>.
39. G. Wyszecki, and W. S. Stiles, *Color Science: Concepts and Methods, Quantitative Data and Formulae*, 2nd ed. (Wiley, 1982).
40. T. Johnson, "Methods for characterizing colour scanners and digital cameras," *Displays* **16**, 183-191 (1996).
41. I. Yilmaz, I. O. Bildirici, M. Yakar, and F. Yildiz, "Color calibration of scanners using polynomial transformation," in *XXth ISPRS Congress Commission V, Istanbul, Turkey*(2004), pp. 890-896.
42. V. Cheung, S. Westland, D. Connah, and C. Ripamonti, "A comparative study of the characterisation of colour cameras by means of neural networks and polynomial transforms," *Coloration Technology* **120**, 19-25 (2004).
43. M. Hébert, and R. D. Hersch, "Review of spectral reflectance models for halftone prints: Principles, Calibration, and prediction accuracy," *Color Research & Application* **40**, 383-397 (2015).
44. P. Bouguer, *Essai d'Optique, sur la gradation de la lumiere* (Claude Jombert, 1729).
45. J. H. Lambert, *Photometria* (1760).
46. M. Hébert, and R. D. Hersch, "Reflectance and transmittance model for recto-verso halftone prints," *J. Opt. Soc. Am. A* **23**, 2415-2432 (2006).
47. J. L. Saunderson, "Calculation of the Color of Pigmented Plastics," *Journal of the Optical Society of America* **32**, 727-729 (1942).
48. S. Q. Duntley, "The Optical Properties of Diffusing Materials," *Journal of the Optical Society of America* **32**, 61-61 (1942).
49. F. C. Williams, and F. R. Clapper, "Multiple Internal Reflections in Photographic Color Prints," *J. Opt. Soc. Am.* **43**, 595-597 (1953).
50. D. B. Judd, "Fresnel reflection of diffusely incident light," *J. Natl. Bur. Standards* **29**, 329 (1942).

51. F. R. Clapper, and J. A. C. Yule, "The Effect of Multiple Internal Reflections on the Densities of Half-tone Prints on Paper," *J. Opt. Soc. Am.* **43**, 600-603 (1953).
52. R. S. Berns, "Spectral modeling of a dye diffusion thermal transfer printer," *J. Electron. Imaging* **2**, 359-370 (1993).
53. A. D. McNaught, and A. Wilkinson, *Compendium of Chemical Terminology* (Blackwell Science, Oxford, U.K., 1997).
54. D. Nébouy, M. Hébert, T. Fournel, and J. L. Lesur, "Visual quality of printed surfaces: study of homogeneity," (2014), pp. 90160C-90160C-90110.
55. Standard, "IEC 13660 Information technology—Office equipment—Measurement of image quality attributes for hardcopy output—Binary monochrome text and graphic images"—ISO," (IEC, 2001).
56. A. Sadovnikov, P. Salmela, L. Lensu, J.-K. Kamarainen, and H. Kälviäinen, "Mottling Assessment of Solid Printed Areas and Its Correlation to Perceived Uniformity," in *Image Analysis*, H. Kalviainen, J. Parkkinen, and A. Kaarna, eds. (Springer Berlin Heidelberg, 2005), pp. 409-418.
57. M. Dube, F. Mairesse, J.-P. Boisvert, and Y. Voisin, "Wavelet Analysis of Print Mottle," *IEEE Transactions on Image Processing* (2005).
58. P.-Å. Johansson, "Optical Homogeneity of Prints," in *Department of Pulp and Paper Chemistry and Technology* (Royal Institute of Technology, Stockholm, 1999).
59. P. Jackman, D.-W. Sun, and G. ElMasry, "Robust colour calibration of an imaging system using a colour space transform and advanced regression modelling," *Meat Science* **91**, 402-407 (2012).
60. D. H. Pritchard, "U.S. Color Television Fundamentals: A Review," *SMPTE Journal* **86**, 819-828 (1977).
61. H. v. Helmholtz, and J. P. C. Southall, "Helmholtz's Treatise on Physiological Optics. Vol. II: The Sensations of Vision, trans. JPC Southall.(Translated from the Third German Edition)," *The Optical Society of America* (1924).
62. ITU, "Studio encoding parameters of digital television for standard 4:3 and wide-screen 16:9 aspect ratios," in *Broadcasting service (television)* (2011).
63. F. Depled, *Evaluation sensorielle Manuel méthodologique* (Tec Et Doc, 2009).
64. A. R. Martinez, N. Richard, and C. Fernandez-Maloigne, "Colour Contrast Occurrence matrix: a vector and perceptual texture feature," presented at the Color and Imaging Conference 23, Darmstadt, Germany 2015.
65. M. Brichon, T. Bugnon, M. Hebert, and R. Hersch, "Deducing ink spreading curves from reflection spectra acquired within printed color images," *Journal of Imaging Science and Technology* **53**, 30502-30501-30502-30507 (2009).
66. B. Froissard, "Assistance visuelle des malvoyants par traitement d'images adaptatif," (Université de Saint-Étienne, 2014).
67. J. Dijk, M. van Ginkel, R. van Asselt, L. van Vliet, and P. Verbeek, "A New Sharpness Measure Based on Gaussian Lines and Edges," in *Computer Analysis of Images and Patterns*, N. Petkov, and M. Westenberg, eds. (Springer Berlin Heidelberg, 2003), pp. 149-156.
68. T. V. Cuong, "S3: A Spectral and Spatial Sharpness Measure," M. C. Damon, ed. (2009), pp. 37-43.
69. D. Shaked, and I. Tastl, "Sharpness measure: towards automatic image enhancement," in *Image Processing, 2005. ICIP 2005. IEEE International Conference on* (2005), pp. I-937-940.
70. G. Matheron, "Eléments pour une théorie des milieux poreux," (1967).
71. J. Serra, "Image Processing and Mathematical Morphology, Part II: Theoretical Advances," (Academic Press, London, 1988).
72. N. Otsu, "A Threshold Selection Method from Gray-Level Histograms," *IEEE Transactions on Systems, Man, and Cybernetics* **9**, 62-66 (1979).
73. B. Delaunay, "Sur la sphère vide. A la mémoire de Georges Voronoï," *Bulletin de l'Académie des Sciences de l'URSS*, 793-800 (1934).
74. D. Nébouy, M. Hébert, T. Fournel, N. Larina, and J.-L. Lesur, "Prediction of the spectral reflectance of laser-generated color prints by combination of an optical model and learning methods," *J. Opt. Soc. Am. A* **32**, 1661-1671 (2015).

75. N. Destouches, N. Crespo-Monteiro, L. Nadar, T. Epicier, Y. Liu, Y. Lefkir, and F. Vocanson, "Laser control of metallic nanoparticles for reversible or permanent color marking," in *International Conference on Small Science*(Orlando, United States, 2012).
76. N. Destouches, J. Martínez-García, M. Hébert, N. Crespo-Monteiro, G. Vitrant, Z. Liu, A. Trémeau, F. Vocanson, F. Pigeon, S. Reynaud, and Y. Lefkir, "Dichroic colored luster of laser-induced silver nanoparticle gratings buried in dense inorganic films," *J. Opt. Soc. Am. B* **31**, C1-C7 (2014).
77. N. Lutz, and G. Zinner, "Plastic body, which is provided in the form of a film, for example, a transfer film or laminate film or which is provided with a film of this type, and method for producing color image on or in a plastic body of this type," (2004), US 2004/0043308 A1.
78. Y. Bielek, and E. Barker, "Laser activated thermochromic compositions," (FLEXCON COMPANY, INC., 2006), WO 2006/113778 A2.
79. L. Fannasch, M. Hennemeyer-Schwenkner, M. Schumacher, and D. Fischer, "Method for the recording of data on/in data supports by means of laser radiation and data supports produced thus," (Orga Kartensysteme, 2006), US 6986926 B2.
80. T. Sakagami, A. Hashimoto, and Y. TERAJI, "Multicolor-development laser marking sheet for card, and laser marking method," (Japan Coloring Co., Ltd., 2013), WO 2013031399 A1.
81. K. Nassau, *Color for science, Art and technology* (Elsevier, 1998).
82. J. Fabian, and H. Hartmann, *Light Absorption of Organic Colorants: Theoretical Treatment and Empirical Rules* (Springer-Verlag Berlin Heidelberg, 1980).
83. R. Johnston-Feller, *Color science in the examination of museum objects: Nondestructive procedures* (Getty Publications, 2001).
84. G. T. Eaton, *Photographic Chemistry: In Black-And-White and Color Photography* (3rd Ed. – Morgan & Morgan Inc., 1980).
85. H. Zollinger, *Color Chemistry: Syntheses, Properties and Applications of Organic Dyes and Pigments* (WILEY-VCH, 2003).
86. LumeJet, "Photographic Quality Digital Printing," <http://www.lumejet.com/technology/photographic-quality-digital-printing>.
87. R. M. Christie, *Colour Chemistry* (The Royal Society of Chemistry, 2001).
88. K. Levenberg, "A Method for the Solution of Certain Problems in Least Squares," *Quarterly Applied Math.* **2**, pp. 164-168 (1944).
89. D. W. Marquardt, "An Algorithm for Least-Squares Estimation of Nonlinear Parameters," *J. Soc. Indust. Appl. Math.* **11**, 431-441 (1963).
90. J. J. Moré, "The Levenberg-Marquardt algorithm: Implementation and theory," in *Numerical Analysis*, G. A. Watson, ed. (Springer Berlin Heidelberg, 1977), pp. 105-116.
91. J. Y. Hardeberg, "On the spectral dimensionality of object colours," *Conference on Colour in Graphics, Imaging, and Vision* **2002**, 480-485 (2002).
92. D.-Y. Tzeng, and R. S. Berns, "A review of principal component analysis and its applications to color technology," *Color Res. Appl.* **30**, 84-98 (2005).
93. T. Bugnon, "Flexible and Robust Calibration of the Yule-Nielsen Model for CMYK Prints," (EPFL, 2011).
94. W. H. Press, S. A. Teukolsky, W. T. Vetterling, and B. P. Flannery, *Numerical recipes in C (2nd ed.): the art of scientific computing* (Cambridge University Press, 1992), chap. 2.6.
95. F. H. Imai, R. S. Berns, and D.-Y. Tzeng, "A comparative analysis of spectral reflectance estimated in various spaces using a trichromatic camera system," *J Imag Sci Tech* **44**, 280–287 (2000).
96. R. S. Berns, "Visible-spectrum imaging techniques: an overview," in *Proceedings of the 9th Congress of the International Colour Association. SPIE* (2002), pp. 475-480.
97. R. Charrière, M. Hébert, A. Trémeau, and N. Destouches, "Color calibration of an RGB camera mounted in front of a microscope with strong color distortion," *Appl. Opt.* **52**, 5262-5271 (2013).
98. X. Zhang, and H. Xu, "Reconstructing spectral reflectance by dividing spectral space and extending the principal components in principal component analysis," *J. Opt. Soc. Am. A* **25**, 371-378 (2008).
99. Free Software Foundation, "Qt Documentation," <http://doc.qt.io/>.

100. A. Karpathy, and L. Fei-Fei, "Deep visual-semantic alignments for generating image descriptions," arXiv preprint arXiv:1412.2306 (2014).

